Compositionally Tuned Single-Phase Oxyfluoride Phosphor Converters for Advanced Full Spectral White Light Emitting Devices

By

Sreevalsa. S
Registration No: 10CC20A39007

A thesis submitted to the
Academy of Scientific & Innovative Research
for the award of the degree of

DOCTOR OF PHILOSOPHY
in
SCIENCE

Under the supervision of
Dr. Subrata Das

CSIR-National Institute for Interdisciplinary Science and Technology (CSIR-NIIST)
Thiruvananthapuram-695019

Academy of Scientific and Innovative Research
AcSIR Headquarters, CSIR-HRDC campus,
Sector 19, Kamla Nehru Nagar,
Ghaziabad, U.P. – 201 002, India
June-2025

Dedicated to my beloved family…

राष्ट्रीय अंतर्विषयी विज्ञान तथा प्रौद्योगिकी संस्थान
वैज्ञानिक तथा औद्योगिक अनुसंधान परिषद् | विज्ञान तथा प्रौद्योगिकी मंत्रालय, भारत सरकार
इंडस्ट्रियल इस्टेट पी.ओ., पाप्पनंकोड, तिरुवनंतपुरम, भारत-695 019

CSIR-NATIONAL INSTITUTE FOR INTERDISCIPLINARY SCIENCE AND TECHNOLOGY (CSIR-NIIST)
Council of Scientific & Industrial Research | Ministry of Science and Technology, Govt. of India
Industrial Estate P.O., Pappanamcode, Thiruvananthapuram, India-695 019

CERTIFICATE

This is to certify that the work incorporated in this Ph.D. thesis entitled, "**Compositionally Tuned Single-Phase Oxyfluoride Phosphor Converters for Advanced Full Spectral White Light Emitting Devices**", submitted by ***Ms. Sreevalsa. S*** to the Academy of Scientific and Innovative Research (AcSIR) in fulfillment of the requirements for the award of the Degree of ***Doctor of Philosophy in Science***, embodies original research work carried-out by the student. We, further certify that this work has not been submitted to any other University or Institution in part or full for the award of any degree or diploma. Research material(s) obtained from other source(s) and used in this research work has/have been duly acknowledged in the thesis. Image(s), illustration(s), figure(s), table(s) etc., used in the thesis from other source(s), have also been duly cited and acknowledged.

Sreevalsa 19/06/2025

Sreevalsa. S

Subrata Das 19/06/2025

Dr. Subrata Das
(Research Supervisor)

Tel : 91 471 2515226 | 2515234 | E-mail : director@niist.res.in | Website : http://niist.res.in

STATEMENTS OF ACADEMIC INTEGRITY

I **Sreevalsa. S**, a Ph.D. student of the Academy of Scientific and Innovative Research (AcSIR) with Registration No. **10CC20A39007** hereby undertake that, the thesis entitled "**Compositionally Tuned Single-Phase Oxyfluoride Phosphor Converters for Advanced Full Spectral White Light Emitting Devices**" has been prepared by me and that the document reports original work carried out by me and is free of any plagiarism in compliance with the UGC Regulations on "*Promotion of Academic Integrity and Prevention of Plagiarism in Higher Educational Institutions (2018)*" and the CSIR Guidelines for "*Ethics in Research and in Governance (2020)*".

19/06/2025

Sreevalsa. S
Thiruvananthapuram
June 2025

It is hereby certified that the work done by the student, under my/our supervision, is plagiarism-free in accordance with the UGC Regulations on "*Promotion of Academic Integrity and Prevention of Plagiarism in Higher Educational Institutions (2018)*" and the CSIR Guidelines for "*Ethics in Research and in Governance (2020)*".

Subrata Das 19/06/2025

Dr. Subrata Das
(Research Supervisor)
Thiruvananthapuram
June 2025

ACKNOWLEDGEMENT

First and foremost, I have great pleasure in expressing my heartfelt gratitude towards ***Dr. Subrata Das****, Principal Scientist and my research supervisor, for suggesting the research problem, and for his sincere guidance throughout my Ph.D. journey, insightful comments, fruitful discussions and immense support, valuable advice, constant encouragement and sincere help in each step of my research period.*

I express my sincere thanks to ***Dr. C. Anandharamakrishnan*** *and* ***Dr. A. Ajayaghosh****, present and former Directors of the CSIR-National Institute for Interdisciplinary Science and Technology, for allowing me to utilize the laboratory facilities.*

I wish my sincere thanks to ***Dr. Jayamurthy P****. and* ***Dr. K. Karunakaran****, present and former AcSIR program coordinators at CSIR-NIIST, for their help during the academic procedures of AcSIR.*

I wish to express my sincere thanks to ***Dr. S. Ananthakumar****,* ***Dr. M. Ravi****, and* ***Dr. S Savithri*** *present and former Heads of MSTD, for allowing me to conduct my research at MSTD.*

I am extremely grateful to Doctoral Assessment Committee members- ***Dr. Achu Chandran, Dr. Ishita Neogi,*** *and* ***Dr. Adersh Asok*** *for their valuable suggestions and constant support throughout my research career.*

I express my sincere thanks to ***Dr. Sushanta Kumar Sahoo, Dr. Sreejakumari, Dr. Sudipta Som, Dr. Mukesh Kumar Pandey, Dr. Shehzad Ahmad, Dr. Santhosh K. Gupta, Parvathy, Ben John, Annu Balhara,*** *and all my Collaborators for their valuable suggestions and collaborations.*

I am extremely grateful to all Scientists in MSTD for fruitful discussions, advice, and help during the period of research work.

I would like to express my very great appreciation to ***Mr. Harish Raj V*** *for SEM analysis****, Mr. Kiran Mohan*** *for HRTEM,* ***Ms. Anjali Santhosh*** *for PXRD analysis, and* ***Mr. A Peer Muhammed*** *for XPS characterizations.*

I am also grateful to my labmates, ***Dr. Thejas K. K., Dr. Malini Abraham, Mr. Ranjith P., Dr. Revathy J. S., Dr. Shisina S, Dr. Divya Saraswathi, Dr. Sariga C. Lal*** *and* ***Ms. Meenu G.*** *for their advice, suggestions, support, and friendly atmosphere in the laboratory.*

Special mention to ***Dr. E. Suresh, Dr. Yadagiri Rachuri, and Dr. Bhavesh Parmar*** *who introduced me to the world of research. They are the first stepping stones for my research career.*

I am extremely grateful to ***Professor Chung-Hsin Lu****, and dear colleagues from National Taiwan University (NTU) for their valuable suggestions, immense support,*

love, care, and memorable companionship during my research internship at NTU.

I am also grateful to my colleagues ***Ms. Nayana Krishna, Ms. Revathy Sreekumar****,* ***Dr. Thejus P. K., Dr. Krishnapriya K V, Ms. Nithyaa J, Ms. Meera Sebastian, Mr. Shanoj P. S., Dr. Roshima K.****,* ***Ms. Sangeetha U. K.*** *and* ***Ms. Nandana Sudhakaran*** *for their advice, suggestions, and excellent companionship.*

I would like to acknowledge ***Ms. Asitha George, Ms. Swathy Lekshmy V. S., Ms. Anagha Thomas, Dr. Praveena NM.,*** *and* ***Ms. Ashwathi V. S.*** *for their immense support and companionship throughout this journey.*

I am extremely grateful to the ***DST-SERB, Ministry of Mines,*** *and* ***CSIR*** *for the financial assistance.*

I wish to express my sincere thanks to the ***Council of Scientific and Industrial Research (CSIR)*** *and the* ***Academy of Scientific and Innovative Research (AcSIR)*** *for academic facilities.*

Words are endless to express a heart full of gratitude for the boundless love, trust, support, and care extended by my parents' ***Subhagan. G*** *and* ***Sreelatha Subhagan*** *who always trusted me and inspired me to dream the highest. I would also like to express my sincere thanks to my brother late* ***Mr. Kiran S****. His memories always gave me the confidence to face problems and resolve challenges in my life.*

I have no words to express my unconditional love and sincere gratitude to my husband, ***Aravind V Suresh,*** *and my little champ* ***Sahasra Sree Aravind,*** *for their endless love, care, and continuous encouragement in times of disappointment and failure. Without their support it's impossible for the successful completion of my Ph.D. work, the way they make me comfortable is wordless.*

I would also like to acknowledge my parents-in-law ***Suresh V. S.*** *and* ***Suma Suresh****, and all my friends, cousins, relatives, and technical and non-technical staff from CSIR-NIIST for their support and help during this journey.*

I also greatly acknowledge my friend ***Ashiq Noushad*** *for his countless support, love, care, and motivation during my professional and personal life.*

Finally, not at the least, I express my sincere thanks to God Almighty for giving me the knowledge, blessings, strength, and courage, for the successful completion of this work.

Sreevalsa. S

Table of contents

List of Figures

List of Tables

List of Symbols and Abbreviations

WLEDs	White Light-emitting diodes
YAG	$Y_3Al_5O_{12}$
α	Alpha
η	Quantum Efficiency
lm	Lumen
W	Watt
D_q	Crystal Field Parameter
β	Nephelauxetic Parameter
τ	Decay time
ΔT	Temperature Difference
E_a	Activation Energy
H	Planks constant
T	Temperature
k_B	Boltzmann constant
NIR	Near-Infrared
UV	Ultraviolet
NUV	Near Ultraviolet
3D	3 dimensional
IC	Internal Conversion
ISC	Intersystem crossover
S1	Singlet state
T1	Triplet state
S0	Ground State
CTB	Charge Transfer Band
QE	Quantum Efficiency
IQE	Internal Quantum Efficiency
EQE	External Quantum Efficiency
CIE	Commission International de I'Eclairage
CRI	Color Rendering Index
CCT	Correlated Color Temperature
LCD	Liquid-Crystal Displays

FIR	Fluorescence Intensity Ratio
QDs	Quantum dots
SSR	Solid-State Reaction
DFT	Density functional theory
XRD	X-ray Diffraction
JCPDS	Joint committee on Powder Diffraction Standards
XPS	X-ray Photoelectron Spectroscopy
EPR	Electro Paramagnetic Resonance
FT-IR	Fourier Transform Infrared
HR-TEM	High-Resolution Transmission Electron Microscope
SEM	Scanning Electron Microscopy
EL	Electroluminescence
PLE	Photoluminescence Excitation
PL	Photoluminescence emission
FWHM	Full width at half maximum
EDS or EDAX	Energy Dispersive X-ray spectrum
SAED	Selected Area Electron Diffraction
DRS	Diffuse Reflectance Spectroscopy
LTPL	Low-temperature Photoluminescence
NW	Nanowire
FFT	Fast Fourier Transform
TS	Tanabe–Sugano
RT	Room temperature
pc-LEDs	Phosphor-converted light-emitting diodes

Preface

In the 21st century, phosphor-converted white light-emitting diodes (pc-WLEDs) are emerging as a new light source for advanced solid-state lighting, lasers, backlight displays, bio-medical imaging, afterglow materials, etc. pc-WLEDs still now retain the market potential because of their remarkable advantages like eco-friendly, high-frequency operation, minimum power consumption, very low heat dissipation, high efficiency and durability than other lighting technologies. In WLED fabrication, phosphor materials are crucial and act as a good colour converter in green lighting sources (LEDs). The Crucial factor that directly influences the performance of LED devices is the phosphor material chosen; it must have an efficient emission nature, high thermal and chemical stability, mild synthetic conditions, etc. Different kinds of phosphors have been examined, including oxides, oxynitrides, sulfides, aluminates etc. However, most of them face problems like low chemical stability, luminescent efficiency loss, complexity in the synthesis process and high cost.

Rare-earth ions doped oxy-fluoride phosphors have shown wide attention towards WLED lighting applications with their tunable luminescence properties. Unlike sulphide and nitride-based hosts, luminescent host matrices have high thermal and chemical stability. Introducing fluoride ions into an oxide crystal lattice leads to a distortion of the centrosymmetric sites of the polyhedrons, which causes unusual spectroscopic properties. Besides that, fluoride host matrices provide high coordination and ionicity of the rare-earth to fluorine bond, resulting in wide bandgap, low phonon energies, and low inter-configurational transitions. In contrast, the oxide host matrices provide high chemical stability and absorption in the UV-vis region. Based on these facts, oxyfluorides, which combine the advantages of both fluorides and oxides, are promising host materials for luminescence properties. Among the oxy-fluoride host matrices, Sr_3AlO_4F is the most generally studied phosphor owing to its good chemical and thermal stability, economical starting materials, facile synthesis conditions, and efficient luminescence properties.

There has been extensive research for developing a single-composition phosphor that can produce multiband emissions. Activators like Eu^{2+} or Ce^{3+} ions can be

codoped into a single system to generate broadband visible emission that can resolve the existing problem of low colour rendering (CRI) and high colour temperature (CCT) and extensive use of blue irradiations in $Y_3Al_5O_{12}$: Ce^{3+} (YAG: Ce) yellow phosphor based solid-state lighting.[7] High CRI could be achieved by adequately mixing red, green and blue emitting phosphors. However, mixing up of various phosphors causes self-absorption and complex packaging problems. In the recently reported oxyfluorides, multiple crystallographic sites could provide versatile cationic environments for Ce^{3+} or Eu^{2+} ions, effectively generating broad emissions from these ions. Eventually, an appropriate cationic replacement can drive the luminescent centres to produce emission wavelength shifts very effectively.

Integrating phosphor powders and LED devices using organic binders is a cost-effective and easy process for assembling pc-LED devices. However, when phosphor powder is glued in organic binders, pc-LEDs face carbonization reactions due to the continuous exposure to the excitation source, which results in the low thermal stability and poor heat resistance of the used binder. To overcome the mentioned problem of epoxy coatings, modern colour converters such as phosphor in glasses (PiGs), phosphor ceramics, and single crystals have been used for advanced lighting applications instead of traditional powder colour converters. They generated uniform white light emission with high luminous efficiency. However, they face poor thermal conductivity, complicated glass synthesis conditions and cost of production issues. Furthermore, the usability of continuous exposure to 460 nm blue laser may cause health issues for humans, and the rigid nature of the composite restricts its application to advanced flexible lighting technologies. To overcome these problems nowadays, the research community has shown great interest in developing polymer composite-based colour converters because of their potential applications towards flexible optoelectronic devices. So, combining polymer matrix with phosphor is a suitable alternative for generating high-performance and thermally stable composite material for LED packages.

The present thesis focused on developing single white light emission under n-UV/ violet excitation from oxyfluoride phosphors and related phosphor-polymer composite films as colour-converting materials for WLED-based lighting applications.

The thesis is organized into six chapters and the overview of each chapter is described as follows:

Chapter 1 provides a consolidated overview of existing techniques for pc-WLEDs, their drawbacks and suitable solutions, precisely discussing single broad-band emitting phosphors. Further, a detailed literature review of recently reported diverse varieties of single broad-band emitting phosphors is elaborated. This chapter also deals with the importance of $Eu^{2+/3+}$ ions doping in generating single white light emission and their luminescence properties, synthesis, and applications towards WLEDs. Special emphasis is given to oxyfluoride phosphors for warm WLEDs and epoxy resin-free phosphor polymer composite as colour converters. Moreover, this chapter also covers the characterization techniques required for the complete study of the synthesized materials.

Chapter 2: **Innovative flexible lighting applications based on host triggered photoluminescence in $Sr_{2.9-3x/2}Ln_xAlO_4F$: $0.1Eu^{3+}$ (Ln = Gd, Y).**

Chapter 2 started with the structural features and luminescence behaviour of Sr_3AlO_4F host. The tetragonal phased Sr_3AlO_4F lattice is highly strained with some oxygen vacancies. The aliovalent substitutions of Sr^{2+} ions with trivalent Gd and Y ions are carried out by synthesizing a series of 0.1 mol% of Eu^{3+} doped $Sr_{2.9-3x/2}Ln_xAlO_4F$ (x = 0.01 to 0.10) were synthesized. All the samples showed intense red-orange emission (Eu^{3+}: $^5D_0 \rightarrow {}^7F_{1,2}$) under the UV and near-UV excitations. The critical concentrations of Gd^{3+} and Y^{3+} up to which the Eu^{3+} emission intensities increased linearly were observed to be x = 0.09 and x = 0.07, respectively. Nevertheless, further enhancement in the Eu^{3+} luminescence of the optimized phosphors was realized by subsequently annealing in low-oxygen atmospheres. The enhancement in oxygen deficiency during the post-annealing in Ar or vacuum led to the energy transfer (O^{2-}-Eu^{3+}) to a greater extent which afterward increased the Eu^{3+} luminescence. The optimized $Sr_{2.765}Gd_{0.09}AlO_4F$: $0.1Eu^{3+}$ and $Sr_{2.795}Y_{0.07}AlO_4F$:$0.1Eu^{3+}$ phosphors showed high red colour purity (~99%), as well as CIE coordinates of (0.62, 0.38), indicated that these phosphors could be appropriate red-emitting components for making flexible optical films for many lighting devices. Therefore, flexible polydimethylsiloxane-based films were also fabricated using

optimized $Sr_{2.765}Gd_{0.09}AlO_4F$: $0.1Eu^{3+}$ phosphor. The electroluminescence of a flexible PDMS-phosphor composite film showed an intense and pure red color with good thermal stability suggesting its suitability in flexible lighting and display devices.

Chapter 3: **Full-color emitting crystal engineered $Sr_3Al_{1-x}Si_xO_{4+x}F_{1-x}$: $Eu^{2+/3+}$ oxyfluorides for developing bendable lighting composites.**

Chapter 3 reports a series of full-colour emitting Eu^{2+}/Eu^{3+}-coexisted $Sr_{2.9}Al_{1-x}Si_xO_{4+x}F_{1-x}$: $0.1Eu^{2+/3+}$ ($SASi_xOF$: $Eu^{2+/3+}$) oxyfluorides, which were synthesized by annealing the solid precursors in an oxygen-deficient atmosphere. The substitution of Si^{4+} ions in Al sites contracted the AlO_4 tetrahedra and could enlarge the Sr sites, and enabled the suitable occupation of Eu^{2+} ions in the Sr1 sites. Eventually, the X-ray photoelectron spectroscopy studies confirmed the valence conversion of europium ions from its trivalent to the divalent state owing to the Si^{4+} ions doping in SAOF: $Eu^{2+/3+}$. Photoluminescence studies of $SA_xSi_{1-x}OF$: $Eu^{2+/3+}$ showed a bluish emission band at 482 nm for the *4f-5d* transition of Eu^{2+} ions along with several sharp peaks above 550 nm owing to the intra *f-f* transition of Eu^{3+} ions. Increasing the Si^{4+} ions' concentration subsequently, enhanced the Eu^{3+} to Eu^{2+} conversion rate and decreased their emission intensity ratio, owing to which the emission color chromaticity was also tuned from orange-red (CIE: 0.48, 0.29) to nearly white (CIE: 0.30, 0.26) and eventually to the bluish region (CIE: 0.18, 0.23). The nearly white light-emitting composition $SASi_{0.03}OF$: $Eu^{2+/3+}$ and the intense bluish light-emitting optimum $SASi_{0.06}OF$: $Eu^{2+/3+}$ phosphors were further chosen for fabricating flexible composites based on phosphor and castor oil (PU). At 150 ºC, the composite showed almost double the emission than the phosphor powders owing to the thermal encapsulation of the powders provided by the PU matrix. The obtained composite started to degrade at a temperature as high as 300 ºC. Therefore, the composite made with near white emitting $SASi_{0.03}OF$: $Eu^{2+/3+}$ phosphor was integrated with a 372 near UV-LED which showed intense cool white emission with the CIE of (0.29, 0.33), CCT of 7562 K, and CRI of 89. The above studies broadly suggested the adaptability of the obtained composites for flexible lighting applications.

Chapter 4: **Governing the crystallographic sites for tuning Eu^{2+} emission in an apatite oxyfluoride host to be applied for superior white light emitting diodes.**

Chapter 4 aimed at the generation of white light from a single-phase composition activated only with europium. The study started with the structural evaluations of Eu^{3+}-activated $Ca_4La_6Si_6O_{24}F_2$ phosphors and Eu^{3+} photoluminescence to elucidate the local environment of rare-earth ions and the symmetric nature of the lattice sites. $Ca_4La_6Si_6O_{24}F_2$ crystallized in the hexagonal *P6₃/m* space group. The predominant $^5D_0$-$^7F_2$ electric dipole transition at 614 nm, and the non-splitting as well as the zero-shifting behaviour of $^5D_0$-$^7F_0$ at 578 nm, suggested that the rare-earth ionic substitutions preferably took place at the larger asymmetric sites. Introducing Sr^{2+} ions in $Ca_4La_6Si_6O_{24}F_2$:Eu^{3+}/Eu^{2+} that is synthesized in a reducing atmosphere suppressed Eu^{3+} emission. From the optimized $Ca_{1.98}Sr_{1.98}La_6Si_6O_{24}F_2$:$0.04Eu^{2+}$, a sequence of M^{2+}-codoped (M=Mg/Ba) $Ca_{1.98}Sr_{1.98}La_6Si_6O_{24}F_2$: $0.04Eu^{2+}$ phosphors were further developed. The substitutions of Mg^{2+} and Ba^{2+} altered the crystal field by changing the lattice parameters. The Mg^{2+} doped samples showed a blue shift from 520 nm (Mg^{2+}=0) to 471 nm (Mg^{2+}=1.0). The Ba^{2+} doped compositions showed a red shift from 520 nm (Ba^{2+}=0) to 536 nm (Ba^{2+}=1.2). The change of symmetry owing to the Mg^{2+}/Ba^{2+} substitution could have led to the centroid shift, which was responsible for the blue- or red-shift of the emission spectra. The XRD of $Ca_{1.38}Sr_{1.38}La_6Si_6O_{24}F_2$:$0.04Eu^{2+}$,$1.2Ba^{2+}$ indicated Ba^{2+}-induced lattice site expansion. Keeping this in view, Eu^{2+} ions concentrations were further enhanced from 0.04 to 0.3, and the resultant photoluminescence was further enhanced and red-shifted. The optimized sample showed better intensity compared to the commercial $Y_3Al_5O_{12}$:Ce^{3+} and exhibited decent photoluminescence above 70% at 150 ^oC as compared with that at room temperature. Finally, several prototype WLEDs were fabricated using the single phosphor $Ca_{1.365}Sr_{1.365}La_6Si_6O_{24}F_2$:$0.07Eu^{2+}$, $1.2Ba^{2+}$ with near-UV and violet-LED chips. The outcomes indicated the promising nature of this single composition phosphor for indoor lighting.

Chapter 5: <u>Violet light excitable, highly efficient single broadband emitting oxyfluoride phosphor and polymer composite for conventional and laser-triggered lighting applications.</u>

Chapter 5 reports full spectral emitting violet-excitable flexible luminescent converters are favourable for user-friendly and human-centric lighting technologies due to simplified white-LED (WLED) integration, lower strained lighting, and long-term colour constancy. This research proposed a new broadband-emitting phosphor

composition $(Sr,Ba)_3(Al,Si)O_4F$: Ce^{3+}, Eu^{2+}, which is structurally optimized based on Eu^{2+} and Ce^{3+} site occupancy. Aiding from the nifty sensitization effect of Ce^{3+} ions, a wider band emission composed of $4f^6 5d^1$ - $4f^7$ transitions of Ce^{3+} and Eu^{2+} ions is effectively recognized under 410 nm violet radiation with a high quantum efficiency of 86% and thermal stability of 78%. High-quality phosphor polymer composite films are fabricated using the emission red-shifted $Sr_{1.995}Ba_{1-x}Al_{0.5}Si_{0.5}O_4F$: $0.025Ce^{3+}$; $0.005Eu^{2+}$ powders and thiourethane (CTU), which do not require any organic binders for WLED assembly, and exhibit high photobleaching and enhanced photoluminescent stability due to polymer encapsulation. The WLEDs assembled by the CTU/40%S_2BAOF: $0.025Ce^{3+}$; $0.005Eu^{2+}$ flexible composite as a single converter layer of a 410 nm violet-LED chip and a violet lesser of 405 nm generate warm white light with high CRI~80 and low CCT~4000 K without a noticeable chromatic shift under various powers and after prolonged illuminations. This research climaxes the potential of structurally distorted phosphor-polymer composites with outstanding lighting stability.

Chapter 6: Summary and future scope

Phosphor-converted white light emitting diodes (pc-WLEDs) are promising in fourth-generation artificial lighting because of their long lifespans, tunable colour, good stability, environmental friendliness, high energy-saving performance, compactness and their potential applications in day-to-day life. The thesis focused on developing single white light emission under n-UV/violet excitation from oxyfluoride phosphors and related phosphor-polymer composite films as the colour converting materials for epoxy resin free WLED based lighting applications. Structural and optical studies of each developed phosphor and phosphor polymer composites have been studied in detail, and these studies were correlated with suitable experimental proofs. The optimized phosphors from each working chapters are utilized for advanced flexible lighting applications.

This research primarily focused on two oxyfluoride host materials, Sr_3AlO_4F and $La_6Ca_4(SiO_4)_6F_2$, with the objective of achieving single warm white light emission suitable for solid-state lighting applications. From Chapters 2 and 3, an in-depth understanding of the structural and optical properties of the Sr_3AlO_4F host was obtained. In Chapter 4, through a strategic cationic substitution approach in the

apatite-type $La_6Ca_4(SiO_4)_6F_2$ host, the broadness and tunability of the emission spectrum were effectively optimized for white light generation. Building upon these insights, Chapter 5 successfully demonstrated the development of a violet-excitable single-component warm white light-emitting phosphor based on the Sr_3AlO_4F host. This optimized phosphor exhibited high color rendering index (CRI), low correlated color temperature (CCT), and high quantum efficiency, highlighting its strong potential for next-generation human-centric lighting and advanced optoelectronic applications.

Chapter 1

Introduction

1. Introduction

1.1. Photoluminescence and phosphors

Photoluminescence is a phenomenon that arises when an external energy excites a substance's electronic state, subsequently releasing light.[1] The source of external energy is mainly from UV, visible, beams of electrons, thermal radiation, or photons, which transform some of the energy into electromagnetic radiation, mostly emitted in the visible region.

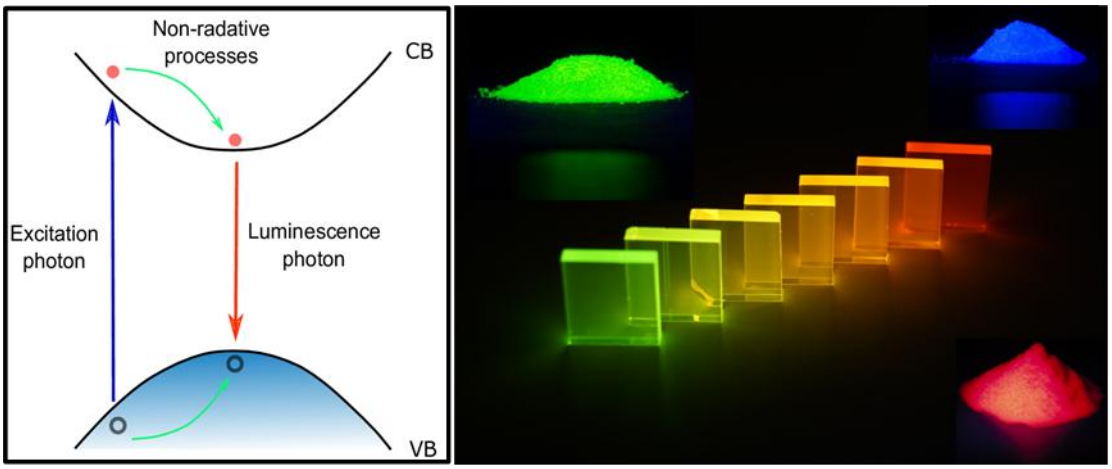

Figure 1.1: *The pictorial illustration of the photoluminescence phenomenon and different phosphor powder illumination under excitation irradiations. (Source: Google, links: https://www.techbriefs.com/,and https://www.imws.fraunhofer.de/)*

Phosphors are known as inorganic light conversion materials, which emit lower energetic photons when exposed to higher energetic ultraviolet or visible photons or an electron beam. They are considered to be the key components of WLEDs. According to Shigeo Shionoya, the term "phosphor" specifically refers to inorganic solid luminescent materials in powder form, composed of crystals or noncrystals.[1, 2] Phosphors are composed of an inorganic matrix known as host and luminescent ions known as activators are embedding into the host matrix. The activator ions undergo electronic transitions into the host by absorbing high energy and resulting in low energy emission, i.e. Stokes emission is called down-conversion phosphors and that luminescent material convert lower energy photons into higher energy are known as up-conversion phosphors.[1]

1.2. Photoluminescence mechanism

Photoluminescence is a phenomenon of light emission as a result of the absorption of photons such as lesser energetic electron beam, ultraviolet radiation or visible lights. This photoluminescence mechanisms are best illustrated with the help of Jablonski diagram, as shown in **Figure 1.2.**[1-3] Depending on the energy of light photon absorbed, the electrons present in the ground state of the molecule jumps to the higher excited states such as S_1, S_2…. or S_n singlet states. This activated electron returns to the ground state by dissipating its energy through following types of processes:

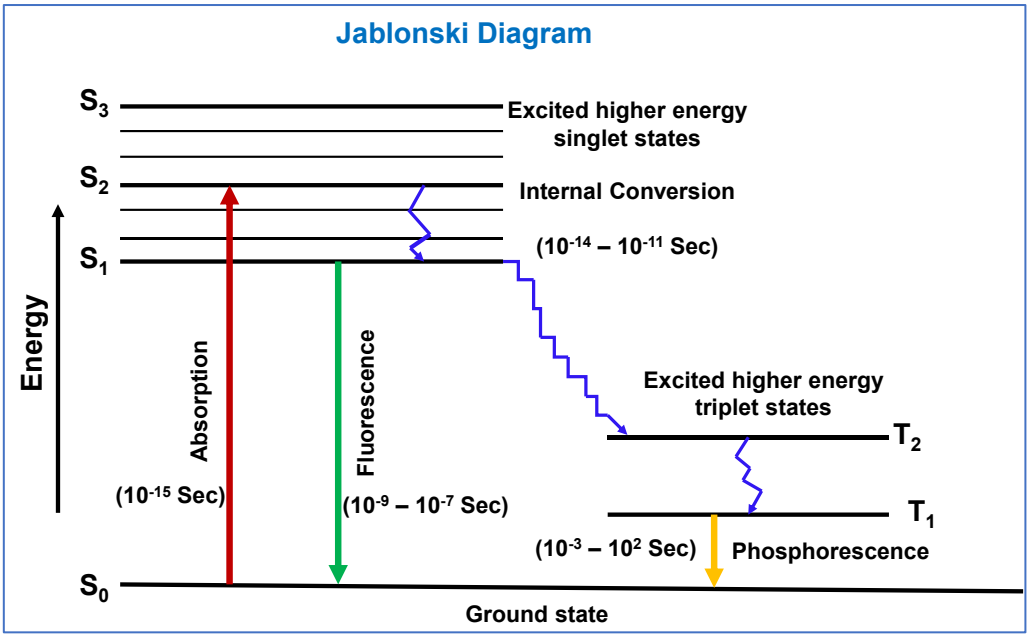

Figure 1.2: *The Jablonski diagram illustrating the various photoluminescence mechanism.*

1.2.1. Non – radiative Transitions

These transitions are radiation less transitions occur due to the transition of activated electrons from higher excited states (S_3, S_2 or T_3, T_2) to the first excited states (S_1 or T_1). Mainly two types of non – radiative transitions are there: Internal conversion (IC) as well as Intersystem crossing (ISC).

Internal conversion (IC): The non-radiative transition happens for the activated molecule through molecular collision and dissipates energy in the form of heat. This phenomenon happens in less than 10^{-11} second.

Intersystem crossing (ISC): The non–radiative transitions happen between states with different multiplicity (from S_1 to T_1 or S_2 to T_2, etc.). The ISC transitions are forbidden and occur at very slow rates.

1.2.2. Radiative transitions

The transition of activated electrons from singlet (S_1) or triplet (T_1) excited states to the ground state (S_0) involves radiative emission. There are two types of radiative emissions are there: Fluorescence and Phosphorescence.

Fluorescence: The radiative transition from S_1 to S_0 results in fluorescence emission. This is an allowed transition and occurs in about 10^{-8} seconds. The emission in fluorescence ceases with the removal of the light source.

Phosphorescence: The forbidden transition from the triplet (T1) to the ground state (S0) results in phosphorescence emission. The period of phosphorescence is longer than fluorescence emission, i.e. about 10^{-3} seconds or greater.

1.3. Phosphor: host and activator

In the making of phosphor based WLEDs mainly focused on two things, phosphor material and LED chips. For LED chips, researchers are mainly investigating its thermal diffusivity, stability, chosen short wavelength chips and focused on the manipulation of high power. Another factor which directly influence the LED device is the phosphor material chosen, it must have high thermal and chemical stability, good luminescent property, mild synthesis condition, etc.[4] Phosphors, known as inorganic color-converters, are the vital WLED components. Usually, they are consisting of a host material and intentionally doped impurities called activators.[1,2] The host materials generally govern the crystal structure and the commonly used host matrix are oxides, fluorides, nitrides, sulphides, oxyfluorides, silicates, oxynitrides, selenides, halides, etc.[1-5]

Whereas the activators act as a luminescent centre integrated into the host matrix which emit light. They are generally transition metals or rare earth metal cations like $Mn^{2+/4+}$, Cu^{+}, Zn^{2+}, Cr^{3+}, Sb^{3+}, Ce^{3+}, Eu^{2+}, Tm^{3+}, Er^{3+}, Tb^{3+}, Pr^{3+}, Dy^{3+}, $Sm^{2+/3+}$ and $Eu^{2+/3+}$, etc.[3] The photoluminescence process in phosphors mainly associated with the

host and within the activator via energy transfer process. [3] The simultaneous effect of both the host and activator ion influences the photoluminescence properties of a phosphor such as shape and intensity of the emission spectra, quantum efficiency, thermal stability, etc.[5] Phosphor materials absorb energy from incident radiation and emit light through various energy transfer processes.

1.3.1. Photoluminescence mechanism in phosphors

1.3.1.1. Intra – configurational transitions

The interaction among the host lattice and the activator ions results in electronic transition within the same shell, i.e. without changing the electronic configuration of the ion, is known as intra-configurational optical transitions. For the case of rare earth ion–activated phosphor, several sharp peaks arise due to the intra-configurational 4f→4f transitions. All the states of $4f^N$ electronic configuration of rare earth ions with identical parity, which make electric dipole transitions parity forbidden. When activator ions undergo a crystal field with poor inversion symmetry, the overlapping of wave functions such as $4f^{N-1}$ 5d into 4f with opposite parity occur. Accordingly, intra-configurational 4f→4f transitions achieve intensity in emission.[3] In the case of transition metal ion–activated phosphor, broad spectral peaks arise due to the intra-configurational 3d→3d transitions as the outcome of the strong interaction of activator ion with the surrounding lattice environment. All the optical transition between states of $3d^N$ electronic configuration of transition metal ions are parity forbidden, but by mixing with odd-parity composition transition of ions become weakly allowed.[3]

1.3.1.2. Inter – configurational transitions

The electronic transitions happen between different atomic shell i.e. with changing the electronic configuration of ions either from 4f shell to 5d shell or vice versa is known as inter – configurational transitions. The excited electrons from 4f orbital to 5d orbital transition will experience interaction with the surrounding vibrating lattice. The corresponding 5d–4f transitions are allowed and broad spectral bands are observed. The energy difference between 4f and 5d electronic levels are highly depends on the strength of neighbouring crystal field environment. As compared with the free ion, the lowest energy level of $4f^{N-1}5d$ configuration having lesser energy upon included in to a host matrix. Similarly, weak crystal field and low covalence of the activator-ligand bond may result lower rate of splitting in $4f^{N-1}5d$ electronic levels of ions in host matrix.[3]

1.3.1.3. Energy transfer interactions

Some cases activator ions in host lattice are enable to give promising luminescence because the host lattice is unable to give absorption. Such cases minute quantities of monovalent or trivalent atoms like Li, Na, K or Bi, Gd, Pr known as sensitizers (S) are co-doped into the systems to enhance the photoluminescence of the activator ions (A). If the excited states of sensitizer and activator are in resonant energy, S transfer its energy from the relaxed excited states to the ground state of A without giving any radiative emissions. There must be a strong interaction between the two centres and have comparable energy levels for the energy exchange interaction among S and A in a phosphor.[3]

1.3.1.4. Charge transfer transitions

Charge transfer transition is an electron transfer transitions happens between donor and acceptor pairs within the same part of the molecule or between two different molecule resulting change in the electronic environment and leads to strong absorption in UV – visible region. Basically, two types of charge transfer transitions are crucial: a ligand to metal charge transfer (LMCT) in which electrons transfer from ligand orbital to metal orbital and metal to ligand charge transfer (MLCT) in which electrons transfer electrons from metal orbital to ligand orbital.

In phosphor materials, which are mainly insulators or semiconductors, absorption usually materialize because of the band to band excitation of electrons. After that the host material show electron transfer emission either by the result of activator to host excitation or inter – band excitation. If the localized excited states of activator are strongly mixed with the orbitals of the surroundings conduction bands, there is a transition of electrons from the activator's ground level to one of its excited states by creating an electron hole pair.[3] Charge transfer transition in phosphor mainly due to donor – acceptor pair emission, including metal to ligand, ligand to metal and metal to metal charge transfer. The broad spectral band is observed due to strong electron-lattice coupling in phosphors. Other type of charge transfer transitions in phosphor are related to the trapping centers. When a foreign atom/molecule incorporated into a crystal system, lattice distortion may occur, results in creating trapping centers with in the energy gap. The electron hole pairs,

i.e. charge carriers may be trapped at these levels and undergo transition upon external stimuli.[6]

1.4. Applications of phosphors

Phosphors have wide range of application in different fields of technologies. Based on the requirements in different fields thousands of possible phosphor material can be developed for different applications such as lasers, display devices, solid state lighting, optical communications, dark glow imaging, sensors, plant growth technology, cathode ray tubes, scintillators, micro-LEDs, etc.[7-9]

1.4.1. Solid state white LEDs

Phosphor-based white light-emitting diodes (pc-WLEDs) are one of the developing technologies in the 21st century to rapidly replacing existing light sources such as incandescent bulbs and fluorescent bulbs for use in the display backlights, indoor and outdoor lighting, etc.[10] These solid state WLEDs have concerned much attention in modern lighting technologies because of their longer life, low heat dissipation, high quantum efficiency, environmentally friendly nature, low energy consumption, higher conversion efficiency of electrical power to optical power, spectral tunability, reduce the dependency of mercury usage, etc.[11-13] This WLEDs are one of the most emerging illumination systems in the future which is replacing traditional incandescent and fluorescent lamps. Because of the promising advantage of WLEDs like compactable size, high brightness, fast switching rates, superior lifetime, and reliability made this suitable

Figure 1.3: *Applications of WLEDs in different sectors. (Source: the information and images were collected from Google)*

for various applications such as high-power automotive headlights, display systems, including landscape decoration, indicators, liquid crystal displays for computers, mobile telephones, TVs, etc.[5] By the usage of WLEDs, instead of other lighting sources it will

reduce environmental pollution and energy consumption in world wide. In the development of human history, WLED plays a remarkable role in different sectors like automotive industries, indoor and outdoor lighting, backlighting, laser technology, medical field, plant growth technologies, future ultimate display systems like micro-LEDs, etc. as shown in **Figure 1.3.**[14,15]

1.4.1.2. Market potential of WLEDs

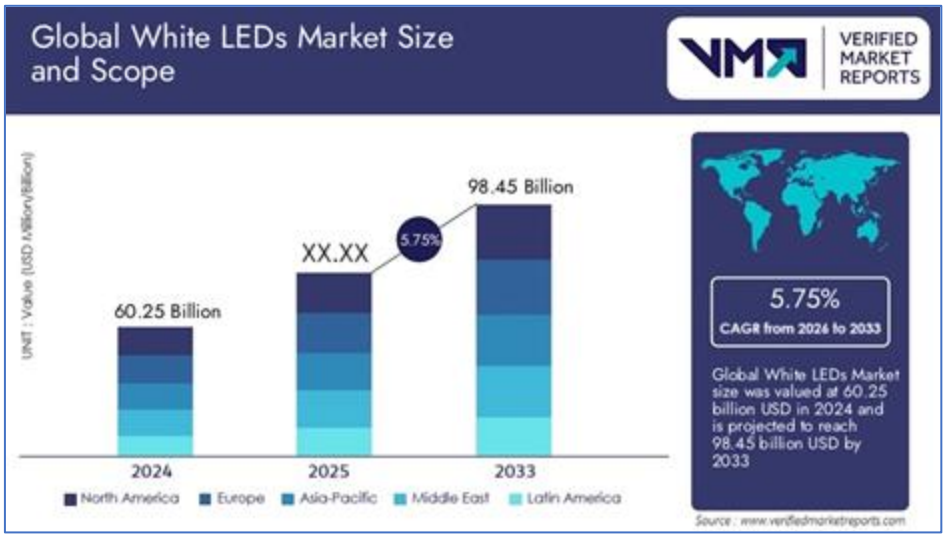

Figure 1.4: *Market Potential Report of WLEDs from https://www.verifiedmarketreports.com/.*

The global market potential of WLEDs grow year by year and is expected to reach USD 98.45 Billion by 2033. The growth rate is estimated with a compound annual growth rate (CAGR) of 5.75% from 2026 to 2033. Many government sectors are taken the initiative for promoting usability of WLEDs in different sectors by circulating awareness of the promising advantage of WLEDs such as energy-efficient lighting, durability of LED products, sustainable lighting, and technological advancements. Based on the reports of U.S. Department of Energy, the LED market will reach $138.8 billion by 2026. Peoples are more concern about their health and conscious about environment. This is the main reason for the increasing market potential of drive the growth of the white LEDs. In terms of energy consumption, WLEDs consume up to 75% less energy than traditional light sources like incandescent bulbs and also the lifetime of WLED is 25 times longer than the conventional light sources. According to the U.S. Energy Information

Administration reports, LED lighting could save more than $30 billion in electricity costs by 2030. The market potential report of WLED is illustrated in **Figure 1.4.**[16]

1.4.1.3. Evolution of phosphor materials in WLEDs

Based on the requirements of each different era, phosphor materials are tuned by their luminescence property, thermal stability and chemical stability of the whole structure for solid state lighting. Initially, people are demanding a white light source with high efficiency, and hence, researchers developed first-generation phosphors for lighting. After that, people are seeking better color performance LED, having high CRI and thermal stability.[5] So, to overcome the pitfalls of 1st generation phosphors, 2nd generation phosphors were developed. To makeover the disadvantages of 1st and 2nd-generation phosphors, researchers are more focused on developing narrowband emitting phosphors with high visual and audio quality to fulfil the demands of the 3rd era for the backlighting system.

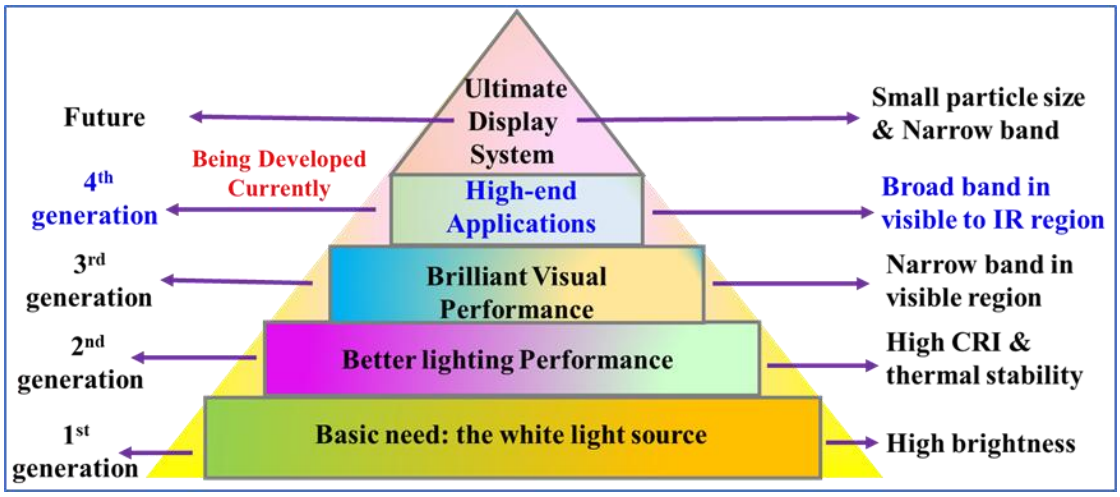

Figure 1.5: *The schematic representation of evolution of phosphor materials in different generations for lighting.*

In the recent era, technologies are more and more advanced and peoples are much more concerned about their health and demanding lighting devices for advanced applications like wearable devices, plant growth technologies, health sectors, food technologies, etc. For satisfying all these demands in the current technologies, broad band phosphors covering from blue to infrared regions are required. And hence fourth

generation phosphors are invented to meet the demands and those are in immature stage and being established presently.[5] Coming to the future of these phosphor materials, they will be used for high end applications like ultimate display systems, more complex devices, micro-LEDs, etc. For the development of this fifth generation of phosphors researchers are focusing on reducing the particle size of the phosphors and narrow band emission to meet the demands. The overall schematic representation of evolution of phosphor materials in different generations for lighting are shown in **Figure 1.5.**[5]

1.4.1.4. Existing technologies for WLEDs development

There are mainly two types of techniques for generating WLEDs: by adopting multi-chip techniques or single-chip method. In multichip method, three different LEDs like blue, green, and red LED chips are mixed together to form white light.[5] Based on our requirements, the produced light color can be adjusted but this method facing problems such as multiple chip usage leads to high cost of production, complicated electronics, different degrading nature of chips with different lifetime and thermal stability causes color distortion of the WLEDs and different driving voltages limits its advanced practical applications. To overcome these issues, nowadays for the commercial WLED products development they are adopted single-chip based techniques with the aid of different phosphors.[5] There are mainly three methods of single-chip based development of WLEDs.

1.4.1.4.1. Combination of yellow phosphors with blue LED chip

In this method, yellow color emitting phosphor powders are combined with the blue light emitting LED chips to generate white light. The commercialized WLEDs are mostly from the combination of a yellow emitting $Y_3Al_5O_{12}:Ce^{3+}$ ($YAG:Ce^{3+}$) phosphor and a blue LED chip to produce cold white light with high brightness and very high correlated color temperature (CCT) greater than 6000 K.[5] This commercialized WLED combination was first invented by Nichia Co. in 1996 (patent no. US 5,998,925).[5] Besides its advantages, the lack of red emission in the spectral region results to low color-rendering index (CRI) < 75 and high correlated color temperatures (CCT). The prolonged blue LED emission cause severe health issues for human like mood disorders, macular degeneration, circadian disruption, etc. By the usage of epoxy resin usage in LED packaging cause degradation problems and low thermal stability of phosphors limits its advanced lighting applications.[17-19]

1.4.1.4.2. Combination of green and red phosphors with blue LED chip

White light emission is produced from the combination of a blue LED chip with green and red color phosphor powders, as shown in **Figure 5(c)**. The combinations mostly produce warm white light emission with higher CRI and the CCT in the range of 3000 to 5000 K.[32] However, the usage of multiple phosphors and highly sensitive longer wavelength red phosphor emission may lead to reduce the luminous efficacy of the WLED device, lowers the lifetime and causes health issues for human.

1.4.1.4.3. Combination of blue, green and red phosphors with UV LED chip

White light can also be produced by mixing the primary RGB emitting phosphors according to the scheme illustrated in **Figure 1.6(d).**[5] Precisely, the white color point can be fixed by specific tuning of the single color emitting phosphors, which is advantageous for the resultant WLED to stand against the discreteness of the used LED chip. Such initiative of using multicolored phosphors and the resultant device can deliver a high CRI. However, the leaked UV photons probably damage the LED encapsulant in a long run and reduce device's lifetime appreciably. Such lighting device also suffers with low light-conversion efficiency, mismatch in multiple phosphors' degradation rates and re-absorption of phosphor materials. This phosphor blends causes color aberrations which is unwanted problem in the practical side of WLEDs.[5] The strong reabsorption of the emission of multiple phosphors may leads to decrease the lumen efficiency (LER) value of the final white light emission.

1.5. Solutions for the existing technology

- Introducing single white light emitting phosphors with high CRI > 65 and low CCT < 5000 K with promising thermal stability.
- Proposing phosphor polymer composites as a suitable alternative for conventional epoxy resin free coating in LEDs.
- Single phase broad band emitting phosphors with high quantum efficiency (QE) comparable with commercial standard.

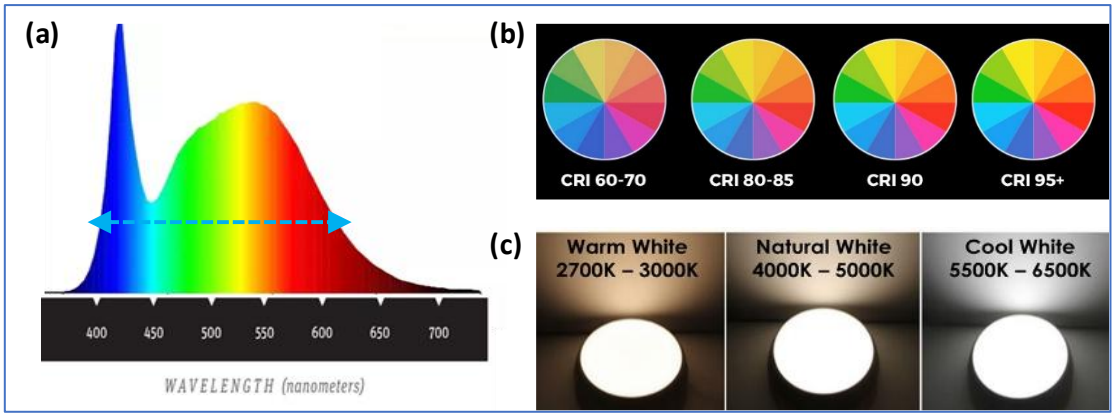

Figure 1.6: *The pictorial representation of (a) full visible spectral features, (b) CRI and (c) CCT formulations for improving the color quality in WLEDs. (Source: Google, links: https://www.nextgenerationled.be/EN/CorrelatedColorTemperature.htm, and (https://mfopto.com/blog/understanding-lighting-metrics/)*

1.5.1. Single broad band emitting phosphors

To overcome the disadvantage of existing techniques like combination of multicomponent phosphors with blue/n-UV LED chips, single phase broad band emitting phosphors showing full visible spectral emission (**Figure 1.6(a)**) under n-UV/violet/blue excitations is the most required and emerging stage.[20] Significant efforts have been made to design white light emission from single phase to overcome the disadvantage of long-term operation of mixed multicolour phosphors. Single component white light emitting phosphor materials has lots of advantages such as avoiding mutual absorption among different phosphors, cost effective, simplify the packaging process, having tunable CRI (**Figure 1.6(b)**), lesser CCT (**Figure 1.6(c)**), and ideal Commission International de I'Eclairage (CIE) chromaticity coordinates and avoiding color drift.[21] So, for developing WLEDs with high quality, the usage of single-phase phosphors with tunable emission is making the device packaging easier and most crucial in this developing era of lighting technologies. Ming Zhao et al. recently reported a new design strategy for developing NUV excited single component white light emission from oxide based $NaLiSiO_4$: Eu^{2+} phosphor.[36] But they failed to achieved warm white light emission with good spectral efficiency and thermal stability from the rigid oxide phosphor. Now researchers are mainly focused on developing a single composition phosphor can produce multiband emissions. Pralong et al. generated white light from a single host $Li_xEu^{II}_xEu^{III}_{0.33-x}Zr_2(PO_4)_3$ by the insertion of lithium into $NaZr_2(PO4)_3$ type Structure.[23] It gave corresponding Eu^{2+} (blue-green) and Eu^{3+} (red) emission under 393 nm excitation

and can produce white light with higher color coordinates. But this approach is specific for this particular type structure. For the development of single broad band emission, host and activators play a major role.

1.6. Host and Activators in pc-WLEDs

For selecting a host material for efficient WLEDs, certain requirements are there: the host material must be thermally and chemically stable with high thermal stability. In addition to that, the host material becomes optically transparent and phosphor production should follow a cheaper and eco-friendly process.[1] In general, commonly used host matrices for pc-WLEDs are garnets, nitrides, sulfides, vanadates, silicates, fluorides, oxynitrides, phosphates, oxyhalides, oxynitrides, etc.[10] One of the commonly used broadband emitting phosphor is yellow emitting garnet structured $Y_3Al_5O_{12}:Ce^{3+}$ (YAG: Ce). This phosphor may possess prominent advantages like efficient absorption of blue light, broadband emission spectra, very good chemical and thermal stability, etc. But it may face problems like low CRI and very high CCT due to the deficiency of red component and exposure of blue light may cause health issues for human.[17,19] Another widely used host matrix for lighting applications is silicate-based host having stable crystal structure and tunable optical properties.[24] As compared with oxide host, sulfide hosts are showing more red shift in emission spectra and combine with Eu^{2+} ion activator ions, broad spectra covering the entire visible region is observed which is suitable for solid state white light technology. But these sulfide hosts are thermally unstable and highly moisture sensitive.[25,26] So, it is very important to introduce new host materials for developing promising phosphors for WLEDs to overcome the existing problems of phosphor materials.

The activator ions will determine the luminescence property of a phosphor. Mainly used dopants for the host matrix are rare-earth ions and transition metals (Ce^{3+}, Eu^{2+}, Tm^{3+}, Er^{3+}, Tb^{3+}, Pr^{3+}, Dy^{3+}, Sm^{3+} $Mn^{2+/4+}$, Cu^{+}, Zn^{2+}, and Cr^{3+}).[12] Because of the presence of inner 4f shell present in rare earth ions showing promising optical performance. The detailed descriptions are included in the coming sections. Large variety of phosphors with tunable emission colours are possible by modifying the composition of the host and the activator ions.

1.6.1. Oxyfluoride hosts

Among the different hosts, oxyfluoride phosphors have gained wide attention towards WLED application because of their noticeable structural stability and rigidity, high thermal and chemical stability, tunable luminescence property, high quantum efficiency, environmental friendliness and low cost of production. The incorporation of fluoride ions into the oxide host lattice leads to distortion of the crystal and local structure among the centrosymmetric cationic sites of polyhedra. The presence of highly electronegative fluoride ions leads to a non-symmetric local environment among oxyfluoride host lattice, leading to a broad emission band and tunable emissive properties.[27] Besides that, fluoride host matrices provide a high coordination number and high ionic rare-earth to fluorine bonding, resulting in a wider bandgap, low phonon energies and minute probability of inter-configurational transitions, whereas the oxides host matrices are known to provide high chemical stability and high absorption in the UV-vis region. Based on these aforementioned facts, the oxyfluorides, which combine the advantages of both fluorides and oxides, are favourable to serve as the host materials for luminescence properties.[29] Among the oxyfluoride host matrices, Sr_3AlO_4F is most generally studied phosphor owing to its good chemical and thermal stability, economical starting materials, facile synthesis conditions, and efficient luminescence properties.[30] Its crystal structure is shown in **Figure 1.7(a)**, and explained in the later part of the thesis.

Sangmoon Park and co-workers reported single-phase Bi^{3+} and Eu^{3+}-codoped Sr_3AlO_4F phosphor shows an obvious luminescent shift from blue to orange-red emission under 318 nm excitation.[31] Jang et al. reported the Eu^{3+}/Dy^{3+} doped and codoped Sr_3AlO_4F phosphor as a prominent host for a white light emitting technology.[32] W. B Im et al. developed greenish white light emission from SBAF: Ce^{3+} phosphor with CRI is 62, CCT is 6500 K and very high quantum efficiency under ultraviolet (UV) LED chip.[31] In addition to that among the oxyfluoride family inorganic compounds of silicate apatite has also been used as a suitable host for phosphors in lighting technology owing to its very good luminescent properties and high chemical and thermal stability.[33] By the introduction of fluoride ion into rare – earth ions doped silicate apatite host can generate potential luminescent properties in solid state lighting due to the presence of mixed ligand system.[34] Recently M. H. Fang et al. illustrated full spectrum lighting Eu^{2+} doped $(Sr,Ba)_5(PO4)_3Cl$ apatite phosphor through cation size-controlled activator ion

redistribution mechanism for tuning the emission color.[35] Based on the literature reports it is found that Sr_3AlO_4F and silicate apatite oxyfluoride phosphors are considered as a prominent host for a white light emitting technology.

1.6.2. Rare earth activators

Rare earth ions play an important role in pc-WLED technology owing to their promising luminescence characteristics. The commonly used luminescent rare earth ions are Ce^{3+}, $Eu^{2+/3+}$, Sm^{3+}, Tb^{3+}, Dy^{3+}, etc. Both $Eu^{2+/3+}$ and Ce^{3+} ions are the usually used activator ions in the host lattice for broadband emission because both Eu^{2+} and Eu^{3+} can act as an emission centre for $Eu^{2+/3+}$ ions and parity allowed electronic transition of Ce^{3+} ions. The parity-forbidden 4f−4f transition in Eu^{3+} activated phosphor leads to a low color rendering index (CRI), and 4f−5d transitions in Ce^{3+}/Eu^{2+} ions cause intensely broad band emission, which is more applicable for white light emitting applications. [1] We are essentially attentive on oxyfluoride phosphors' luminescent centres based on rare earth $Eu^{2+/3+}$, Ce^{3+} ions. Because of the inner allowed energy levels of rare earth ions, a wide range of excitation and emission that covers the entire visible region is possible as well as energy transfer among other rare earth ions also occurs.[44,50] To explore new phosphors with high CRI, doped activators play a major role in inorganic host matrices. For the case of rare earth activators, europium ions are the most usually used activators in the host lattice because both Eu^{2+} and Eu^{3+} can act as an emission center. The parity-forbidden 4f−4f transition in Eu^{3+} activated phosphor leads to a low color rendering index (CRI) and 4f−5d transitions in Eu^{2+}cause intensely broad band emission, which is more applicable for white light emitting applications. Most commonly there are two kinds of emission spectra of rare earth ions in phosphors are observed: inter-configurational 5d–4f electronic transition of rare earth ions giving broad band spectra and intra-configurational 4f–4f electronic transitions of rare earth activators giving narrow band emission spectra.[1,3] The detailed photoluminescent behaviour of rare earth ions towards host matrix in phosphors are described below.

1.6.2.1. Inter-configurational 5d–4f electronic transitions of $Eu^{2+}$and Ce^{3+}

The parity allowed electric dipole 5d–4f transition of Ce^{3+} and Eu^{2+} ions exhibit broad band emission with large oscillator strengths and short lifetimes. The spectroscopic properties of 5d electrons of Ce^{3+} and Eu^{2+} ions are strongly influenced by the surrounding host lattice because of the unshielded nature of 5d shells from their nearest

$5s^2$ and $5p^6$ shells. The energy difference between the ground ($4f^n$) and excited state ($4f^{n-1}5d^1$) of free Ce^{3+} or Eu^{2+} ions are 50000 cm^{-1}(≈ 6.2 eV) and 34 000 cm^{-1}(34000 cm^{-1}) respectively. According to the semiempirical Dorenbos model, the energy gap between ground and excited states of free rare earth ions are strongly influenced by the host lattice which is mainly depends on two phenomena known as spectroscopic redshift and Stokes shift. The spectroscopic red shift is the sum of both crystal field splitting and the centroid shift that happens in the f–d transition in the host lattice. The Stokes shift is dependable with the nature of the host lattice.[1,3] The spectroscopic red shift is strongly influenced by two effects such as covalency effect/nephelauxetic effect and the crystal field splitting effect. The detailed schematic representation of energy level splitting of free activator ions (Ce^{3+} and Eu^{2+}) into the host lattice, with the influence of crystal environment, as shown in **Figure 1.7(b)**. Detailed descriptions are included in working chapters.

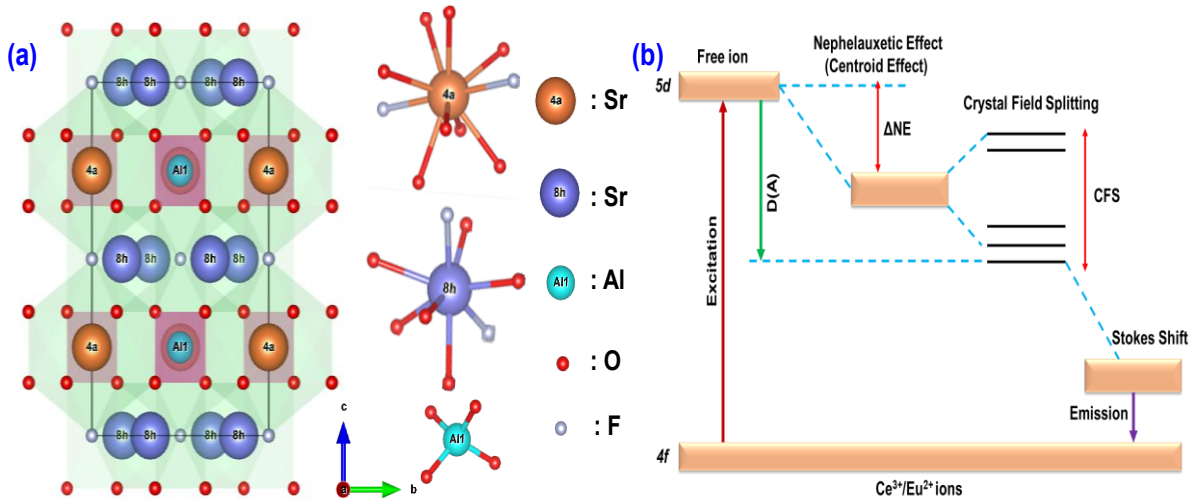

Figure 1.7: *The schematic representation of (a) the crystal structure of Sr_3AlO_4F host. (b) energy level splitting of free rare earth activator ions ($Ce^{3+}$and Eu^{2+}).*

Coming to the detailed description, as compared with the centroid position of the 5d – levels of free ion, with the variation of covalency between the activator ions and the neighbouring anionic ligands in the host lattice (nephelauxetic effect), downward shift of the centroid position happens, which is known as centroid shift. Depending on the covalency of the metal-ligand bond lengths of activator ions and surrounding anions as well as polarizability nature of surrounding ligands will influence centroid shift

phenomena in phosphors. A mathematical formula is proposed by Jørgensen for defining the nephelauxetic ratio (β) by relating to ligand (h) and metal ion (k) is given below,[51]

$$(1 - \beta) = hk \qquad (1.1)$$

The nephelauxetic effect is directly proportional to the extent of the covalent nature of activator ions and the surrounding anionic ligand strength. The order of ligand strength is quoted as follows; zero ligands < F^- < H_2) < NH_3 < Cl^- < Br^- < N^{3-} < I^- < O^{2-} < S^{2-}, etc. As the extent of covalency increases in the crystal lattice, the extent of repulsion between activator ion and their neighbouring anions decreases and consequently the energy of excited levels of 5d orbital decreases and extend of centroid shift enhanced.[5]

For the discussion of crystal field splitting, there is a strong interaction happens between the 5d electrons of activator ions and neighbouring anionic ligands present in the host lattice. Consequently, the degenerated 5d orbital of activator ion may further split into five 5d states. The energy difference between the lowest level of 5d orbital and highest level of 5d states are known as crystal field splitting. The crystal field splitting is directly related to the symmetry, size, coordination environment of activator ions in the polyhedron and bond length among ligands and activator ions. Based on point charge model the crystal field strength present in a host can be calculated based on bond length between activator ions and ligands in the host lattice is,

$$D_q = \frac{Ze^2r^4}{6R^5} \qquad (1.2)$$

where D_q is the crystal field splitting parameter, Z is the anion valency, e is the electron charge, r is the radius of the d-orbital wavefunction, and R is the bond length between an activator ion and ligands in the host lattice.[5] For a similar crystal geometry, D_q is depending on R all other parameters are common for a given coordination geometry. If the distance between ligands and activator ion is decreases i.e. volume of the crystal lattice decreases, there may be more overlapping of ligand orbital and metal orbitals, this may increase the crystal field splitting of 5d states consequently red shift of emission is observed. By the influence of both the crystal field splitting and nephulastic effect

changes occurs during the host composition variation the emission color, efficiency and intensity of the phosphors can be adjustable.

1.6.2.2. Inter-configurational 4f–4f electronic transition of rare earth ions (Eu^{3+})

The 4f electrons are protected by the nearest filled $5s^25p^6$ orbitals from the surrounding environment. The 4f–4f transitions are parity-forbidden and give sharp spectral emission with excellent coherence properties and long lifetimes. The emission color is independent of the surrounding environment of the activator ions and depends on the electronic transition of that particular activator ion. Because in the case of 4f orbital, having small electron–phonon coupling strengths, low exchange perturbations, smaller radial extension, and smaller electron–phonon coupling strengths than 5s and 5p orbitals. For example, Eu^{3+} emits red light corresponding to the $^5D_0 \rightarrow {}^7F_J$ electronic transition, $^5D_4 \rightarrow {}^7F_J$ transition of Tb^{3+} ions giving green light, $^4G_{5/2} \rightarrow {}^6H_J$ transition of Sm^{3+} ions giving orange light, and as a result of $^4F_{9/2} \rightarrow {}^6H_J$ transition of Dy^{3+} giving blue/yellow light. Because of the parity-forbidden transition, they have low molar absorption coefficients in the n-UV and blue ranges due to which most of the RE^{3+} ions are unsuitable for solid-state lighting, except for the Eu^{3+} ions with deep red emission in a host having high efficiency.[1,3]

1.6.2.3. Energy transfer mechanism among rare earth activators ($Eu^{2+}$and Ce^{3+})

To enhance the emission intensity of activator ions, sometimes sensitizer(S) ions which is capable of transfer its energy to activator ions are codoped into the host lattice. As compared with the other rare earth ions like Tb^{3+}, Dy^{3+}, Eu^{3+}, and Sm^{3+}, etc. Eu^{2+} and Ce^{3+} ions are act as very good sensitizer for energy transfer mechanism owing to their highly efficient n-UV/blue light absorption. Researchers are utilizing this energy transfer mechanism among rare earth ions the emission colour can be tuned in single phase phosphors via varying the sensitizer activator doping ratio. For the effective energy transfer among rare earth ions happens only when the energy levels of both S and A should be comparable, there must be a strong spectral overlap between the emission spectra of sensitizer and excitation spectra of activator. The interaction occurs may be either exchange interactions or electric multipole interactions. The energy transfer mechanism can be confirmed from the lifetime measurement of sensitizer as follows,

$$\eta_T = 1 - \frac{\tau_s}{\tau_{so}} \qquad (1.3)$$

where η_T is the energy transfer efficiency, τ_s and τ_{so} represents the lifetime of sensitizer in the presence and absence of activator ions.[54] The energy transfer mechanism is confirmed from the lifetime curve fitting method is as on increasing activator ion concentration the lifetime of sensitizer must be decreases then only effective energy transfer happens among both the rare earth ions. The energy transfer mechanism and nature of interaction among sensitizer and activators are studied by using Dexter's energy transfer expression and Reisfeld's approximation as below:

$$\frac{Iso}{Is} \alpha C^{\alpha}/3 \qquad (1.4)$$

Here, C is the total doped concentration of sensitizer and activator ions, I_{so} and I_s are the luminescence intensities of sensitizer in the absence and presence of activator ions in phosphors. The value of α equal to 3, 6, 8, and 10 corresponds to exchange interaction, dipole–dipole (d – d), dipole–quadrupole (d – q), and quadrupole–quadrupole (q – q) multipolar interactions respectively.

1.7. Emission tunning strategies used in rare earth activated phosphors

1.7.1. By modifying the chemical composition of host

As discussed in section 1.6, the photoluminescence behavior of activator ion can be directly depended on the surrounding environment of host lattice. The excitation and emission can be range can be tuned by suitably change the chemical composition of the host matrix with suitable ionic substitution. The wavelength shift in rare earth ion transition is observed due to the change in composition of the host through suitable substitution of existing elements in the host by other elements having different ionic radii may create crystal distortion. The elemental substitutions in the host may either cationic substitution, anionic substitution or cationic–anionic substitution.

1.7.1.1. Cationic substitution strategy

In this compositional change strategy selectively substitute cations in a host matrix. In a host matrix there are two kinds of cations are there cations present in the ionic complexes like Al^{3+} in $(AlO_4)^{3-}$, Si^{4+} in $(SiO_4)^{4-}$, and B^{3+} in $(BO_3)^{3-}$, etc. and cations in

the host lattice as alkali metal ions (Li^+, Na^+, and K^+), alkaline earth metal ions (Mg^{2+}, Ca^{2+}, Sr^{2+}, and Ba^{2+}), and rare earth metal ions (Y^{3+}, Gd^{3+}, Sc^{3+}, La^{3+}, and Lu^{3+}). The cationic substitution enforced crystal field splitting is schematically illustrated in **Figure 1.7**. In this work the Sr^{2+} ions in the host lattice are substituted by smaller and bigger cations like Mg^{2+} and Ba^{2+} ions. By the replacement of Sr^{2+} ions with smaller Mg^{2+} cations cause smaller crystal field splitting and results in blue spectral shift. Similarly, by the substitution of larger Ba^{2+} ions with Sr^{2+} ions will reduce the activator ion and ligand bond length, resulting red shift in emission spectra owing to experience higher magnitude of crystal field splitting. By varying the concentration of cationic substitution of Sr^{2+} ions with Mg^{2+} and Ba^{2+} ions we can tune the emission color of phosphor through blue and red shift phenomena. The detailed description of this work is included in Chapter 4. Coming to cations present in the ionic complexes, by the substitution of different cations in the ionic complex of the host may causes crystal coordination environment distortion among the activator ions and will leads luminescence changes in the given phosphors. We reported single white light emission from one of the promising oxyfluoride host through simply the cationic substitution of Al^{3+} ions in the AlO_4^- ionic complex with Si^{4+} ions as included in Chapter 3. The simultaneous substitution of host cations and cations in the ionic complex of host also be possible for tuning the emission color of the activator ion in a phosphor material.[5]

1.7.1.2. Anionic substitution strategy

Another method for color tuning in phosphor material is anionic substitution in host lattice. By the anionic substitution in the host may change the activator ligand interactions in the crystal lattice i.e. change in nephelauxetic effect. Smaller electronegativity of anions may lead to stronger covalency and higher electronegativity of anions may enhance the extend of crystal field splitting of the 5d orbital of rare earth ions resulting red shift in emission spectra and vice versa. The ascending order of the nephelauxetic effect (centroid shift) of an anion is given below: $F^- < O^{2-} < N^{3-} < S^{2-} < Se^{2-}$. For example, Ju et al. reported a green phosphor Sr_2SiO_4: Eu^{2+}, by the anionic substitution of N^{3-} ions in the lattice leads to red shift in emission spectra from green to red as shown in Fig. 6. As comparing O^{2-} and N^{3-} ions, N^{3-} ions showing higher nephelauxetic effect than O^{2-} ions in Sr_2SiO_4 host towards Eu^{2+} ion activator. Resulting increase in the covalence between Eu^{2+} ion activator and anions may cause red shift in emission spectra.[5]

1.7.1.3. Cationic - anionic substitution strategy

The combination of both the cationic and anionic substitution in a host lattice is a very good method for tuning the emission color of a phosphor by altering the crystallographic environment around the rare earth activator ions. Many literature reports are included the detailed description of this mixed cationic – anionic substitution strategy for the spectral shift in phosphors due to the variation in nephelauxetic effect and crystal splitting in the 5d orbitals of activator. The generally occur cation – anion substitution in a host lattice are: $Al^{3+} + O^{2-} \leftrightarrow Si^{4+} + N^{3-}$; $Si^{4+} + O^{2-} \leftrightarrow Al^{3+} + F^{-}$, $Y^{3+} + C^{4-} \leftrightarrow Sr^{2+} + N^{3-}$, and $Si^{4+} + O^{2-} \leftrightarrow P^{5+} + N^{3-} \leftrightarrow Al^{3+} + F^{-}$, etc. This cationic–anionic substitution strategy gives an insightful way of tuning the emission color of phosphors but still now this method is in the developing stage.[5]

1.7.2. Energy transfer process

The detailed description of the energy transfer mechanism in rare-earth activated phosphors is described in section 1.6.2.3. For tuning the emission color, codoping with a sensitizer into the host lattice is a common practice in phosphor material luminescence study. Sensitizer can act as two roles at a time; they can transfer their energy to activator ions and can emitting individually. The common "sensitizer + activator" groups used are: Ce^{3+}/Eu^{2+}–Tb^{3+}, Ce^{3+}–Dy^{3+}, Ce^{3+}/Eu^{2+}–Tb^{3+}–Sm^{3+}, Ce^{3+}/Eu^{2+}–Tb^{3+}–Eu^{3+}, Ce^{3+}–Eu^{2+}, $Ce^{3+}/Eu^{2+}/Tb^{3+}$–Mn^{2+}.

1.8. Phosphor polymer composites

Conventionally surface coating of LED carried out by mixing phosphor powder with organic resin. Which are facing problems like optical performance loss due to the scattering and reabsorption effect of phosphor, thermal instability and long-time usage leads to crack the organic resin and detaching of epoxy layer. In order to overcome these problems nowadays researchers are focused on developing polymer composite as color converter because of its potential applications towards optoelectronic devices, biological imaging, photo voltaic applications, solid state lighting, etc. So, combining polymer matrix with phosphor is a suitable alternate for generating high performance and thermally stable composite material for LED package instead of organic resin or silicon-based phosphor binders. Because of its characteristic advantages like high refractive index, solubility in aqueous solutions, transparent, flexible, high thermal and moisture

stability, non-absorption in visible region, good binding, transparency, eco-friendly nature, flexibility and reliable optical performance applicable for potential flexible lighting devices. The important thing is that while choosing the polymer as matrix it should not be affected the optical properties of the phosphor powders.[38,39]

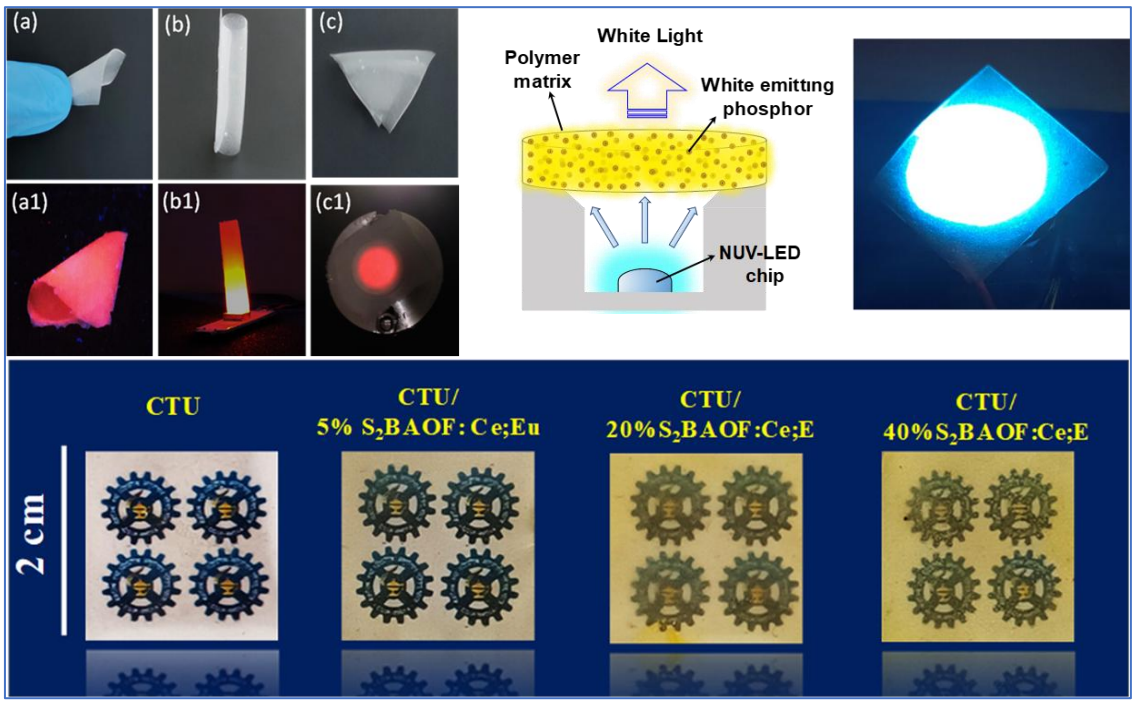

Figure 1.8: *Some of the digital images of developed phosphor polymer composites in the working chapters 2, 3 and 5.*

1.9. General parameters used in WLED characterisations

1.9.1. Commission International de I'Eclairage (CIE)

The CIE diagram is defining the exact emission color of a phosphor material. By the spectral energy distribution of phosphors can be determined by counting simulated colors characterized by X, Y, and Z, commonly known as tristimulus values. It is considered that any color is formed by the color coordinateds combination of primary colors (red, green, and blue). The chromaticity coordinates, denoted by (x, y), signify the X, Y, Z ratios of the light to the total of the three tristimulus standards corresponding Planckian locus is represented in a CIE diagram as shown in **Figure 1.9**. In the CIE diagram, the determined position of a particular color is known as chromaticity point of that color.[3]

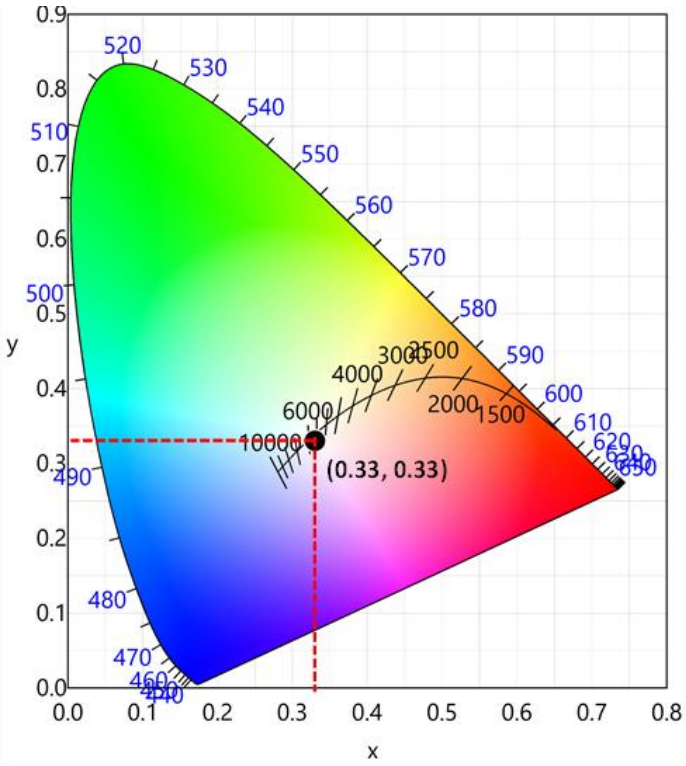

Figure 1.9: *The CIE chromaticity diagram.*

1.9.2. Color rendering index (CRI)

The CRI is a quantifiable amount of the capacity of a light source to generate exact color of the object as compared with the natural light source. A comparison procedure of eight color samples' reflection spectra with the standard reference source under light source is used for calculating the exact value of CRI. The variation of color appearance of eight samples and reference source under the light source is calculated and subtract those values from 100 will give the exact CRI of that specific color under the light source.[3]

1.9.3. Correlated color temperature (CCT)

The CCT is referred to as the color explained in terms of temperature. This parameter is relating white light source's temperature according to the reference opaque black body radiator for the sample source and have the color closest to that of white light source and having same chromaticity coordinates. High color temperature appears to be a cold light with higher color saturation and brightness as well as low CCT exhibit warm light.[3]

1.9.4. Color purity

The color purity in phosphors is calculated through the formula outlined by Fred Schubert.:

$$\text{Color purity} = \sqrt{\frac{(x-x_i)^2+(y-y_i)^2}{(x_d-x_i)^2+(y_d-y_i)^2}} \times 100\ \% \qquad (1.5)$$

where the coordinates (x_i, y_i) denote the position of the white illuminating source (0.333, 0.333), while (x_d, y_d) represent the corresponding coordinates of the governing wavelength of emission.[3]

1.9.5. Photoluminescence lifetime

The photoluminescence lifetime is defined as the time required for the excited electrons to return to their normal ground state. This lifetime decay study is mainly determined from the non-radiative emission process. For materials exhibiting fluorescence, the lifetime is ~10^{-5} – 10^{-8} s, while for those exhibiting phosphorescence, the lifetime is >10^{-4} s. Under an excitation source, the activator ions undergo transitions to an excited state. The population of the excited state after t s, N (t), can be expressed as:

$$N(t) = N_o e^{-(\frac{t}{\tau})} \qquad (1.6)$$

where, N_0 is the population at t = 0s, and τ is the excited state lifetime.[2]

1.9.6. Luminous flux

The luminous flux specifies the entire number of photons emitted by a lighting device per unit of time as apparent by the human eye, attending as the photometric quantity of radiant flux in radiometry. This measure is quantified in lumens (lm).[3]

1.9.7. Luminous efficacy

The luminous efficacy is basically the ratio of the emitted photons to the absorbed photons, which is indicating the emissive efficiency of a luminescent material. It is quantified as the ratio of the entire luminous flux to the input power. This measure is quantified in lumens per watt (lm/W).[3]

1.9.8. Quantum efficiencies

Internal Quantum Yield: The internal quantum yield (η_{int}) of a phosphor represents the ratio of emitted photons to absorbed photons.

$$\eta_{IQE} = \frac{\int L_S}{\int E_R - \int E_S} \qquad (1.7)$$

External Quantum Yield: The external quantum yield (η_{ext}) signifies the ratio of emitted photons to incident photons.

$$\eta_{EQE} = \frac{\int L_S}{\int E_R} \qquad (1.8)$$

here, $\int L_S$ means the combined area below the emission curve, and $\int E_S$ and $\int E_R$ signify the area under the excitation spectral curve with and without the sample in an integrating sphere, respectively.[40,41]

1.9.9. Thermal stability

The operating temperature of high-power LEDs can be reached up to 150 °C. At elevated temperatures, the electrons present in the phosphors are allowed to returning to the ground state without causing any radiative emission. This nonradiative relaxation may leads to reduce the efficiency of the LEDs. That is when the operating temperature of LED increases in normal case thermal quenching may happen means phosphor efficiency become degraded. The thermal stability of a luminescent material corresponds to its capability to limit nonradiative relaxation and compensate for the emission loss. To minimize this problem specific host selection is required with high structural rigidity and wide bandgap, which would prevent electron-phonon interactions and will reduce nonradiative transitions.[42]

1.10. Objectives of the thesis

- Development of isovalent/aliovalent ions substituted polycrystalline oxyfluoride phosphors by a solid-state diffusion technique.
- Tuning the emission to warm white light via cationic substitution-based Eu^{3+}-to-Eu^{2+} valence transition strategies in europium-doped oxyfluoride system.
- Fabricating phosphor polymer composites as a suitable alternative for conventional epoxy coating in LEDs.
- Fabrication, characterizations and optimization of phosphor-converted white LEDs.

1.11. List of References

(1) C. C. Lin, W. T. Chen, R. S. Liu, Phosphors for White LEDs; 2017, 181-222.

(2) W. M. Yen, S. Shionoya, H. Yamamoto, Phosphor Handbook, Second Edition; 2007; Vol. 2.

(3) R. S. Liu, X. J. Wang, Phosphor Handbook Fundamentals of Luminescence; CRC press, United States, 2021.

(4) N. W. Wang, Y. Kaihatsu, F. Iskandar, K. Okuyama, Highly Luminous Hollow Chloroapatite Phosphors Formed by a Template-Free Aerosol Route for Solid-State Lighting; Chem. Mater., 2009, 21, 4685–4691.

(5) M. H. Fang, Z. Bao, W. T. Huang, R. S. Liu, Evolutionary Generation of Phosphor Materials and Their Progress in Future Applications for Light-Emitting Diodes; Chem. Rev. 2022, 122, 11474−11513.

(6) J. Feng, Z. Wang, H. Xu, M. Jia, y. Wei, Z. Fu, The Charge Transfer Band as a Key to Study the Site Selection Preference of Eu^{3+} in Inorganic Crystals; Inorg. Chem. 2021, 60, 19440−19447.

(7) N. S. Satpute, S. J. Dhoble, Role of Rare-Earth Ions for Energy-Saving LED Lighting Devices in Energy Materials: Fundamentals to Applications; Elsevier, 2021.

(8) J.Sun, Y.Du, Z.Luo, H. Guo, Y.Liu, P. Sun, J. Jiang, Enhanced X-Ray Imaging with Gd_2O_2S:Pr-Epoxy Composite Films: Synthesis, High-Resolution Performance, and Flexibility. ACS Appl. Electron. Mater. **2024**, *6* (4), 2782–2787.

(9) R. Sekar, A. Ravitchandiran, S. Angaiah, Recent Advances and Challenges in Light Conversion Phosphor Materials for Third-Generation Quantum-Dot-Sensitized Photovoltaics. ACS Omega **2022**, *7* (40), 35351–35360.

(10) Thejas, K. K.; Abraham, M.; Kunti, A. K.; Tchernycheva, M.; Ahmad, S.; Das, S. Review on Deep Red-Emitting Rare-Earth Free Germanates and Their Efficiency as Well as Adaptability for Various Applications. Appl. Mater. Today **2021**, *24*,

(11) X. Zhang, Z. An, R. Dong, Y. Song, K. Zheng, Y. Sheng, Z. Shi, H. Zou, Properties and application of single Eu^{2+}-activated color tuning phosphors, ACS Sustain. Chem. Eng. 7 (2019) 10724–10733.

(12) Y. Chen, Z. Wang, W. Ding, X. Li, Q. Bao, J. Liu, K. Qiu, X. Meng, Z. Yang, P. Li, A single-phase white light emitting phosphor $Ba_3Y(PO_4)_3:Ce^{3+}$ /Eu^{2+}/Mn^{2+}: luminescence, energy transfer and thermal stability, J. Lumin. 210 (2019) 322–334.

(13) N. Zhang, Y.T. Tsai, M.H. Fang, C.G. Ma, A. Lazarowska, S. Mahlik, M. Grinberg, C.Y. Chiang, W. Zhou, J.G. Lin, J.F. Lee, J. Zheng, C. Guo, R.S. Liu, Aluminate red phosphor in light-emitting diodes: theoretical calculations, charge varieties, and high-pressure luminescence analysis, ACS Appl. Mater. Interfaces 9 (2017) 23995–24004.

(14) W. Ye, C. Zhao, X. Shen, C. Ma, Z. Deng, Y. Li, Y. Wang, C. Zuo, Z. Wen, Y. Li, X. Yuan, C. Wang, Y. Cao, High Quantum yield $Gd_{4.67}Si_3O_{13}$: Eu^{3+} red - emitting phosphor for tunable white light - emitting devices driven by UV or Blue LED, ACS Appl. Electron. Mater. (2021) 2–11.

(15) M. Yazdan Mehr, A. Bahrami, W.D. van Driel, X.J. Fan, J.L. Davis, G.Q. Zhang, Degradation of optical materials in solid-state lighting systems, Int. Mater. Rev. 65 (2020) 102–128.

(16) Global White LEDs Market Size and Scope, *https://www.verifiedmarketreports.com/*.

(17) Y. Chen, W. Ding, P. Li, X. Li, Q. Bao, J. Liu, K. Qiu, X. Meng, Z. Yang, Z. Wang, A single-phase white light emitting phosphor $Ba_3Y(PO_4)_3$:Ce^{3+}/Tb^{3+}/Mn^{2+}: luminescence, energy transfer and thermal stability, RSC Adv. 9 (2019) 30406–30418.

(18) S.A. Khan, H. Zhong, W. Ji, L.Y. Hao, H. Abadikhah, X. Xu, N.Z. Khan, S. Agathopoulos, Single-phase white light-emitting $Ca_xBa_{(9-x)}Lu_2Si_6O_{24}$:$Eu^{2+}$/ Mn^{2+} phosphors, ACS Omega 2 (2017) 6270–6277.

(19) H. Zhang, D. Yuan, X. Mi, X. Liu, J. Lin, Color tuning in $Ca_{3-x}M_x(PO_4)_2$:Eu^{2+}(M = Sr, Ba) phosphors via cation substitution, Dalton Trans. 49 (2020) 8949–8958.

(20) J. Hou, J. Wu, Y. Fang, Y. W. L. Dong, G. Zhang, Y. Liu, H. Chen, G. Li, Cs_2MnCl_4:Eu^{2+}: A Near-Violet Light-Triggered Single-Component White Light Emitter, ACS Appl. Mater. Interfaces 2024, 16, 30176−30184.

(21) S.A. Khan, A. Jalil, Q. Ullah Khan, R.M. Irfan, I. Mehmood, K. Khan, M. Kiani, B. Dong, N.Z. Khan, J.L. Yu, L. Zhu, S. Agathopoulos, New physical insight into crystal structure, luminescence and optical properties of YPO_4:Dy^{3+}\$Eu^{3+}$\$Tb^{3+}$ single-phase white-light-emitting phosphors, J. Alloy. Compd. 817 (2020) 152687.

(22) W. Ran, J. Geng, Z. Zhou, C. Zhou, F. Wang, M. Zhao, T. Yan, Narrow-band green phosphor $RbK_2Na(Li_3SiO_4)_4$:Eu^{2+} with excellent thermal stability and high efficiency for wide color gamut displays, J. Mater. Chem. C, 2024,12, 19148-

1915.

(23) M P. Saradhi, V. Pralng, u. V. Varadaraju, B. Raveau, Facile Chemical Insertion of Lithium in $Eu_{0.33}Zr_2(PO_4)_3$—An Elegant Approach for Tuning the Photoluminescence Properties, Chem. Mater. 2009, 21, 9, 1793–1795.

(24) Park, J. K., Choi, K. J., Yeon, J. H., Lee, S. J., Kim, C. H. Embodiment of the warm white-light-emitting diodes by using a Ba^{2+} codoped Sr_3SiO_5:Eu phosphor. Appl. Phys. Lett. 88, 043511, 2006.

(25) Duan, C. J., Delsing, A. C. A., Hintzen, H. T. Photoluminescence properties of novel red-emitting Mn2+-activated MZnOS (M= Ca, Ba) phosphors. Chem. Mat., 21, 1010, 2009.

(26) Kuo, T. W., Liu, W. R., Chen, T. M. High color rendering white light-emittingdiode illuminator using the red-emitting Eu^{2+}-activated CaZnOS phosphors excited by blue LED. Opt. Express, 18, 8187, 2010.

(27) S. Sreevalsa, P. Ranjith, S. Ahmad, S.K. Sahoo, S. Som, M.K. Pandey, S. Das, Host sensitized photoluminescence in $Sr_{2.9-3x/2}Ln_xAlO_4F$: $0.1Eu^{3+}$ (Ln = Gd, Y) for innovative flexible lighting applications, Ceram. Int. 46 (2020) 21448–21460.

(28) S. Sreevalsa, A. P. Parvathy, K. S. Sahoo and S. Das, Full- Color Emitting Crystal Engineered $Sr_3Al_{1-x}Si_xO_{4+x}F_{1-x}$:$Eu^{2+/3+}$ Oxyfluorides for Developing Bendable Lighting Composites, J. Alloys Compd., 2021, 880, 160483.

(29) S. Subhagan, S. Ahmad, P. Kundu, M. K. Pandey, S. Som, S. Das, Governing the crystallographic sites for tuning Eu^{2+} emission in an apatite oxyfluoride host to be applied for superior white light emitting diodes Dalt. Trans. **2022**, *51*, 14601.

(30) W. B. Im, S. Brinkley, J. Hu, A. Mikhailovsky, P. S. Denbaars, R. Seshadri, $Sr_{2.975-x}Ba_xCe_{0.025}AlO_4F$: A Highly Efficient Green-Emitting Oxyfluoride Phosphor for Solid State White Lighting, Chem. Mater., 2010, 22, 2842–2849.

(31) M. Noh, S. h. Cho, S. Park, Tunableluminescence in Bi^{3+} and Eu^{3+} co-doped Sr_3AlO_4F Oxyfluorides phosphors , Journal ofLuminescence161(2015)343–346.

(32) B. Vengala, G. Bhaskar, W. H. Joo, J. Kiwan, S. D. Soo, Y. S. Soo, J. Jung, Luminescence and energy transfer of Eu^{3+} or/and Dy^{3+} co-doped in Sr_3AlO_4F phosphors with NUV excitation for WLEDs, Journal of Alloys and Compounds, 2012, 538, 85–90.

(33) M. Kirm, E. Feldbach, H. Mägi, V. Nagirnyi, E. Tõldsepp, S. Vielhauer, T. Jüstel, T. Jansen, M. N. Khaidukov, N. V. Makhov, Silicate Apatite Phosphors for Pc-LED Applications, Proc. Est. Acad. Sci., 2017, 66, 383.

(34) K. Li, D. Geng, M. Shang, Y. Zhang, H. Lian and J. Lin, Color-Tunable Luminescence and Energy Transfer Properties of $Ca_9Mg(PO_4)_6F_2:Eu^{2+}$, Mn^{2+} Phosphors for UV-LEDs, J. Phys. Chem. C, 2014, 118, 11026–11034.

(35) L. Zhu, Z. Huang, M. S. Molokeev, X. Min, Y. Liu, M. Fang, X. Wu, Influence of cation substitution on the crystal structure and luminescent properties in apatite structural $Ba_{4.97-x}Sr_x(PO_4)_3Cl:0.03Eu^{2+}$ phosphors, Chemical Physics Letters, 2016, 658, 248-253.

(36) A. Arredondo, H. Desirena, I. Moreno and I. E. Hinostroza, Dual Color Tuning in Ce^{3+}-Doped Oxyfluoride Ceramic Phosphor Plate for White LED Application, J. Am. Ceram. Soc., 2019, 102, 1425–1434.

(37) B. Shao, J. Huo, H. You, Prevailing Strategies to Tune Emission Color of Lanthanide-Activated Phosphors for WLED Applications, Adv. Optical Mater. 2019, *7*, 1900319

(38) A. Potdevin, G. Chadeyron, S. Thérias, R. Mahiou, Luminescent Nanocomposites Made of Finely Dispersed Y3Ga5O12:Tb Powder in a Polymer Matrix: Promising Candidates for Optical Devices*Langmuir* **2012**, *28*, 13526.

(39) J. Dang, Z. Yang, W. Guo, Y. Ji, H. Wang, J. Deng, M. Wang, In Situ Fabrication of Mn-Doped 2D Perovskite-Polymer Phosphor Films with Green-Red Dual Emissions for Yellow Lighting, *Adv. Mater.* Interfaces **2021**, *8*, 2100560.

(40) Abraham, M.; Thejas, K. K.; Kunti, A. K.; Amador-Mendez, N.; Hernandez, R.; Duras, J.; Nishanth, K. G.; Sahoo, S. K.; Tchernycheva, M.; Das, S. Strategically Developed Strong Red-Emitting Oxyfluoride Nanophosphors for Next-Generation Lighting Applications. *Adv. Opt. Mater.* **2024**, 2401356.

(41) Smet, P. F.; Parmentier, A. B.; Poelman, D. Selecting Conversion Phosphors for White Light-Emitting Diodes. *J. Electrochem. Soc.* **2011**, *158* (6), R37–R54.

(42) Sun, Z.; Sun, B.; Zhang, X.; Wen, D.; Dai, P. Superb Thermal Stability Purple-Blue Phosphor through Synergistic Effect of Emission Compensation and Nonradiative Transition Restriction of Eu^{2+} *Mater. Today Chem.* **2022**, *24*, 100877.

Chapter 2

Innovative flexible lighting applications based on host triggered photoluminescence in $Sr_{2.9-3x/2}Ln_xAlO_4F$: $0.1Eu^{3+}$ (Ln = Gd, Y)

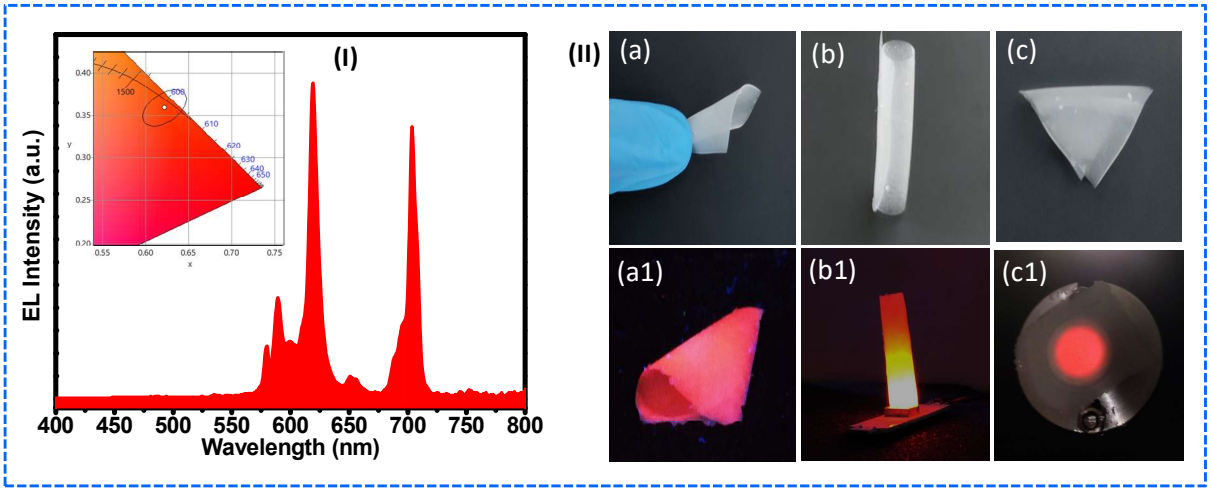

2.1 Abstract

Tetragonal structured Sr_3AlO_4F is under highly strained as reported from its global instability index (GII) estimation. Moreover, our results of X-ray photoelectron spectroscopy (XPS) also ascertained that the structure of Sr_3AlO_4F was under highly strained with some oxygen vacancies. Herein, aliovalent substitutions of divalent Sr ions with trivalent Gd and Y ions were carried out to improve the stability of Sr_3AlO_4F lattice. To gain high red photoluminescence from this structure, a series of $Sr_{2.9-3x/2}Ln_xAlO_4F$: $0.1Eu^{3+}$ (x = 0.01−0.10) phosphors were synthesized. The intensities and positions of the reflections in the powder X-ray diffraction patterns closely resembled with the tetragonal Sr_3AlO_4F. All the samples showed intense red-orange emission ($^5D_0 \rightarrow {}^7F_{1,2}$) at excitation with UV and near-UV light. The critical concentration of Gd^{3+} and Y^{3+} up to which the Eu^{3+} emission intensities increased linearly were observed to be x = 0.09 and x = 0.07, respectively. The reason behind the quenching of luminescence was found to be dipole−dipole interaction. Nevertheless, further enhancement in the luminescence of the optimized phosphors was realized by subsequently annealing in reducing the atmosphere of Ar and vacuum. The enhancement in oxygen deficiency during post-annealing in Ar or vacuum led the energy transfer (O^{2-}-Eu^{3+}) to a greater extent which subsequently increased the luminescence intensity. The various radiative properties of the emission bands were also analyzed through the Judd-Ofelt theory. The optimized $Sr_{2.765}Gd_{0.09}AlO_4F$:$0.1Eu^{3+}$ and $Sr_{2.795}Y_{0.07}AlO_4F$:$0.1Eu^{3+}$phosphors showed high red color purity (~99 %), and proper correlated color temperature (~1300 K), as well as CIE coordinates of (0.62, 0.38), indicated that these phosphors could be appropriate red-emitting components for making flexible optical films for many lighting devices. Therefore, flexible polydimethylsiloxane (PDMS) based films were also fabricated using optimized $Sr_{2.765}Gd_{0.09}AlO_4F$: $0.1Eu^{3+}$ phosphors. The electroluminescence (EL) of a flexible PDMS-phosphor composite film device showed a cool-red color suggesting its suitability in flexible display devices.

2.2 Introduction

Research on the development of the efficient inorganic phosphor materials has been carried out using two general approaches viz. by exploring newer optical host lattices or by adopting different manufacturing strategies, surface modification, and color-optimization of emission in well-established optical host matrices.[1] The fluoride-containing oxide hosts doped with rare-earth ions have shown great potential as light-

emitting diode (LED) phosphors with their tunable luminescence properties.[2-5] The introduction of fluoride ions into an oxide crystal lattice leads to a distortion of the coordination polyhedrons i.e. generation of non-centrosymmetric sites, which causes unusual spectroscopic properties.[6] Moreover, the fluoride host matrices are known to provide a wide bandgap, low phonon energy and inter-configurational transitions whereas the oxides host matrices are known to provide high chemical stability and high absorption in UV-visible region.[7] Based on aforementioned facts, the oxyfluorides which combine the advantages of both fluorides and oxides are favorable to serve as the host materials for luminescence properties. Additionally, the ionic radii of O^{2-} and F^{-} ions are also comparable and thus stable crystals can be obtained in oxyfluorides at various O/F ratios. Recently, anion ordered oxyfluorides having composition Sr_3AlO_4F is emerging as one of the most widely investigated oxyfluorides phosphor due to its good chemical and thermal stability, facile synthesis conditions, and efficient luminescence properties.[8-12] Lin and co-workers demonstrated white-light emission from the single-phase Sr_3AlO_4F: $Tm^{3+}/Tb^{3+}/Eu^{3+}$ under the excitation of 360 nm using UV-InGaN LED.[12] Bandi et al. reported $Sr_3AlO_4F:Eu^{3+}/Dy^{3+}$ as a prominent white-light- emitting phosphor under the near-UV excitation.[13]

The structure of Sr_3AlO_4F consists of two different sites for Sr atoms. The Sr1 atom located in the layer of $[AlO_4]^{5-}$ tetrahedra is coordinated by two apical fluorine and eight oxygen atoms.[12] On the other hand, the Sr2 atom is coordinated by two fluorine atoms within its plane and three oxygen atoms on each side of its plane.[12] The global instability index (GII) of Sr_3AlO_4F as estimated by Quilty and co-workers is very high (0.33) indicating that the structure of this phase is under high strained.[14] The majority of the strain comes from the extremely under-bonded Sr(2) and the slightly over bonded Sr(1). The bond valence sum (BVS) for the structure refinement of Sr_3AlO_4F suggests that Sr2 is somewhat under bonded with BVS=1.35, while Sr1 has BVS=2.25 which is closer to its formal oxidation state of 2.[14] Due to under bonded Sr2 atom, Sr_3AlO_4F lattice can easily adopt oxygen vacancies, and thus can accommodate considerable amount of trivalent ions substitutions at Sr2 sites. From density functional theory (DFT) calculations, the substitution of La^{3+} at the 8h site in place of Sr^{2+} is slightly more energetically favorable than its substitution at the 4a site, but only by 0.14 eV.[15] The excess charge generated due to trivalent substitution can be compensated by the diffusion of oxygen vacancies into the crystal lattice sites. Thus the strain present in a Sr_3AlO_4F

lattice could be tailored by the chemical substitutions of Sr ions with aliovalent trivalent ions. It is well-known that lattice defects (cation or anion vacancies) always existed in materials. These cationic or anionic vacancies can produce local potentials, which lead to the vacancies trapping the electrons or holes. The production of vacancies could be altered by providing different atmospheric conditions during the preparation of the materials. For example, in a low oxygen atmosphere, the oxygen vacancies, which trap the electrons, are easily generated in oxide-based phosphor materials.[16]

In this working chapter, a series of Gd^{3+} and Y^{3+} doped Sr_3AlO_4F samples have been synthesized by substituting Gd^{3+} and Y^{3+} for the Sr2 site. A facile solid-state methodology has been used to produce highly crystalline and homogeneous products. The luminescence properties of a series of 0.1 mol% of Eu^{3+} doped $Sr_{2.9-3x/2}Ln_xAlO_4F$ (x = 0.01−0.10) samples have also been studied to find the optimized doping concentration of trivalent ions. The optimized sample is used to generate a red-emitting component for fabricating flexible optical film. Both Gd^{3+} and Y^{3+} doped samples showed high red color purity, CCT and, CRI which makes the red phosphor a suitable component for the white-LEDs and flexible optical film. In addition, a transparent flexible polymer composite film was also fabricated through the one-pot in-situ cross-linking process to display tuneable light emission. Herein, Polydimethylsiloxane (PDMS) has been used as a host polymer matrix due to its good transparency, high moldability, and flexibility.

2.3 Experimental Section

2.3.1. Preparation of phosphor

A series of $Sr_{2.9-3x/2}Ln_xAlO_4F$: $0.1Eu^{3+}$(Ln^{3+} = Gd, Y; x = 0.01 to 0.1) samples were synthesized by solid-state methodology. The stoichiometric amounts of $SrCO_3$ (99.999%), SrF_2 (99.999%), Al_2O_3 (99.999%), Ln_2O_3 (99.99%) and Eu_2O_3 (99.999%) obtained from Sigma-Aldrich were thoroughly mixed in an agate mortar for 30 min. Additionally, 2.5 wt% of NH_4F as a flux was added to carry out a homogeneous reaction. The homogeneously grounded mixture was subjected to heating in an alumina crucible at 500 °C for 3 h and then at 1100 °C for 4 h. The optimum samples were post-annealed at 1100 °C in a tubular furnace for 2 h either in presence of 99.5% Ar or under vacuum.

2.3.2. Preparation of $Sr_{2.765}Gd_{0.09}AlO_4F$: $Eu_{0.1}$phosphor / PDMS film

Herein, 0.25 g of optimized $Sr_{2.765}Gd_{0.09}AlO_4F$: $Eu_{0.1}$ sample dispersed in acetone was transferred into a beaker containing 5 g of siloxane elastomer resin (Sylguard 184) and then subjected to stirring (500 rpm) at room temperature for 20 min. Subsequently, 0.5 g of cross-linker was also added to this resultant mixture and further stirred for 10 min to ensure uniform dispersion. The resin was then placed in a vacuum desiccator to release the air bubbles and subsequently cast on a glass plate. The uniformity in the thickness of the film was maintained at 300 microns. Initially, the film was allowed to stand for 12 h at room temperature and then it was cured at 70 °C for 1 h. The film was peeled off from the glass plate. The schematic diagram of the fabrication process of the $Sr_{2.765}Gd_{0.09}AlO_4F$: $Eu_{0.1}$ phosphor-PDMS film is shown as **Fig. 2.1**.

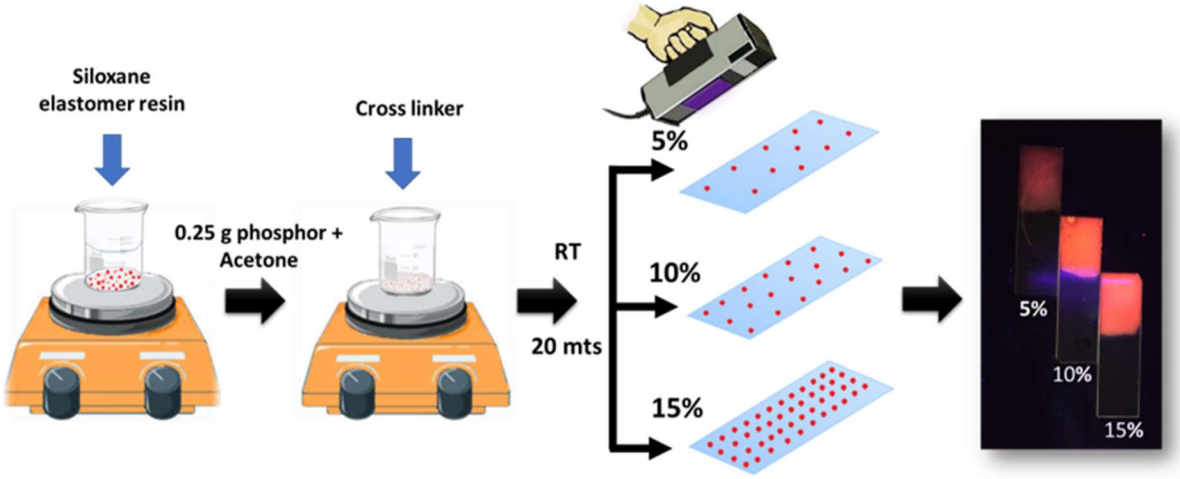

Figure 2.1: *The schematic representation of the fabrication process of the* $Sr_{2.765}Gd_{0.09}AlO_4F$: $Eu_{0.1}$ *phosphor-PDMS film.*

2.3.3. Characterizations

The XPS measurements were recorded in a PHI 5000 Versaprobe Scanning ESCA Microprobe. The core-level spectrum of Al 2p, Sr 3d, O 1s, and F 1s were obtained using Al Kα radiation (1.487 keV) at a resolution of 0.1 eV. The position of peaks of these four elements was calibrated by using the reference of C 1s core-level spectrum (285.0 eV). The core-level spectrum was fitted using the Gaussian-Lorentzian distribution function to find the areas of chemically distinct species. The PXRD of synthesized samples were measured using Philip's x'pert pro diffractometer, Ni filtered Cu-K_α (λ = 1.54 Å). The

photoluminescence (PL) characteristics were measured using Yvon Fluorolog 3 spectrofluorimeter having an exciting source of 450W Xenon flash lamp. The Commission Internationale de I'Eclairage (CIE) coordinates were obtained from the PL spectra using the color calculator software.

2.4 Results and Discussions

2.4.1 Structural evaluations

A survey XPS spectrum of Sr_3AlO_4F is presented in Fig. 2.S1, from where the presence of Sr, Al, O, and F atoms can be observed. The core-level spectrum of Sr 3d is deconvoluted by two peaks centered at 133.90 and 135.65 eV which are attributed to Sr $3d_{5/2}$ and Sr $3d_{3/2}$, respectively with an intensity ratio of 1:0.60 (**Fig. 2.2 (a)).**[16] The core-level spectrum of Al 3p is centered at 73.92 eV which is a characteristic of Al atoms in an oxygen environment (**Fig. 2.2 (b)**). The core-level spectrum of O1s was also deconvoluted into two peaks. The main constituent of the peak O_I having a binding energy of 531.87 eV, is due to the lattice oxygen. While the trivial constituent O_{II} having a binding energy of 532.91 eV, is because of the defect-oxide i.e. oxygen vacancies.[17] The area of the lattice oxygen and oxygen vacancies in this crystal was found to be 71.70% and 28.30%, respectively. The presence of high oxygen vacancies is expected due to the highly under bonded Sr2 and Al atoms. The core-level spectrum of F 1s has been deconvoluted into two peaks centered at 685.05 and 686.56 eV and their equivalent % analytical area is 33.93% and 66.06%. In Sr_3AlO_4F, each fluorine atom is surrounded by two Sr1 and four Sr2 with a bond length of 2.7859 Å and 2.5188 Å respectively. The minor component of the peak F_I with a binding energy of 685.05 eV, is ascribed to the higher bond length of two F-Sr1 bonds, and the major component F_{II}, with a binding energy of 686.56 eV, is attributed to the smaller bond length of four F-Sr2 bonds. Moreover, the integrated analytical ratio of Sr1 to the Sr2 is also 1:2 (related to their empirical ratio) which confirmed the absence of cationic vacancy. Consequently, like the results of BVS and GII calculations reported by Quilty and co-workers, our results of XPS also ascertained that the Sr_3AlO_4F is under highly strained with some oxygen vacancies.[14]

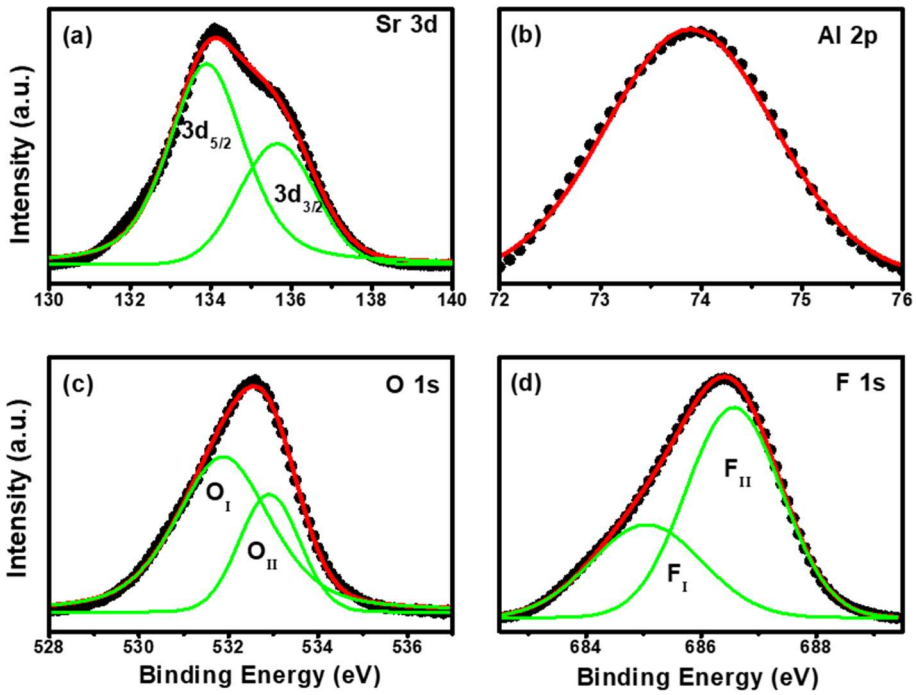

Figure 2.2: *High-resolution XPS spectrum of (a) Sr 3d, (b) Al 2p, (c) O 1s, and (d) F 1s in the Sr_3AlO_4F sample.*

While the survey XPS spectrum of $Sr_{2.985}Ln_{0.1}AlO_4F$ (Ln = Gd or Y) samples are shown in **Fig. 2.3 (a)**, the core level spectrum of Gd 4d and Y 3d of $Sr_{2.985}Gd_{0.1}AlO_4F$ and $Sr_{2.85}Y_{0.10}AlO_4F$ are shown as **Fig. 2.3 (b)** and **(c),** respectively. The core-level spectrum of Gd 4d has been deconvoluted into two peaks centered at 143.79 eV and 144.67 eV which are corresponding to Gd $4d_{3/2}$ and Gd $4d_{5/2}$. Similarly, the core-level spectrum of Y 3d was deconvoluted into two peaks centered at 155.89 eV and 159.75 eV which are corresponding to Gd $4d_{3/2}$ and Gd $4d_{5/2}$.

The Le-Bail refinement of the PXRD pattern of the Sr_3AlO_4F sample is shown in **Fig.2.S2.** The peak positions and the intensities of the observed PXRD pattern of the Sr_3AlO_4F sample are matching well with the tetragonal form of Sr_3AlO_4F (JCPDS. 89-4485) having the space group (I4/mcm #140). The Le-bail refined crystallographic data produced an excellent agreement between the simulated and experimental pattern with lattice constants of a = 6.7706 (3) Å and c = 11.1547 (2) Å. The PXRD patterns of the $Sr_{2.9-3x/2}Ln_xAlO_4F$: $0.1Eu^{3+}$(Ln = Gd or Y) phosphors are depicted in **Fig. 2.4 (a)** and **(b)**. The intensities and positions of the observed reflections in their PXRD patterns have closely resembled with the tetragonal Sr_3AlO_4F (JCPDS No. 89-4485) with a slight shift

to the lower 2θ side. The enlarged version of the XRD patterns around the strongest diffraction peak of the phosphors at 2θ = 30° shows a distinct peak shift, as elaborated in **Fig. 2.4** Based on the Vegard's law, the substitution of smallerLn^{3+} ions in place of Sr^{2+} ions should contract the lattice.[18] However, in the present case, the enhancement in the lattice parameter can be attributed to the excess charge when a divalent Sr^{2+} ion is substituted by this trivalent Gd^{3+} or Y^{3+}ions.[19] This excess charge neutralization would require diffusion of oxygen vacancies into the crystal lattice sites that would, in turn, lead to a lattice expansion.[19] The expansion of lattice constants can also be explained based on the change in covalency of the Sr–O bond when Sr^{2+} ions are partially substituted by less electropositive Gd^{3+}or Y^{3+}ions. The Pauling scale of electronegativity values of Sr^{2+}, Gd^{3+}, $Y^{3+}$and $F^-$is 0.95, 1.20, 1.22 and 3.44, respectively. The smaller the difference in electronegativity of metal ions and oxide ions, the greater will be the covalency which in turn increases the lattice parameter. Similar results were also reported earlier by the Thampi and co-workers wherein the Gd^{3+} ions of the $Gd_2Zr_2O_7$ system were partially substituted by Ca^{2+} ions which lead to a slight red shift of the reflections.[19]

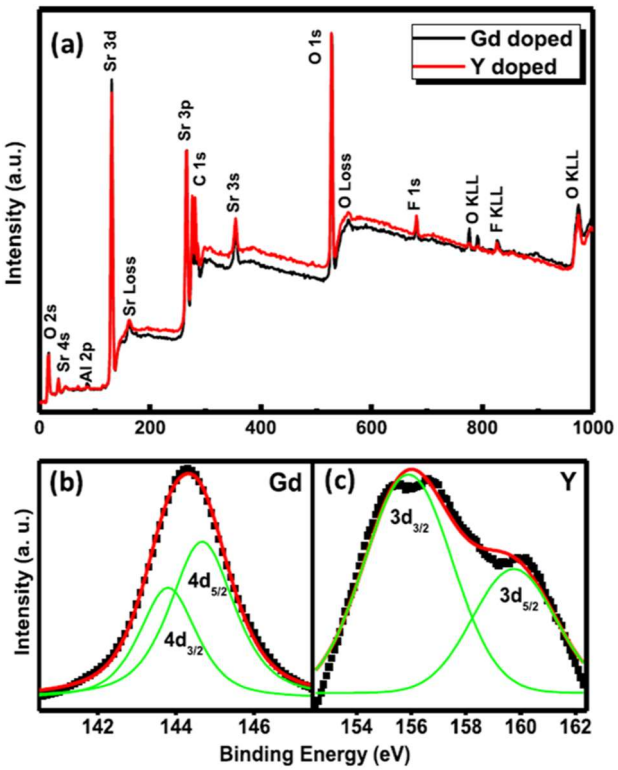

Figure 2.3: (a) *Survey XPS spectra of* $Sr_{2.985}Ln_{0.01}AlO_4F$ *(Ln = Gd, Y). High-resolution XPS spectrum of* ***(b)*** *Gd (in* $Sr_{2.985}Gd_{0.01}AlO_4F$*) and* ***(c)*** *Y (in* $Sr_{2.985}Y_{0.01}AlO_4F$*).sample.*

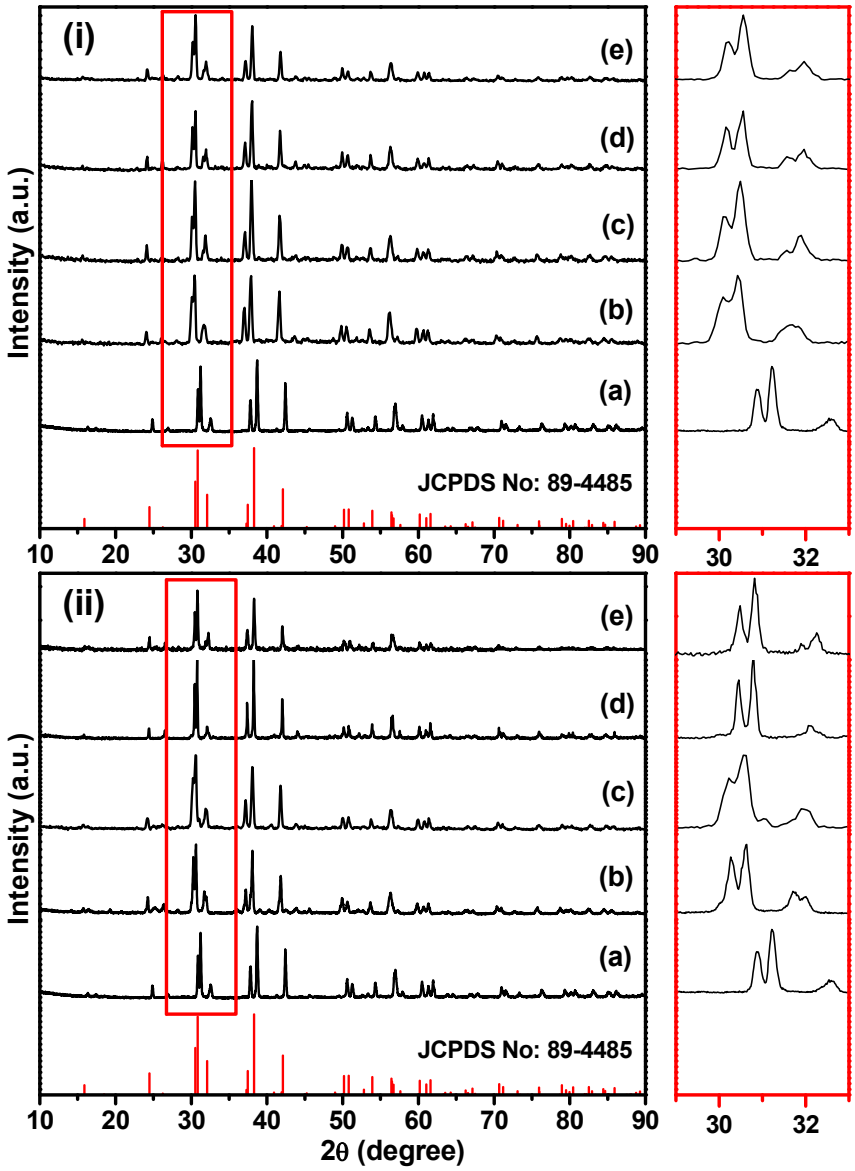

Figure 2.4: *PXRD patterns of the (i) $Sr_{2.9-3x/2}Gd_xAlO_4F$: $0.1Eu^{3+}$ ((a) x =0, (b) x= 0.03, (c) x =0.05, (d) x =0.09, (e) x = 0.1) and (ii) $Sr_{2.9-3x/2}Y_xAlO_4F$: $0.1Eu^{3+}$ ((a) x = 0, (b) x = 0.03, (c) x = 0.05, (d) x = 0.07, (e) x = 0.1) phosphors along with the standard pattern of Sr_3AlO_4F as the reference.*

2.4.2. Optical evaluations

Fig. 2.5 shows the PL excitation spectra of Sr_3AlO_4F: 0.1Eu, $Sr_{2.765}Gd_{0.09}AlO_4F$: $0.1Eu^{3+}$ and $Sr_{2.795}Y_{0.07}AlO_4F$: $0.1Eu^{3+}$ phosphors recorded by monitoring 618 nm emission. The spectra consists of several sharp peaks at 361, 379, 395, 414 and 463 nm due to the intra *f–f* Eu^{3+} transitions $^7F_0 \rightarrow {}^5D_4$, $^7F_0 \rightarrow {}^6G_{2-6}$, $^7F_0 \rightarrow {}^5L_6$, $^7F_0 \rightarrow {}^5D_3$ and $^7F_0$

→ $^5D_2$, respectively.[20] Along with Eu^{3+} transitions, symmetrically broad CTB emission centered at 285 nm is also observed indicating that there is an intense interaction of Eu^{3+} ions with O^{2-} ions, which enhances the chances of mixing of *4f* and *2p* orbitals of Eu^{3+} and O^{2-} ions, respectively.[21] Since the covalent character of Gd-O or Y-O bonds is greater than the covalent character of Sr-O bonds, the intensity of CTB and intra *f–f* Eu^{3+} transitions increased upon the substitution of trivalent ions for Sr^{2+} ions.[22]

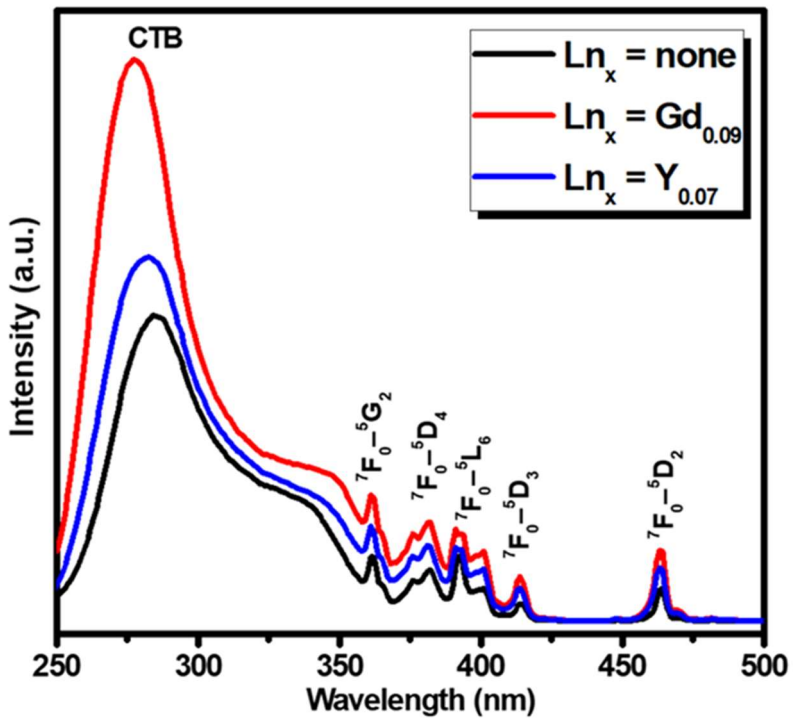

Figure 2.5: *PL excitation spectra of $Sr_{2.9}AlO_4F$: $0.1Eu^{3+}$, $Sr_{2.765}Gd_{0.09}AlO_4F$: $0.1Eu^{3+}$ and $Sr_{2.795}Y_{0.07}AlO_4F$: $0.1Eu^{3+}$ phosphors.*

Fig. 2.6 depicted the PL emission plots of $Sr_{2.9-3x/2}Ln_xAlO_4F$: $0.1Eu^{3+}$(Ln = Gd or Y) phosphors recorded at the excitation wavelengths of 285 and 393 nm, respectively. The spectra consist of several sharp peaks at 535, 557, 580, 591, 619, and 651 nm owing to the intra *f–f* Eu^{3+} transitions.[20] The electric dipole hypersensitive transition $^5D_0 \rightarrow {}^7F_2$ (619 nm) is found to be intense than the magnetic dipole transition $^5D_0 \rightarrow {}^7F_1$ (591 nm), indicating that the Eu^{3+} ions are embedded in a small symmetric environment lacking with any inversion center.[21] Meanwhile, the presence of $^5D_0 \rightarrow {}^7F_0$ transition at 580 nm further corroborates that the Eu^{3+} ions are situated in a low symmetric site.[21] This further confirmed that the Eu^{3+} ions are situated at the non-centrosymmetric Sr2 sites.

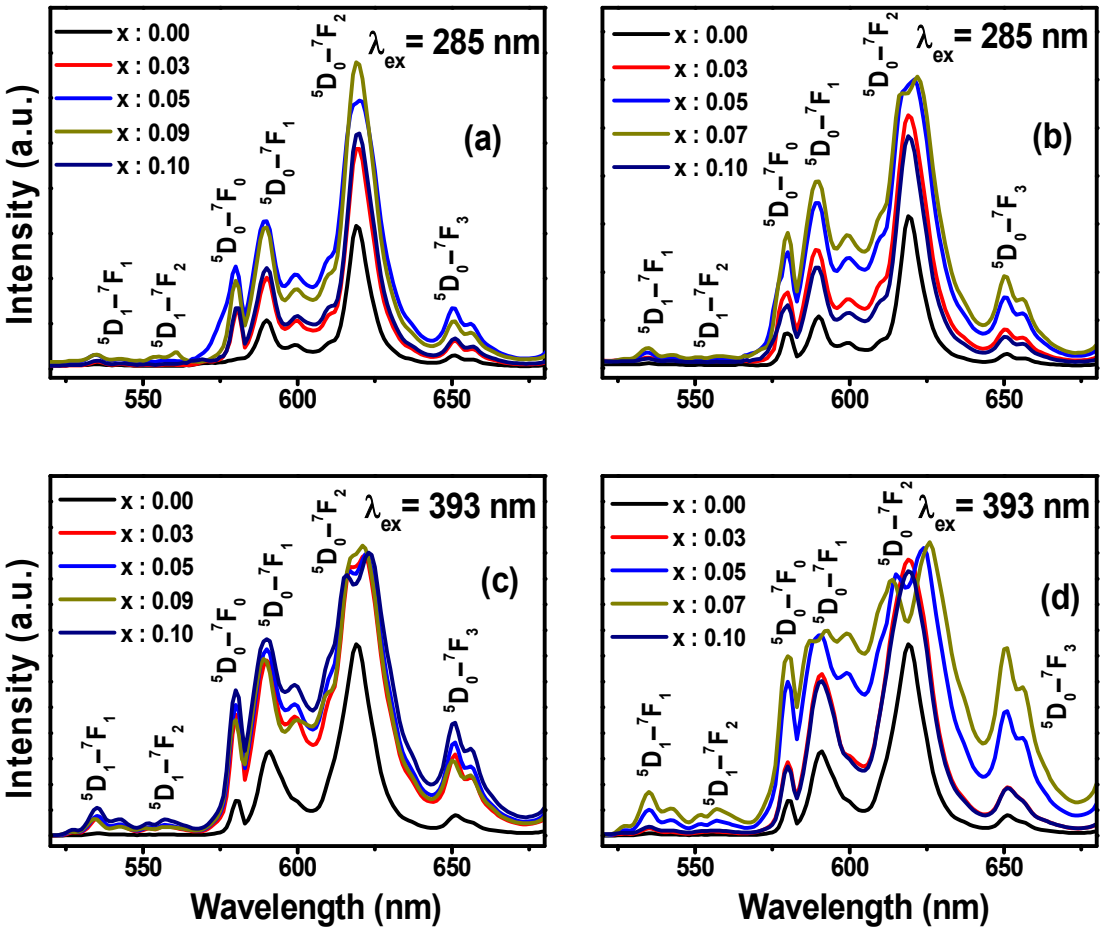

Figure 2.6: *PL emission spectra of the $Sr_{2.9-3x/2}Gd_xAlO_4F$: $0.1Eu^{3+}$ (at the excitations of (a) 285 nm and (c) 393 nm) and $Sr_{2.9-3x/2}Y_xAlO_4F$: $0.1Eu^{3+}$ (at the excitations of (b) 285 nm and (d) 393 nm) phosphors.*

The variation of the asymmetric ratio (red/orange), known as the relative intensity ratio of the electrical dipole to magnetic dipole transition [I ($^5D_0 \rightarrow {}^7F_2$) / I ($^5D_0 \rightarrow {}^7F_1$)] with the incorporation of Ln^{3+} ions (Ln = Gd, Y) are shown in Table 2.1. Higher the value of asymmetry ratio, the higher would be the color purity.[23] This ratio as a function of the Ln^{3+} content in the present host is not greatly diverted, demonstrating that the general Eu^{3+} local environment is independent of the Ln^{3+} doping content. The manifestation of the luminescence emission from highly excited states including $^5D_1$ and $^5D_2$ indicated the incompetent non-radiative relaxation to the $^5D_0$ level induced by the strong electron-phonon coupling.[24] The strong electron-phonon coupling also promotes the non-radiative

transition rate (W_{NR}) via a multi-phonon process. The value of W_{NR} in the present phosphors are estimated using the modified Van Dijk and Schuurmans's formula:[25]

$$W_{NR} = \beta_{el}\exp[-\alpha(\Delta E - 2h\omega_{max})] \qquad (2.1)$$

where $h\omega_{max}$ is representing the active phonons energy, β_{el}= 10^7 s^{-1} and α= 4.5 (±) × 10^{-3} cm. The multi-phonon relaxation probability was found to be 332 s^{-1}, which is not enough to cause efficient quenching.[25] The critical concentration of $Gd^{3+}$and Y^{3+} up to which the emission intensities linearly increased are x = 0.09 and x = 0.07, respectively. Beyond this concentration, the PL intensity reduced. It is quite normal that the substitution of Sr^{2+} sites by Ln^{3+} will lead to the irregularity of crystal structure through forming the cation vacancy and interstitial anion in the hosts for the charge compensation, as reported in detail by Jing and co-workers [26]. Above a particular concentration of Ln^{3+} (Ln = Gd, Y), such interstitial defects capture radiative electrons effectively, which could be the reason for PL intensity decreasing as Ln^{3+} (Ln = Gd, Y) content reach beyond the critical concentration as mentioned above [26–29]. Therefore, the decrease of photoluminescence in the present systems above the critical concentrations might be due to the energy migration occurred from Eu^{3+} sublattice to the defects, which attribute to the exchange interactions [26]. It is known that the heat treatment in an oxygen-deficient environment can convert lattice oxygen into the surface oxygen vacancies [26,29].

Table 2.1: *Calculated JO parameters for the optimized samples prepared in air and post annealed in vacuum.*

Phosphors	Ω_2 ($\times 10^{20}$ cm^2)	$A_{0\text{-}2}$ (s^{-1})	τ_{rad}(ms)	Assy. Rat.
Ln (0.00)	2.84	88.8	6.2	1.69
Y (0.07)	2.88	94.3	6.9	1.72
Gd (0.09)	2.94	95.3	6.7	1.73
Y (Vacuum)	2.76	96.4	6.8	1.84
Gd (Vacuum)	2.77	96.6	6.8	1.84

To observe the influence of post - annealing on the PL properties of present samples in different heating atmospheres, the optimized as-prepared $Sr_{2.765}Gd_{0.09}AlO_4F$: $0.1Eu^{3+}$ and

$Sr_{2.795}Y_{0.07}AlO_4F$: $0.1Eu^{3+}$phosphors were subsequently heated for 1 h at 1000ºC in a reducing atmosphere of 99.5% Ar and vacuum. Their emission spectra collected at the excitations of 285 and 393 nm are depicted in **Fig. 2.7.** Generally, it is well accepted that the stabilization of Eu^{2+}cations is triggered in reducing atmosphere, while Eu^{3+} cations were naturally stabilized in the air or oxygen-rich environment.[30] However, the broad emission of Eu^{2+} ions was not observed in any of the PL and PLE spectrum of the of $Sr_{2.9-3x/2}Ln_xAlO_4F$: $0.1Eu^{3+}$ (Ln^{3+} = Gd, Y; x = 0.01 to 0.1) samples. Moreover, Fig. 6 shows that post vacuum annealing is quite effective in enhancing the red emission of the $Sr_{2.765}Gd_{0.09}AlO_4F$: $0.1Eu^{3+}$ and $Sr_{2.795}Y_{0.07}AlO_4F$: $0.1Eu^{3+}$ phosphors. The annealing in a vacuum helps in the creation of oxygen vacancies as reported by other research groups.[31,32]

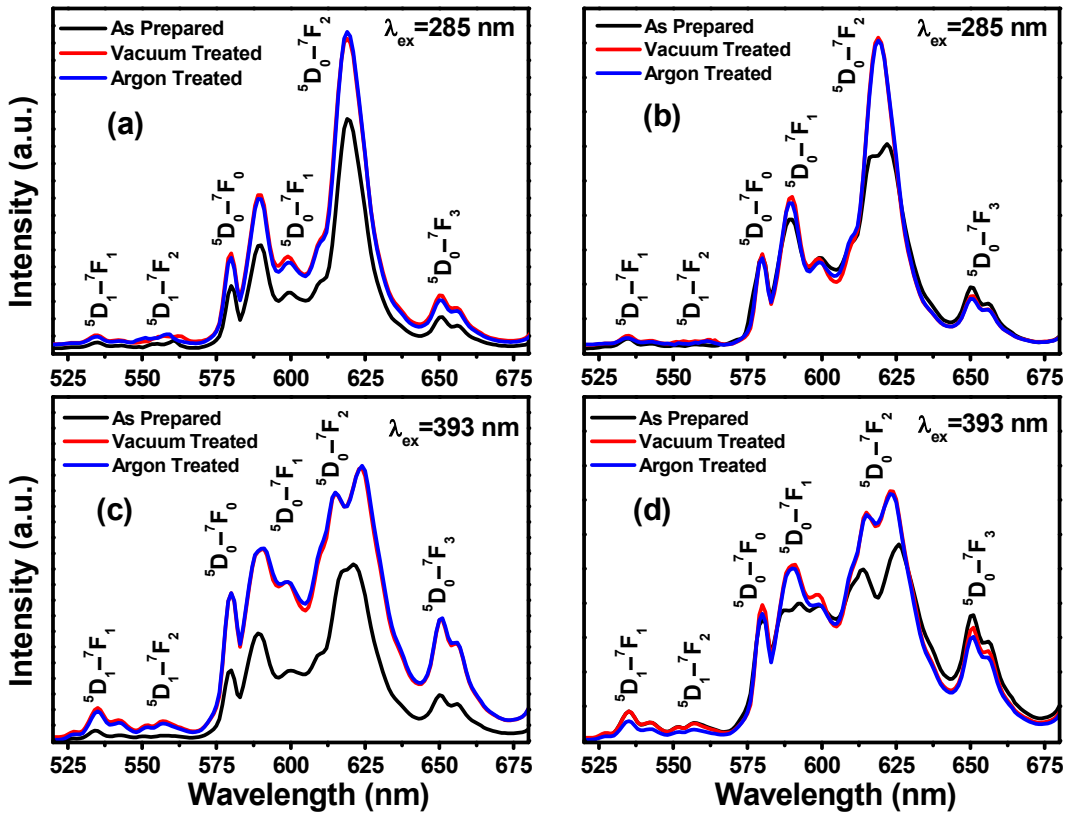

Figure 2.7: *PL emission spectra of the $Sr_{2.765}Gd_{0.09}AlO_4F$: $0.1Eu^{3+}$(at the excitations of (a) 285 nm and (c) 393 nm) and $Sr_{2.795}Y_{0.07}AlO_4F$: $0.1Eu^{3+}$ (at the excitations of (b) 285 nm and (d) 393 nm) phosphors post treated in vacuum.*

To find the relationship between the oxygen vacancies and red emission in the vacuum-annealed samples, we first examine the PL spectrum of $Sr_{2.985}Ln_{0.01}AlO_4F$ samples (Ln = Gd, Y), and their results are shown in **Fig. 2.7(a)** and **(b)**. At the UV excitation of 245 nm, intense blue-light emission curves centered at 415 nm have been observed for all the samples, which were annealed at 1000 °C in vacuum or the Ar atmosphere. The broadband at 415 nm is attributed to the emission from a localized electron-hole pair i.e. oxygen vacancies and its emission intensity increased upon post - annealing in Ar or vacuum, as shown in **Fig. 2.8.**[33] Thus, the post- vacuum annealing of these optimized samples creates more oxygen vacancies as compared to their as-synthesized samples. Most importantly, the excitation band of the optimized Eu^{3+}-doped phosphors is overlapping with the blue emission of oxygen vacancies of the samples without Eu^{3+} ions **(Fig. 2.8 (a) & (b)).** Consequently, the effective resonance-type energy transfers from host donor to Eu^{3+} acceptor might be possible as the oxygen vacancies related emission of the host samples disappeared upon Eu^{3+}doping. Thus, the observed enhancement in Eu^{3+} emission after the vacuum or Ar heat treatment could be due to the oxygen vacancies enhanced by the post-vacuum/Ar annealing.

The XPS of as-synthesized and vacuum-annealed $Sr_{2.985}Gd_{0.01}AlO_4F$ samples was also characterized to study the effect of post-vacuum / Ar annealing on its oxygen vacancies (**Fig. 2.9(a)**). The O1s core-level spectrums of as-synthesized and vacuum-annealed $Sr_{2.985}Gd_{0.01}AlO_4F$ samples were also deconvoluted into two peaks and are shown as **Fig. 2.9 (b)** and **(c).** In case of as obtained $Sr_{2.985}Gd_{0.01}AlO_4F$ sample, the area of the oxygen vacancies peak (O_{II}) decreases from 28.30% (as in Sr_3AlO_4F) to 16.82%. The decreased in oxygen vacancy content is due to the substitution of trivalent Gd^{3+} ions for divalent Sr^{2+} ions followed by diffusion of non-lattice oxygen ions into the crystal lattice sites. However, the converse effect was observed under vacuum treatment of this sample, wherein the absence of oxygen atmosphere leads to loss of lattice oxygen and subsequent oxygen vacancies peak (O_{II}) area increases to 24.62%.

In this research, we observed the Ln^{3+} co-doping (Ln = Gd, Y) effects in the emission nature of Eu^{3+} within the Sr_3AlO_4F host. Simultaneously, the post-heat treatment of the optimized compositions in the reduction atmosphere appreciably enhanced the Eu^{3+} emission intensity. To study the above-mentioned changes in the emission intensity of Eu^{3+} ions, the Judd–Ofelt (J-O) spectroscopic parameters are also calculated **[34,35].** The

details of the J-O parameters and the calculation procedures are mentioned in the supporting information and their results are tabulated in **Table 2.1.** Likewise, a higher asymmetric ratio, the high value of Ω_2 also suggested the presence of asymmetric environment at the Eu^{3+} site. From the calculated values of Ω_2 listed in Table 2.1, it can be seen that these values enhanced with the incorporation of Ln^{3+} ions (Ln = Gd, Y) in $Sr_{2.9}AlO_4F$: $0.1Eu^{3+}$, which indicates the higher asymmetric environment of Eu^{3+} ions in the Ln^{3+} doped host matrix.

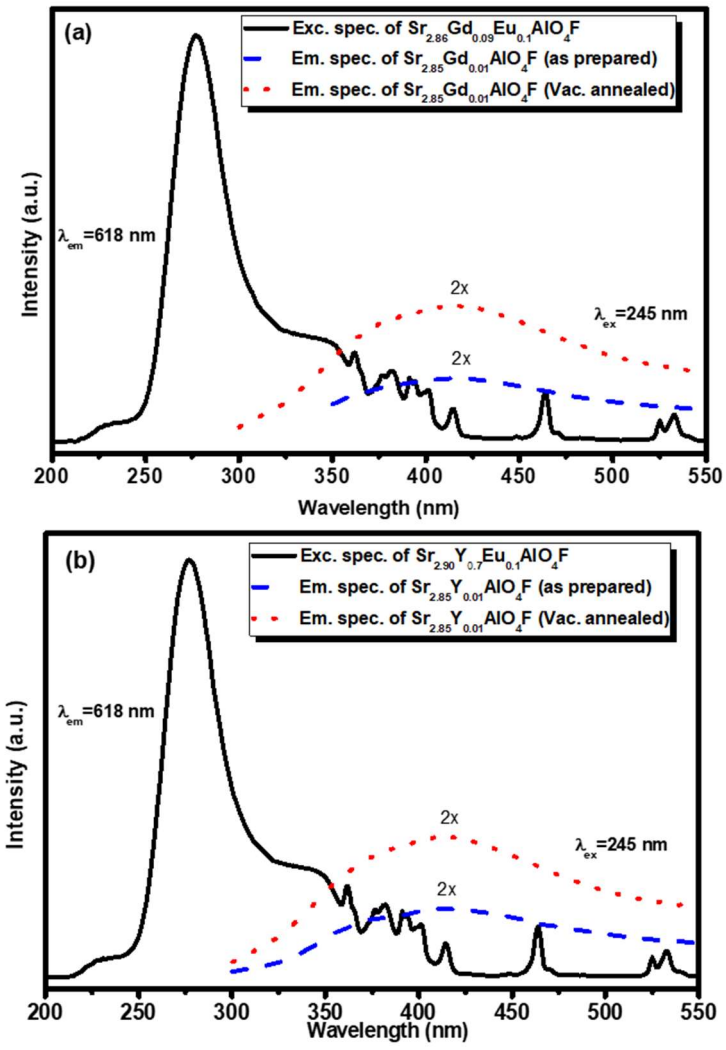

Figure 2.8: *(a) PL excitation spectrum (PLE) of $Sr_{2.765}Gd_{0.09}AlO_4F$: $0.1Eu^{3+}$ and the emission spectra (PL) of Sr2.985Gd0.01AlO4F (as obtained and post treated in vacuum). (b) PL excitation spectrum (PLE) of $Sr_{2.795}Y_{0.07}AlO_4F$: $0.1Eu^{3+}$ and the emission spectra (PL) of $Sr_{2.985}Y_{0.01}AlO_4F$ (as obtained and post treated in vacuum).*

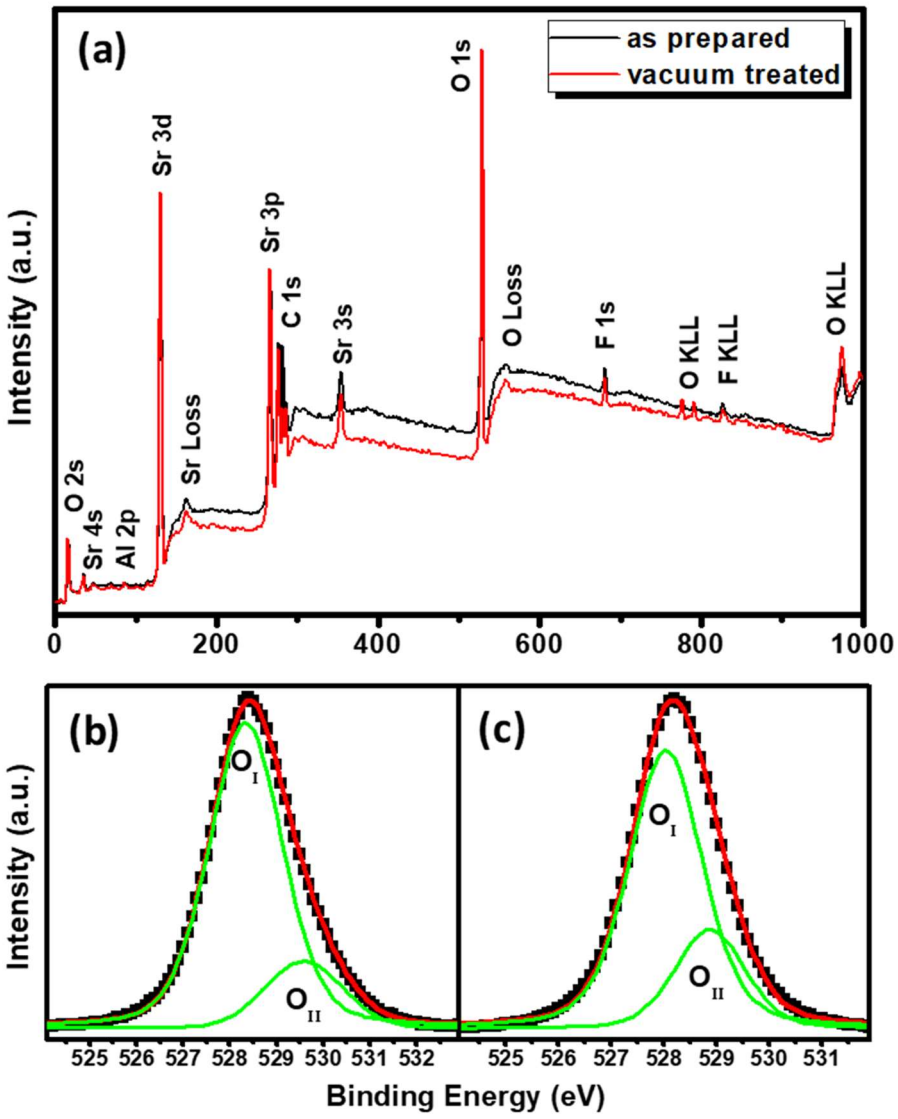

Figure 2.9: *(a) A comparison of the XPS survey spectrum of* $Sr_{2.985}Gd_{0.01}AlO_4F$ *(as obtained and post-treated in a vacuum). (b, c) High-resolution XPS spectrum of oxygen in the* $Sr_{2.985}Gd_{0.01}AlO_4F$ *sample ((b) as obtained and (c) post-treated in a vacuum).*

The value of Ω_2 is very sensitive to the ligand environment, which can be observed by the change of its value with various synthesis ambiance. The high Ω_2 value indicates the possession of high charge density for Eu^{3+} ions, which polarizes the O^{2-} anion to a much greater extent. This results in a larger extent of molecular orbital overlap between the f orbital of the Eu^{3+}ion and the p orbital of the O^{2-} ion, resulting in expansion of the electron cloud and the formation of a bond having less ionic and more covalent character. The decrease in Ω_2 value owing to the post- heat treatment in a vacuum is because of the

decreases in orbital overlapping between Eu^{3+} and O^{2-} or because of the creation in oxygen vacancies.[35] **Fig. 2.10 (a)** elaborates on the crystal diagram of $Sr_{2.9-3x/2}Ln_xAlO_4F$: $0.1Eu^{3+}$. As reported previously, the tetragonal structured Sr_3AlO_4F phase having space group of *I4/mcm* is consist of with 10-fold and 8-fold coordinated Sr sites, and 4-fold-coordinated Al^{3+} cation sites.[7] The smaller Ln^{3+} cations (Ln = Gd, Y) properly occupy the 8-fold Sr sites. One important point to note that the post-heat treatment of the optimized phosphors in the reduction atmosphere dose not able to reduce Eu^{3+} to Eu^{2+}. It can be thought that Eu^{3+} ions are stabilized owing to the Ln^{3+}-co-doping. The incorporation of a Ln^{3+}ion into the Sr^{2+} site produces a chemically induced defect which subsequently generates an acceptor level that can capture one electron. A single Ln^{3+} ion, situated in the Sr site, can reimburse one Eu^{3+} ion. The oxygen vacancies created from the reduction atmosphere cannot affect Ln^{3+} ions (Ln = Gd, Y). Therefore, the Eu^{3+} ions, which are replaced by Ln^{3+} ions situated in Sr^{2+} sites are remained as Eu^{3+} and cannot be converted to Eu^{2+}. However, the created oxygen vacancies act as the sensitizer and transfer their energies to Eu^{3+} during the excitation process according to the energy level diagram scheme shown in **Fig. 2.10 (b)**.

To further investigate the energy transfer mechanism between the oxygen vacancies and Eu^{3+} ions, the comparative lifetime analysis has been characterized for the optimized phosphors (as obtained and post vacuum treated), and the results are shown in **Fig. 2.9(c).** The corresponding luminescence decay curves can be fitted by a second-order exponential decay mode via the equation reported elsewhere **[12]**. The average decay times for the as-obtained and post vacuum treated $Sr_{2.765}Gd_{0.09}AlO_4F$: $0.1Eu^{3+}$ are determined to 0.82 and 0.97 ms, respectively. While that for as-obtained and post vacuum treated phosphors $Sr_{2.795}Y_{0.07}AlO_4F$: $0.1Eu^{3+}$ was calculated to be 0.75 and 0.94 ms, respectively. The results show that the average decay time for the Eu^{3+} ions enhanced owing to the post vacuum treatment, which is a good of supporting evidence for the energy transfer from the created oxygen vacancies to Eu^{3+} ions in the optimized phosphors. However, we are unable to record the lifetime of host emission in the phosphors which are contained with Eu^{3+} doping since none of the Eu^{3+} doped samples show host emission. From **Fig. 2.8**, it is seen that the emission intensity of the $Sr_{2.985}Gd_{0.01}AlO_4F$ and $Sr_{2.985}Y_{0.01}AlO_4F$ enhance due to the post vacuum treatment, which indicates that there is an enhancement in the oxygen vacancies due to the vacuum treatment. Such enhanced photon energy is completely diminishing with the subsequent enhancement of Eu^{3+}

emission intensity further due to the vacuum treatment. This might be supporting the predictions of energy transfer mechanisms from oxygen vacancies to Eu^{3+} ions.

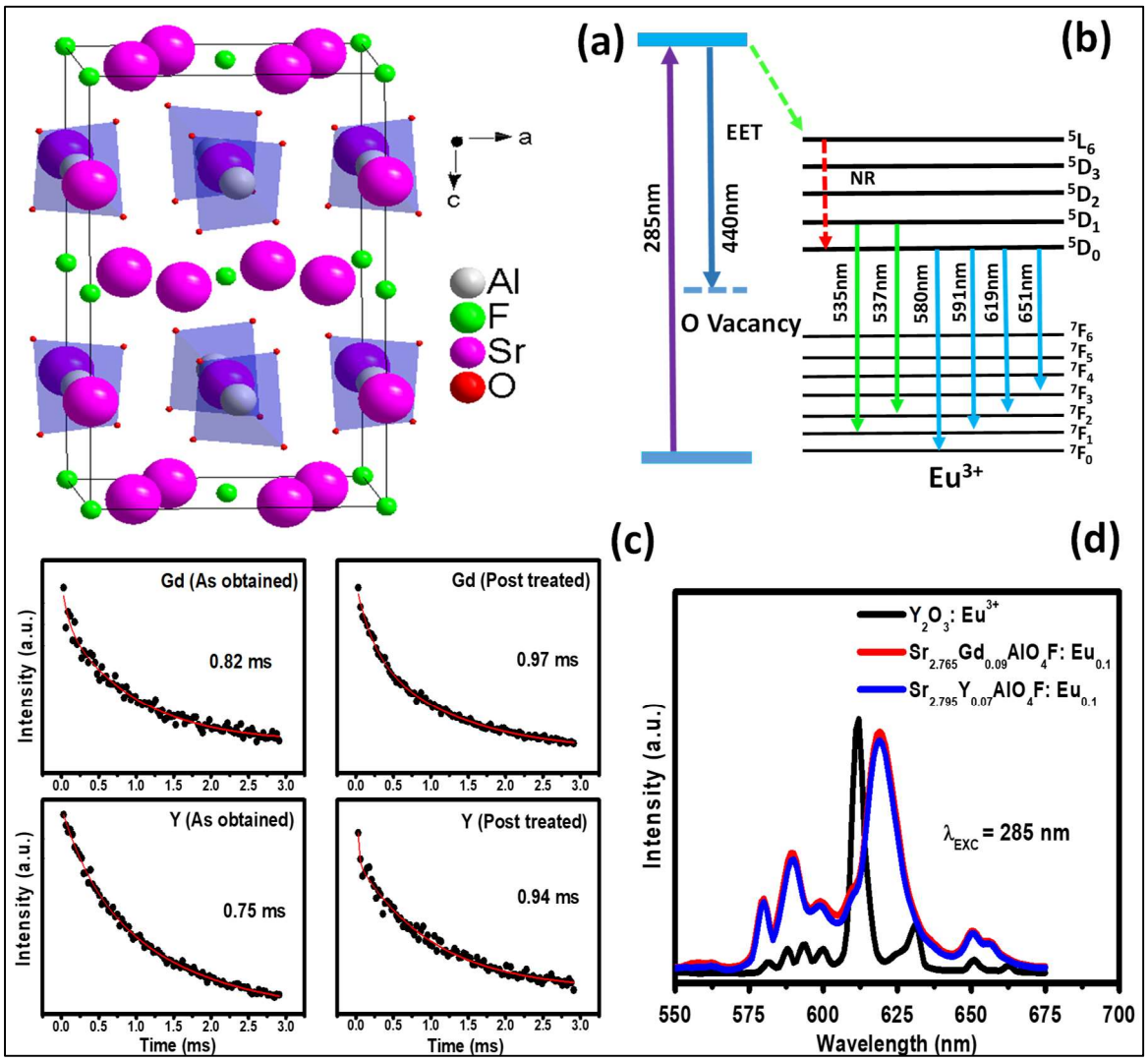

Figure 2.10: *(a) Crystal structure of Sr_3AlO_4F. (b) Energy level scheme sowing the energy transfer between oxygen vacancies to Eu^{3+} ions in the phosphors post-treated in a reduction atmosphere. (c) Comparative emission decay curves of $Sr_{2.765}Gd_{0.09}AlO_4F$: $0.1Eu^{3+}$ and $Sr_{2.795}Y_{0.07}AlO_4F$: $0.1Eu^{3+}$ (as-obtained and post vacuum treated). (d) Comparative PL emission spectra of Y_2O_3: Eu^{3+} ions and optimized phosphors post treated in vacuum.*

The emission of optimized samples post-treated in a vacuum has also been recorded under the excitation of 285 nm and compared with the commercially established Y_2O_3: Eu^{3+} red phosphor, which was prepared via the solid-state reaction method (**Fig. 2.10**

(d)). The detail composition Y_2O_3: Eu^{3+}, as well as the synthesis procedures, are reported elsewhere [36]. The results, depicted in **Fig. 2.10 (d),** indicates that the PL emission intensity of the present phosphors under optimized conditions are comparative with that of the commercial sample. However, the red emission peak position of the present samples is situated at a deeper red side than that of Y_2O_3: Eu^{3+}. Besides, the full width half maxima of the red peak are comparatively higher than that of the Y_2O_3: Eu^{3+}. These results support the high red color purity of the present samples (**Table 2.2**), which could be very useful for many optoelectronic applications where pure and intense red emission is the crucial parameter.

The CIE (X, Y) illustration exhibiting the coloring chromaticity of the optimized phosphors for the emission spectra recorded under λex = 285 and 393 nm excitations are shown in **Fig. 2.11.** As seen from the CIE diagram, the color coordinates for all the samples lie within the red-orange area, and the emission color also does not vary appreciably because of the post-heat treatment in argon or a vacuum atmosphere. The color purity was further investigated as mentioned in Refs. [37,38]. The color coordinates (x, y), CRI and color purity calculated from the emission spectra under 285 and 393 nm excitations for the optimized phosphors are depicted in **Table 2.2** The color purity of emission from all the samples was above 95.0%, indicating the formation of high-quality red-emitting phosphor indicating the present phosphors can be useful as pure red-colored light sources under UV light for display/lamp applications.

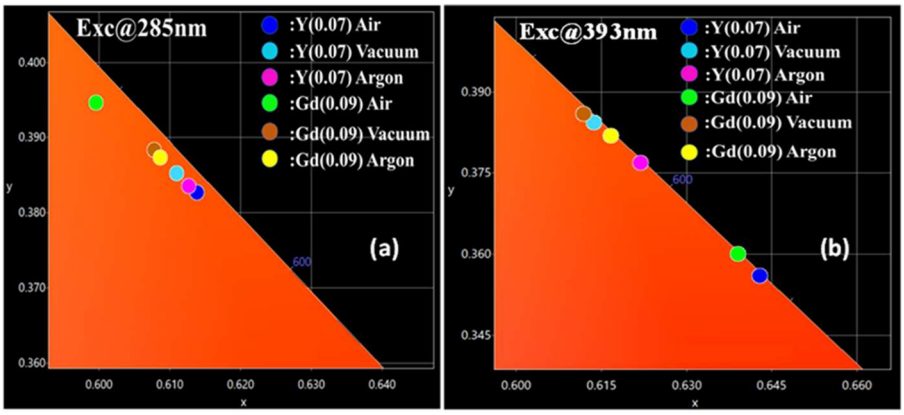

Figure 2.11: *CIE color diagram of $Sr_{2.765}Gd_{0.09}AlO_4F$: $0.1Eu^{3+}$ and $Sr_{2.795}Y_{0.07}AlO_4F$: $0.1Eu^{3+}$ phosphors obtained at various conditions ((a) under 285 nm and (b) 393 nm excitations).*

Table 2.2. *CIE, CCT, CRI and color purity for the optimized samples prepared in air and post annealed in vacuum and argon.*

Conc. (mol)	CRI		CIE		Color Purity (%)	
	285 nm	393 nm	285 nm	393 nm	285nm	393nm
Y(0.07) (Air)	55	28	(0.61, 0.38)	(0.64, 0.36)	99.1	99.8
Y(0.07) (Vacuum)	55	48	(0.61, 0.38)	(0.61, 0.38)	99	99.5
Y(0.07) (Argon)	54	41	(0.61, 0.38)	(0.62, 0.38)	99	99.8
Gd(0.09) (Air)	62	34	(0.60, 0.39)	(0.64, 0.36)	98.4	99.8
Gd(0.09) (Vacuum)	56	49	(0.61, 0.39)	(0.61, 0.38)	99	99.5
Gd(0.09) (Argon)	57	45	(0.61, 0.39)	(0.62, 0.38)	99	99.7

The flexibility of the $Sr_{2.765}Gd_{0.09}AlO_4F$: $Eu_{0.1}$ phosphor/PDMS composite film has been tested under different bending conditions. **Fig. 2.12 (a, b & c)** represents the composites at various bending or twisting conditions, while **Fig. 2.12 (d, e & f)** are representing the corresponding images of the composites under the same conditions with those in **Fig. 2.12(a, b & c)**, respectively with the UV illuminations. The photographs show that the composites are showing excellent red color display under the UV exposure in various bending modes without any color or intensity degradation. Furthermore, the good color uniformity indicates the uniform distributions of the phosphor particles within the PDMS films.

For the lighting applications, an ideal phosphor system must have appreciable thermal stability of up to 200 °C. Therefore, we have tested the TG-DTA analysis of the $Sr_{2.765}Gd_{0.09}AlO_4F$: $Eu_{0.1}$ phosphor/PDMS composite to check its thermal stability (**Fig. 2.S3**). The PDMS composite film began to degrade at above 270 °C only while the

maximum rate of degradation is noticed at even much higher temperature (465 °C), confirming its suitability for lighting applications. Thermal degradation may occur due to excess heating wherein long chains of PDMS polymer break into low-molar-mass cyclic siloxane oligomers [39,40]. To further study the lighting efficiency, the electroluminescence (EL) spectrum of the 15 wt% phosphor loaded PDMS composite upon the exposure of a UV LED (280 nm) operated at 500 mA current is also recorded and shown as **Fig. 2.12(g).** As seen from the figure, the characteristics Eu^{3+} emission peaks appear and thus the luminescence properties of the phosphor remain unaltered even after its loading in PDMS. The results of emission intensity, chromaticity coordinates (0.62, 0.36) and red color purity (96%) indicating the capability of the optimized phosphor as a red component in LED systems.

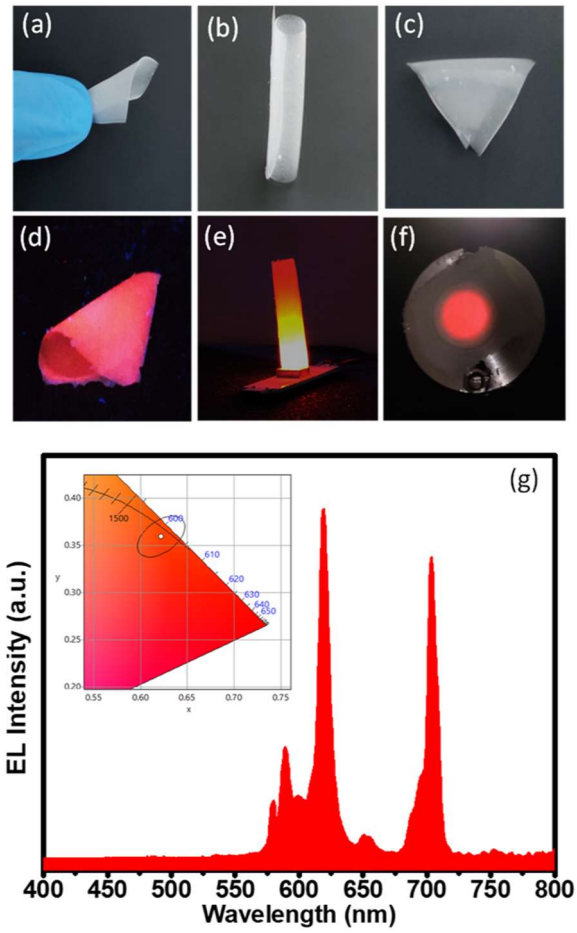

Figure 2.12. *$Sr_{2.765}Gd_{0.09}AlO_4F$: $0.1Eu^{3+}$/PDMS composites in various bending conditions (a–c) without illuminations and (d-f) with UV illumination. (g) EL spectrum and the corresponding CIE diagram of [post vacuum treated $Sr_{2.765}Gd_{0.09}AlO_4F$: $0.1Eu^{3+}$ phosphor.*

2.5. Conclusions

The structure of the tetragonal Sr_3AlO_4F phase was stabilized by aliovalent substitutions of Sr^{2+} ions with trivalent Gd and Y ions. A series of fixed content of Eu^{3+}-doped $Sr_{2.9-3x/2}Ln_xAlO_4F$ (x = 0.01-0.10) red phosphors were synthesized using solid-state synthesis methodology. All the samples showed intense red-orange emission ($^5D_0 \rightarrow {}^7F_{1,2}$) under the ultra-violet and blue excitations, indicated their suitability as high efficient red phosphor. The critical concentration of Gd^{3+} and Y^{3+} were observed to be x = 0.09 and x = 0.07, respectively, beyond which, quenching of the emission was observed. These two optimized samples were annealed in reducing atmosphere of Ar and vacuum to further enhance their optical efficiency. The increase in oxygen deficiency during post-annealing in Ar or vacuum led to the energy transfer (O^{2-}-Eu^{3+}) with a greater extent which subsequently increased the luminescence intensity of the optimized phosphors. The EL of flexible optimized $Sr_{2.765}Gd_{0.09}AlO_4F$: $0.1Eu^{3+}$/ PDMS composite film showed a cool-red color suggesting their suitability in flexible display devices.

2.6. References

(1) S. Ahmad, G.V. Prakash, R. Nagarajan, Hexagonally ordered KLaF4 host: phasecontrolled synthesis and luminescence studies, Inorg. Chem. 51 (2012) 12748–12754.

(2) W.B. Im, N. George, J. Kurzman, S. Brinkley, A. Mikhailovsky, J. Hu, B.F. Chmelka, S.P. DenBaars, R. Seshadri, Efficient and color-tunable oxyfluoride solid solution phosphors for solid-state white lighting, Adv. Mater. 23 (2011) 2300–2305.

(3) J. Sun, G. Sun, Y. Sun, Luminescence properties and energy transfer investigations of $Sr_3AlO_4F:Ce^{3+},Tb^{3+}$ phosphor, Ceram. Int. 40 (2014) 1723–1727.

(4) A.A. Setlur, E.V. Radkov, C.S. Henderson, J.H. Her, A.M. Srivastava, N. Karkada, M.S. Kishore, N.P. Kumar, D. Aesram, A. Deshpande, B. Kolodin, L.S. Grigorov, U. Happek, Energy-efficient, high-color-rendering LED lamps using oxyfluoride and fluoride phosphors, Chem. Mater. 22 (2010) 4076–4082.5.

(5) Z. Xia, R.S. Liu, K.W. Huang, V. Drozd, $Ca_2Al_3O_6F:Eu^{2+}$: a green-emitting oxyfluoride phosphor for white light-emitting diodes, J. Mater. Chem. 22 (2012) 15183–15189.

(6) Z. Xia, M.S. Molokeev, A.S. Oreshonkov, V.V. Atuchin, R.S. Liu, C. Dong, Crystal and local structure refinement in $Ca_2Al_3O_6F$ explored by X-ray diffraction and Raman spectroscopy, Phys. Chem. Chem. Phys. 16 (2014) 5952–5957.

(7) W. Chen, Effect of composition on the luminescence of Ce^{3+} activated Sr_3AlO_4F phosphor for light-emitting diode, J. Alloys Compd. 550 (2013) 320–325.

(8) W. Chen, H. Liang, M. Xie, Q. Su, Photoluminescence and low voltage cathodoluminescence of $Sr_3AlO_4F:Eu^{3+}$, J. Electrochem. Soc. 157 (2010) J21–J24.

(9) J. Sun, G. Sun, Y. Sun, Luminescence properties and energy transfer investigations of $Sr_3AlO_4F:Ce^{3+}$, Tb^{3+} phosphor, Ceram. Int. 40 (2014) 1723–1727.

(10) W.B. Im, S. Brinkley, J. Hu, A. Mikhailovsky, S.P. DenBaars, R. Seshadri, $Sr_{2.975-x}Ba_xCe_{0.025}AlO_4F$: a highly efficient green-emitting oxyfluoride phosphor for solid state white lighting, Chem. Mater. 22 (2010) 2842–2849.

(11) J.S. Lee, S. Unithrattil, W.B. Im, Color-tunable binary solid-solution phosphor, $(Sr_3SiO5)_{1-x}(Sr_3AlO_4F)_x$, for white LEDs: energy transfer mechanism between Ce^{3+} and Tb^{3+}, J. Alloys Compd. 555 (2013) 297–303.

(12) M. Shang, G. Li, X. Kang, D. Yang, D. Geng, J. Lin, Tunable luminescence and energy transfer properties of $Sr_3AlO_4F:RE^{3+}$ (RE = Tm/Tb, Eu, Ce) phosphors, ACS Appl. Mater. Interfaces 3 (2011) 2738–2746.

(13) V.R. Bandi, B.K. Grandhe, H.J. Woo, K. Jang, D.S. Shin, S.S. Yi, J.H. Jeong, Luminescence and energy transfer of Eu3+ or/and Dy^{3+} co-doped in Sr_3AlO_4F phosphors with NUV excitation for WLEDs, J. Alloys Compd. 538 (2012) 85–90.

(14) C.D. Quilty, M. Avdeev, J.D. Driskell, E. Sullivan, Structural characterization and photoluminescence in the rare earth-free oxy-fluoride anti-perovskites $Sr_{3-x}Bi_{2x/3}AlO_4F$ and $Sr_{3-x}Bi_{2x/3}GaO_4F$, Dalton Trans. 46 (2017) 4055–4065.

(15) K.A. Denault, N.C. George, S.R. Paden, S. Brinkley, A.A. Mikhailovsky, J. Neuefeind, S.P. DenBaars, R. Seshadri, A green-yellow emitting oxyfluoride solid solution phosphor $Sr_2Ba(AlO_4F)_{1-x}(SiO_5)$ $x:Ce^{3+}$ for thermally stable, high color rendition solid state white lighting, J. Mater. Chem. 22 (2012) 18204–18213.

(16) L.K. Bharat, G.S.R. Raju, J.S. Yu, Red and green colors emitting spherical-shaped calcium molybdate nanophosphors for enhanced latent fingerprint detection, Sci. Rep. 7 (2017) 11571.

(17) J.F. Moulder, J. Chastain, Handbook of X-ray Photoelectron Spectroscopy: A Reference Book Of Standard Spectra For Identification And Interpretation of XPS Data. Physical Electronics Division, Perkin-Elmer Corporation, 1992.

(18) K.T. Jacob, S. Raj, L. Raneesh, Vegard's law: a fundamental relation or an approximation? Int. J. Mater. Res. 98 (9) (2007) 776–779.

(19) V. Thampi, P.R. Padala, A.N. Radhakrishnan, Induced oxygen vacancies and their

effect on the structural and electrical properties of a fluorite-type $CaZrO_3$–$Gd_2Zr_2O_7$ system, New J. Chem. 39 (2015) 1469–1476.

(20) L. Li, W. Chang, W. Chen, Z. Feng, C. Zhao, P. Jiang, Y. Wang, X. Zhou, A. Suchocki, Double perovskite $LiLaMgWO_6:Eu^{3+}$ novel red-emitting phosphors for solidsate lighting: synthesis, structure and photoluminescent properties, Ceram. Int. 43 (2017) 2720–2729.

(21) S. Shisina, S. Das, S. Som, S. Ahmad, V. Vinduja, P. Merin, N.K. Gopalan, P. Kumari, M.K. Pandey, Structure and optoelectronic properties of palmierite structured $Ba_2Y_{0.67\delta0.33}V_2O_8$: Eu^{3+} red phosphors for n-UV and blue diode based warm white light systems, J. Alloys Compd. 802 (2019) 723–732.

(22) N.S. Singh, R.S. Ningthoujam, M.N. Luwang, S.D. Singh, R.K. Vatsa, Luminescence, lifetime and quantum yield studies of $YVO_4:Ln^{3+}$ (Ln^{3+} = Dy^{3+}, Eu^{3+}) nanoparticles: concentration and annealing effects, Chem. Phys. Lett. 480 (2009) 237–242.

(23) Y. Hua, S.K. Hussain, J.S. Yu, Eu^{3+}-activated double perovskite Sr_3MoO_6 phosphors with excellent colorpurity for high CRI WLEDs and flexible display film, Ceram. Int. 45 (2019) 18604–18613.

(24) Y. Tian, B. Chen, R. Hua, J. Sun, L. Cheng, H. Zhang, X. Li, J. Zheng, T. Yu, L. Huang, H. Yu, Optical transition, electron-phonon coupling and fluorescent quenching of $La_2(MoO_4)_3:Eu^{3+}$ phosphor, J. Appl. Phys. 109 (2011) 1–7.

(25) J.M.F. Van Dijk, M.F.H. Schuurmans, On the nonradiative and radiative decay rates and a modified exponential energy gap law for 4f-4f transitions in rare-earth ions, J. Chem. Phys. 78 (1983) 5317–5323.

(26) H. Jing, C. Guo, N. Zhang, Z. Ren, J. Bai, Effects of Eu^{3+} sites on photoluminescence in $Ba_2Ln(BO_3)_2Cl$ (Ln = Gd, Y) hosts, ECS J. Solid State Sci. Technol. 2 (2013) R1–R4.

(27) F.V.E. Hensling, D.J. Keeble, J. Zhu, J, UV radiation enhanced oxygen vacancy formation caused by the PLD plasma plume, Sci. Rep. 8 (2018) 8846.

(28) B.P. Singh, A.K. Parchur, R.S. Ningthoujam, A.A. Ansari, P. Singha, S.B. Raib, Enhanced photoluminescence in $CaMoO_4:Eu_{3+}$ by Gd^{3+} co-doping, Dalton Trans. 43 (2014) 4779–4789.

(29) Y. Wei, G. Xing, K. Liu, New strategy for designing orangish-red-emitting phosphor via oxygen-vacancy-induced electronic localization, Light Sci. Appl. 8 (2019) 15.

(30) K. Szczodrowski, J. Barzowska, N. Górecka, M. Grinberg, Stabilization of Eu^{3+} under a reductive atmosphere by the Al^{3+} co-doping of $Sr_2SiO_4:Eu^{2+}/Eu^{3+}$, RSC Adv. 6

(2016) 48001–48008.
(31) B. Ding, C. Han, L. Zheng, Tuning oxygen vacancy photoluminescence in monoclinic Y_2WO_6 by selectively occupying yttrium sites using lanthanum, Sci. Rep. 5 (2015) 9443.
(32) F. Hensling, C. Xu, F. Gunkel, Unraveling the enhanced oxygen vacancy formation in complex oxides during annealing and growth, Sci. Rep. 7 (2017) 39953.
(33) S. Ahmad, M. Kharkwal, Govind, R. Nagarajan, Application of $KZnF_3$ as a single source precursor for the synthesis of nanocrystals of ZnO_2:F and ZnO:F; synthesis, characterization, optical, and photocatalytic properties, J. Phys. Chem. C 115 (2011) 10131–10139.
(34) G.S. Ofelt, Intensities of crystal spectra of rare-earth ions, J. Chem. Phys. 37 (2005) 511–520.
(35) T.S. Sreena, P. Rao, L. Francis, A.K.V. Raj, P. Babu, Structural and photoluminescence properties of stannate based displaced pyrochlore-type red phosphors: $Ca_{3-x}Sn_3Nb_2O_{14}$:xEu^{3+}, Dalton Trans. 44 (2015) 8718–8728.
(36) S. Som, S. Das, S. Dutta, H.G. Visser, M.K. Pandey, R.K. Dubeye, S.K. Sharma, Synthesis of strong red emitting Y_2O_3:Eu^{3+} phosphor by potential chemical routes: comparative investigations on the structural evolutions, photometric properties and Judd–Ofelt analysis, RSC Adv. 5 (2015) 70887–70898.
(37) J. Liang, Synthesis and photoluminescence characteristics of high color purity $Ba_3Y_4O_9$:Eu^{3+} red-emitting phosphors with excellent thermal stability for warm WLED application, RSC Adv. 8 (2018) 32111–32118.
(38) C.S. McCamy, Correlated color temperature as an explicit function of chromaticity coordinates, Color Res. Appl. 17 (1992) 142–144.
(39) C. Camino, S.M. Lomakin, M. Lazzari, Polydimethylsiloxane thermal degradation, Part 1. Kinetic aspects, Polymer 42 (2001) 2395–2402.
(40) G. Camino, S.M. Lomakin, M. Lageard, Thermal polydimethylsiloxane degradation, Part 2. The degradation mechanisms, Polymer 43 (2002) 2011–2015.

Supplementary Information

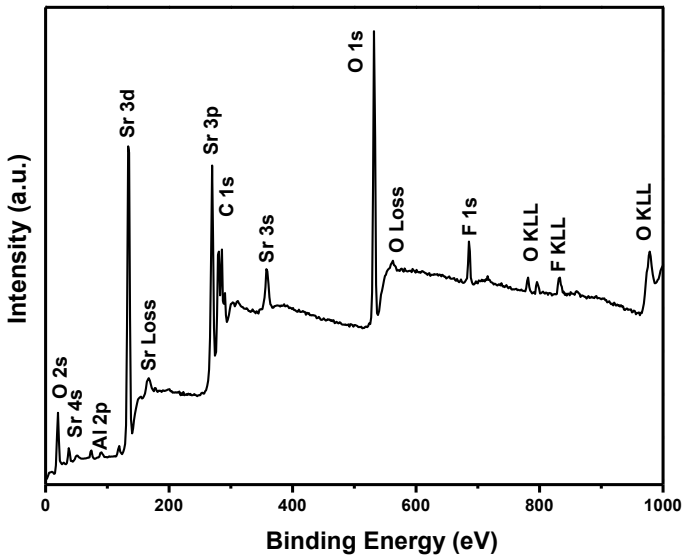

Fig. 2.S1. *Survey XPS spectrum of tetragonal Sr_3AlO_4F sample.*

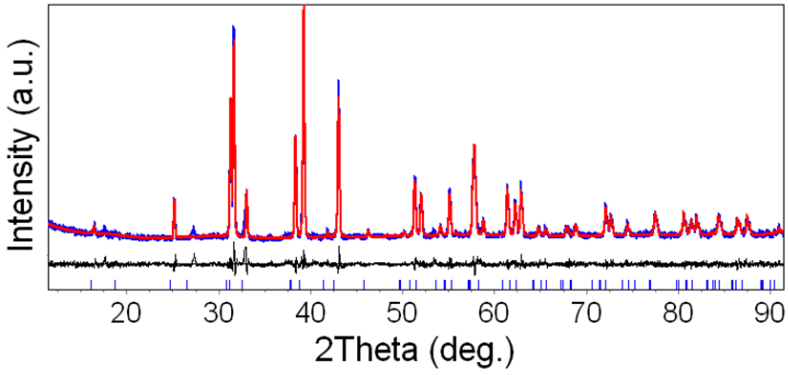

Fig. 2.S2. *Le Bail fit (red line) of the observed PXRD pattern (blue line) of the tetragonal Sr_3AlO_4F sample and residuum.*

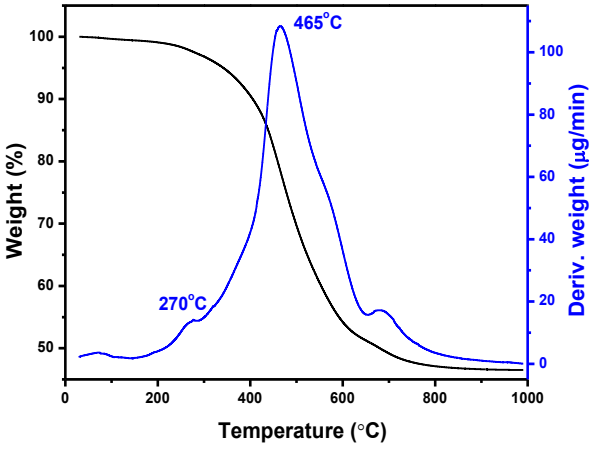

Fig. 2.S3 *TG-DTA trace of PDMS-Phosphor composite.*

Chapter 3

Full-color emitting crystal engineered $Sr_3Al_{1-x}Si_xO_{4+x}F_{1-x}$: $Eu^{2+/3+}$ oxyfluorides for developing bendable lighting composites

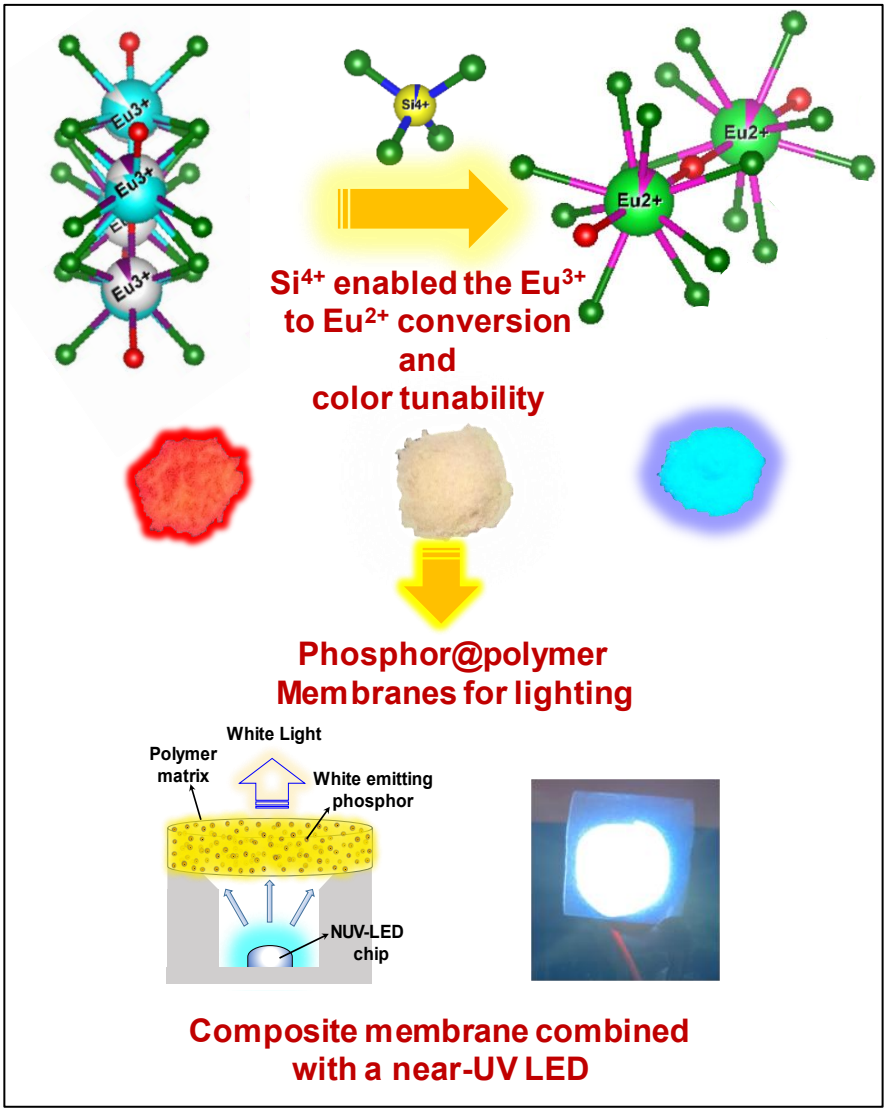

3.1 Abstract

A series of full-color emitting Eu^{2+}/Eu^{3+}-coexisted $Sr_{2.9}Al_{1-x}Si_xO_4F$: $0.1Eu^{2+/3+}$ ($SA_{1-x}Si_xOF$: $Eu^{2+/3+}$) oxyfluoride phosphors were synthesised by annealing the solid precursors in oxygen deficient atmosphere. The structural changes in Sr_3AlO_4F (SAOF) owing to the Si^{4+} ions' doping were visualized from the Rietveld refinement analysis. The substitution of Si^{4+} ions in Al sites contracted the AlO_4 tetrahedra and could enlarged the Sr sites, and enabled the suitable occupation of Eu^{2+} ions in the Sr1 sites. Eventually, the X-ray photoelectron spectroscopy studies confirmed the valence conversion of europium ions from its trivalent to divalent state owing to the Si^{4+} ions doping in SAOF: $Eu^{2+/3+}$. Photoluminescent studies of $SA_xSi_{1-x}OF$: $Eu^{2+/3+}$ showed an intense blue emission at 482 nm for the *4f-5d* transition of Eu^{2+} ions along with several sharp peaks above 55 nm owing to the intra *f-f* transition of Eu^{3+} ions. Increasing the Si^{4+} ions' concentration subsequently, enhanced the Eu^{3+} to Eu^{2+} conversion rate decreased their emission intensity ratio, owing to which the emission color chromaticity was also tuned from orange red (CIE: 0.48, 0.29) to near white (CIE: 0.30, 0.26) and eventually to bluish region (CIE: 0.18, 0.23). The nearly white light emitting composition $SASi_{0.03}OF$: $Eu^{2+/3+}$ and the intense bluish light emitting optimum $SASi_{0.06}OF$: $Eu^{2+/3+}$ phosphors were further chosen for fabricating flexible composites based on phosphor and castor oil (CAO). At 150 ºC, the composite showed almost double PL emission than the phosphor powders owing to the thermal encapsulation of the phosphor powders provided by the CAO matrix. Eventually, the obtained composite started to degrade at the temperatures as high as 300 ºC. Therefore, the composite made with near white emitting $SASi_{0.03}OF$: $Eu^{2+/3+}$ phosphor was integrated with a 365 near UV-LED which showed intense bluish white emission with the CIE of 0.29, 0.32, CCT of 7629, and CRI of 96. The above studies broadly suggested the adaptability of the obtained composites for flexible lighting applications.

3.2 Introduction

In the present era of lighting technology, white light emitting diodes (W-LEDs) using phosphor luminescence (pc W-LEDs) have concerned foremost attention because of their exclusive characteristics including higher energy efficiency, robustness, long durability, eco-friendly and flexibility compared to existing lighting options **[1-4].** Because of these features, pc-LEDS are enormously used in home, in vehicles, in backlight display, and public street lighting **[5]**. One of the most widespread technologies to produce pc W-LEDs

is the combining a 460 nm blue InGaN-LED chip and a broad yellow emitting garnet ($Y_3Al_5O_{12}$: Ce^{3+}) phosphor is associated with multiple issues including poor thermal and chemical stability, luminescence efficiency loss, and low color rendering (CRI) [6-9]. Meanwhile, the silicone matrix used for dispersing phosphors and to integrate with blue-LED chips turns to yellowish tinge owing to the degradation of methyl groups which produce several sub band defects and subsequently detach from the assembly at high operating temperatures. Such detachment issues result in lowering the optical performance of W-LEDs and possible leakage of excitation light supplied from the LEDs [5,10].

Recently, ultraviolet-excited single-phased phosphors have been widely used by altering doping ion concentration for attaining white light because of their substantial advantages like high CRI, a bigger choice of existing phosphors, and an appropriate color temperature (CCT) [11,12]. In the above series, rare-earth ions doped oxyfluorides are emerged as the promising phosphors for pc-LEDs owing to their efficient and tuneable luminescence properties [13,14]. Introducing F^- ions into an oxide matrix results distorted centrosymmetric sites of the cationic polyhedrons, which origins exciting optical behaviours including high absorption in UV region and intense emission in the visible region.

Among the oxyfluoride host matrices, Sr_3AlO_4F is the most studied phosphor for solid state lighting applications owing to its facile and simple synthesis, cheap raw materials, and efficient as well as tuneable luminescent characteristics [15,16]. It is crucial to mention that for producing white light, pc LEDs strongly relied on Eu^{2+} and Ce^{3+} ions which are able to produce broad band emission covering the entire visible region because of their allowed *d-f* transitions [17]. In Sr_3AlO_4F host lattice, the wavelength of $4f^N \rightarrow 4f^{N-1}5d^1$ transitions from these ions can be enhanced by selective cationic substitutions elevating the covalent Eu^{2+} or Ce^{3+}-ligand bonds and anion polarizabilities, owing to which, Sr_3AlO_4F phosphors strongly absorb UV and near-UV radiations and emit in broad visible spectral zones [18]. Earlier, W. B. Im *et al.* reported $Sr_{2.975}Ce_{0.025}Al_{1-x}Si_xO_{4+x}F_{1-x}$ compositions, which are highly color-tunable (from 474 to 537 nm) that can be efficiently used in solid-state lighting [19]. Here, smaller Si^{4+} ions are replacing larger Al^{3+} cations along with the substitution of smaller F^- ions via larger O^{2-} ions which alter the lattice parameters and subsequently produced distortions in the Al/Si tetrahedral,

which produced emission redshift [19]. Zheng *et al.* reported a composition of $Sr_{2.97-1.5x}Ca_xAl_{1-2y}Mg_ySi_yO_4F$: $0.02Ce^{3+}$ with intense yellow light emitting nature maximum at 545 nm upon 430 nm excitation. The substitution of Mg^{2+} and Si^{4+} ions into the Al sites and replacement of Sr^{2+} via Ca^{2+} in Sr_3AlO_4F: Ce^{3+} not only enhanced the emission intensity but also redshift the emission curve from 460 nm to 545 nm [20]. Lee *et al.,* reported Ce^{3+}-incorporated $(Sr_3SiO_5)_{1-x}$ - $(Sr_3AlO_4F)_x$ solid solutions which exhibited wide yellow–orange emission band that has been widen and red-shifted owing to Tb^{3+}-codoping [21]. Nevertheless, Eu^{2+}-doped Sr_3AlO_4F compositions are not reported as the single white emitting composition so far because of the fact that the coordination environment and the size of the crystal site of this host may not be able to change the valence state of europium ions.

Recently, the changing the covalency and polarizability of activator - ligand bonds in phosphors has received considerable attention to covert Eu valance state from 3+ to 2+ [22-24]. With this strategy, it is possible to make Eu^{2+} and Eu^{3+} ions' coexisted phosphors having the ability to emit tuneable emission color including white light emission owing to the combination of different emissions from different valences. Gao *et al.* reported new phosphor compositions of $MgSrLa_{8-x}(SiO_4)_6O_2$: xEu where the activated europium ions could able to exist in both Eu^{2+} as well as Eu^{3+} forms by occupying non-equivalent crystallographic positions in a lattice [25]. This strategy generated multiple luminescent centers which are able to produce even white light by combining the broad bluish green emission of Eu^{2+} ions and sharp the green-yellow-red emission of Eu^{3+} ions. Z. An and co-workers recently reported color-tunable $Ca_{20}Al_{26}Mg_3Si_3O_{68}$: Eu^{2+}, Eu^{3+} phosphors where they achieved multicolour emission owing to the occupation of europium ions (divalent and trivalent) at distinct crystallographic sites [26].

Inspired by the above studies, in this work we synthesized a novel oxyfluoride phosphor $Sr_{2.9}Al_{1-x}Si_xO_4F$: $0.1Eu^{2+/3+}$ which can generate single white light emission under UV excitation. Replacing Al^{3+} with Si^{4+} ions enlarged the activator sites that enabled Eu^{3+} ions to be reduced to Eu^{2+} ions. Varying the Si^{4+} ions doping concentration tuned the emission colour from orange-red to near white and eventually to bluish zone. The most suitable compositions were further to fabricate proposed phosphor polymer composites in order to avoid silicon-based phosphor binders for device applications. Here we choose castor oil (CAO) as the polymer host matrix because of its good binding,

transparency, eco-friendly nature and flexibility. Combining polymer matrix with phosphor could be a suitable alternate for generating high performance and thermally stable composite materials for LED packaging. These composite films could able to maintain certain distance between the phosphor and LED chip for improving the life time of the fabricated LED by the ease of heat dissipation.

3.3 Experimental section

3.3.1 Preparation of a phosphor

A series of $Sr_{2.9}Al_{1-x}Si_xO_{4+x}F_{1-x}$: $0.1Eu^{2+/3+}$ ($SA_{1-x}Si_xOF$: $Eu^{2+/3+}$ (x = 0.0, 0.01, 0.03, 0.05, 0.06, 0.1, 0.12, and 0.15) phosphors were synthesized through conventional solid-state method. The stoichiometric amounts of $SrCO_3$ (99.999%), SrF_2 (99.999%), Al_2O_3 (99.999%), SiO_2 (99.99%), and Eu_2O_3 (99.999%) obtained from Sigma-Aldrich were ground together in an agate mortar for 30 min. For maintain the homogeneity of mixing 2.5 wt.% NH_4F as a flux was added. The grounded mixture was transferred into an alumina crucible and preheated at 650 °C for 3 h and then annealed in a tube furnace under the near vacuum atmosphere of 10^{-3} torr at 1150 °C for 4 h.

3.3.2 Preparation of Composite

Appropriate amounts of castor oil (CO) and aliphatic isocyanate is taken in a beaker with an NCO/OH ratio of 1:1. The mixture was stirred at 600 rpm for 15–20 min maintaining the temperature at 70 °C with the help of an oil bath. After the reaction, polyurethane pre-polymer was cast on a glass slide and kept for 2 h in an air-oven at 90 °C for complete curing. The Same procedure was adopted for preparing CO composites with appropriate phosphor content. The reaction scheme for CO synthesis is shown in **Fig.3.1**

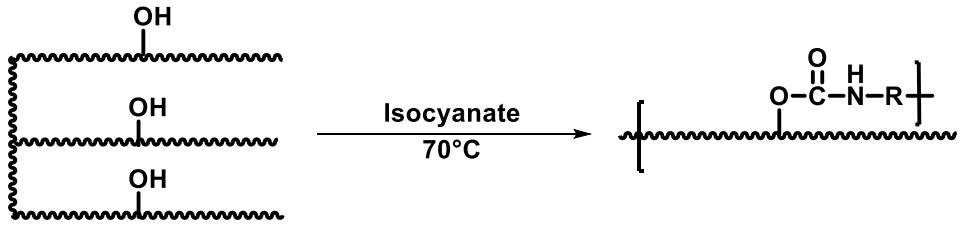

Figure 3.1: *Schematic representation of Synthesis of polyurethane from castor oil.*

3.3.3 Material Characterization

The crystal structure of the samples was examined by collecting the X-ray powder diffraction (XRD) patterns using a Phillip's X'pert pro diffractometer with Ni-filtered Cu-K_α radiation. The proposed crystal structure was generated using VESTA software. The X-ray photoelectron spectroscopy (XPS) studies for all the samples were performed using a PHI 5000 VersaProbe II equipped with a micro-focused (200 µm, 15 kV) monochromatic Al-Kα X-ray source (1486.6 eV). The morphological studies of the samples were also carried out using a high-resolution transmission electron microscope (HR-TEM), JEOL JEM-F200. The photoluminescence excitation and emission spectra were investigated using a Yvon Fluorolog 3 spectrofluorimeter with a 450 W Xenon flash lamp as the exciting source. The low-temperature photoluminescence studies were carried out using a laser excitation source of wavelength 266 nm with a laser power of 10 mW. The cathodoluminescence (CL) measurements were carried out with the help of an Attolight Chronos CL-Scanning Electron Microscopy system. The electroluminescence properties of the obtained devices were measured using a high-sensitivity CCD spectrophotometer (Maya 2000 Pro).

3.4 Results and discussions

3.4.1 Structural analysis using XRD and XPS

The Rietveld refinement on the powder XRD patterns of $Sr_{2.9}Al_{1-x}Si_xO_{4+x}F_{1-x}$: $0.1Eu^{2+/3+}$ ($SASi_xOF$: $Eu^{2+/3+}$; x = 0.0, 0.01) samples annealed in the oxygen-deficient atmosphere at 1150 °C for 4 h are shown in **Fig. 3.2.** The diffraction patterns of both the samples agree well with the tetragonal phase of Sr_3AlO_4F [space group: *I4/mcm*]. Meanwhile, the incorporation of Si^{4+} ions results in the generation of several impurity peaks of Sr_3SiO_5 (JCPDS: 26-0984 and 06-0341) and Sr_2SiO_4 (JCPDS 18-1281), which are marked with asterisks, as can be seen in **Fig. 3.2.** The estimated lattice parameters, atomic coordinates, and bond lengths are given in **Table 3.S1**, **Table 3.S2**, and **Table 3.S3**, respectively. The cell parameters of SAOF are refined to be a = b = 6.7537 Å, and c = 11.2126 Å. These estimated cell parameters are very close to the previous reported results on the same host material [22]. Meanwhile, the successful incorporation of Si^{4+} ions in to the Al^{3+} sites can be realized from the slightly altered lattice parameters, as shown in **Table 3.S1**. It can be noted from **Table 3.S1** that the values of a and b are slightly enlarged while c is contracted owing to the Si^{4+} doping in to the Sr_3AlO_4F host, which is in line with the observations and interpretations reported by W. Bin et al. [21].

Furthermore, the replacing of a Al^{3+} ion by a Si^{4+} ion into the Al^{3+} site create an excess cationic charge, which can be compensated due to the stoichiometric substitution of F^- ion by O^{2-} ion. A similar interpretation on charge compensation has also been reported earlier in the case of few rare-earth-doped oxyfluoride phosphors [21,32]. However, the refined values of a, b and c of $SASi_{0.01}OF$: $0.1Eu^{2+/3+}$ slightly reduced in comparison with $SASi_{0.01}OF$ (**Table 3.S1**) might be due to the anomalous reductions and substitutions of europium ions.

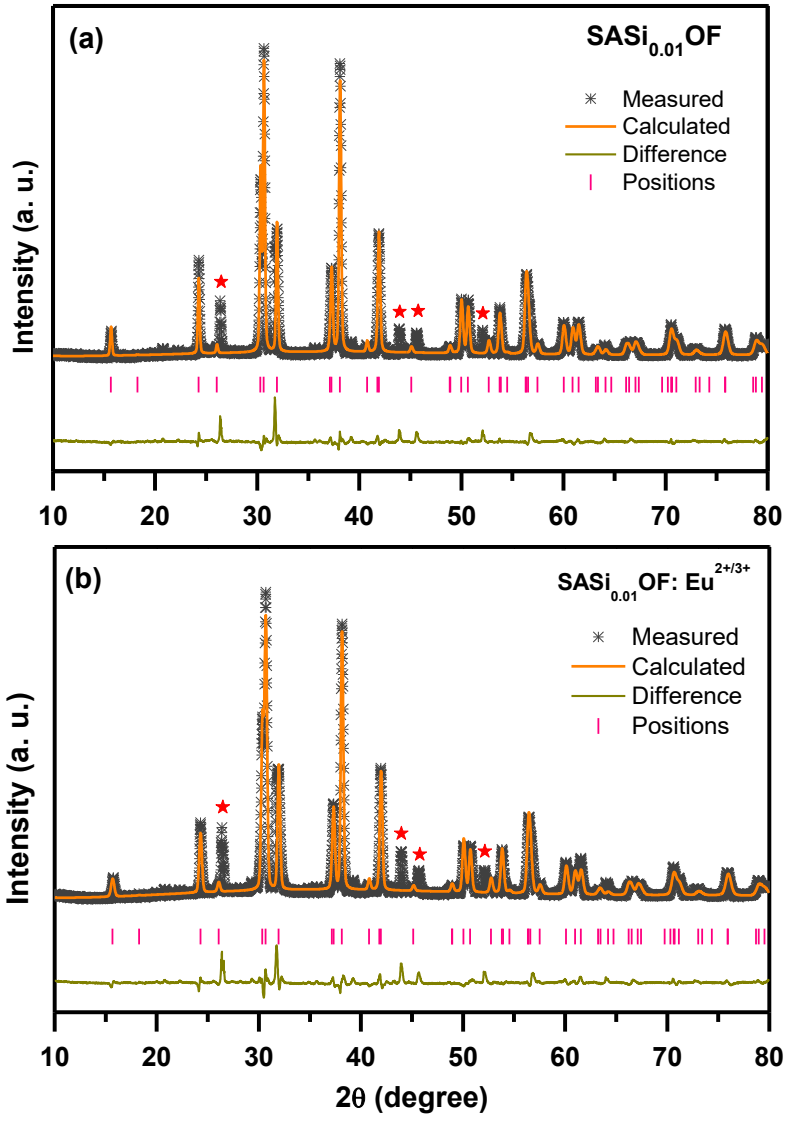

Figure 3.2: *Rietveld refined XRD patterns of* ***(a)*** *SASiOF, and* ***(b)*** *$SASi_{0.01}OF: Eu^{2+/3+}$ samples.*

Fig. 3.3 shows the crystal structure representation of $SASi_{0.01}OF$. In this structure there exist two different Sr sites: 10 coordinated *4a* sites and 8 coordinated *8h* sites. A *4b* site is engaged by Al, *4c* is captured by F atoms, and O atoms are believed to occupy the *16l* site, respectively. It consists of arranging alternatively $Sr(1)O_8F_2/AlO_4$ and $Sr(2)O_6F_2$ polyhedron along the c axis. SAOF belongs to the tetragonal Cs_3-$CoCl_5$-family (space group *I4/mcm*) and is narrowly linked to the tetragonal Sr_3SiO_5 (space group *P4/ncc*). From the bond length calculation obtained from the refinement of SAOF (listed in **Table 3.S3**), it is clear that the *4a* site is much larger than that of the *8h* site. The incorporation of Si^{4+} ions into the Al^{3+} sites contract the AlO_4 tetrahedral sites because of the smaller ionic substitution. It may affect the neighbouring two Sr polyhedrons since AlO_4 tetrahedra are linked to $Sr(1)O_8F_2$ and $Sr(2)O_6F_2$ through oxygen bridging by the edge and corner-sharing. Due to the inductive effect by the substitution of Si^{4+} ions in Al^{3+} sites, the AlO_4 tetrahedra contracted, and the neighbouring Sr^{2+} sites get enlarged, which is also supported by the calculated bond lengths, as shown in **Table 3.S2**.

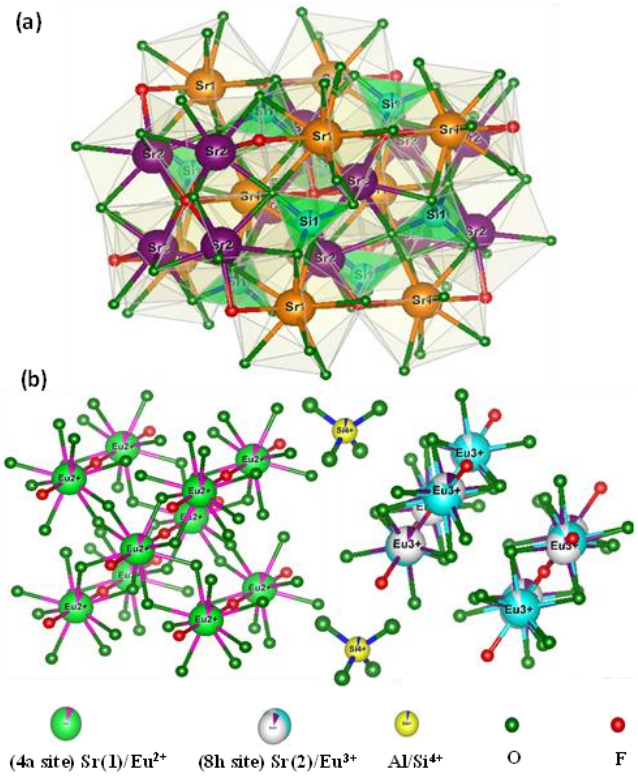

Figure 3.3: (a) *The basic crystal structure, and* ***(b)*** *the different coordination environment of Sr1, Sr2 and Al sites in* $SASi_{0.01}OF: Eu^{2+/3+}$.

After the doping of Si^{4+} ions, the average bond length of Al-O decreases, and Sr(1)-O/F and Sr(2)-O/F bond lengths are considerably enhanced as compared to the SAOF sample. Among the two polyhedrons, $Sr(1)O_8F_2$ is closely related with the AlO_4 tetrahedra owing to two edges and two corner-sharing. Hence, the *4a* site is more suitable for Eu^{2+} ions' occupation than the *8h* site, which is also clear from the bond length calculation indicated in **Table 3.S2**. The average bond length of Sr(1)-O/F is more than that of Sr(2)–O/F. Hence, the substitution of Si^{4+} ions can enlarge the Sr^{2+} sites and subsequently enhance the occupation of Eu^{2+} ions. From the refinement data of $SASi_{0.01}OF: Eu^{2+/3+}$ it is also clear that because of Si^{4+}-doping, the Al-O bond length decreases and Sr(1)-O/F bond length increases. The basic crystal diagram of SASiOF and the corresponding coordination environments of all sites are represented in **Fig. 3.3 (a)** and **3.3 (b)**, respectively. Therefore, it can be concluded that increasing the Si^{4+} ions' content during the synthesis in the oxygen-deficient atmosphere accelerates the conversion of more and more Eu^{3+} ions to Eu^{2+} ions, and these valence states of europium can able to coexist in corresponding *8h* and *4a* sites, respectively.

According to the previous report, Eu^{3+} ions (r^{8h} = 1.066 Å) tend to substitute in the 8h sites if Sr^{2+} sites (r^{8h} = 1.26 Å) in the Sr_3AlO_4F host via forming surplus positive charges [33]. Such an extra amount of positive charges can easily be compensated via the minor off-stoichiometric adjustment between O^{2-} and F^-, and creates some cation vacancies [32]. Additionally, the high-temperature annealing process at vacuum conditions is also responsible to create certain interstitial defects in the host which can act as the electron donor to Eu^{3+} ions and subsequently reduce them to Eu^{2+} [24,32]. However, the complete reduction of Eu^{3+} is not seen in SAOF: $Eu^{2+/3+}$. The local surroundings and size of the substituted crystal-site also contribute substantially in the Eu^{3+} reduction. In most of the strontium hosts, Eu^{3+} can easily reduce to its divalent form during the synthesis in a reduction atmosphere [34,35]. But the reduction of Eu^{3+} is not observed in Sr_3AlO_4F: Eu compositions synthesized in reduction atmosphere [26,36]. Recently, Fang et al. reported the photoluminescence behaviour of Eu-doped Sr_3AlO_4F synthesized in a reduction atmosphere. But they have only observed Eu^{3+} emission without any wideband emission related to Eu^{2+} ions because of the strong oxidative lattice around the Sr^{2+} sites [26].

The efficient reduction of Eu^{3+} ions are not observed in Sr^{2+} sites of Sr_3AlO_4F host might be also due to the large ionic radii of Eu^{2+} ions (r^{8h} = 1.25 Å, r^{4a} = 1.35 Å) in the

8-fold and 10-fold coordination, which are comparable with the Sr^{2+} ions (r^{8h} = 1.26 Å, r^{4a} = 1.36 Å). Moreover, both the Sr^{2+} sites are enclosed densely by AlO_4 tetrahedral units, which is also preventing the substitution of Eu^{2+} ions in the Sr^{2+} sites. In order to enlarge the Sr^{2+} sites, we have incorporated $Si^{4+} - O^{2-}$ into the SAOF structure to replace Al^{3+} - F^- resulting in $Sr_{2.9}Al_{1-x}Si_xO_{4+x}F_{1-x}$: $0.1Eu^{2+/3+}$ ($SASi_xOF$: $Eu^{2+/3+}$). This substitution might shrink the AlO_4 tetrahedral units owing to the smaller ionic radii of Si^{4+} ions (r^{4b} = 0.26 Å) than that of Al^{3+} ions (r^{4b} = 0.39 Å). The shrinkage of AlO_4 sites might reduce the strength of the oxidative lattice in the surrounding of the Sr^{2+} sites and enlarged them subsequently. The lower bond length of Al/Si-O in $SASi_{0.01}OF$ than the bond length of Al-O in SAOF is also supporting the above prediction (**Table 3.S3**). Meanwhile, bigger O^{2-} anions (r^{16l} = 1.40 Å) are also assumed to replace smaller F^- anions (r^{4c} = 1.33 Å) to achieve charge balance for the present framework and create some oxygen interstitial defects. These defects probably act as suitable electron donors to Eu^{3+} ions for their reduction. Meanwhile, the enlarged Sr^{2+} sites accelerate their reduction.

A survey XPS spectrum of $SASi_{0.03}OF$: $Eu^{2+/3+}$ heat-treated in the oxygen-deficient environment, shown in **Fig. 3.4 (a),** confirming the existence of Sr, Al, O, F, Si, and Eu. More precisely, **Figs. 3.4 (b) - (g)** represent the core spectra of Al, Si, O, F, and Eu, respectively. The spectrum of Al 2p (**Fig. 3.4 (b)**) is obtained at 71.68 eV, which is slightly shifted towards the lower energy than the standard value [37, 38], indicating the proper binding of Si^{4+} ions in the Al sites. The lower shifting of binding energy value is might be due to shorter ionic radii of Si^{4+} ions than Al^{3+} ions. The core-level spectrum of Si 2p (**Fig. 3.4 (c)**) consists of two peaks centered at 99.37 eV corresponds to the Si 2p, and 101.21 eV is attributed to the SiO_2 phase **[39]**. This may cause the appearance of the Sr_3SiO_5 and Sr_2SiO_4 phases **[40]**. From the XPS results, we can conclude that the excess Si^{4+} ions may be adsorbed (such as SiO_2) on the oxygen-deficient region thereby diminishing the surface oxygen peak and subsequent formation of silicon dioxide. The above phenomenon can also be justified from the core level XPS spectrum of O 1S (**Fig. 3.4 (d)**), which elaborates two peaks at 528.92 eV and 529.11 eV corresponds to the lattice oxygen.

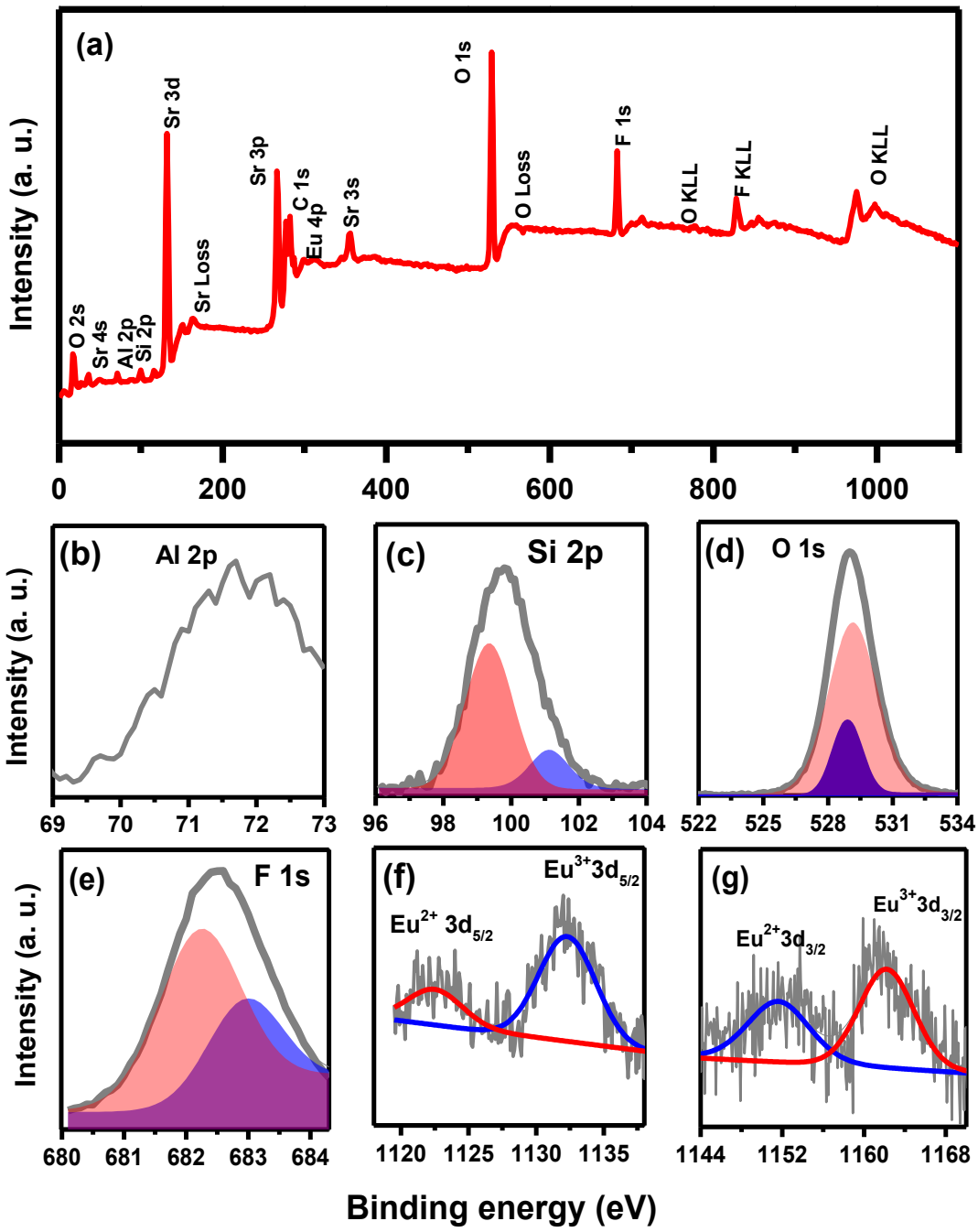

Figure 3.4: (a) *Survey spectrum of $SAlSi_{0.03}OF: Eu^{2+/3+}$.* ***(b) – (g)*** *represents the core level spectra of each element.*

The core-level spectrum of F 1s (**Fig. 3.4 (e)**) is deconvoluted into two peaks centered at 682.26 eV and 683.01 eV [39]. The peak FI is corresponding to the two longer bond lengths of Sr1 – F. While peak FII corresponds to the shorter Sr2-F bond length. Under the vacuum condition, the surface oxygen can diffuse into the lattice site as oxide ions and electrons. In the deficiency of oxygen more Eu^{3+} ions can receive those electrons and

can be reduced to Eu^{2+}. This kind of coexistence of Eu^{3+} and Eu^{2+} ions also confirmed by XRD results. The XPS spectra of Eu 3d consist of four peaks corresponding to Eu^{2+} $3d_{5/2}$ (1122.52 eV), Eu^{3+} $3d_{5/2}$ (1132.23 eV), Eu^{2+} $3d_{3/2}$ (1151.57 eV) and Eu^{3+} $3d_{3/2}$ (1162.23 eV), respectively (**Fig 3.4 (f) and (g)).** The difference in binding energy values of Eu $3d_{3/2}$ and Eu $3d_{5/2}$ of Eu^{3+} (29.86 eV) and Eu^{2+} (29.15 eV) is closer to their standard separation gap (29.8 eV) **[39]**. The XPS results broadly indicate that under the low oxygen atmosphere and by the doping of Si^{4+} ions enhance the possibility of formation of Eu^{2+} ions.

3.4.2 Optical characterizations using UV-Vis DRS and photoluminescence Study

The UV-Vis DRS of SAOF and SASiOF samples, shown in **Fig. 3.5 (a),** exhibit almost 100 % reflectance in the wavelength range of 350 – 700 nm and steep slopes in 250 to 325 nm. Both the samples show a host absorption band maximized at 241 nm. Compare to SAOF, the intensity of this band is reduced in SASiOF, which might be due to the reduction of surface oxygen charge carrier's content due to the Si^{4+} ions' incorporation into SAOF. The inset of **Fig. 3.5 (a)** shows the PL emission spectra of SAOF and SASiOF at 241 nm UV excitation, which is showing that after Si^{4+} ions' doping, SAOF host emission intensity attributed to the oxygen vacancies is reduced. The XPS core spectra of O 1s and Si 2p already indicated that excess Si^{4+} cations can adsorb free surface O^{2-} ions to form SiO_2. As a result of the low content of free O^{2-} ions, the host emission due to charge transfer decreases after the doping of Si^{4+} ions in SAlOF.

Fig. 3.5 (b) elaborate DRS of various content of Si^{4+}-doped $SA_{1-x}Si_xOF$: $Eu^{2+/3+}$ phosphors. Without Si^{4+} ions, SAOF: $Eu^{2+/3+}$ phosphor exhibits an additional absorption band peaked at around 295 nm corresponds to the O^{2-} - Eu^{3+} charge transfer band. Besides, several sharp peaks are observed between 350 to 480 nm corresponding to the intra *f-f* Eu^{3+} transitions (inset graph in **Fig. 3.5 (b)).** Introducing a small amount of Si^{4+} ions in the Al sites of SAOF: $Eu^{2+/3+}$ phosphor results in broadband absorption in the region of 225 to 450 nm owing to the $4f^6 5d^1$ - $4f^7$ transitions of Eu^{2+} ions. Meanwhile, the DRS results of $SA_{1-x}Si_xOF$: $Eu^{2+/3+}$ phosphors show almost 90 % reflectance in the visible region (450 to 700 nm). The intensity of Eu^{2+} absorption is increased with the increase in Si^{4+} ions in SASiOF: $Eu^{2+/3+}$ because of the subsequent enhancement in the conversion rate of Eu^{3+} to Eu^{2+}.

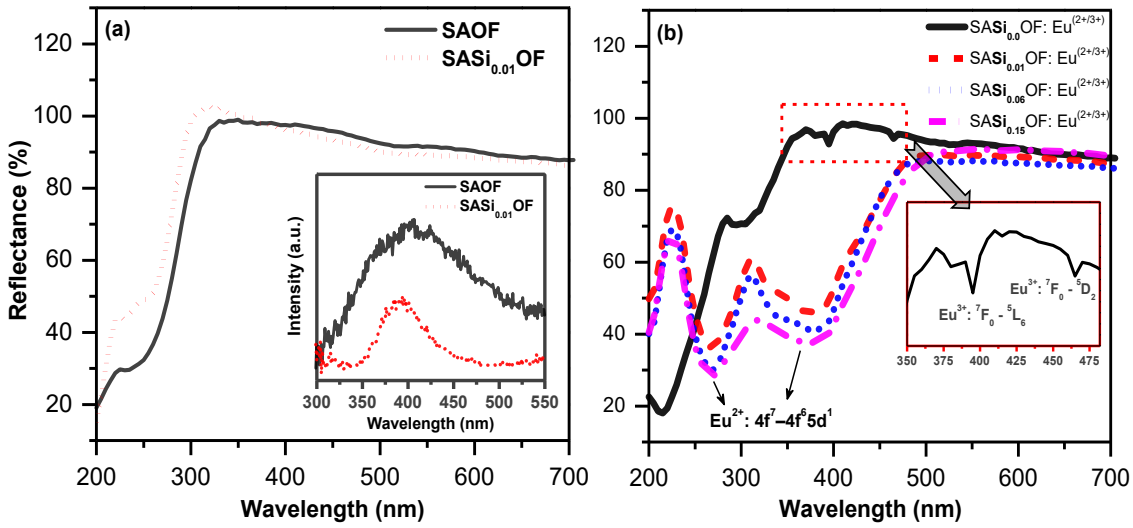

Figure 3.5: (a) *UV-Vis diffuse reflectance spectra and of SAOF and SASiOF samples. Inset shows the PL emission spectra of corresponding samples recorded at 241 nm UV excitation.* ***3.5 (b)*** *UV-Vis diffuse reflectance spectra of $SASi_xOF$: $Eu^{2+/3+}$ phosphors.*

Fig. 3.6 shows the spectral overlap between the excitation spectrum of $SASi_{0.01}OF$: $Eu^{2+/3+}$ and the emission spectrum of SASiOF, which indicates the phenomenon of energy transfer between the self-activated host and the activator ions. The emission spectrum of SASiOF, recorded upon 240 nm excitation, shows a self-activated emission at 416 nm owing to the trapped exciton emission of a defect center in SASiOF. Reportedly, these defects might be related to the anion-deficient nonstoichiometric species which is normally produced during the heating in an oxygen-deficient atmosphere [41]. It is clear from the emission spectra of $SASi_{0.01}OF$: $Eu^{2+/3+}$ that the corresponding emission intensity of the SASiOF host is significantly diminishes owing to the activator ions doping. Also, the emission spectrum of $SASi_{0.01}OF$: $Eu^{2+/3+}$ comprises a broad emission band in the range of 375 to 525 nm which is attributed to the *4f - 5d* transitions of Eu^{2+} ion and several sharp peaks located in the 550 to 675 nm region owing to the *f-f* transitions of Eu^{3+} ions. This result indicates the existence of both europium valency in $SASi_{0.01}OF$: $Eu^{2+/3+}$, and suggesting the tunable emission color can be obtained via tuning the Eu^{2+} to Eu^{3+} ions ratio.

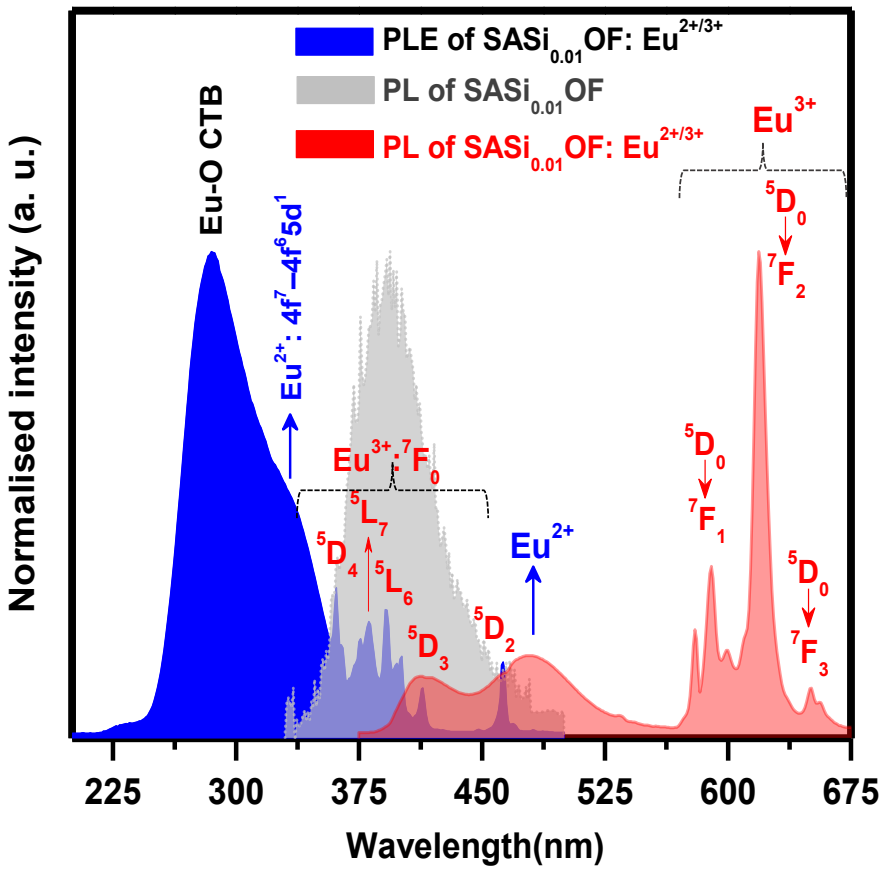

Figure 3.6: *Spectral overlap between the excitation spectrum of $SASi_{0.01}OF: Eu^{2+/3+}$ and the emission spectrum of $SASi_{0.01}OF$. The emission spectrum of SASiOF is also added to realize the self-activated emission of SASiOF and its energy transfer process to activators.*

For the precise tuning of emission color, additional insights on the energy levels of both europium ions in the Si^{4+}- doped SAOF and the corresponding energy exchange procedures among the host and activators. Therefore, **Fig. 3.7 (a)** displays the excitation spectrum of SASiOF peaking at 241 nm, which is deconvoluted into two Gaussian curves, which could be attributed to the band to band transitions (P1) and absorption via the defect states (P2) situated near to the conduction band. In the deconvoluted excitation spectra of $SASi_{0.01}OF: Eu^{2+/3+}$ **(Fig. 3.7 (b)),** P1 belongs to Eu^{3+} - O charge transfer band and P2 is attributed to the *4f - 5d* transitions of Eu^{2+} ions. In addition, the sharp excitation peaks due to the intra-configurational *4f–4f* transitions of Eu^{3+} can also be observed above 340 nm. The deconvoluted excitation spectra of $SASi_{0.06}OF: Eu^{2+/3+}$ phosphor (shown in Fig. 6 (c)) consists of a host excitation peaked at 241 nm and five *4f - 5d* transition peaks

of Eu^{2+} ions. Because of the incorporation of Si^{4+} ions in SAOF: Eu phosphor, the O^{2-} - Eu^{3+} charge transfer band disappears and various Eu^{2+} *4f – 5d* transition peaks arise. The probable energy level diagram of Eu^{2+} and Eu^{3+} ions in the SASiOF host is elaborated in **Fig. 3.7 (c).**

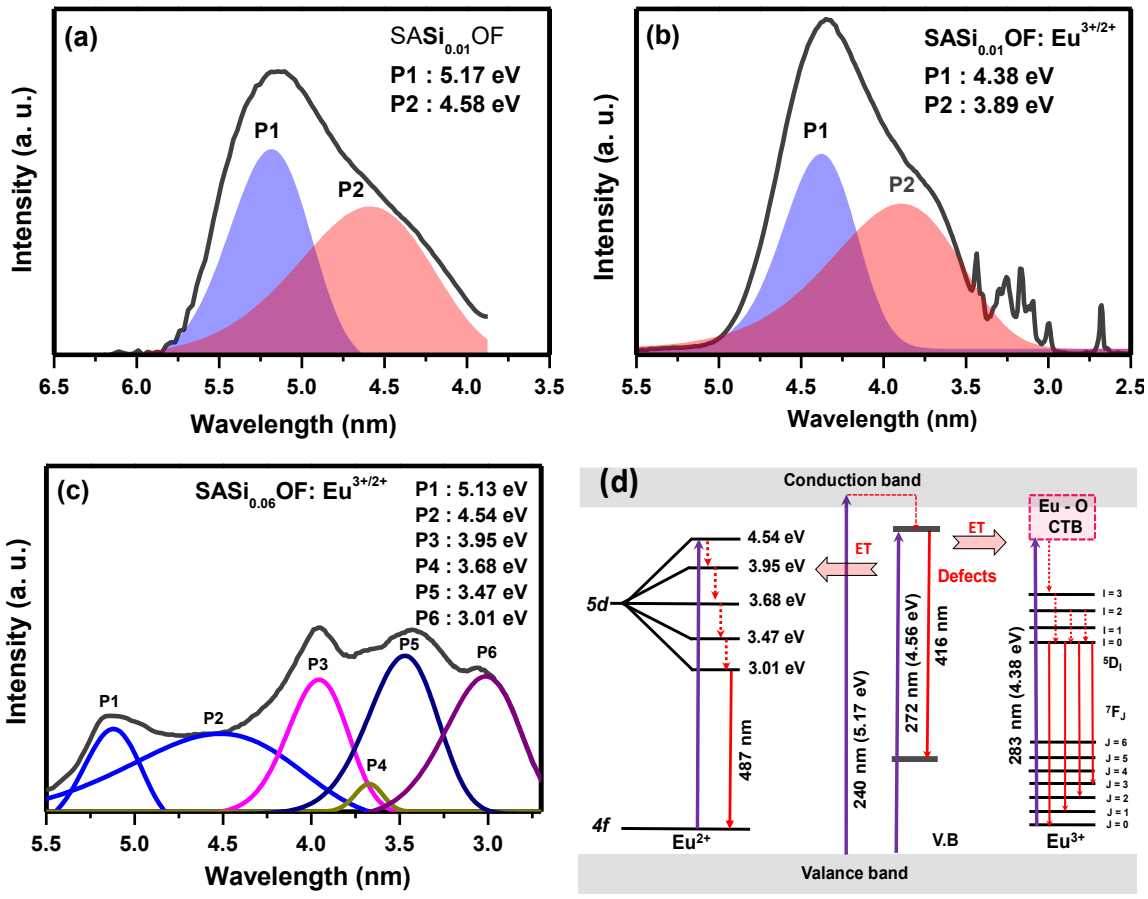

Figure 3.7: *Deconvoluted excitation spectra of* ***(a)*** *SASiOF,* ***(b)*** *$SASi_{0.01}OF: Eu^{2+/3+}$, and* ***(c)*** *$SASi_{0.06}OF: Eu^{2+/3+}$.* ***(d)*** *Illustration of the most probable energy transfer mechanisms in $SASiOF: Eu^{2+/3+}$.*

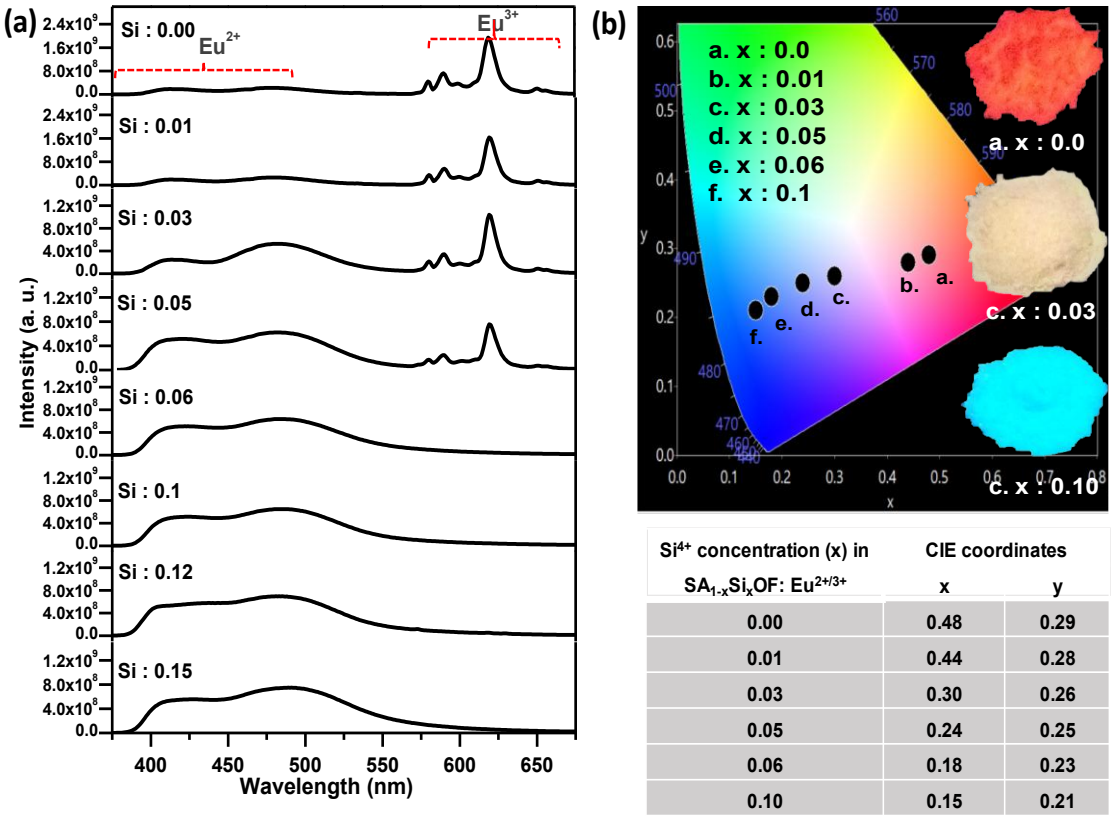

Si^{4+} concentration (x) in $SA_{1-x}Si_xOF: Eu^{2+/3+}$	CIE coordinates	
	x	y
0.00	0.48	0.29
0.01	0.44	0.28
0.03	0.30	0.26
0.05	0.24	0.25
0.06	0.18	0.23
0.10	0.15	0.21

Fig. 3.8: (a) *The emission spectra of* $SA_{1-x}Si_xOF: Eu^{2+/3+}$ $(0 \leq x \leq 0.15)$ *excited by 370 nm.* ***(b)*** *CIE chromaticity diagram and* ***(c)*** *corresponding CIE coordinates of* $SA_{1-x}Si_xOF: Eu^{2+/3+}$ $(0 \leq x \leq 0.1)$ *recorded at 370 nm excitation.*

The emission spectra of a series of $SASi_xOF: Eu^{2+/3+}$ (x = 0.0 - 0.15) phosphors, recorded at 360 nm, is shown in **Fig. 3.8**. A broadband peaked at 482 nm is attributed to the $4f^65d^1$ - $4f^7$ allowed transitions of Eu^{2+} ions. Whereas several sharp peaks of $^5D_0 \rightarrow {}^7F_J$ transitions of Eu^{3+} ions are observed in the 550 to 675 nm region having the intense red peak at 620 nm owing to the $^5D_0 \rightarrow {}^7F_2$ transitions. As the doping concentration of Si^{4+} ion increases emission intensity of characteristic *5d - 4f* transition of Eu^{2+} ions increases and the emission intensity results from the *f–f* transitions of Eu^{3+} ions decreases. At a particular concentration (x = 0.06) of Si^{4+} ions, the red-orange emission band of Eu^{3+} completely diminished, while the board bluish band intensity of Eu^{2+} ions reach maximum. These results indicate that as the concentration of Si^{4+} ions enhances, more Eu^{3+} ions are reduced to Eu^{2+} ions. From the XRD refinement results, it is already observed that both valence states of Eu coexist in $SA_{1-x}Si_xOF$: Eu samples because of the annealing in the oxygen-deficient atmosphere, which is proved again by the

photoluminescent studies. Meanwhile, the emission color of $SA_{1-x}Si_xOF: Eu^{2+/3+}$ phosphors is also tuned from red-orange (x = 0.0; CIE: 0.48, 0.29) to nearly white (x = 0.03; CIE: 0.30, 0.26) and eventually to bluish color (x = 0.06; CIE: 0.18, 0.23) simply by altering the doping concentration of Si^{4+} ions. The corresponding CIE chromaticity diagram of $SASi_xOF: Eu^{2+/3+}$ phosphors monitored on 360 nm near-UV excitation, is shown in **Fig. 3.8**. The inset images under near-UV light well illustrated the color tuning, and directly supporting the emission results of $SA_{1-x}Si_xOF: Eu^{2+/3+}$ phosphors. It is worth mentioning that at an intermediate concentration (x = 0.03) of Si^{4+} ions, both emission peak intensity of Eu^{2+} ions and Eu^{3+} ions are able to tune the emission color to near white indicating the potential of the present host as a single white emitting composition.

3.4.3 Structural and optical characterizations of $SASi_{0.06}OF: Eu^{2+/3+}$ @ CAO composites for their usage in lighting devices

From IR spectra as shown in **Fig. 3.9(a)**, the esterification reaction of the polyol is confirmed by the appearance of characteristic C = Oband at 1745 cm^{-1} (SASi0.03OF: $Eu^{2+/3+}$ @ CO). The strong band at 1242 cm−1 attributed to the C-O stretching further revealed the esterification of polyol. The presence of a medium absorption band at 3350 cm^{-1} corresponds to N-H (secondary) stretching in the urethane and the peak at 1517 cm^{-1} indicates the urethane linkage (C—N—H). The strong intense band at 2261 $cm^{-1,}$ which corresponds to —N═C═O stretching in isocyanate got completely disappeared in polyurethane. The bands analogous to N-H bending at 710–780 cm^{-1} confirms the formation of CO. The peaks at 2922 and 2857 cm−1 are attributed to the methylene (CH_2) asymmetric and symmetric stretching vibration of the hydrocarbon chain of castor oil and methyl group (CH_3) stretching that appeared at 3016 cm^{-1} in both polyurethane and castor oil [45].

The thermal stability of polyurethane and its composite is analyzed by TGA analysis and the thermogram profile is depicted in **Fig. 3.9(b)**. It is important to note that CO is thermally stable up to 230 °C. The initial degradation occurs at 235–240 °C due to the decomposition of urethane linkage, which is unstable compared to other bonding. The next stage of degradation in the range of 380–410 °C corresponds to the decomposition of high energy doublebonds and single bonds including alkyl chain, dissociation of the ester bond through chain scission, dehydrogenation, and depolycondensation of alkyl

groups. The thermal parameters, listed in **Table 3.S4**, show minor improvement in CO matrix after adding phosphor. The higher residue content in the case of CO composite is due to the presence of non-degraded phosphor [46,47].

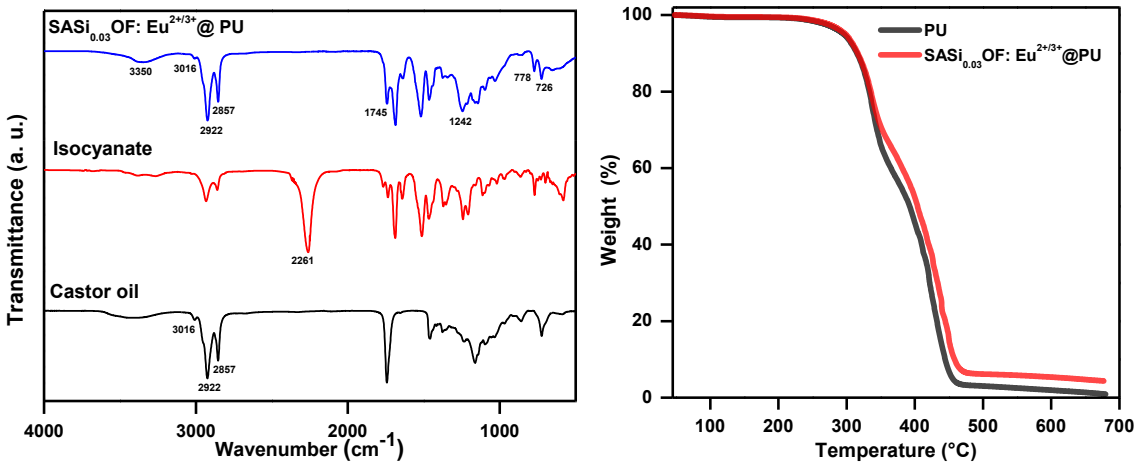

Figure 3.9: *(a) IR analysis of castor oil, isocyanate and $SASi_{0.03}OF: Eu^{2+/3+}$ @ CO. (b) Thermogravimetric profile of CO and $SASi_{0.03}OF: Eu^{2+/3+}$ @ CO.*

Fig. 3.10(a) and (b) display the optical microscopic images of only CO and $SASi_{0.06}OF: Eu^{2+/3+}$ @ CO composites, respectively, along with their real digital images (insets). The transparency of the CO can be well understood in **Fig. 3.10(a)**, whereas **Fig. 3.10(b)** indicates the even distribution of phosphor particles in the CO matrix. It can be realized from the insets that the transparency of the composite (inset of Fig. 3.10(b)) is reduced owing to the phosphor incorporation. However, due to the transparent nature of CO (inset of **Fig. 3.10(a)**), excitation photons can be easily absorbed by the phosphor particles. Finally, we have checked the device preformation of the fabricated composites. These composite membranes could be used to develop resin-free pc- LED systems for various lighting applications. **Fig. 3.10(c)** describes the schematic representation of a pc-LED device having a phosphor – polymer composite layer illuminated by a near-UV LED chip.

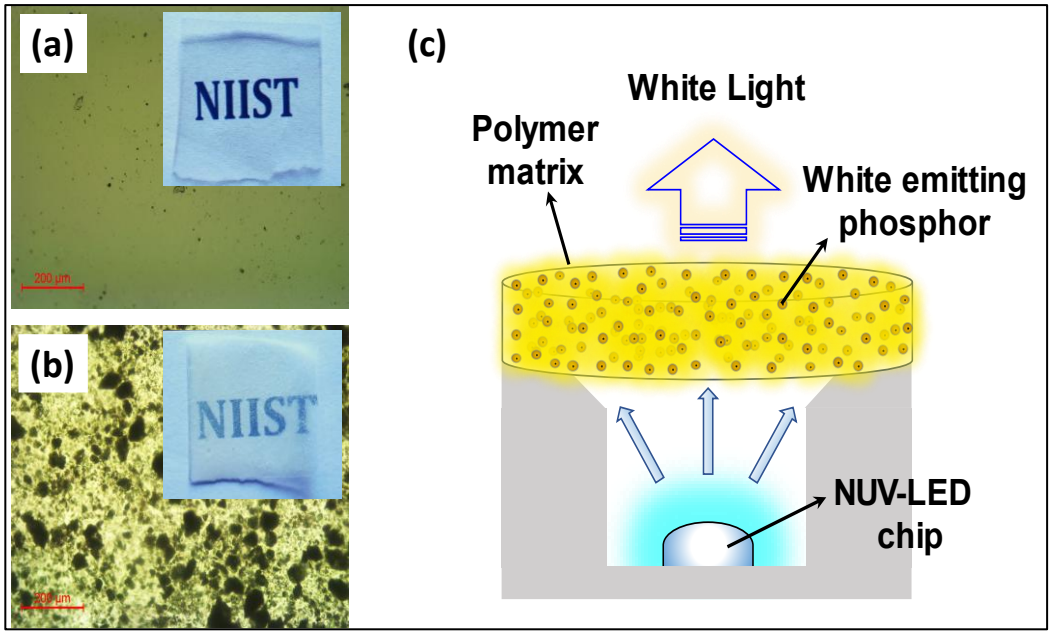

Figure 3.10: *Optical microscopic image and direct digital image (insets) of (a) a CAO matrix, and (b) a SASi$_{0.06}$OF: Eu$^{2+/3+}$ @ CAO composite.* ***(c)*** *Schematic representation of a pc LED device considering the phosphor @ polymer composite layer and a near-UV LED.* ***(d)*** *Real image of a SASi$_{0.06}$OF: Eu$^{2+/3+}$ @ CAO composite under 372 nm near-UV LED illumination.*

The thermal quenching properties of SASi$_{0.06}$OF: Eu$^{2+/3+}$ phosphor and SASi$_{0.06}$OF: Eu$^{2+/3+}$ @ CO composite from ambient to 150 °C temperature and the results are presented in **Fig. 3.11 (a).** Because ofthe increase in operating temperature of the LED, the phosphor emissive performance usually degrades owing to the elevated nonradiative transitions. Here also it is observed that at the elevated temperatures, the emission efficiency of SASi$_{0.06}$OF: Eu$^{2+/3+}$ phosphor decreases gradually with the partial blue shift of the emission band. SASi$_{0.06}$OF: Eu$^{2+/3+}$ phosphor shows only 20% emission intensity compare to the ambient temperature intensity at 150 °C. While the composite shows almost double intensity SASi$_{0.06}$OF: Eu$^{2+/3+}$ phosphor at 150 °C since the encapsulated polymer is acting like a protective layer to the phosphor particles. Eventually, a W-LED is also fabricated using the 372 nm near-UV LED and a composite membrane made from CO loaded with 10 wt% SASi$_{0.03}$OF: Eu$^{2+/3+}$ phosphor. The recorded EL spectrum at 500 mA, shown in **Fig. 10 (b),** shown cool white emission having the CIE of (0.29, 0.33), CCT of 7562 K, and CRI of 89. The inset of **Fig. 10 (b)** is illustrating the image of a SASi$_{0.03}$OF: Eu$^{2+/3+}$ @ CO composite under the illumination of a near-UV 372 nm LED.

The intensity and color uniformity of the emitted light indicate the appropriate distribution of phosphor particles in the polymer matrix. The white light-emitting phosphor – polymer membranes, developed in the current research, maybe potential in making lighting and display devices.

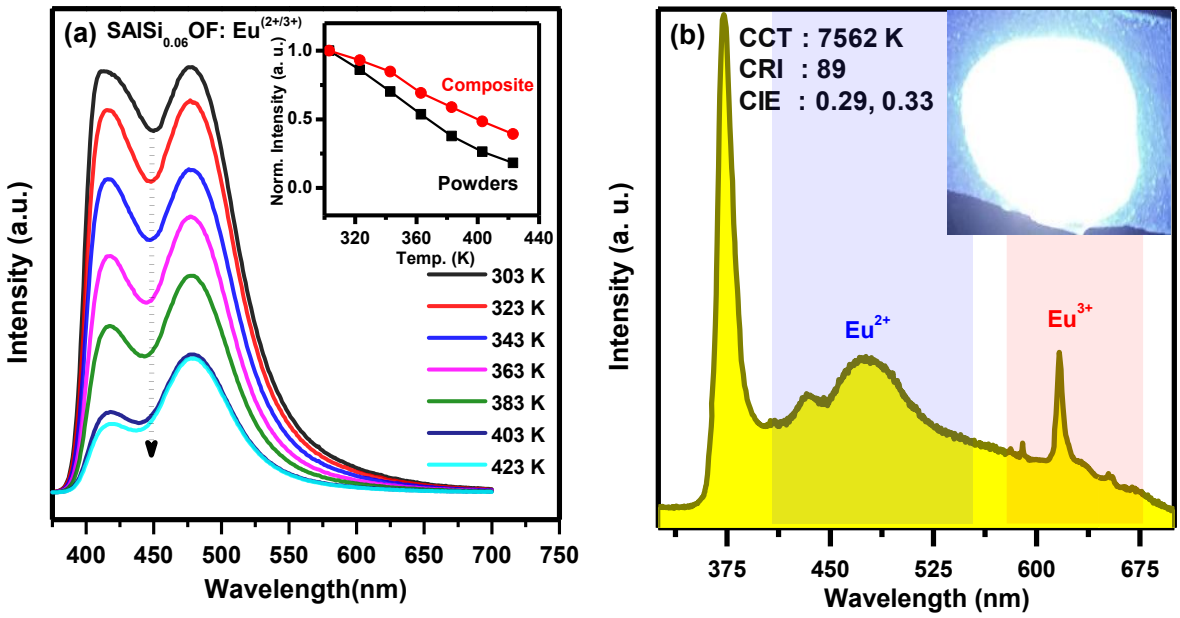

Figure 3.11: (a) *Temperature-dependent PL emission spectra of $SASi_{0.06}OF: Eu^{2+/3+}$ phosphor under 360 nm excitation. The inset shows the PL intensity variation of $SASi_{0.06}OF: Eu^{2+/3+}$ phosphor powders and $SASi_{0.06}OF: Eu^{2+/3+}$ @ CAO composite.* ***(b)*** *EL spectrum of $SASi_{0.03}OF: Eu^{2+/3+}$ / CAO composite sample incorporated in 372 nm LED chips.*

3.5 Conclusions

This work reported various Si^{4+}-codoped $Sr_{2.9}Al_{1-x}Si_xO_4F: 0.1Eu^{2+/3+}$ oxyfluoride phosphors with the simultaneous existence of Eu^{2+} and Eu^{3+} ions. The substitution of Si^{4+} ions in Al sites contracted the AlO_4 tetrahedral sites and enlarges the Sr sites. Such lattice modifications because of the cationic substitutions enabled the occupancy of Eu^{2+} ions, and thus change the valence of Eu^{3+} to Eu^{2+}. Due to the above valence change of europium ions, the broad bluish emission band of Eu^{2+} ions increased gradually along with the subsequent decrement in the sharp red-orange emission peaks due to the intra *f-f* transitions of Eu^{3+} ions. Because of this, the overall emission color was also tuned from orange-red to near-white and eventually to bluish. The optimum blue-emitting

$SASi_{0.06}OF: Eu^{2+/3+}$ and nearly white emitting $SASi_{0.03}OF: Eu^{2+/3+}$ phosphors were utilized further to make phosphor-polymer flexible composites along with castor oil (CAO). Integration of $SASi_{0.03}OF: Eu^{2+/3+}$ @ CAO composite along with a 372 nm near-UV LED produced cool white emission having the chromaticity coordinates of (0.29, 0.32), CCT of 7629 K, and CRI of 96. Therefore, the substitution of Si^{4+} ions in $Sr_{2.9}AlO_4F: 0.1Eu^{2+/3+}$ successfully tuned the important activator sites as well as changed the Eu valence and an altered amount of Si^{4+} ions' concentration generated nearly white light emission. The outcomes are unreported so far for Sr_3AlO_4F based oxyfluorides for flexible lighting applications.

3.6 References

[1] X. Zhang, Z. An, R. Dong, Y. Song, K. Zheng, Y. Sheng, Z. Shi, H. Zou, Properties and Application of Single Eu^{2+}-Activated Color Tuning Phosphors. ACS Sustain. Chem. Eng. 7 (2019) 10724–10733. https://doi.org/10.1021/acssuschemeng.9b01401.

[2] Y. Chen, Z. Wang, W. Ding, X. Li, Q. Bao, J. Liu, K. Qiu, X. Meng, Z. Yang, P. Li, A single-phase white light emitting phosphor $Ba_3Y(PO_4)_3:Ce^{3+}/Eu^{2+}/Mn^{2+}$: Luminescence, energy transfer and thermal stability, J. Lumin. 210 (2019) 322–334. https://doi.org/10.1016/j.jlumin.2019.02.041.

[3] N. Zhang, Y.T. Tsai, M.H. Fang, C.G. Ma, A. Lazarowska, S. Mahlik, M. Grinberg, C.Y. Chiang, W. Zhou, J.G. Lin, J.F. Lee, J. Zheng, C. Guo, R.S. Liu, Aluminate Red Phosphor in Light-Emitting Diodes: Theoretical Calculations, Charge Varieties, and High-Pressure Luminescence Analysis, ACS Appl. Mater. Interfaces. 9 (2017) 23995–24004. https://doi.org/10.1021/acsami.7b06840.

[4] W. Ye, C. Zhao, X. Shen, C. Ma, Z. Deng, Y. Li, Y. Wang, C. Zuo, Z. Wen, Y. Li, X. Yuan, C. Wang, Y. Cao, High Quantum yield $Gd_{4.67}Si_3O_{13}: Eu^{3+}$ Red - emitting phosphor for tunable white light - emitting devices driven by UV or Blue LED, ACS Appl. Elec. Mater. (2021) 2–11. https://doi.org/10.1021/acsaelm.1c00012.

[5] M. Yazdan Mehr, A. Bahrami, W.D. van Driel, X.J. Fan, J.L. Davis, G.Q. Zhang, Degradation of optical materials in solid-state lighting systems, Int. Mater. Rev. 65 (2020) 102–128. https://doi.org/10.1080/09506608.2019.1565716.

[6] Y. Chen, W. Ding, P. Li, X. Li, Q. Bao, J. Liu, K. Qiu, X. Meng, Z. Yang, Z. Wang, A single-phase white light emitting phosphor $Ba_3Y(PO_4)_3:Ce^{3+}/Tb^{3+}/Mn^{2+}$: Luminescence, energy transfer and thermal stability, RSC Adv. 9 (2019) 30406–30418. https://doi.org/10.1039/c9ra05995d.

[7] H. Guo, X. Huang, Y. Zeng, Synthesis and photoluminescence properties of novel highly thermal-stable red-emitting $Na_3Sc_2(PO_4)_3:Eu^{3+}$ phosphors for UV-excited white-light-emitting diodes, J. Alloys Compd. 741 (2018) 300–306. https://doi.org/10.1016/j.jallcom.2017.12.316.

[8] S.A. Khan, H. Zhong, W. Ji, L.Y. Hao, H. Abadikhah, X. Xu, N.Z. Khan, S. Agathopoulos, Single-Phase White Light-Emitting $Ca_xBa_{(9-x)}Lu_2Si_6O_{24}:Eu^{2+}/Mn^{2+}$ Phosphors, ACS Omega. 2 (2017) 6270–6277. https://doi.org/10.1021/acsomega.7b00985.

[9] H. Zhang, D. Yuan, X. Mi, X. Liu, J. Lin, Color tuning in $Ca_{3-x}M_x(PO_4)_2:Eu^{2+}$(M = Sr, Ba) phosphors via cation substitution, Dalt. Trans. 49 (2020) 8949–8958. https://doi.org/10.1039/d0dt01130d.

[10] H. Yoo, Y. Kouhara, H.C. Yoon, S.J. Park, J.H. Oh, Y.R. Do, Sn-P-F containing glass matrix for the fabrication of phosphor-in-glass for use in high power LEDs, RSC Adv. 6 (2016) 111640–111647. https://doi.org/10.1039/C6RA23294A.

[11] X. Yang, J. Chen, C. Chai, S. Zheng, C. Chen, Near ultraviolet excited white light emitting diode (WLED) based on the blue $LiCaPO_4:Eu^{2+}$ phosphor, Optik (Stuttg). 198 (2019) 163238. https://doi.org/10.1016/j.ijleo.2019.163238.

[12] S.A. Khan, A. Jalil, Q. Ullah Khan, R.M. Irfan, I. Mehmood, K. Khan, M. Kiani, B. Dong, N.Z. Khan, J.L. Yu, L. Zhu, S. Agathopoulos, New physical insight into crystal structure, luminescence and optical properties of $YPO_4:Dy^{3+}\backslash Eu^{3+}\backslash Tb^{3+}$ single-phase white-light-emitting phosphors, J. Alloys Compd. 817 (2020) 152687. https://doi.org/10.1016/j.jallcom.2019.152687.

[13] C. Suresh, H. Nagabhushana, G.P. Darshan, R.B. Basavaraj, B. Daruka Prasad, S.C. Sharma, M.K. Sateesh, J.P. Shabaaz Begum, Lanthanum oxyfluoride nanostructures prepared by modified sonochemical method and their use in the fields of optoelectronics and biotechnology, Arab. J. Chem. 11 (2018) 196–213. https://doi.org/10.1016/j.arabjc.2017.03.006.

[14] Z. Zhao, K. Li, C. Liu, Q. Yin, J. Han, J. Heo, Intense up-conversion emission from Er^{3+}/Yb^{3+} ion co-doped transparent oxyfluoride glass-ceramics containing $Y_5O_4F_7$ nanorods for optical thermometry, J. Mater. Chem. C. 7 (2019) 6134–6143. https://doi.org/10.1039/c9tc00280d.

[15] H. Ji, J. Xu, K. Asami, J. Ueda, M.G. Brik, S. Tanabe, Local coordination, electronic structure, and thermal quenching of Ce^{3+} in isostructural Sr_2GdAlO_5 and Sr_3AlO_4F

phosphors, J. Am. Ceram. Soc. 102 (2019) 1316–1328. https://doi.org/10.1111/jace.15985.

[16] M. Shang, G. Li, X. Kang, D. Yang, D. Geng, J. Lin, Tunable luminescence and energy transfer properties of $Sr_3AlO_4F:RE^{3+}$ (RE = Tm/Tb, Eu, Ce) phosphors, ACS Appl. Mater. Interfaces. 3 (2011) 2738–2746. https://doi.org/10.1021/am200534u.

[17] S.P. Lee, S. De Liu, T.S. Chan, T.M. Chen, Synthesis and Luminescence Properties of Novel Ce3+ and Eu^{2+}-Doped Lanthanum Bromothiosilicate $La_3Br(SiS_4)_2$ Phosphors for White LEDs, ACS Appl. Mater. Interfaces. 8 (2016) 9218–9223. https://doi.org/10.1021/acsami.5b12125.

[18] G. Li, Y. Tian, Y. Zhao, J. Lin, Recent progress in luminescence tuning of Ce^{3+} and Eu^{2+}-activated phosphors for pc-WLEDs, Chem. Soc. Rev. 44 (2015) 8688–8713. https://doi.org/10.1039/c4cs00446a.

[19] X. Zheng, H. Luo, J. Liu, P. Liu, X. Yu, $Sr_3AlO_4F:Ce^{3+}$-based yellow phosphors: Structural tuning of optical properties and use in solid-state white lighting, J. Mater. Chem. C. 1 (2013) 7598–7607. https://doi.org/10.1039/c3tc31460j.

[20] W. Bin Im, N. George, J. Kurzman, S. Brinkley, A. Mikhailovsky, J. Hu, B.F. Chmelka, S.P. Denbaars, R. Seshadri, Efficient and color-tunable oxyfluoride solid solution phosphors for solid-state white lighting, Adv. Mater. 23 (2011) 2300–2305. https://doi.org/10.1002/adma.201003640.

[21] W. Bin Im, N. George, J. Kurzman, S. Brinkley, A. Mikhailovsky, J. Hu, B.F. Chmelka, S.P. Denbaars, R. Seshadri, Efficient and color-tunable oxyfluoride solid solution phosphors for solid-state white lighting, Adv. Mater. 23 (2011) 2300–2305, https://doi.org/10.1002/adma.201003640

[22] X. Zheng, H. Luo, J. Liu, P. Liu, X. Yu, $Sr_3AlO_4F:Ce^{3+}$-based yellow phosphors: Structural tuning of optical properties and use in solid-state white lighting, J. Mater. Chem. C 1 (2013) 7598–7607, https://doi.org/10.1039/c3tc31460j

[23] J.S. Lee, S. Unithrattil, W. Bin Im, Color-tunable binary solid-solution phosphor, $(Sr_3SiO_5)_{1-x}(Sr_3AlO_4F)_x$, for white LEDs: Energy transfer mechanism between Ce^{3+} and Tb^{3+}, J. Alloys Compd. 555 (2013) 297–303. https://doi.org/10.1016/j.jallcom.2012.12.050.

[24] M. Peng, G. Hong, Reduction from Eu^{3+} to Eu^{2+} in $BaAl_2O_4$:Eu phosphor prepared in an oxidizing atmosphere and luminescent properties of $BaAl_2O_4$:Eu, J. Lumin. 127 (2007) 735–740, https://doi.org/10.1016/j.jlumin.2007.04.012

[25] Y.H. Cho, D.H. Park, B.T. Ahn, Synthesis and characterization of Eu^{2+} doped $BaAl_2S_4$ phosphor by vacuum heat treatment, Proc. Int. Meet. Inf. Disp. 2006 (2006) 39–42.

[26] Y. Fang, Y.Q. Li, T. Qiu, A.C.A. Delsing, G. de With, H.T. Hintzen, Photoluminescence properties and local electronic structures of rare earth-activated Sr_3AlO_4F, J. Alloy. Compd. 496 (2010) 614–619, https://doi.org/10.1016/j.jallcom.2010.02.130

[27] X. Liu, W. Xie, Y. Lü, J. Feng, X. Tang, J. Lin, Y. Dai, Y. Xie, L. Yan, Multichannel Luminescence Properties of Mixed-Valent Eu^{2+}/Eu^{3+} Coactivated $SrAl_3BO_7$ Nanocrystalline Phosphors for Near-UV LEDs, Inorg. Chem. 56 (2017) 13829–13841. https://doi.org/10.1021/acs.inorgchem.7b01938.

[28] F. Ruan, D. Deng, M. Wu, C. Wu, S. Xu, Tunable single-host full-color-emitting $Ca_9Zn_{1.5}(PO_4)_7$: Eu, Tb phosphor via Eu^{2+}/Eu^{3+} dual-emitting, J. Lumin. 198 (2018) 1–9. https://doi.org/10.1016/j.jlumin.2018.02.022.

[29] B. Marí, K.C. Singh, N. Verma, M. Mollar, J. Jindal, Luminescence Properties of Eu^{2+}/Eu^{3+} Activated Barium Aluminate Phosphors with Gd^{3+} Concentration Variation, Trans. Indian Ceram. Soc. 74 (2015) 157–161. https://doi.org/10.1080/0371750X.2015.1082932.

[30] X. Gao, H. Liu, X. Yang, Y. Tian, X. Lu, L. Han, A novel Eu^{3+}/Eu^{2+} co-doped $MgSrLa_8(SiO_4)6O_2$ single-phase white light phosphor for white LEDs, RSC Adv. 7 (2017) 1711–1717. https://doi.org/10.1039/c6ra25792e.

[31] Z. An, W. Liu, Y. Song, X. Zhang, R. Dong, X. Zhou, K. Zheng, Y. Sheng, Z. Shi, H. Zou, Color-tunable Eu^{2+},Eu^{3+} co-doped $Ca_{20}Al_{26}Mg_3Si_3O_{68}$ phosphor for w-LEDs, J. Mater. Chem. C. 7 (2019) 6978–6985. https://doi.org/10.1039/c9tc01974j.

[32] K.W. Huang, W.T. Chen, C.I. Chu, S.F. Hu, H.S. Sheu, B.M. Cheng, J.M. Chen, R.S. Liu, Controlling the activator site to tune europium valence in oxyfluoride phosphors, Chem. Mater. 24 (2012) 2220–2227, https://doi.org/10.1021/cm3011327

[33] A.A. Setlur, D.G. Porob, U. Happek, M.G. Brik, Inhomogenous broadening, charge compensation, and luminescence quenching in Ce^{3+} -Doped Sr_3AlO_4F phosphors, ECS J. Solid State Sci. Technol. 5 (2016) R3089–R3095, https://doi.org/10. 1149/2.0111601jss

[34] D. Kim, E. Lee, D. Ha, J. Lee, J.S. Bae, S. Il Ahn, I. Chung, S.J. Kim, J.C. Park, Highly luminous and green-emitting Eu^{2+} activated $Eu_{1-x}Sr_xAl_2O_4$ ($0 \leq x \leq 1$) materials for NUV-LEDs, Mater. Chem. Phys. 233 (2019) 185–193, https://doi.org/10.1016/j.matchemphys.2019.05.052

[35] Z. Wang, X. Hou, Y. Liu, Z. Hui, Z. Huang, M. Fang, X. Wu, Luminescence properties and energy transfer behavior of colour-tunable white-emitting Sr4Al14O25 phosphors with co-doping of Eu^{2+}, Eu^{3+} $Mn^{4+}$and, RSC Adv. 7 (2017) 52995–53001, https://doi.org/10.1039/c7ra07970b

[36] S. Sreevalsa, P. Ranjith, S. Ahmad, S.K. Sahoo, S. Som, M.K. Pandey, S. Das, Host sensitized photoluminescence in $Sr_{2.9-3x/2}Ln_xAlO_4F$: $0.1Eu^{3+}$ (Ln = Gd, Y) for innovative flexible lighting applications, Ceram. Int. 46 (2020) 21448–21460, https://doi.org/10.1016/j.ceramint.2020.05.243

[37] S. Oswald, H. Wirth, Core-level shifts at B- and Al-doped 6H-SiC studied by XPS, Surf. Interface Anal. 27 (1999) 136–141. https://doi.org/10.1002/(SICI)1096-9918(199903)27:3<136::AID-SIA492>3.0.CO;2-Z.

[38] S. Kim, M.C. Kim, S.H. Choi, K.J. Kim, H.N. Hwang, C.C. Hwang, Size dependence of Si 2p core-level shift at Si nanocrystal/ SiO_2 interfaces, Appl. Phys. Lett. 91 (2007) 1–4. https://doi.org/10.1063/1.2776014.

[39] J.F. Moulder, W.F. Stickle, P.E. Sobol, K.D. Bomben, Handbook of X-ray Photoelectron Spectroscopy, 1992.

[40] G. Cheng, Q. Liu, L. Cheng, L. Lu, H. Sun, Y. Wu, Z. Bai, X. Zhang, G. Qiu, Synthesis and luminescence property of Sr_3SiO_5:Eu^{2+} phosphors for white LED, J. Rare Earths 28 (2010) 526–528, https://doi.org/10.1016/S1002-0721(09)60146-0

[41] J. Wang, H. Lin, Q. Huang, G. Xiao, J. Xu, B. Wang, T. Hu, Y. Wang, Structure and luminescence behavior of a single-ion activated single-phased $Ba_2Y_3(SiO_4)_3F$:Eu white-light phosphor, J. Mater. Chem. C 5 (2017) 1789–1797, https://doi.org/10. 1039/c6tc04350j

[42] A.K. Kunti, L. Ghosh, S.K. Sharma, H.C. Swart, Synthesis and luminescence mechanism of white light emitting Eu^{3+} doped $CaZnV_2O_7$ phosphors, J. Lumin. 214 (2019) 116530, https://doi.org/10.1016/j.jlumin.2019.116530

[43] A.K. Kunti, N. Patra, R.A. Harris, S.K. Sharma, D. Bhattacharyya, S.N. Jha, H.C. Swart, Structural properties and luminescence dynamics of $CaZrO_3$:Eu^{3+}phosphors, Inorg. Chem. Front. (2021) 821–836, https://doi.org/10. 1039/d0qi01178a

[44] A.K. Kunti, S.K. Sharma, R.J. Choudhary, H.C. Swart, Structural and luminescence properties of laser assisted Eu^{3+} doped $BaZrO_3$ thin films, J. Alloy. Compd. 801 (2019) 99–111, https://doi.org/10.1016/j.jallcom.2019.06.063

[45] Y. Chen, Castor oil-based polyurethane resin for low-density composites with bamboo charcoal, Polymers (2012) 1100, https://doi.org/10.3390/polym10101100

[46] M. Malik, R. Kaur, Mechanical and thermal properties of castor oil–based polyurethane adhesive: effect of TiO_2 filler, Adv. Polym. Technol. 37 (1) (2018) 1–7, https://doi.org/10.1002/adv.21637

[47] K.P. Somani, S.S. Kansara, N.K. Patel, A.K. Rakshit, Castor oil based polyurethane adhesives for wood-to-wood bonding, Int. J. Adhes. Adhes. 23 (4) (2003) 269–275, https://doi.org/10.1016/S0143-7496(03)00044-7

3.7 Supplementary Information

Table 3.S1 *The lattice parameters of the Rietveld refined samples.*

Lattice parameters	SAOF	$SASi_{0.01}OF$	$SASi_{0.01}OF: Eu^{2+/3+}$
a [Å]	6.7537(20)	6.7727(22)	6.7634(7)
b [Å]	6.7537(20)	6.7727(22)	6.7634(7)
c [Å]	11.21269(4)	11.1219(5)	11.1072(12)
V [$Å^3$]	506.4(4)	510.157(29)	508.08(14)

Table 3.S2 *The atomic coordinates and fractional occupancies of the Rietveld refined samples.*

Sample	Atom	Site	x	y	z	Occ.
SAOF	Sr(1)	4a	0.0	0.0	0.25	1
	Sr(2)	8h	0.16960	0.66960	0.0	1
	Al	4b	0.0	0.5	0.25	1
	F	4c	0.0	0.0	0.0	1
	O	16l	0.14180	0.64180	0.64960	1
$SASi_{0.01}OF$	Sr(1)	4a	0.0	0.0	0.25	1
	Sr(2)	8h	0.16782	0.66782	0.0	1
	Al	4b	0.0	0.5	0.25	0.99
	Si	4b	0.0	0.5	0.25	0.01
	F	4c	0.0	0.0	0.0	1
	O	16l	0.13856	0.63856	0.65470	1
$SASi_{0.01}OF: Eu^{2+/3+}$	Sr(1)	4a	0.0	0.0	0.25	0.9
	Eu(1)	4a	0.0	0.0	0.25	0.1
	Sr(2)	8h	0.16536	0.66536	0.0	0.9
	Eu(2)	8h	0.16536	0.66536	0.0	0.1
	Al	4b	0.0	0.5	0.25	0.99
	Si	4b	0.0	0.5	0.25	0.01
	F	4c	0.0	0.0	0.0	1
	O	16l	0.13131	0.63131	0.66050	1

Table 3.S3: *Selected bonds and corresponding bond lengths that exist between the elements in the following samples.*

SAOF		**$SASi_{0.01}OF$**		**$SASi_{0.01}OF: Eu^{2+/3+}$**	
Bond type	**Bond length [Å]**	**Bond type**	**Bond length [Å]**	**Bond type**	**Bond length [Å]**
Sr(1)-O x 8	2.7909(8)	Sr(1)-O x 8	2.82779(8)	Sr(1)/Eu(1)-O x 8	2.82752(8)
Sr(1)-F x 2	2.77807(4)	Sr(1)-F x 2	2.78048(4)	Sr(1)/Eu(1)-F x 2	2.7768(4)
Sr(1)-Sr(2)	3.74284(8)	Sr(1)-Sr(2)	3.7529(8)	Sr(1)/Eu(1)-Sr(2)/Eu(2)	3.75286(8)
Sr(2)-O x 4	2.68734(6)	Sr(2)-O x 4	2.70285(6)	Sr(2)/Eu(2)-O x 4	2.69394(6)
Sr(2)-O x 2	2.4512(3)	Sr(2)-O x 2	2.52976(3)	Sr(2)/Eu(2)-O x 2	2.63822(3)
Sr(2)-F x 2	2.50823(6)	Sr(2)-F x 2	2.52056(6)	Sr(2)/Eu(2)-F x 2	2.52455(2)
Al-O x 4	1.7547(4)	Al/Si-O x 4	1.6984(4)	Al/Si-O x 4	1.6018(4)

Table 3.S4: *Thermal parameters of PU and $SASi_{0.03}OF: Eu^{2+/3+}$ @ PU*

Sample	**T_{onset}**	**T_5**	**T_{10}**	**T_{50}**	**T_{endset}**
PU	237	295	314	392	465
$SASi_{0.03}OF:Eu^{2+/3+}$ @ PU	241	299	316	403	480

Chapter 4

Governing the crystallographic sites for tuning Eu^{2+} emission in an apatite oxyfluoride host to be applied for superior white light emitting diodes.

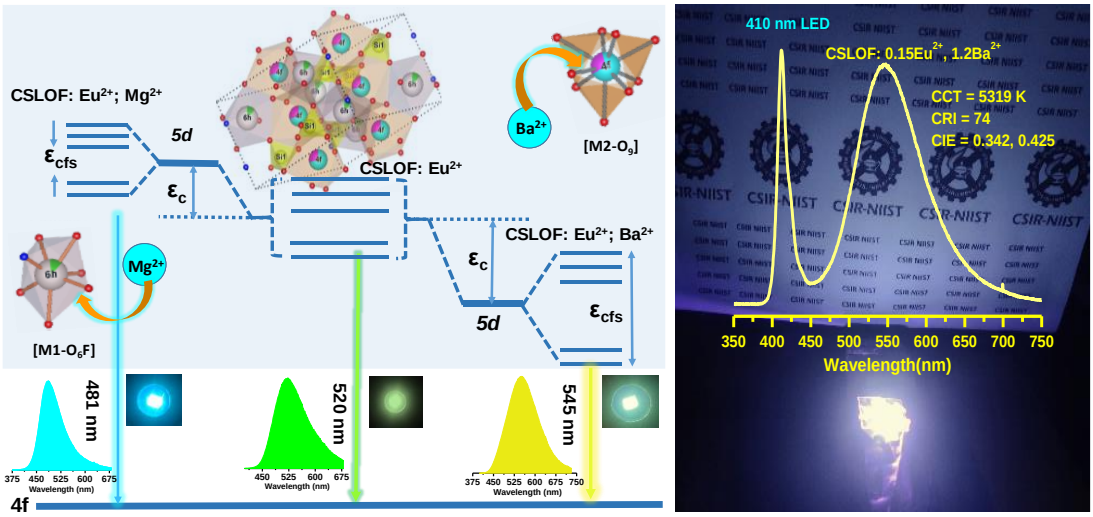

4.1 Abstract

Single white-light-emitting phosphors for near-UV-converted white light-emitting diodes (WLEDs) are the best alternatives to tricolour phosphors' blends and the blue light converted yellow emitting garnets. Nevertheless, achieving white light with elevated colour rendering (CRI) from a single-phase phosphor activated with a lone activator ion is a major challenge. This study aimed at the generation of white light from a single-phase composition activated only with europium. The study started with the structural evaluations of Eu^{3+}-activated $Ca_4La_6Si_6O_{24}F_2$ phosphors using X-ray diffractions (XRD) and Eu^{3+} photoluminescence to elucidate the local environment of rare-earth ions and the symmetric nature of the lattice sites. $Ca_4La_6Si_6O_{24}F_2$ crystallized in the hexagonal $P6_3/m$ space group. The predominant $^5D_0$-$^7F_2$ electric dipole transition at 614 nm, and the non-splitting as well as the zero-shifting behaviour of $^5D_0$-$^7F_0$ at 578 nm, suggested that the rare-earth ionic substitutions preferably took place at the larger asymmetric sites. Introducing Sr^{2+} ions in $Ca_4La_6Si_6O_{24}F_2$:Eu^{3+}/Eu^{2+} that is synthesized in a reducing atmosphere suppressed Eu^{3+} emission. From the optimized $Ca_{1.98}Sr_{1.98}La_6Si_6O_{24}F_2$:$0.04Eu^{2+}$, a sequence of M^{2+}-codoped (M=Mg/Ba) $Ca_{1.98}Sr_{1.98}La_6Si_6O_{24}F_2$: $0.04Eu^{2+}$ phosphors were further developed. The substitutions of Mg^{2+} and Ba^{2+} altered the crystal field by changing the lattice parameters. The Mg^{2+} doped samples showed a blue-shift from 520 nm (Mg^{2+}=0) to 471 nm (Mg^{2+}=1.0). Whereas the Ba^{2+} doped compositions showed a red-shift from 520 nm (Ba^{2+}=0) to 536 nm (Ba^{2+}=1.2). The change of symmetry owing to the Mg^{2+}/Ba^{2+} substitution could have led to the centroid shift, which was responsible for the blue- or red-shift of the emission spectra. The XRD of $Ca_{1.38}Sr_{1.38}La_6Si_6O_{24}F_2$:$0.04Eu^{2+}$,$1.2Ba^{2+}$ indicated Ba^{2+}-induced lattice site expansion. Keeping this in view, Eu^{2+} ions concentrations were further enhanced from 0.04 to 0.3, and the resultant photoluminescence was further enhanced and red-shifted. The optimized sample showed better intensity compared to the commercial $Y_3Al_5O_{12}$:Ce^{3+} and exhibited decent photoluminescence above 70% at 150°C as compared with that at room temperature. Finally, several prototype WLEDs were fabricated using the single phosphor $Ca_{1.365}Sr_{1.365}La_6Si_6O_{24}F_2$:$0.07Eu^{2+}$, $1.2Ba^{2+}$ with near-UV and violet-LED chips. The outcomes indicated the promising nature of this single composition phosphor for indoor lighting.

4.2 Introduction

The present era of lighting technology witnessed the enormously increased usage of phosphor-converted white light-emitting diodes because of their significant advantages including adorable emission behaviour, long lifetime, the high thermal stability of luminescence high temperature with standing power, better colour rendering, high efficiency, and very low energy consumption with good stability [1-3]. Generating white light from the combination of a tricolour LED chips is become limited owing to the high price and complex drive circuit [4]. While the production of white light using phosphor-converted LEDs (pc-LEDs) has become mainstream. Nowadays, the modification and construction of WLEDs are mainly focused on phosphors and LED chips. The Crucial factor that directly influences the performance of LED devices is the phosphor material chosen, it must have efficient emission nature, high thermal and chemical stability, mild synthetic conditions, etc. [5].

The widely used method for fabricating WLED is combining InGaN blue-LED chip with yellow emitting $Y_3Al_5O_{12}$: Ce^{3+} phosphor [6, 7]. But the prolonged blue-LED emission causes severe health issues for humans, such as mood disordering, macular degeneration, circadian disruption, etc. [8]. To reduce the usage of blue-LED chips, nowadays near-UV LEDs (n-UV LEDs) are used as the excitation sources for obtaining the primary colour emissions from corresponding phosphor materials [9]. The n-UV LEDs offer a long lifetime, and greater reliability, and enable lighting designers to achieve better CRI at a given colour point [10]. However, suitable single white emitting phosphor systems for the commercial n-UV LEDs are rarely obtained, due to the undefined distribution and uncontrolled emission behaviour of rare-earth ions.

These days, important research is focused on developing broad band emitting n-UV excited oxyfluoride phosphors for lighting applications as an outcome of their high quantum efficiency and noticeable structural stability and rigidity [11]. Most importantly, the existence of fluorine ions introduces robust electronegativity, which can generate flexible emissive property [12]. In the recently reported oxyfluorides, the presence of multiple crystallographic sites could able to provide versatile cationic environments for Ce^{3+} or Eu^{2+} ions, which are effective in generating broad emissions from these ions [13]. Eventually, an appropriate cationic replacement can drive the luminescent centers to produce emission wavelength shifts very effectively. Paulraj *et al.* recently reported a

broad band emitting $Ca_4F_2Si_2O_7$: Ce^{3+} phosphor based on the occupation of Ce^{3+} ions in multiple crystallographic sites in the host under n-UV excitation. In this host, Ce^{3+} ions can emit broad band emissions because of their accommodation at four available polyhedrons of Ca atoms such as CaF_4O_3 and $CaFO_6$, CaF_5O_3, and CaF_5O [10]. W. B. Im *et al.* reported intense green-emitting $Sr_{2.975-x}Ba_xCe_{0.025}AlO_4F$ oxyfluoride phosphors in response of 400 nm excitation [14]. In this system, Sr and Ba atoms are associated with the SrO_6F_2 and BaO_8F_2 polyhedral units, which are substituted by Ce^{3+} ions and result in a broad band emission. Similar to Ce^{3+} systems, Eu^{2+}-activated phosphors are also able to generate broadband emission bands, and hence, they are considered the potential for WLED applications [15].

Silicate apatite-based phosphors are emerging as promising hosts for rare-earth thanks to their high chemical and thermal stability [16]. Apatite host compounds crystallize in a hexagonal system with a $P6_3/m$ space group with the general structural formula $M_{10}(XO_4)_6Y_2$, in which M corresponds to divalent cations like Mg^{2+}, Ca^{2+}, Sr^{2+}, Ba^{2+}, etc. X represents Si^{4+}, Ge^{4+}, P^{5+}, As^{5+}, etc. which forms tetrahedrons with oxygen, and Y represents anions like O^{2-}, F^-, and Cl^-. In this structure, M ions are situated in two sites; one is a seven-coordinated *6h* site with C_s point symmetry, and the other is a nine-coordinated *4f* site with C_3 point symmetry [17-19]. These hosts show decent luminescent properties because of the strong covalent X-O frameworks connected to two cationic polyhedrons through edge and corner-sharing, which distort the coordination environment around the cations [17].

Following the general structural formula of apatite, Njema *et al.* reported the structural features of $Ca_{10-x}Ln_x(PO_4)_{6-x}(SiO_4)_xF_2$ phosphosilicate [20, 21]. In this structure, the incorporation of La^{3+} and $(SiO_4)^{4-}$ pairs for Ca^{2+} and $(PO_4)^{3-}$ expanded [Ca/La-O9] and [Ca/La-O6F] polyhedrons, and contracted the [Si/P-O4] tetrahedrons. The expansion of nine and seven coordinated polyhedrons makes them suitable for the larger ionic substitutions [20, 21]. To produce multiple-coloured emissions including white light, apatite could be the ideal host because of the allowed tuning of various crystal sites either by multiple activators doping mechanisms or via the cationic substitution strategies within these hosts [22-26]. Fluorapatite structure ($M_{10}(XO_4)_6F_2$) is known for its abundant nature and high stability. The presence of fluoride ions in this system can generate potential luminescent properties in solid-state lighting due to the presence of a mixed ligand

system [19]. Among the fluorapatite family, $Ca_{10}(PO_4)_6F_2$ is the most widely investigated composition for various applications because of its robust tolerance to numerous replacements [19]. In the present work, $Ca_4La_6Si_6O_{24}F_2$ composition has been designed initially via the partial substitution of Ca^{2+} by La^{3+} and then $(PO_4)^{3-}$ was completely substituted by $(SiO_4)^{4-}$. The study of the structural and luminescence property of this phosphor containing different valance of europium ions to achieve tuneable broadband emission is not reported yet.

In the europium doped host lattice, both the valance of Eu (2+ and 3+) coexists in the host. The parity-forbidden sharp *4f−4f* transitions in Eu^{3+} activated phosphor lead to a low colour rendering index (CRI) and *4f−5d* transitions in Eu^{2+} cause intensely broad band emission, which is more applicable for white-light-emitting applications [27]. The spectroscopic properties of Eu^{3+} ions highly depend on the local environment. For instance, if the dopant enters the specific site under examination, then its emission behaviour depends on the symmetry of the site, which can be changed because of the slight alteration in the ligand field. Thus, characteristics of any crystallographic site could be revealed by studying the splitting of the emission bands of the Eu^{3+} ions located at that specific site [28]. Therefore, Eu^{3+} ions' luminescence is a good probe and is favourable to the investigation of the symmetry of various sites of any host material. Because of the similar ionic radius, the site occupancy for Eu^{3+} in the $Ca_4La_6Si_6O_{24}F_2$ host can be, to some extent, considered as a reference for broadband emitting Eu^{2+} ions in the same host matrix. Meanwhile, adjusting the concentrations and emission ratio of Eu^{3+} and Eu^{2+} ions could effectively tune the emission colour. For example, Y. Zhang *et al.* generated a series of $Ca_{0.99+x}Y_{1-x}Al_{1-x}Si_xO_4$: $Eu_{0.01}$ phosphors where the substitution of Al^{3+}–Y^{3+} by Si^{4+}–Ca^{2+} has been initiated. Such a strategy shrinks the $[AlO_6]$ octahedrons, followed by expanding the $[CaO_9]$ polyhedrons, which enhanced the Eu^{3+}–to–Eu^{2+} reduction effectively [29]. Recently, our group has also reported cool white-light-emitting $Sr_{2.9}Al_{1-x}Si_xO_4F$: $0.1Eu^{2+/3+}$ phosphors through a similar cation substitution strategy [30]. Nonetheless, a high Eu^{2+}–to–Eu^{3+} ratio is required for generating a wide gamut for WLEDs, and the search for finding a suitable oxyfluoride host that can accommodate large sized Eu^{2+} ions is still in progress.

As per the above discussions, we initiated our research for developing broad band emitting and apatite structured Eu^{2+} doped oxyfluoride systems for the wide gamut

WLED applications. Initially, a series of intense green-emitting $Ca_2Sr_2La_6Si_6O_{24}F_2$: Eu^{2+} phosphors were synthesized. Herein, X-ray diffraction Rietveld refinement tool and Eu^{3+} spectroscopy was used to identify the site occupancy, symmetry, and lattice distortion in the $Ca_2Sr_2La_6Si_6O_{24}F_2$ host. The emission of Eu^{2+} was further tuned from green to cyan and to greenish-yellow via the doping of Mg^{2+} and Ba^{2+} ions into the appropriate lattice sites, respectively. The optimized phosphors were having comparable emission intensity with commercial $Y_3Al_5O_{12}$: Ce^{3+} phosphors. Eventually, the optimized systems showed adequate photoluminescent intensity at 150°C. These research outcomes make the presently optimized systems interesting for WLED applications.

4.3 Experimental Section

4.3.1 Preparation of a Phosphor

A series of $Ca_4La_6Si_6O_{24}F_2$: xEu^{3+} (CLOF: xEu^{3+}; x = 0.0, 0.01 to 0.1) and $Ca_2Sr_2La_6Si_6O_{24}F_2$:$xEu^{2+}$ (CSLOF: xEu^{2+}; x = 0.0 to 0.055) phosphors were synthesized through conventional solid-state method. The stoichiometric amounts of $CaCO_3$ (99.999%), $SrCO_3$ (99.999%), La_2O_3 (99.999%), SiO_2 (99.99%), NH_4F (99.99%), and Eu_2O_3 (99.999%) purchased from Sigma-Aldrich were ground together in an agate mortar for 30 min. After the homogeneous mixing, the grounded mixture was transferred into an alumina crucible and annealed at 1300 °C for 4 h in a reduction atmosphere (10%H_2 - 90%N_2). For convenience, the $Ca_4La_6Si_6O_{24}F_2$ sample will be named CLOF and all other synthesised phosphors are represented accordingly, as illustrated in **Table 4.1**.

Table 4.1: *Short representations of the obtained samples*

Synthesised Phosphor	**Short Representation**
$Ca_4La_6Si_6O_{24}F_2$	CLOF
$Ca_{4-3x/2}La_6Si_6O_{24}F_2$: xEu^{3+}	CLOF: xEu^{3+}
$Ca_2Sr_2La_6Si_6O_{24}F_2$	CSLOF
$Ca_{2-x}Sr_{2-x}La_6Si_6O_{24}F_2$: xEu^{2+}	CSLOF: xEu^{2+}
$Ca_{1.98-y}Sr_{1.98-y}La_6Si_6O_{24}F_2$: $0.04Eu^{2+}$; yMg^{2+}	CSLOF: $0.04Eu^{2+}$, yMg^{2+}
$Ca_{1.98-z}Sr_{1.98-z}La_6Si_6O_{24}F_2$: $0.04Eu^{2+}$; zBa^{2+}	CSLOF: $0.04Eu^{2+}$, zBa^{2+}

4.3.2 Material Characterization

The structural part of synthesized phosphors was studied by using a PC-controlled X-ray Diffractometer powder collected using EMPYREAN 3 Malvern PANalytical B.V with Cu-Kα radiation (wavelength: 1.54056 Å). The structure and lattice parameters of the samples are refined by the Rietveld method using the GSAS software. The elemental composition of the synthesised phosphor were analysed by using transmission electron microscope (TEM), FEI Tecnai F20, operated at 300 kV. The photoluminescence excitation (PLE) and emission (PL) were measured using a YvonFluorolog 3 spectrofluorimeter with a 450 W Xenon flash lamp source. The electroluminescence spectra of synthesized phosphors were recorded by using a CCE spectrophotometer (OCEAN-FX-XRI-EX).

4.4 Results and discussions

4.4.1 Structural characterizations of $Ca_{4-3x/2}La_6Si_6O_{24}F_2$: xEu^{3+} (CLOF: xEu^{3+}) and $Ca_{2-x}Sr_{2-x}La_6Si_6O_{24}F_2$: xEu^{2+} (CSLOF: xEu^{2+})

Fig. 4.1(a) and **4.1(b)** represent the Rietveld refinement patterns of $Ca_4La_6Si_6O_{24}F_2$ (CLOF) host and $Ca_{3.94}La_6Si_6O_{24}F_2$: $0.04Eu^{3+}$ (CLOF: $0.04Eu^{3+}$) phosphor, respectively. The estimated structural parameters are tabulated in Table S1. As per the refinement data analysis, both undoped and doped apatite phosphors belonging to the hexagonal structure with *$P6_3/m$* space group without any predominant impure phase (ICSD # 170852). The probable crystal structure and coordination environment for different cationic sites of the CLOF host are shown in **Fig. 4.1(c).** The structure consists of two independent crystallographic cationic sites: seven coordinated *6h* sites and nine coordinated *4f* sites. Both the sites are asymmetric. The *6h* sites are occupied by M1 (La^{3+}/Ca^{2+}) cations, which form a distorted pentagonal bipyramid [M1-O_6F] with C_s point symmetry. Whereas M2 (La^{3+}/Ca^{2+}) cations occupy *4f* sites and form a three-fold capped trigonal prism [M2-O9] with C_3 point symmetry. Simultaneously, Si^{4+} ions are tetrahedrally coordinated with oxygen atoms to form [Si-O_4] polyhedrons. Each [M1-O_6F] polyhedron is connected with the [SiO_4] tetrahedron by edge or corner-sharing. The [M2-O_9] polyhedrons are on a three-fold axis and each of these polyhedrons is connected with three [SiO_4] tetrahedrons through edge-sharing.

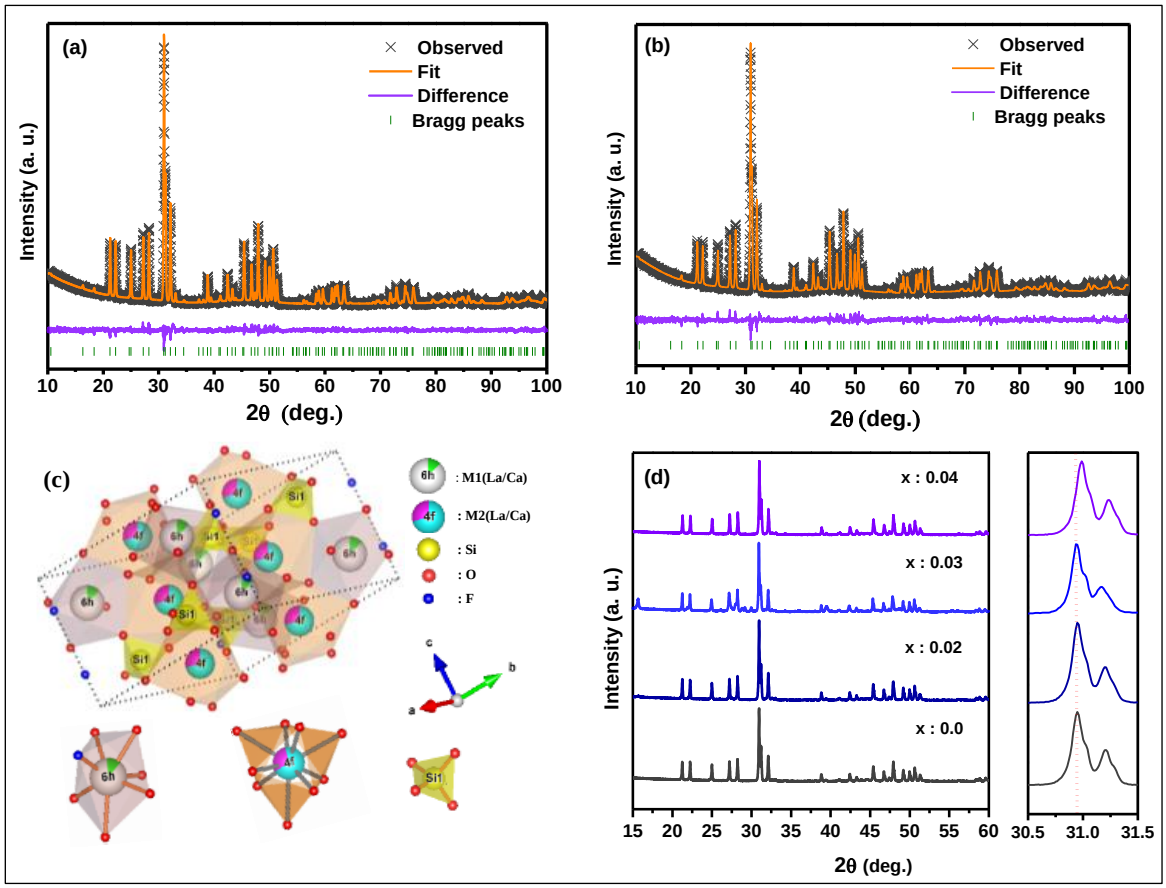

Fig. 4.1: *Rietveld refinement of* ***(a)*** *CLOF and* ***(b)*** *CLOF: 0.04Eu^{3+}.* ***(c)*** *Crystal structure and different coordination environment of CLOF: 0.04Eu^{3+}.* ***(d)*** *Powder XRD patterns of CLOF: xEu^{3+} (x = 0, 0.02, 0.03, and 0.04).*

In the CLOF host, 75% of *6h* sites are occupied by La^{3+} ions and 25% of them are occupancy by Ca^{2+} ions. While the occupancy of La^{3+} and Ca^{2+} ions in *4f* sites are predicted to be 37.5% and 62.5%, respectively, as indicated in **Table S2.** Among the two cationic sites, the nine coordinated *4f* site is having a larger size than the seven coordinated *6h* sites. The ionic radii of La^{3+} and Ca^{2+} ions in the nine and seven coordinated sites are (La^{3+}: R_{4f} = 1.216 Å; R_{6h} = 1.10 Å) and (Ca^{2+}: R_{4f}= 1.18 Å; R_{6h} = 1.06 Å), respectively. After incorporating Eu^{3+} ions into the CLOF host, the cell volume and lattice parameters are found to be decreased slightly due to the substitution of smaller Eu^{3+} ions (Eu^{3+}: R_{4f}= 1.12 Å; R_{6h} = 1.01 Å) at both the ionic sites (**Table 4.S1**). Eventually, the average (La2/Ca2-O) bond length at the *4f* sites is slightly contracted (CLOF = 2.657 Å, CLOF: Eu^{3+} = 2.629 Å) while the average (La1/Ca1-O) bond length at the *6h* site remained almost unchanged (CLOF = 2.549 Å, CLOF: Eu^{3+} = 2.547 Å) due

to the Eu^{3+} ions' doping in the CLOF host. Such observations confirm that *4f* sites could be preferable for Eu^{3+} ions' substitution. The powder diffraction pattern of a series of synthesized $Ca_{4-3x/2}La_6Si_6O_{24}F_2$: xEu^{3+} (CLOF: xEu^{3+}) phosphors, shown in **Fig. 4.1(d),** does not elaborate on any characteristic impure phase after increasing the Eu^{3+} ions' concentrations. In addition, there is a slight shift of the main diffraction peak of CLOF after increasing Eu^{3+} ion concentration towards the right is observed, which ensures the preferable substitution of Eu^{3+} ions at the larger Ca^{2+}/La^{3+} ionic sites in the host lattice. Normally, it would be quite difficult to accommodate Eu^{2+} ions into the CLOF host because of the large ionic radii difference of a Eu^{2+} ion in the two cationic sites (Eu^{2+}: R_{4f} = 1.3 Å; R_{6h} = 1.2 Å). The comfortable substitution of Eu^{2+} ions in this host might need cationic site expansion. Thus, larger Sr^{2+} ions are incorporated into the CLOF host. **Fig. 4.2(a)** and **4.2(b)** represent the Rietveld refinement patterns of $Ca_2Sr_2La_6Si_6O_{24}F_2$ (CSLOF) and $Ca_{1.98}Sr_{1.98}La_6Si_6O_{24}F_2$: $0.04Eu^{2+}$ (CSLOF: $0.04Eu^{2+}$) phosphors. The parameters evaluated from the crystal structure refinement are listed in Table S1. The lattice parameters of CSLOF are found to be increased as compared with the CLOF host due to the larger Sr^{2+} ions' incorporation (R_{4f} = 1.31 Å; R_{6h} = 1.21 Å) into the host lattice compare to Ca^{2+}/La^{3+} ions owing to which more Eu^{2+} ions can be easily accommodating in the cationic sites. The average metal-oxygen bond lengths in *4f* and *6h* cationic sites are slightly enhanced from 2.657 to 2.668 Å and 2.549 to 2.560 Å, respectively, after the Sr^{2+} ions' incorporation (**Fig. 4.2(c)). Fig. 4.2(d)** shows the powder diffraction patterns of a series of $Ca_{2-x}Sr_{2-x}La_6Si_6O_{24}F_2$: xEu^{2+} (CSLOF: xEu^{2+}) phosphors. With the increase in Eu^{2+} concentrations, there is no characteristic phase change appears indicate the proper incorporation of Eu^{2+} ions in the lattice without causing any phase defects. Eventually, the lattice parameters are also increased slightly owing to the Eu^{2+}-doping into the CSLOF host (**Table 4.S1**). Replacing Ca^{2+} ions with relatively bigger Eu^{2+} ions could be the reason for the left-shift and the lattice expansion. Fig. S1 describes the HRTEM spectrum and elemental mapping of undoped CSLOF. All its constituent elements, i.e., Ca, La, Si, O, and F in particular, are distributed homogeneously, with no clustering or segregation of any elements. Thus, the results of electron mapping further ascertained the uniform substitution of elements and the formation of single-phase phosphor.

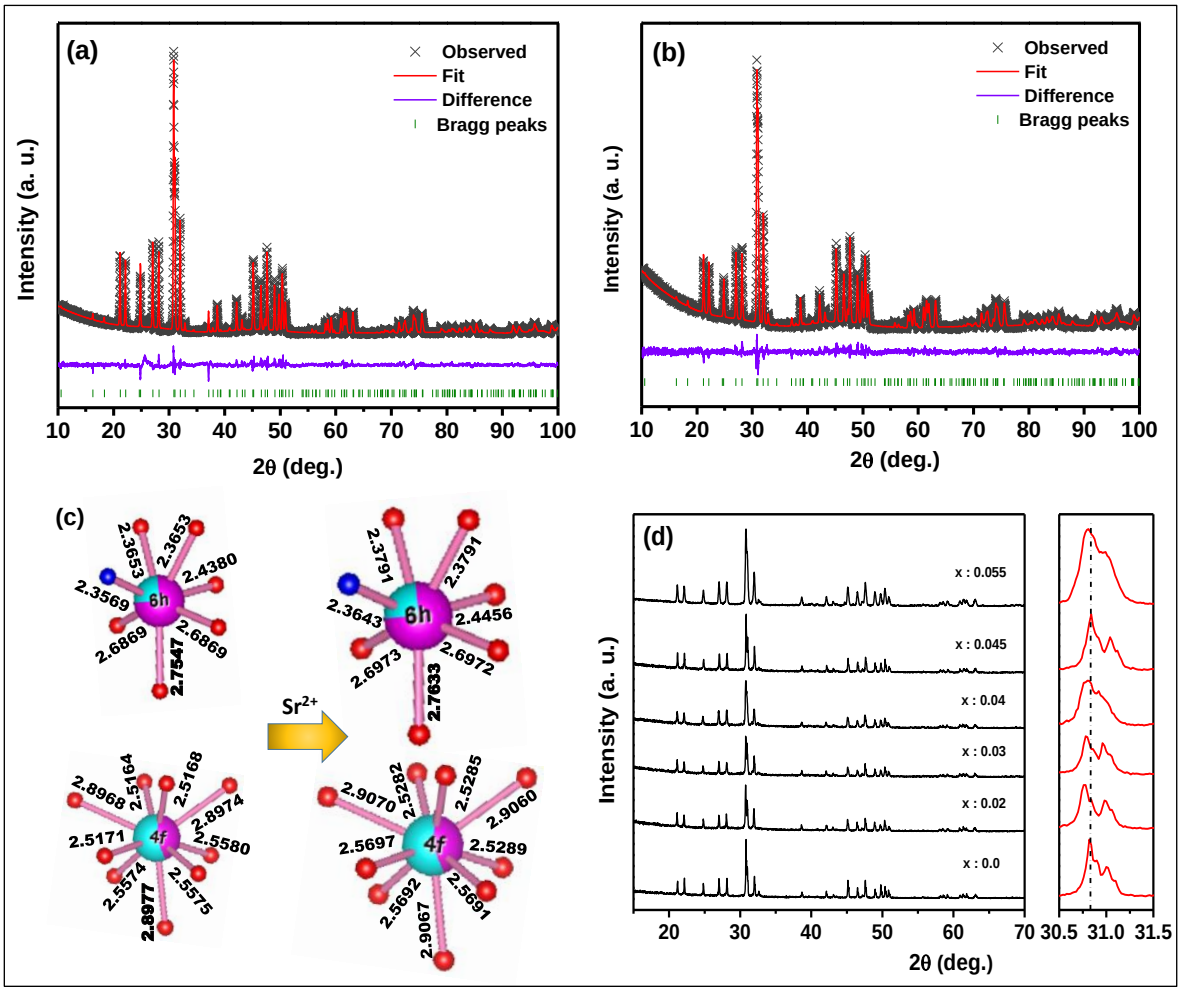

Fig. 4.2: *Rietveld refinement of* ***(a)*** *CSLOF and* ***(b)*** *CSLOF: 0.04Eu^{2+}.* ***(c)*** *Schematic representation of average metal - oxygen bond length variation in undoped CLOF and CSLOF.* ***(d)*** *XRD patterns of CSLOF: xEu^{2+} (x = 0, 0.02, 0.03, 0.04, 0.045, and 0.055).*

4.4.2. Photoluminescence of $Ca_{4-3x/2}La_6Si_6O_{24}F_2$: xEu^{3+} (CLOF: xEu^{3+}) synthesized in air

It is analysed from the XRD of CLOF: Eu^{3+} that Eu^{3+} ions are preferably occupying in non - centrosymmetric *4f* sites which is larger size than the asymmetric *6h* sites. This prediction might be supported by the M-O bond length calculation in *4f* and *6h* sites. Based on ionic radii, Eu^{3+} ions can replace both La^{3+} and Ca^{2+} ions in the CLOF host. It is already mentioned in the XRD section that the occupancy of Ca^{2+} ions is much higher in *4f* sites and the occupancy of La^{3+} ions is higher in the *6h* sites (**Table 4.S2**). For the suitable occupation of bigger Eu^{2+} ions in the CLOF system, identifying the nature of site symmetry and the appropriate cation is very important. Eventually, the emission intensity

of the activator ion directly depends on the crystallographic site symmetry of that particular host. Herein, Eu^{3+} ions' spectroscopy is used as the structural probe to get more insights on the site symmetries in the present host system. **Fig. 4.3(a)** represents the comparative photoluminescence of $C_{3.94}LOF: 0.04Eu^{3+}$ and $CL_{5.96}OF: 0.04Eu^{3+}$ samples synthesized in the air by replacing the Ca^{2+} ions and La^{3+} ions with Eu^{3+} ions, respectively. Both the combinations show similar photoluminescence since Eu^{3+} ions substituted Ca^{2+} and La^{3+} ions which are sharing similar lattice sites and having similar ionic radii with that of Eu^{3+}. However, the excitation spectra of $C_{3.94}LOF: 0.04Eu^{3+}$ exhibit a slightly red-shifted charge transfer band (CTB) of O^{2-} to Eu^{3+} ions in comparison to the CTB of $CL_{5.96}OF: 0.04Eu^{3+}$. In $C_{3.94}LOF: 0.04Eu^{3+}$ system, Eu-O bond might be more covalent than that in $CL_{5.96}OF: 0.04Eu^{3+}$ owing to the charge difference between Ca^{2+} and Ln^{3+} (Ln = La^{3+}, Eu^{3+}) ions. This could be the reason for the redshift of the CTB band when Eu^{3+} ions replace Ca^{2+} ions rather than La^{3+} ions. According to Feng *et al.,* the CTB red-shift can be observed in the case of Eu^{3+} ions substituting the less electronegative metal ions and vice versa [31]. La^{3+} ion (13.07×10^{-30} m^3) has a higher polarizability value than that of the Ca^{2+} ion (5.91×10^{-30} m^3) because of this reason red-shift in CTB might be observed in $C_{3.94}LOF: 0.04Eu^{3+}$ as compared with $CL_{5.96}OF: 0.04Eu^{3+}$ [20].

Fig. 4.3(b) shows the PLE of a series of $Ca_{4-3x/2}La_6Si_6O_{24}F_2: xEu^{3+}$ (CLOF: xEu^{3+}) samples recorded at 614 nm. The spectra consist of a broad band covering from 240 to 340 nm corresponding to the O^{2-}-Eu^{3+} CTB and several sharp lines are observed in the region after 350 nm due to the intra-configurational *f-f* transitions of Eu^{3+} ions. A redshift in the CTB is observed up to x = 0.04 above which the CTB peak shifted to the lower wavelength side. This is attributed to the occupation of Eu^{3+} ions at *4f* sites with C_3 symmetry. In CLOF: $0.04Eu^{3+}$, the average metal-oxygen bond length in *4f* sites (2.629 Å) is observed to be higher than that in the *6h* sites (2.547 Å). The larger bond length in *4f* sites might reduce the energy of CTB and may cause the initial red-shift. Above a certain level of doping concentration, Eu^{3+} ions started to occupy smaller *6h* sites with C_s symmetry and having shorter bond lengths, and thus a blue shift in excitation is observed [31].

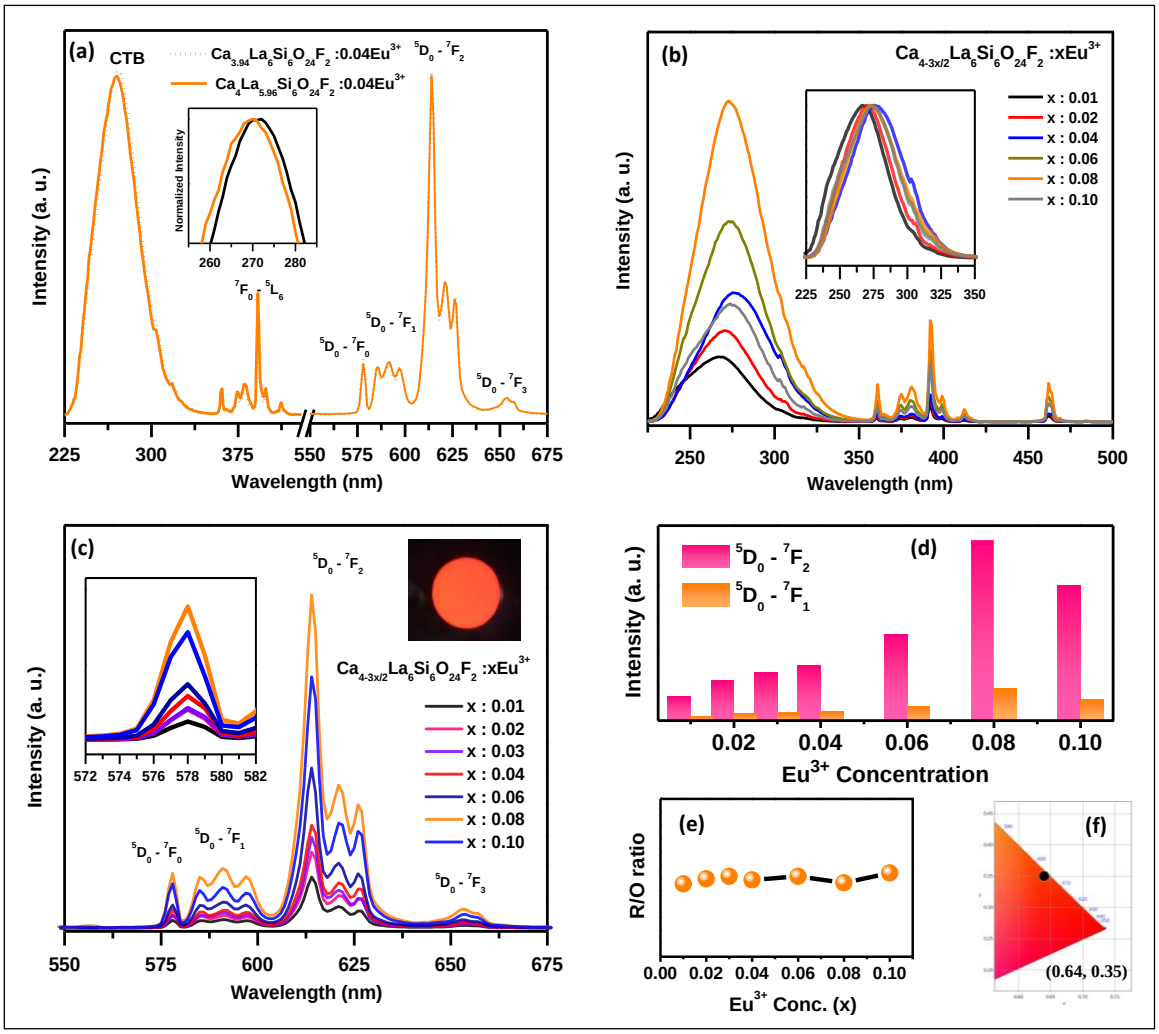

Fig. 4.3: (a) *The comparative photoluminescence excitation and emission spectra of* $Ca_{3.94}La_6Si_6O_{24}F_2$*: 0.04*$Eu^{3+}$ *and* $Ca_4La_{5.96}Si_6O_{24}F_2$*: 0.04*$Eu^{3+}$ *samples synthesized in air and recorded at 614 nm and 280 nm, respectively.* ***(b)*** *Excitation and* ***(c)*** *emission spectra of* $Ca_{4-3x/2}La_6Si_6O_{24}F_2$*: x*$Eu^{3+}$ *(x = 0.01, 0.02, 0.04, 0.06, 0.08, and 0.10) recorded at 614 nm and 280 nm, respectively.* ***(d)*** *The variation of the intensity of red (*$^5D_0$ *-* $^7F_2$*) and orange (*$^5D_0$ *-* $^7F_1$*) transitions, and* ***(e)*** *the variations in the red-to-orange ratio for* $Ca_{4-3x/2}La_6Si_6O_{24}F_2$*: x*$Eu^{3+}$ *phosphors.* ***(f)*** *CIE diagram and colour coordinates of CLOF: 0.08*Eu^{3+} *phosphor under 280 nm UV illumination.*

Fig. 4.3(c) describes the PL emission spectra of a series of CLOF: xEu^{3+} phosphors synthesized in air and excited under 280 nm CTB peak wavelength. The emission spectra are consisting of several sharp peaks of Eu^{3+} ions' intra f-f transitions. Herein, the sharp emission at 585 nm ($\Delta J = \pm 1$) corresponds to the electric dipole transition ($^5D_0$ - $^7F_1$). The most intense peak at 614 nm ($\Delta J = \pm 2$) corresponds to the magnetic dipole transition

($^5D_0$ - $^7F_2$), which means that Eu^{3+} ions are located at non-centrosymmetric sites [32]. Although both the sites in CLOF do not possess a centre of symmetry, however, the 4f site having C_3 point symmetry is comparatively lesser asymmetric than the 6h site with C_s point symmetry. Moreover, the observed peak at 578 nm is because of the $^5D_0$ -$^7F_0$ forbidden transition, and it determines Eu^{3+} ions' site occupancy in CLOF host. According to the electric dipole selection rule, the $^5D_0$ -$^7F_0$ transition usually appears for Eu^{3+} ions, which are situated at low symmetries like C_s, C_1, C_2, C_3, C_4, C_6, C_{2V}, C_{3V}, C_{4V}, and C_{6V}, respectively [33]. Therefore, the aforementioned observation shows that Eu^{3+} ions might have occupied both of the sites in the CLOF host. However, the zero splitting and non-shifting behaviour of $^5D_0$ -$^7F_0$ transition due to the increase of Eu^{3+} ions' concentrations might be due to more preferable occupancy of Eu^{3+} ions in 4f sites, which is bigger and asymmetric than the 6h sites.

The inset of **Fig. 4.3(c)** represented the direct PL image of the optimum CLOF: $0.08Eu^{3+}$ sample under the response of a 280 nm UV source. Fig. 4.3(d) represents the intensity variations of $^5D_0$ -$^7F_2$ and $^5D_0$ -$^7F_1$ transitions in the emission spectra of CLOF: xEu^{3+} phosphors. It is observed that, on increasing Eu^{3+} ions' concentration, the intensity of the corresponding transition increases systematically up to x = 0.08 (critical concentration). However, their asymmetric ratio (red to orange ratio) plotted as a function of Eu^{3+} ions' concentrations does not appreciably change (**Fig. 4.3(e)**). Because of the above reasons, the overall emission colour not change considerably with Eu^{3+} ions' concentrations. The colour chromaticity (CIE) coordinates of optimum CLOF: $0.08Eu^{3+}$ phosphor is represented in Fig. 4.3(f). Based on the report of Duke *et al.*, a compound with high symmetry has minimal distortion and can produce narrowband emission from Ce^{3+} or Eu^{2+} ions and vice versa by the suitable cationic substitutions **[34]**. In the CSLOF host, both the cationic sites are asymmetric in nature, therefore, more lattice distortion can be expected due to which broad emission can be predicted if the valance of europium ions could be changed from 3+ to 2+.

4.4.3 Photoluminescence of $Ca_{2-x}Sr_{2-x}La_6Si_6O_{24}F_2$: xEu^{2+} (CSLOF: xEu^{2+}) synthesized in reduction atmosphere

According to the Dorenbos predictions, the variation in covalency or polarizability always leads to the centroid shift in Eu polyhedra. Theoretically, the centroid shift is inversely proportional to cationic electronegativity **[35]**. The energy difference between

the lowest and the highest *5d* level is related to the symmetry and size of the Eu^{2+} coordination polyhedrons [36]. In the CLOF host, the Ca^{2+} ions are less electronegative than the La^{3+} ions based on Pauling electronegativity scale of periodic elements. Hence, the broad emission from Eu^{2+} polyhedrons situated at the Ca atomic sites can be preferably tuned to get the desired wavelength emission via the cationic substitution strategies. Therefore, we have synthesized $Ca_{3.96}La_6Si_6O_{24}F_2$: $0.04Eu^{2+}$ **(**CLOF: $0.04Eu^{2+}$) and $Ca_{1.98}Sr_{1.98}La_6Si_6O_{24}F_2$: $0.04Eu^{2+}$ **(**CSLOF: $0.04Eu^{2+}$) at the N_2-H_2 reduction atmosphere. **Fig. 4.4 (a)** and **(b)** represent the excitation and emission spectra of CLOF: $0.04Eu^{2+}$ and CSLOF: $0.04Eu^{2+}$ recorded at 520 nm and 340 nm, respectively. The asymmetric broadband excitation of CLOF: $0.04Eu^{2+}$ covering from 250 to 450 nm further deconvoluted into six Gaussian components located at 281 nm (P1; 4.40 eV), 293 nm (P2: 4.20 eV), 320 nm (P3: 3.89 eV), 340 nm (P4: 3.66 eV), 370 nm (P5: 3.35 eV) and 400 nm (P6: 3.10 eV). While the deconvoluted peak positions for CSLOF: $0.04Eu^{2+}$ phosphor is observed at 267 nm (P1: 4.64 eV), 290 nm (P2: 4.27 eV), 327 nm (P3: 3.79 eV), 350 nm (P4: 3.53 eV), 363 nm (P5: 3.42 eV) and 396 nm (P6: 3.13 eV), respectively. The peak P1 represents the CTB of the activator ion to a ligand of the host. The other peaks from P2 to P5 correspond to the *5d – 4f* electronic transitions of Eu^{2+} ions, which are generated because of the variation of crystallographic changes around the five degenerated *d* orbitals of Eu^{2+} ions. A possible schematic energy level diagram for the degenerated *5d* orbitals is also proposed in **Fig. 4.4(c)**. As seen from the PLE of CLOF: $0.04Eu^{2+}$ and CSLOF: $0.04Eu^{2+}$, after the introduction of the Sr^{2+} ions, the peak intensity of the CTB band (P1) is decreased and shifted towards the lower wavelength region (from 281 to 267 nm). The incorporation of Sr^{2+} ions might reduce Eu^{3+} ions in the lattice and hence reducing the excitation charge transfer energy and thus the CTB band (P1) intensity [37].

The incorporation of Sr^{2+} ions into the CLOF host lattice also results in lattice expansion, due to which Eu^{3+} ions might be easily reduced to Eu^{2+} ions preferably in the larger cationic sites. Huang et al. introduced a crystal chemistry approach to reduce Eu^{3+} to Eu^{2+} ions in the lattice by replacing appropriate ions with dopant like Si^{4+} ions and enlarge Ca^{2+} site which enable Eu^{3+} reduction [38]. The Eu^{2+} occupancy is expected to enhance in the nine-coordinated *4f* sites which substantially accelerate Eu^{3+} ions' occupation to the seven-coordinated *6h* sites. Thus, the average Eu-O bond length in the *4f* sites of CSLOF: $0.04Eu^{2+}$ will be higher than in CLOF: $0.04Eu^{3+}$, consequently the

CTB energy (P1) in CSLOF: 0.04Eu^{2+} blue shifted to 267 nm. Because of this reason, the CTB (P1) of Eu^{3+} ions in CSLOF: 0.04Eu^{2+} appeared at 267 nm [37]. The other five Eu^{2+} ions transition peaks are more dominant as well as the peak broadening is also observed owing to the incorporation of Sr^{2+} ions. After the incorporation of larger Sr^{2+} ions into the CLOF host, certain lattice expansion around the crystallographic sites of the activator ions might be taken place, which might reduce the strain on Eu^{2+} ions' occupancy. Such lattice modifications due to the introduction of Sr atoms are also confirmed through the XRD refinement data of CLOF and CSLOF, as indicated in the XRD analysis part.

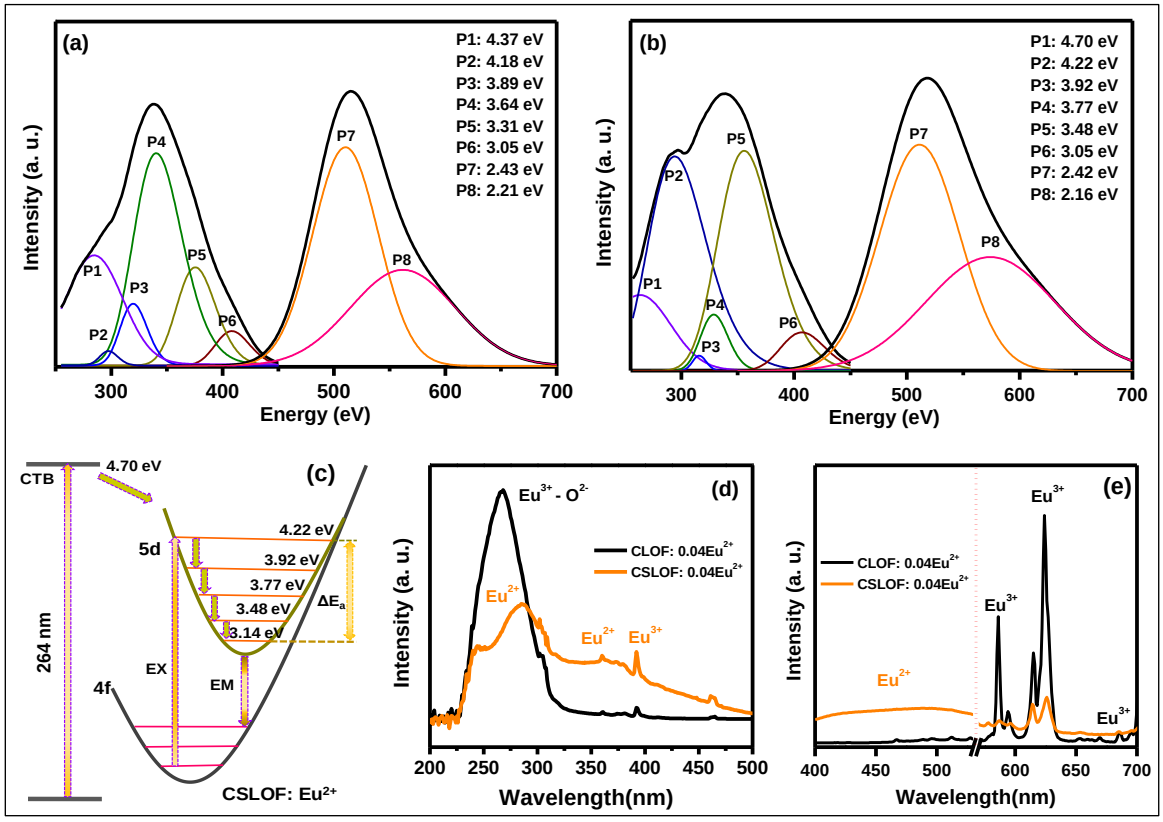

Fig. 4.4: *The deconvoluted excitation and emission spectra of (a) CLOF: 0.04Eu^{2+} and (b) CSLOF: 0.04Eu^{2+} synthesized in N_2-H_2 atmosphere and recorded at 520 nm and 340 nm, respectively. (c) Schematic energy level diagram for CSLOF: 0.04Eu^{2+}. Comparative (d) excitation and (e) emission spectra of CLOF: 0.04Eu^{2+} and CSLOF: 0.04Eu^{2+} recorded at 280 nm and 614 nm, respectively.*

To confirm the change in Eu valance from 3+ to 2+ due to the Sr^{2+} incorporation in CLOF, the comparative excitation and emission spectra of CLOF: $0.04Eu^{2+}$ and CSLOF: $0.04Eu^{2+}$ are also recorded at 614 nm emission of Eu^{3+}: $^5D_0$ - $^7F_2$ transition and 280 nm of O^{2-}-Eu^{3+} CTB excitation, as shown in Fig. 4.4(d) and **Fig. 4.4(e)**, respectively. On recording excitation at 614 nm, it is found that in CLOF: $0.04Eu^{2+}$ no dominant Eu^{2+} ions' 4f-5d transition peak appears rather than intense O^{2-}-Eu^{3+} CTB. After the incorporation of Sr^{2+} ions (CSLOF: $0.04Eu^{2+}$) the intensity of Eu^{3+} ions' CTB band decreases, and the asymmetric broadband of Eu^{2+} ions appears. Similar phenomena are also observed from the emission spectra recorded at 280 nm (**Fig. 4.4(e)**). It is observed that the emission spectra of CLOF: $0.04Eu^{2+}$ contain several sharp peaks of intra f-f Eu^{3+} ions only and broad emitting Eu^{2+} ions' peaks are not observed. However, in the CSLOF: $0.04Eu^{2+}$ system, Eu^{3+} ions' emission drastically decreased and the broad emission of Eu^{2+} ions increased. This is because the incorporation of Sr^{2+} ions results in increasing the structural defects and enhanced the lattice size, consequently, more Eu^{3+} ions are converted to Eu^{2+} ions. In addition, there is a slight change in the emission behaviour of Eu^{3+} ions in CSLOF: $0.04Eu^{2+}$ observed in the spectra as the red to orange ratio ($^5D_0$ - $^7F_2$ to $^5D_0$ - $^7F_1$) intensity is decreased effectively compared to that in CLOF: $0.04Eu^{2+}$. The enhanced occupation of Eu^{2+} ions in the 4f and 6h sites might reduce the number of Eu^{3+} ions in both the asymmetric sites.

The PL emission spectra of CLOF: $0.04Eu^{2+}$ and CSLOF: $0.04Eu^{2+}$ exhibit an intense green-emitting asymmetric band peaked at 520 nm covering the range of 450 nm to 600 nm due to the *5d-4f* electronic transitions of Eu^{2+} ions. The observed emission spectra are deconvoluted into two broad Gaussian bands peaked at 510 nm (P7: 2.43 eV) and 564 nm (P8: 2.21 eV) for CLOF: $0.04Eu^2$ (**Fig. 4.4(a)**), and at 512 nm (P7: 2.42 eV) and 580 nm (P8: 2.16 eV) for CSLOF: $0.04Eu^{2+}$ (**Fig. 4.4(b)**). This asymmetric behaviour of the emission band indicates multiple crystallographic site occupancy of Eu^{2+} ions. Based on the empirical formula proposed by Van Uitert, the Eu^{2+} ions' occupancy on both the cationic sites can be explained via the equation,

$$E(cm^{-1}) = Q[1 - (V/4)^{\frac{1}{V}} \times 10^{-\left(\frac{nE_ar}{80}\right)}] \qquad (4.1)$$

where E is the emission band of Eu^{2+} ion, Q is the lower d-band position for free Eu^{2+} ion (Q = 34000 cm^{-1}), V represents the Eu^{2+} valence (V = 2), r is the cationic radius substituted by Eu^{2+} ion, E_a is the electron affinity and n represents the coordination number of Eu^{2+} ion occupied site [39]. Accordingly, E directly depends on the coordination number of the cationic sites in the particular host lattice. Conferring to this formula, lower wavelength emission corresponds to the sites with high coordination numbers and vice versa. Consequently, in the emission spectra of CLOF: $0.04Eu^{2+}$ and CSLOF: $0.04Eu^{2+}$, the peak P7 represents the $4f^6 5d^1$-$4f^7$ transition of Eu^{2+} ions located in the nine coordinated *4f* sites. Whereas, P8 represents emission from Eu^{2+} ions occupied in the seven coordinated *6h* sites. Comparing both the Eu^{2+} ions' occupied polyhedrons $[M\text{-}O_6F]_{6h}$ and $[M\text{-}O_9]_{4f}$, Eu^{2+} ions in the *6h* sites are surrounded by more non-equivalent anionic atoms than Eu^{2+} ions occupied in the *4f* sites. Because of this reason, Eu^{2+} ions in the *6h* sites might experience higher crystal field splitting than Eu^{2+} ions situated in the *4f* sites. Because of larger splitting, Eu^{2+} ions occupied in the *6h* sites exhibited higher wavelength emission (P8) than Eu^{2+} ions located in the *4f* sites **[40]**.

It can be predicted that the transitions from Eu^{2+} ions are observed in both the cationic sites and among them P7 has a higher intensity than P8 which means that more number of Eu^{2+} ions are preferably occupied by bigger *4f* sites. Compare to CLOF: $0.04Eu^{2+}$, the emission spectra of CSLOF: $0.04Eu^{2+}$ slightly red-shifted. Additionally, a broadening of the emission peak is also observed after the introduction of Sr^{2+} ions. The XRD analysis indicated that by the introduction of Sr^{2+} ions in CLOF: Eu^{3+}, the average metal-oxygen length in *4f* and *6h* coordination is changed (from CLOF: Eu^{3+}; 2.629 Å to CSLOF: Eu^{2+}; 2.668 Å and from CLOF: Eu^{3+}; 2.547 Å to CSLOF: Eu^{2+}; 2.560 Å, respectively). Such bond length distortion reduces the strain in the lattice and more trivalent Eu ions are changed to their divalent analogue and the peak broadening is observed. Eventually, the increment in the FWHM value due to the presence of Sr^{2+} ions also illustrates the enhancement of Eu^{2+} ions' occupancy in both the cationic sites.

Fig. 4.5 (a) describes the excitation and emission spectra of a series of CSLOF: xEu^{2+} phosphors recorded in the range of 520 – 562 nm and 322 – 340 nm, respectively. As the Eu^{2+} ions' doping concentration increases, the peak intensity also increases and reaches the maximum at x = 0.04, above which quenching of emission intensity is

observed. The concentration quenching behaviour of Eu^{2+} ions is studied by evaluating the critical distance (R_C) based on the Blasse equation reported elsewhere [41]:

$$R_c \approx 2\left[\frac{3V}{4\pi X_C N}\right]^{1/3} \qquad (4.2)$$

where V is the volume of the unit cell (582.65 $Å^3$), N is the number of molecules per unit cell (2) and X_C is the critical concentration of Eu^{2+} ion (0.04) for CSLOF: $0.04Eu^{2+}$ phosphor. The critical distance is found to be 24.05 Å. The R_c value is greater than 5 Å indicating that the exchange interaction is not dominant in Eu^{2+} ions in the CSLOF host.

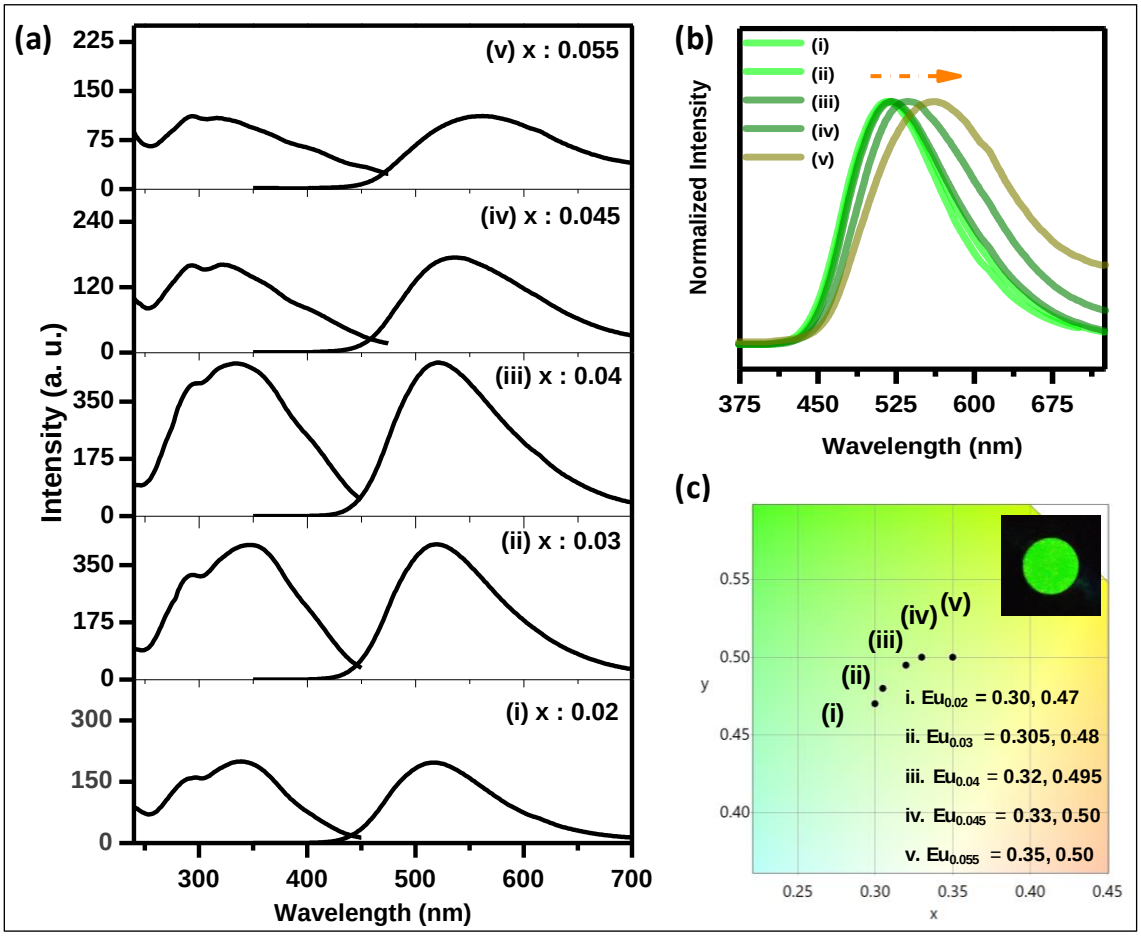

Fig. 4.5: (a) *The excitation and emission spectra of CSLOF: xEu^{2+} (x = 0.02, 0.03, 0.04, 0.045, 0.055) phosphors recorded in the range of 520 – 562 nm and 322 – 340 nm, respectively.* ***(b)*** *Red-shift in emission spectra as a function of increasing Eu^{2+} ions' concentration.* ***(c)*** *CIE diagram and colour coordinates for the corresponding emission spectra of CSLOF: xEu^{2+} phosphors along with the luminescence photograph of the optimum CSLOF: $0.04Eu^{2+}$ phosphor.*

The emission spectra CSLOF: xEu^{2+} consist of asymmetric broadband ranging from 450 nm to 650 nm arising due to the $4f^6 5d^1$ - $4f^7$ electronic transitions of Eu^{2+} ions. The reason for an asymmetric band is due to the difference in the occupation of Eu^{2+} ions on the multiple crystallographic sites of the host. In addition to the intensity variation, the red-shift of the emission band is also observed during the increment in Eu^{2+} ions' concentration, as shown in **Fig. 4.5 (b)**. The substitution of Eu^{2+} ions at the smaller cationic sites of CSLOF: $0.04Eu^{2+}$causes higher relaxation of equilibrium distance of the excited states of Eu^{2+} ions and results in the emission Stokes shift [42, 43]. **Fig. 4.5 (c)** describes the CIE diagram and calculated colour coordinates for the emission spectra of CSLOF: xEu^{2+} phosphors along with the luminescence photograph of the optimum CSLOF: $0.04Eu^{2+}$ phosphor. There is a gradual emission shift from greenish (0.30, 0.47) to yellowish-green (0.35, 0.50) with the increase in Eu^{2+} ions' concentration.

4.4.4 Photoluminescence of $Ca_{1.98-y}Sr_{1.98-y}La_6Si_6O_{24}F_2$: $0.04Eu^{2+}$, yMg^{2+} (CSLOF: Eu^{2+}, yMg) and $Ca_{1.98-z}Sr_{1.98-z}La_6Si_6O_{24}F_2$: $0.04Eu^{2+}$, zBa^{2+} (CSLOF: Eu^{2+}, zBa) synthesized in N_2-H_2 atmosphere.

According to the structural and optical outcomes of europium ions' doped CSLOF systems, a controlled operation of the Eu^{2+} ionic distributions in the multiple cationic sites can result in flexible colour output from the presently adopted compositionally tuned single-phased system. Eventually, a compositionally tuned white emitting system can also be achieved via modifying the CSLOF: Eu^{2+} system. With such an aim, the emission property of CSLOF: $0.04Eu^{2+}$ phosphor has been further tuned by altering the distortion of metal-anion polyhedrons with the suitable cationic substitution strategy. To the optimum CSLOF: $0.04Eu^{2+}$ green-emitting composition, smaller Mg^{2+} ions' substitution for relatively larger Sr^{2+} and Ca^{2+} ions are focused initially.

Fig. 4.6(a) represents the excitation and emission spectra of a series of CSLOF: $0.04Eu^{2+}$; yMg^{2+} (y = 0.0 to 1.0) phosphors recorded in the range of 480–505 nm and 330–340 nm, respectively. The intensity of the emission peak gradually increases (**Fig. 4.6(a)**) and the emission band becomes narrower with the increase of Mg^{2+} ions' concentration, as visible in **Fig. 4.6(b).** Smaller-sized Mg^{2+} ions prefer to occupy the *6h* sites. In order to minimize the distortion, more Eu^{2+} ions are then substituted at the *4f* sites, which results in narrower emission. Moreover, a blue-shift in the emission peak from 520 nm to 481 nm is also noted, as visible in **Fig. 4.6(c).** This is again attributed to

the preferential occupation of more Eu^{2+} ions in the nine-coordinated *4f* sites, since the larger coordination gives lower wavelength emission. The CIE diagram and the colour coordinates of the corresponding emission spectra along with the luminescence photograph of the CSLOF: $0.04Eu^{2+}$; yMg^{2+} phosphors are shown in **Fig. 4.6(d).** Clearly, the emission blue-shift from the greenish (0.27, 0.44) to cyan-blue (0.18, 0.25) region with the increase of Mg^{2+} ion concentration from y = 0.0 to 1.0 can be realized via the digital images.

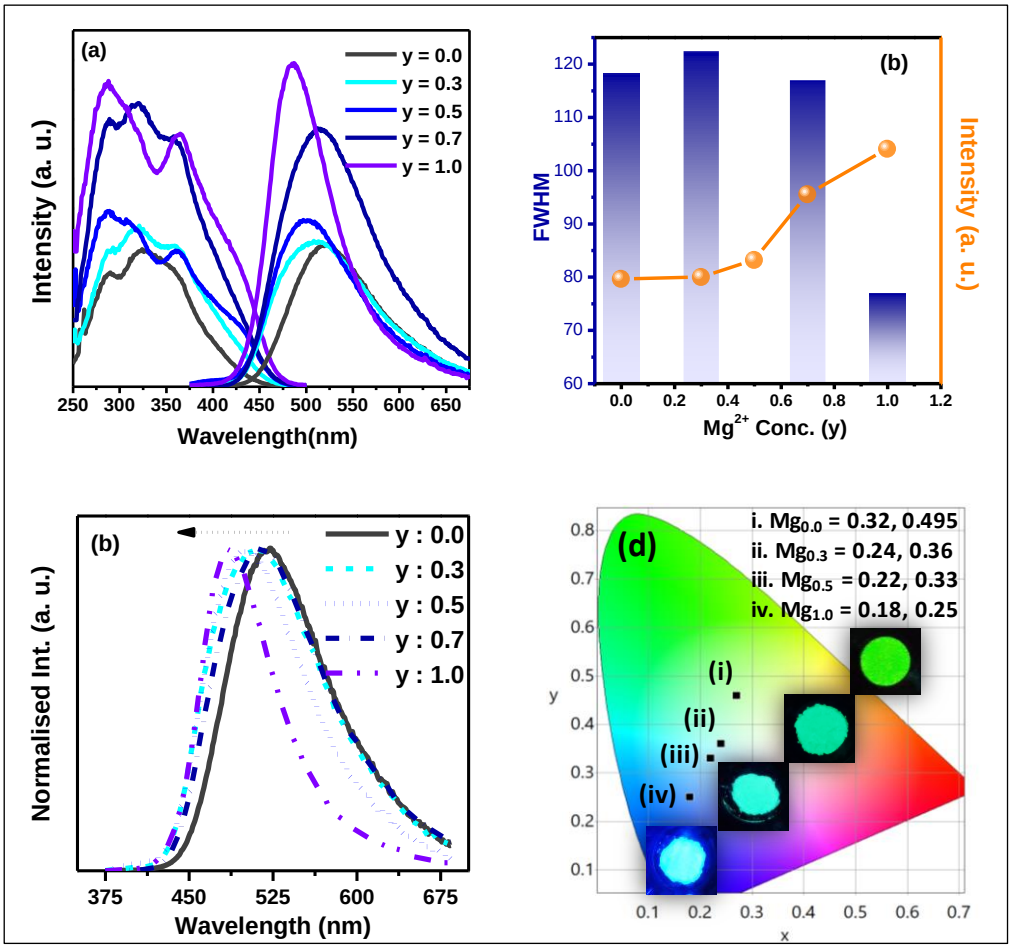

Fig. 4.6: (a) *The excitation and emission spectra of CSLOF: $0.04Eu^{2+}$; yMg^{2+} phosphors recorded in the range of 480 - 505 nm and 330 - 340 nm, respectively.* ***(b)*** *The variations in intensity and FWHM of the emission spectra with the increase in Mg^{2+} ion concentration.* ***(c)*** *Blue-shift in emission spectra as a function of increasing Mg^{2+} ions' concentration.* ***(d)*** *CIE diagram for the corresponding emission spectra of CSLOF: $0.04Eu^{2+}$, yMg^{2+} phosphors along with the corresponding luminescence photographs.*

The PL results of CSLOF: Eu^{2+} are further probed via synthesizing a series of CSLOF: $0.04Eu^{2+}$; zBa^{2+}. **Fig. 4.7(a)** represents the excitation and emission spectra of CSLOF: $0.04Eu^{2+}$; zBa^{2+} (z = 0.0 to 2.0) phosphors recorded in the range of 520 - 540 nm and 360 nm, respectively. With increasing Ba^{2+} ions' concentration, the emission intensity as well as broadening of emission peak gradually increases and reaches a maximum at z = 1.2, and after that, the luminescence quenching occurred. Initially, larger Ba^{2+} ions occupied both the available cationic sites. This might have enhanced the polyhedrons' size which then efficiently accommodated Eu^{2+} ions. The significant enhancement of FWHM indicates the possibility of generating broader emissions covering the entire visible spectra. The emission intensity variation and FWHM changes are also shown in **Fig. 4.7(b).** It is also observed that on increasing Ba^{2+} ions' concentration, a red-shift in emission spectra from the greenish (520 nm) to yellowish-green (540 nm) region is observed (**Fig. 4.7(c)).** The chromaticity diagram and the colour coordinates along with the luminescence photographs of the corresponding emission spectra of CSLOF: $0.04Eu^{2+}$; zBa^{2+} phosphors are shown in Fig. 4.7(d). A slight red-shift has been noted from greenish (0.29, 0.45) to greenish-yellow (0.31, 0.45) with the increase of Ba^{2+} ions' concentration.

The overall energy splitting mechanism in Mg^{2+} or Ba^{2+} codoped $Ca_{1.98}Sr_{1.98}La_6Si_6O_{24}F_2$: $0.04Eu^{2+}$ phosphors is illustrated in **Fig. 4.7(e).** As illustrated in Fig. 4.7(e), the 5d energy band of the activated Eu^{2+} ions are influenced by the cationic substitutions in the host lattice, which consequence in the crystal field splitting (ε_{cfs}) and centroid shift (ε_c). Due to the substitution of smaller Mg^{2+} ions for larger Ca^{2+}/Sr^{2+} ions at *6h* sites, the [M1-O_6F] polyhedrons might be contracted due to the preferable substitution of smaller-sized Mg^{2+} ions to the *6h* sites. Subsequently, [M2-O_9] polyhedrons could be expanded. Because of this reason, Eu^{2+} ions situated at the *4f* sites might experience lesser ε_{cfs} in CSLOF: $0.04Eu^{2+}$; Mg^{2+} rather than in CSLOF: $0.04Eu^{2+}$, which led to a blue-shift in the emission peak from 520 nm to 481 nm. As compared with the XRD refinement data of CSLOF: $0.04Eu^{2+}$, the cell volume enhanced from 582.65 [$Å^3$] to 590.42 [$Å^3$] for CSLOF: $0.04Eu^{2+}$; $1.2Ba^{2+}$ might be caused by the replacement of Ba^{2+} ions with Eu^{2+} ions [44]. When less electronegative and larger Ba^{2+} ions are introduced in the cationic sites of CSLOF: $0.04Eu^{2+}$, it causes an enhancement in the lattice size and also increased the centroid shift (ε_c) of the *5d* orbital of Eu^{2+} ions. This

reduces the energy gap between *5d - 4f* electronic transition of Eu^{2+} ions and results in a higher wavelength emission [45, 46].

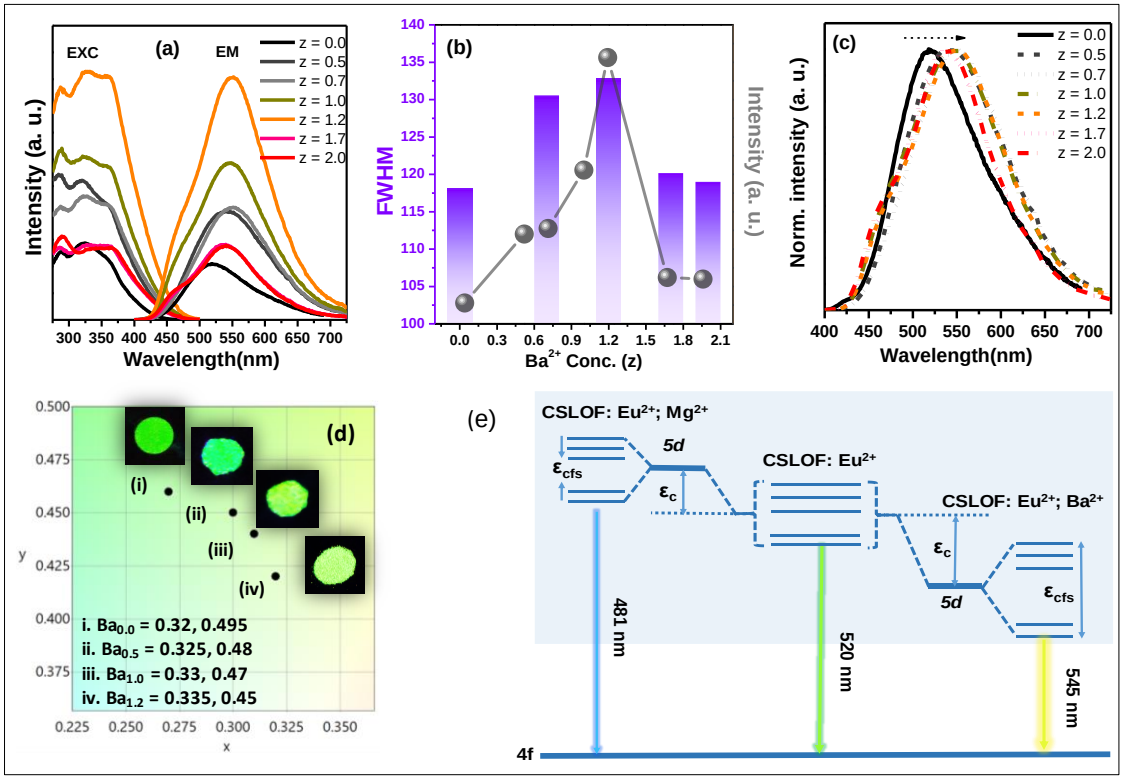

Fig. 4.7: (a) *The excitation and emission spectra of CSLOF: 0.04Eu^{2+}, zBa^{2+} (z = 0, 0.5, 1.0, and 1.2) phosphors recorded in the range of 520 - 540 nm and 360 nm, respectively.* ***(b)*** *Variation in the intensity and FWHM of the emission spectra with the increase in Ba^{2+} ions' concentration.* ***(c)*** *Red-shift in the emission spectra as a function of increasing Ba^{2+} ions' concentration.* ***(d)*** *CIE diagram and colour coordinates for the corresponding emission spectra of CSLOF: 0.04Eu^{2+}; zBa^{2+} (z = 0, 0.5, 1.0, and 1.2) phosphors along with the luminescence photographs of the phosphors;* ***(e)*** *Overall energy splitting diagram of Mg^{2+} or Ba^{2+}-codoped $Ca_{1.98}Sr_{1.98}La_6Si_6O_{24}F_2$: 0.04$Eu^{2+}$ phosphors.*

Since the ionic radius of Ba^{2+} ion is larger than Ca^{2+}/Sr^{2+} ion, the cationic replacement of Ca^{2+}/Sr^{2+} by Ba^{2+} in $Ca_{1.98}Sr_{1.98}La_6Si_6O_{24}F_2$: 0.04$Eu^{2+}$ should enhance the lattice size of $Ca_{1.98}Sr_{1.98}La_6Si_6O_{24}F_2$: 0.04$Eu^{2+}$. For validation, the Rietveld refinement has also been carried out for the XRD pattern of CSLOF: 0.04Eu^{2+}; 1.2Ba^{2+} using a similar structure used for the Ca^{2+}/Sr^{2+} analogue, as shown in **Fig. 4.8(a)**. Compared to

CSLOF: $0.04Eu^{2+}$, the lattice parameters as well as the lattice volume of CSLOF: $0.04Eu^{2+}$; $1.2Ba^{2+}$ are slightly enhanced (**Table S1**). The lattice expansion can also be verified from higher [M-O] bond length values at different sites of CSLOF: $0.04Eu^{2+}$; $1.2Ba^{2+}$ compare to the [M-O] bond lengths of CSLOF: $0.04Eu^{2+}$, as shown in the inset of **Fig. 4.8(a).** Such lattice expansion may allow more Eu^{2+} ions to be occupied in the lattice sites of CSLOF: $0.04Eu^{2+}$; $1.2Ba^{2+}$. Keeping the structural results of CSLOF: $0.04Eu^{2+}$; $1.2Ba^{2+}$ in view, the Eu^{2+} ions' concentration of optimum $Ca_{1.38}Sr_{1.38}La_6Si_6O_{24}F_2$: $0.04Eu^{2+}$, $1.2Ba^{2+}$ phosphor has been further enhanced from 0.04 to 0.3. **Fig. 4.8(b)** represents the XRD patterns of a series of $Ca_{1.38-n}Sr_{1.38-n}La_6Si_6O_{24}F_2$: nEu^{2+},$1.2Ba^{2+}$ (n = 0.04 to 0.3) phosphors. The basic crystal structure has not been altered due to the increasing Eu^{2+} ions' concentrations. However, the successful adaptation of Eu^{2+} ions (higher than n = 0.04) can be confirmed in the magnified XRD patterns where the main diffraction peaks continuously shift toward higher 2θ with increasing n value from 0.04 to 0.3 (**Fig. 4.8(b)**).

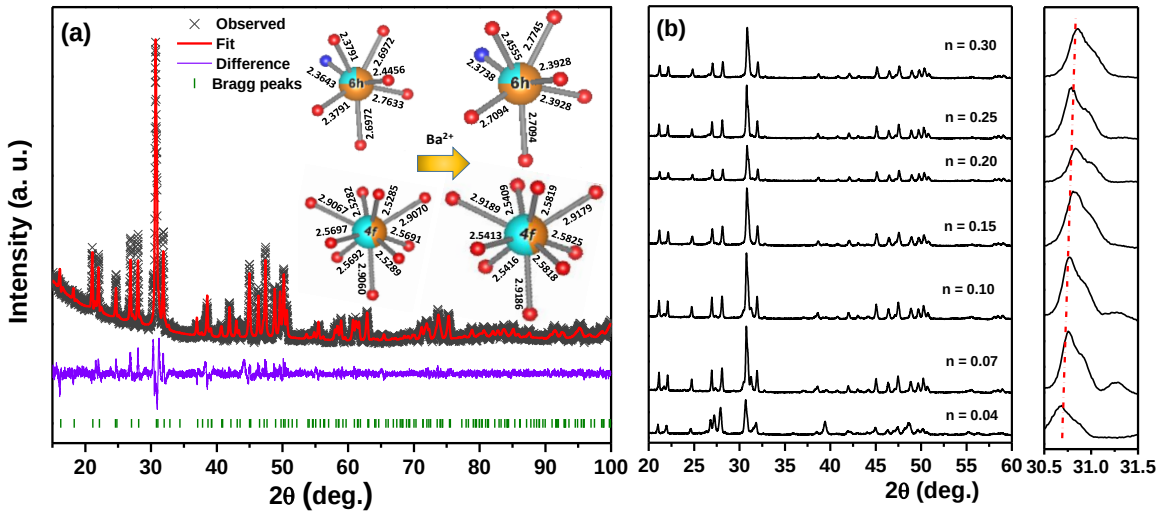

Fig. 4.8: (a) *Rietveld refinement of CSLOF: $0.04Eu^{2+}$, $1.2Ba^{2+}$. Inset: Schematic representation of average metal - oxygen bond length variation in CSLOF: $0.04Eu^{2+}$, zBa^{2+} (z = 0 and 1.2).* ***(b)*** *XRD patterns of a series of CSLOF: nEu^{2+},$1.2\ Ba^{2+}$ (n = 0.04 to 0.3).*

Fig. 4.9(a) represents the photoluminescence of a series of $Ca_{1.38-n}Sr_{1.38-n}La_6Si_6O_{24}F_2$: nEu^{2+},$1.2Ba^{2+}$ (n = 0.04 to 0.3) phosphors recorded at 360 nm. On increasing Eu^{2+} ions' concentration, the emission intensity increases initially and reaches a maximum at n = 0.07, above which luminescence quenching is observed. Based on the

Blasse's equation [41], the critical distance is calculated to be 20.01 Å for CSLOF: 0.07Eu^{2+},1.2Ba^{2+}. Eventually, a slight emission red-shift is also observed from 540 nm to 545 nm at higher Eu^{2+} concentrations, as shown in **Fig. 4.9(a)**. The ionic radius of Eu^{2+} ion is smaller than that of Ba^{2+} ion, which might increase lattice covalency, and hence longer wavelength emission has been observed [46, 47]. The overall colour tuning from greenish-yellow (0.30, 0.49) to yellowish region (0.34, 0.45) can be realized from the colour chromaticity diagram, and from the corresponding luminescence photographs, as shown in **Fig. 4.9(c). Fig. 4.9(d)** represents the comparative emission spectra of commercial $Y_3Al_5O_{12}$: Ce^{3+} with $Ca_{1.38-n}Sr_{1.38-n}La_6Si_6O_{24}F_2$: n$Eu^{2+}$,1.2$Ba^{2+}$ (n = 0.07, 0.15) phosphors recorded at 460 nm and 360 nm, respectively. Not only the emission intensity but the emission FWHM of the optimized phosphors are found to be comparable with those of the commercial phosphor.

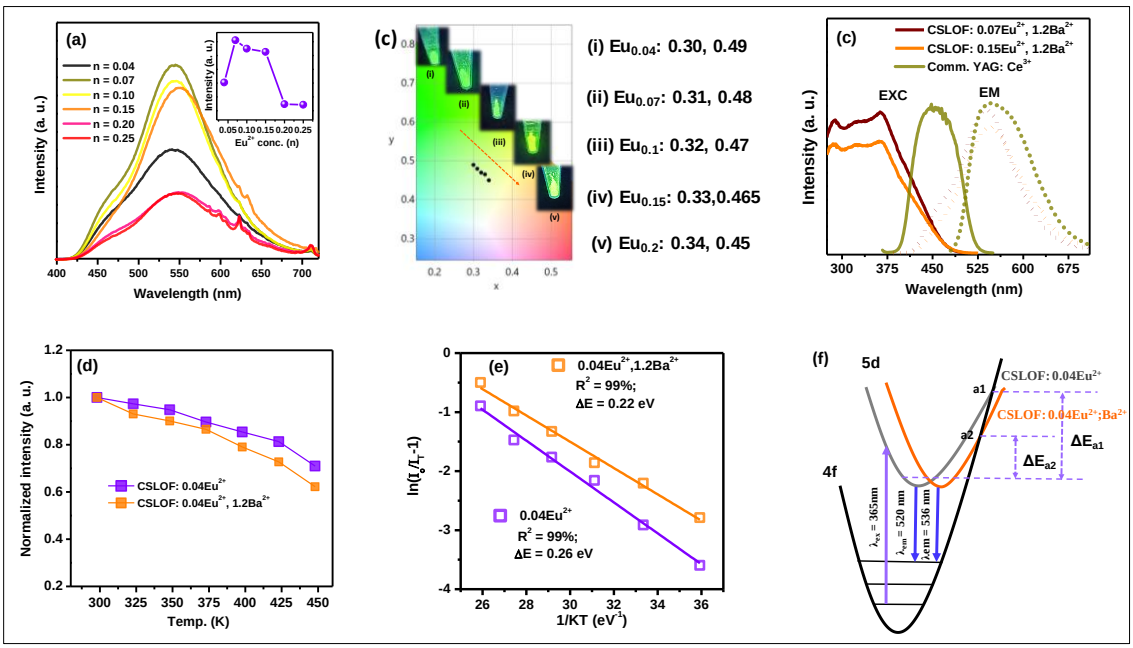

Fig. 4.9 (a) *The emission spectra of CSLOF: nEu^{2+}; 1.2Ba^{2+} (n = 0.04 to 0.25) phosphors recorded at 360 nm.* ***(b)*** *CIE diagram and colour coordinates for the corresponding emission spectra of CSLOF: nEu^{2+}; 1.2Ba^{2+} along with the luminescence photographs of the phosphors.* ***(c)*** *The comparative excitation and emission spectra of commercial $Y_3Al_5O_{12}$: Ce^{3+} and with CSLOF: nEu^{2+};1.2Ba^{2+} (n = 0.07, 0.15).* ***(d)*** *Temperature dependant PL intensity variation of CSLOF: 0.04Eu^{2+}, zBa^{2+} (z = 0 and 1.2) phosphors recorded at 360 nm.* ***(e)*** *Arrhenius fitting of CSLOF: 0.04Eu^{2+}, zBa^{2+} (z = 0 and 1.2) phosphors.* ***(f)*** *The energy level diagram illustrates the relation between non-radiative relaxation process and wavelength shift.*

The temperature dependant PL intensity variation of CSLOF: $0.04Eu^{2+}$, zBa^{2+} (z = 0 and 1.2) phosphors as a function of temperature from 300 to 450 K recorded at 360 nm excitation is shown in **Fig. 4.9(e)**. As the temperature increases, the PL emission intensity decreases gradually due to the relaxation of non-radiative transitions leading to the emission quenching of Eu^{2+} ions' transitions [47]. At 423 K, the PL emission intensity of CSLOF: $0.04Eu^{2+}$ retained almost 81% of its initial intensity, showing the high thermal stability of the phosphor suitable for the WLED applications. While the PL emission intensity of CSLOF: $0.04Eu^{2+}$, $1.2Ba^{2+}$ reduced to 72% of the room temperature emission intensity. The thermal stability of the phosphor can be described by the Arrhenius equation,

$$I_T = \frac{I_0}{1+c\exp\left(-\frac{\Delta E}{kT}\right)} \qquad (4.3)$$

where I_0 and I_T is the initial emission intensity and emission intensity at various temperatures, c is a constant for a certain host, ΔE is the activation energy, k is the Boltzmann's constant (8.62×10^{-5} eV K^{-1}), and T is the temperature in K [48]. The inset of Fig. 4.9(e) shows the plots between In [(I_0 / I_T) -1] vs [1000/T] and the slopes of the corresponding lines give the activation energy (ΔE). The activation energy of CSLOF: $0.04Eu^{2+}$ is found to be 0.26 eV, which supports the high thermal stability of this composition [49]. While the activation energy of CSLOF: $0.04Eu^{2+}$, $1.2Ba^{2+}$ phosphor is observed to be reduced to 0.22 eV. **Fig. 4.9(f)** shows the energy level diagram of CSLOF: $0.04Eu^{2+}$, zBa^{2+} (z = 0 and 1.2). In this figure, the cross-over points of the ground state and the excited state are denoted by a1 and a2 for CSLOF: $0.04Eu^{2+}$, zBa^{2+} (z = 0 and 1.2) phosphors, respectively. The activation energy is the energy difference between the CRP and the lowest excited state as indicated in **Fig. 4.9(f).** As temperature increases, electrons are stimulated from the lowest excited level to the highest excited level (engaged with the CRP) because of the phonon energy and return back to the ground state through non-radiative emission [50]. This phenomenon reduces the emission intensity of Eu^{2+} ions at higher temperatures. Eventually, Ba^{2+} ions' introduction to CSLOF: $0.04Eu^{2+}$ caused a centroid shift followed by the emission red-shift. This lowers the ground and excited state CRP from a1 (CSLOF: $0.04Eu^{2+}$) to a2 (CSLOF: $0.04Eu^{2+}$, $1.2Ba^{2+}$) [51]. Consequently, the energy difference between the highest excited state and the lowest excited state reduces owing to which non-radiative relaxation takes place more rapidly in the case of CSLOF: $0.04Eu^{2+}$, $1.2Ba^{2+}$ than CSLOF: $0.04Eu^{2+}$. Due to this reason, the

activation energy is observed to be reduced from ΔE_{a1} = 0.26 eV (CSLOF: 0.04Eu^{2+}) to ΔE_{a2} = 0.22 eV (CSLOF: 0.04Eu^{2+}, 1.2Ba^{2+}). However, no wavelength shift is observed upon increasing the temperature, which indicates that there is no predominant colour loss happening for phosphors owing to the enhancement in temperatures. The relation between the Stokes shift and the non-radiative relaxation process is described in the energy level diagram as shown in **Fig. 4.9(f).**

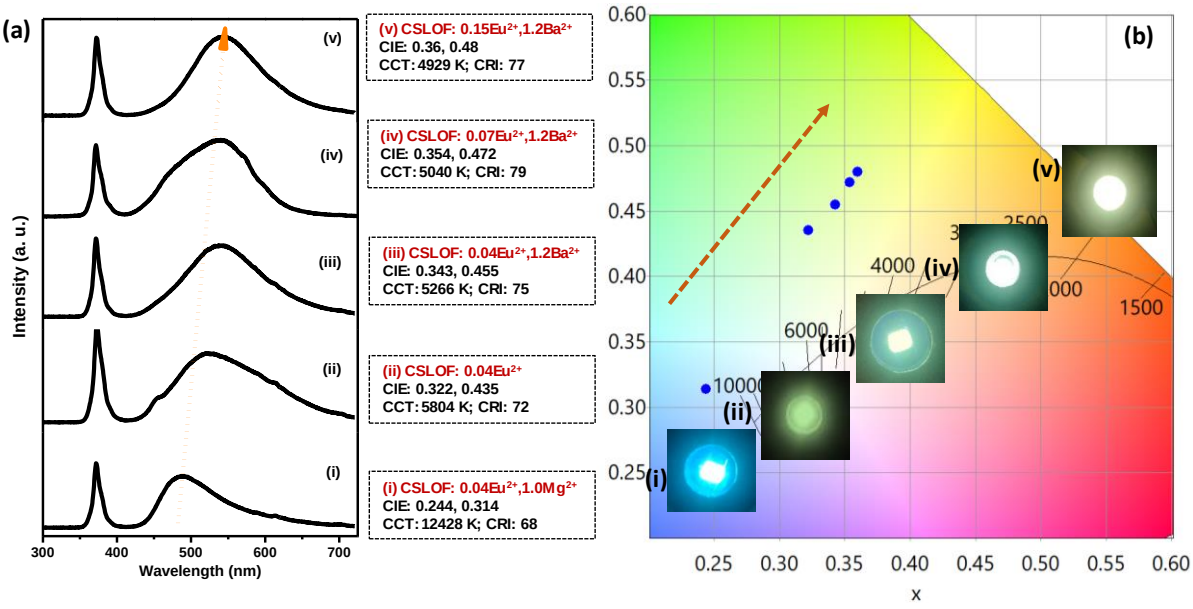

Fig. 4.10: (a) *The electroluminescent spectra of (i) CSLOF: 0.04Eu^{2+}, 1.0Mg^{2+}, (ii) CSLOF: 0.04Eu^{2+}, (iii) CSLOF: 0.04Eu^{2+}, 1.2Ba^{2+}, (iv) CSLOF: 0.07Eu^{2+}, 1.2Ba^{2+}, and (v) CSLOF: 0.15Eu^{2+}, 1.2Ba^{2+} recorded with a 370 nm n-UV LED chip.* ***(b)*** *The corresponding chromaticity diagram, colour coordinates and the digital images of the obtained pc-LEDs are also illustrated.*

To understand the practical performance of the optimized yellow, green, and blue emitting phosphors, these phosphors are deposited on to a 370 nm n-UV LED chip. **Fig. 4.10(a):** (i to v) to **Fig. 4.10(b)**: (i to v) represent the electroluminescent (EL) spectra and CIE diagram of cyan-blue emitting CSLOF: 0.04Eu^{2+}, 1.0Mg^{2+}, green emitting CSLOF: 0.04Eu^{2+}, zBa^{2+} (z = 0 and 1.2) and yellow emitting CSLOF: nEu^{2+}, 1.2Ba^{2+} (n = 0.07 and 0.15) phosphors, respectively. The estimated colour coordinates, CCT, and CRI values are also mentioned in the insets of **Fig. 4.10(a).** The 370 nm n-UV converted EL spectrum of the cyan-blue emitting CSLOF: 0.04Eu^{2+}, 1.0Mg^{2+} is having the CCT of

12428 K and CRI of 68 (**Fig. 4.10(a):** (i)). However, the combination of 370 nm n-UV LED chip and CSLOF: $0.04Eu^{2+}$ phosphor exhibits a green band maximum at 520 nm with the CCT of 5804 K and CRI of 72 (**Fig. 10(a)**: **(ii)).** The cationic substitution strategy via the smaller sized Mg^{2+} ions in CSLOF: $0.04Eu^{2+}$ phosphor considerably tuned the colour chromaticity from greenish (0.322, 0.435) to the cyan-blue region (0.244, 0.314), as shown in **Fig. 10(a & b): (i to ii).** Whereas, CSLOF: $0.04Eu^{2+}$, $1.2Ba^{2+}$ resulted in a red-shifted EL spectrum from green (0.322, 0.435) to greenish-yellow (0.343, 0.455). The corresponding CCT and CRI of CSLOF: $0.04Eu^{2+}$, $1.2Ba^{2+}$ are observed to be 5266 K and 75, respectively (**Fig. 10(a & b): (iii)).** Eventually, the EL spectral emission of CSLOF: $0.04Eu^{2+}$, $1.2Ba^{2+}$ has been further tuned via enhancing the Eu^{2+} concentrations. The observed CCT and CRI values for CSLOF: nEu^{2+}, $1.2Ba^{2+}$ (n = 0.07, 0.15) are observed to be (5040 K, 79) and (4929 K, 77), respectively. Whereas the chromaticity coordinates are also shifted from greenish yellow (0.343, 0.455) to yellow region (0.36, 0.48) due to the increase in Eu^{2+} concentrations from 0.04 to 0.15 in CSLOF: nEu^{2+}, $1.2Ba^{2+}$ (n = 0.04, 0.07, 0.15), as shown in **Fig. 10(a & b):** (iii) to (v). The inset of Fig. 4.10(b): (i) to (v) show the photographs of the 370 nm LED packages using cyan-blue emitting CSLOF: $0.04Eu^{2+}$, $1.0Mg^{2+}$, green emitting CSLOF: $0.04Eu^{2+}$, zBa^{2+} (z = 0 and 1.2) and yellow emitting CSLOF: nEu^{2+}, $1.2Ba^{2+}$ (n = 0.07 and 0.15) phosphors, respectively, under a forward bias current of 350 mA.

A WLED has also been fabricated via depositing CSLOF: $0.15Eu^{2+}$, $1.2Ba^{2+}$ phosphor on a 410 nm violet-LED chip, and the corresponding EL spectrum is illustrated in **Fig. 4.11(a).** Herein, the driving current that is having a substantial effect on the EL performance of the phosphor based WLEDs, has been varied. At 50 mA of current, this combination emits white light having a CCT of 5319 K and a CRI of 66. Eventually, the CIE coordinates are observed to be (0.342, 0.425), as shown in **Fig. 4.11(b).** Clearly, the broad emission of CSLOF: $0.15Eu^{2+}$, $1.2Ba^{2+}$ phosphor substantially increased along the sharper LED emission at 410 nm with the increase in driven current. Meanwhile, no emission saturation has been seen in the yellow phosphor might be due to the presence of a high concentration of Eu^{2+} luminescent centers. With the increase of current from 50 mA to 90 mA, the CCT and the CRI values are changed from 5319 K to 4689 K and 74 to 70, respectively. Most importantly, the CIE coordinates are also slightly tuned from (0.342, 0.425) to (0.324, 0.413), as can be seen in **Fig. 4.11(b).** The digital image of fabricated WLEDS indicates warm white light emission. The insets in **Fig.**

4.11(a) present the as appeared direct images of a prototype WLED and its illumination capacity. These results demonstrate that CSLOF: nEu^{2+}, $1.2Ba^{2+}$ (n = 0.07, 0.15) compositions are promising for the n-UV and violet-LED based pc-white-LEDs.

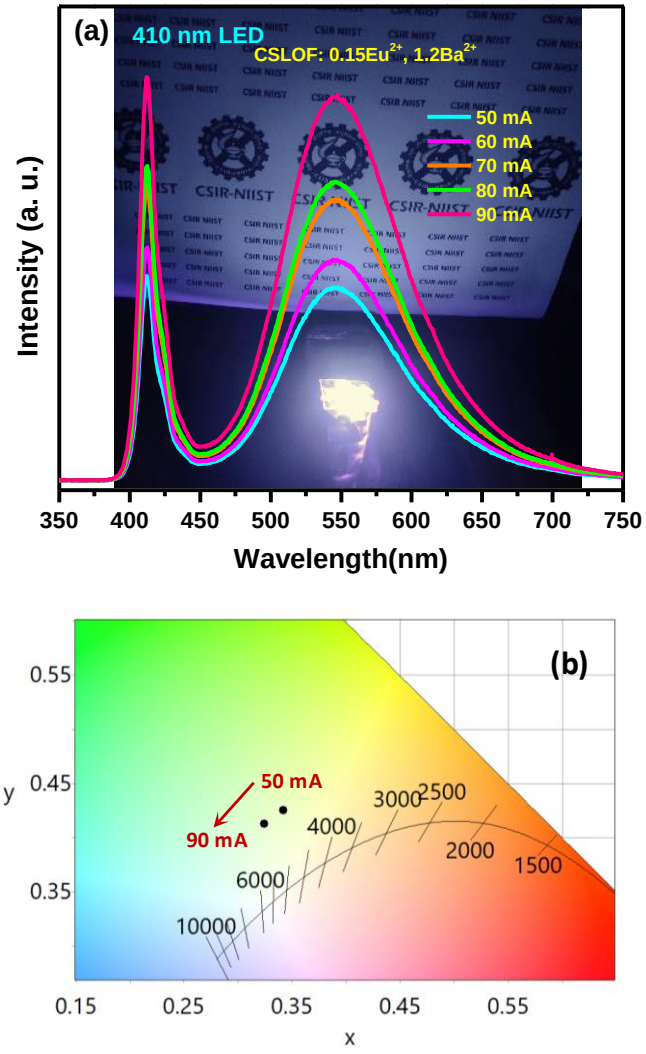

Fig. 4.11: (a) *The electroluminescent spectra and (b) the corresponding chromaticity diagram of CSLOF: $0.15Eu^{2+}$, $1.2Ba^{2+}$ recorded with a 410 nm violet-LED chip at different currents. Inset: the digital images of the obtained pc-LEDs operated at 90 mA.*

4.5. Conclusions

A sequence of M^{2+} (M = Mg/Ba) codoped $Ca_{1.98-x}Sr_{1.98-x}La_6Si_6O_{24}F_2$: $0.04Eu^{2+}$ phosphors were synthesised based on multiple cationic substitution strategies to achieve multicolour emission from a single composition. The detailed structural studies of $(Ca, Sr)_{3.96}La_6Si_6O_{24}F_2$: $0.04Eu^{2+}$ revealed that broadband green emission

could be tuned to either blue or yellow spectral region via the smaller or larger cationic substitutions. As per this thought, smaller Mg^{2+} ions and bigger Ba^{2+} ions were codoped in $(Ca, Sr)_{3.96}La_6Si_6O_{24}F_2$: $0.04Eu^{2+}$ to study the individual sequences. The incorporation of Mg^{2+} and Ba^{2+} ions showed blue-shift from 520 nm to 481 nm and red-shift from 520 nm to 545 nm, respectively, owing to the variation of the crystal field environment around the activator ions. The expanded lattice sites due to the Ba^{2+} codoping allowed more Eu^{2+} ions' to be accommodated in the expanded lattice sites. The resultant photoluminescence was further improved and red-shifted in emission because of the enrichment of more Eu^{2+} ions in the lattice. As compared with the commercial $Y_3Al_5O_{12}$: Ce^{3+}, the presently optimized phosphors showed comparable intensity with the commercial $Y_3Al_5O_{12}$: Ce^{3+}, and had exhibited enough thermal stability (70% at 150ºC to be used for WLEDs. The WLEDs fabricated using the optimized sample and commercial n-UV and violet LEDs showed remarkable CCT and CRI. The present research provided a promising hint for developing colour-tuneable apatite phosphors for the n-UV and violet LED-based single component WLEDs.

4.6. References

(1) Z. Xia, Z. Xu, M. Chen and Q. Liu, Recent developments in the new inorganic solid-state LED phosphors, Dalton Trans., 2016,45, 11214-11232.

(2) T. Hasegawa, M. Iwaki, R. Tanaka, S. W. Kim, S. Yin and K. Toda, Phase stabilization of red-emitting olivine-type NaMgPO4:Eu^{2+} phosphors via molten-phase quenching, Inorg. Chem. Front., 2020, 7, 4040-4051.

(3) M. Cao, J. Tian, W. Zhuang, R. Liu, Y. Liu, G. Chen, G. Zhou, L. Wang and J.Wang, Multisite Cation Regulation of Broadband Cyan-Emitting $(Ba_{1-x}Sr_x)_9Lu_2Si_6O_{24}/Eu^{2+}$Phosphors for Full-Spectrum WLEDs, Inorg. Chem., 2022, 61, 1805–1815.

(4) Y. Zhu, Y. Liang, S. Liu, H. Li, J. Chen and W. Lei, A strategy for realizing tunable luminescence and full-color emission in $Sr_3Gd_2(Si_3O_9)_2$:Eu phosphors by introducing dual functional Mn2+, Inorg. Chem. Front., 2018, 5, 2527-2539.

(5) N. W. Wang, Y. Kaihatsu, F. Iskandar and K. Okuyama, Highly Luminous Hollow Chloroapatite Phosphors Formed by a Template-Free Aerosol Route for Solid-State Lighting. Chem. Mater., 2009, 21, 4685–4691.

(6) Y. Liu, G. Liu, J. Wang, X. Dong and W. Yu, Single-Component and Warm-White-Emitting Phosphor Transfer , and Tunable Color, Inorg. Chem., 2014, 53, 11457–11466.

(7) A. De, B. Samanta, K. A. Dey, N. Chakraborty, K. T. Parya, S. Saha and K. U. Ghorai, $ZnAl_2O_4:Eu^{3+}$ Nanoparticle Phosphors Co-Doped with Li^+ for Red Light-Emitting Diodes, ACS Appl. Nano Mater., 2022, 5, 331–340.

(8) S. Hariyani, and J. Brgoch, Advancing Human-Centric LED Lighting Using $Na_2MgPO_4F : Eu^{2+}$, ACS Appl. Mater. Interfaces, 2021, 13, 16669–16676.

(9) C.Yan, X. Du, J. Li, X. Ding, Z. Li, and Y. Tang, Effect of Excitation Wavelength on Optical Performances of Quantum-Dot-Converted Light-Emitting Diode, Nanomaterials, 2019, 9 (8).

(10) P. Arunkumar, H. Y. Kim and Bin. W. Im, Versatile $Ca_4F_2Si_2O_7$ Host from Defect-Induced Host Emission to White-Light-Emitting Ce^{3+}-Doped $Ca_4F_2Si_2O_7$ Phosphor for Near-UV Solid-State Lighting, J. Phys. Chem. C, 2016, 120, 4495–4503.

(11) Dai, P.; Cao, J.; Zhang, X.; Liu, Y. Bright and High-Color-Rendering White Light-Emitting Diode Using Color-Tunable Oxychloride and Oxyfluoride Phosphors. J. Phys. Chem. C 2016, 120, 18713–18720.

(12) P. Ranjith, S. Sreevalsa, P. Patra, S. Som, A. Menon, K. Jayanthi, K. Annapurna, N. M. Anoop Krishnan, A. R. Allu and S. Das, Realizing cool and warm white-LEDs based on color controllable (Sr,Ba)2Al3O6F:Eu2+ phosphors obtained via a microwave-assisted diffusion method, Phys. Chem. Chem. Phys., 2021,23, 15245-15256.

(13) A. Arredondo, H. Desirena, I. Moreno and I. E. Hinostroza, Dual Color Tuning in Ce^{3+}-Doped Oxyfluoride Ceramic Phosphor Plate for White LED Application. J. Am. Ceram. Soc. 2019, 102, 1425–1434.

(14) W.B. Im, S. Brinkley, J. Hu, A. Mikhailovsky, P. S. Denbaars, R. Seshadri, $Sr_{2.975-x}Ba_xCe_{0.025}AlO_4F$: A Highly Efficient Green-Emitting Oxyfluoride Phosphor for Solid State White Lighting, Chem. Mater., 2010, 22, 2842–2849.

(15) Z. Ming, J. Qiao, S. M. Molokeev, J. Zhao, C. H. Swart, and Z. Xia, Multiple Substitution Strategies toward Tunable Luminescence in $Lu_2MgAl_4SiO_{12}:Eu^{2+}$ Phosphors, Inorg. Chem., 2020, 59, 1405–1413.

(16) M. Jiao, L. Dong, Q. Xu, L. Zhang, D. Wang and C.u Yang, The structures and luminescence properties of $Sr_4Gd_3Na_3(PO_4)_6F_2:Ce^{3+},Tb^{3+}$ green phosphors with zero-thermal quenching of Tb^{3+} for WLEDs, Dalton Trans., 2020, 49, 667-674.

(17) M. Kirm, E. Feldbach, H. Mägi, V. Nagirnyi, E. Tõldsepp, S. Vielhauer, T. Jüstel, T. Jansen, M. N. Khaidukov, and N. V. Makhov, Silicate Apatite Phosphors for Pc-LED Applications, Proc. Est. Acad. Sci., 2017, 66, 383.

(18) Z. Xia, S. M. Molokeev, Bin. W. Im, S. Unithrattil, and Q. Liu, Crystal Structure and Photoluminescence Evolution of $La_5(Si_{2+X}B_{1-x})(O_{13-X}N_x):Ce^{3+}$ Solid Solution Phosphors, J. Phys. Chem. C, 2015, 119, 9488–9495.

(19) K. Li, D. Geng, M. Shang, Y. Zhang, H. Lian, and J. Lin, Color-Tunable Luminescence and Energy Transfer Properties of $Ca_9Mg(PO_4)_6F_2:Eu^{2+}$, Mn^{2+} Phosphors for UV-LEDs, J. Phys. Chem. C 2014, 118, 11026−11034

(20) H. Njema, K. Boughzala, H. Boughzala and K. Bouzouita, Structural analysis by Rietveld refinement of calcium and lanthanum phosphosilicate apatites, J. Rare Earths, 2013, 31, 897–904.

(21) H. Njema, M. Debbichi, K. Boughzala, M. Said and K. Bouzouita, Structural, electronic and thermodynamic properties of britholites $Ca_{10-x}La_x(PO_4)_{6-x}(SiO_4)_xF_2$ ($0 \leq x \leq 6$): Experiment and theoryMater. Res. Bul*l.*, 2014, 51, 210–216.

(22) Q. Guo, L. Liao and Z. Xia, Luminescence properties and energy transfer in $La_6Ba_4(SiO_4)_6F_2:Ce^{3+},Tb^{3+}$ phosphors, *J. Lumin.*, 2014, 145, 65–70.

(23) J. Ding, Q. Wu, Y. Li, Q. Long, C. Wang and Y. Wang, $Sr_{7.3}Ca_{2.7}(PO_4)_6F_2:Eu^{2+},Mn^{2+}$: a novel single-phased white light-emitting phosphor for NUV-LEDs, *Dalt. Trans.*, 2015, 44, 9630–9636.

(24) N. An, F. Xu, Q. Guo, L. Liao, L. Mei and H. Liu, Structure and luminescence properties of a novel broadband green-emitting oxyapatite-type phosphorLEDs, RSC Adv., 2020, 10, 11608–11614.

(25) R. Li, J. Zhang, Z. Qui, J. Han, J. Zhang, W. Zhou, L. Yu and S. Lian, Multispectral Tunability in Single Eu^{2+}-doped $(Br,Sr)_5(PO_4)_3Br$ Phosphor, Inorg. Chem. Front., 2020, 7, 2515–2522.

(26) H. M. Fang, C. Ni, X. Zhang, T. Y. Tsai, S. Mahlik, A. Lazarowska, M. Grinberg, S. H. Sheu, F. J. Lee, M. B. Cheng, and S. R. Liu, Enhance Color Rendering Index via Full Spectrum Employing the Important Key of Cyan Phosphor, ACS Appl. Mater. Interfaces, 2016, 8, 30677–30682.

(27) Y. Pan, W. Wang, Y. Zhu, H. Xu, L. Zhou, M. H. Noh, H. J. Jeong, X. Liu, and L. Li, $Eu^{3+/2+}$ Co-Doping System Induced by Adjusting Al/Y Ratio in Eu Doped $CaYAlO_4$: Preparation, Bond Energy, Site Preference and $^5D_0$-$^7F_4$ Transition Intensity, RSC Adv., 2018, 8, 23981–23989.

(28) D. V. Deyneko, I. V. Nikiforov, D. A. Spassky, Y. Y. Dikhtyar, S. M. Aksenov, S. Y. Stefanovich and B. I. Lazoryak, Luminescence of Eu^{3+} as a probe for determination of

the local site symmetry in the β-$Ca_3(PO_4)_2$ related structures, *CrystEngComm*, 2019, 21, 5235–5242.

(29) Y. Zhang, X. Li, K. Li, H. Lian, M. Shang and J. Lin, Crystal-Site Engineering Control for the Reduction of Eu^{3+} to Eu^{2+} in $CaYAlO_4$: Structure Refinement and Tunable Emission Properties, ACS Appl. Mater. Interfaces, 2015, 7, 2715–2725.

(30) S. Sreevalsa, A. P. Parvathy, K. S. Sahoo, S. Das, Full-Color Emitting Crystal Engineered $Sr_3Al_{1-x}Si_xO_{4+x}F_{1-x}$: $Eu^{2+/3+}$ Oxyfluorides for Developing Bendable Lighting Composites, J. Alloys Compd., 2021, 880, 160483.

(31) J. Feng, Z. Wang, H. Xu, M. Jia, Y. Wei, and Z. Fu, The Charge Transfer Band as a Key to Study the Site Selection Preference of Eu^{3+} in Inorganic Crystals, Inorg. Chem., 2021, 60, 19440–19447.

(32) V. D. Deyneko, V. I. Nikiforov, A. D. Spassky, Y. Y. Dikhtyar, M. S. Aksenov, Y. S. Stefanovich, and I. B. Lazoryak, Luminescence of Eu^{3+} as a Probe for the Determination of the Local Site Symmetry in β-$Ca_3(PO_4)_2$-Related Structures, Cryst Eng Comm., 2019, 21, 5235–5242.

(33) K. S. Gupta, C. Reghukumar and M. R. Kadam, Eu^{3+} Local Site Analysis and Emission Characteristics of Novel $Nd_2Zr_2O_7$:Eu Phosphor: Insight into the Effect of Europium Concentration on Its Photoluminescence Properties, RSC Adv., 2016, 6, 53614–53624.

(34) C. A. Duke, S. Hariyani, and J. Brgoch, $Ba_3Y_2B_6O_{15}$:Ce^{3+} - A High Symmetry, Narrow-Emitting Blue Phosphor for Wide-Gamut White Lighting. Chem. Mater. 2018, 30, 2668–2675.

(35) S. Wang, Z. Song, Y. Kong, Z. Xia, and Q. Liu, 5d-Level Centroid Shift and Coordination Number of Ce^{3+} in Nitride Compounds, J. Lumin., 2018, 200, 35–42.

(36) M. Xie, H. Wei and W. Wu, Site occupancy studies and Luminescence Properties of Emission Tunable Phosphors $Ca_9La(PO_4)_7$: Re(Re = Ce^{3+}, Eu^{2+}), Inorg. Chem., 2019, 58, 1877–1885.

(37) J. Feng, Z. Wang, H. Xu, M. Jia, Y. Wei, and Z. Fu, The Charge Transfer Band as a Key to Study the Site SelectionPreference of Eu^{3+} in Inorganic Crystals, Inorg. Chem., 2021, 60, 19440–19447.

(38) K. W. Huang, W. T. Chen, C. I. Chu, S. F. Hu, H. S. Sheu, B. M. Cheng, J. M. Chen and R. S. Liu, Controlling the Activator Site to Tune Europium Valence in Oxyfluoride Phosphor, Chem. Mater., 2012, 24, 2220-2227.

(39) X. Zhang, Z. An, R. Dong, Y. Song, K. Zhang, Y. Sheng, Z. Shi and H. Zou, Properties and Application of Single Eu^{2+} - Activated Color Tuning Phosphors, ACS Sustainable Chem. Eng., 2019, 7, 10724–10733.

(40) H. Jiang, Y. Jia, T. Qu, Y. Pan, K. Yang and H. Luo, Yellow Persistant Phosphors $Ba_{13.35}Al_{30.7}Si_{5.3}O_{70}:Eu^{2+}$, from the Energy Regulation of Rare Earth Ions, ACS Omega., 2019, 4, 6923–6930.

(41) A. De. B. Samanta, A. K. Dey, N. Chakraborty, T. K. j Parya, S. Saha, and U. K. Ghorai, $ZnAl_2O_4:Eu^{2+}$ Nanoparticle phosphors Co-doped with Li+ for Red Light-Emitting Diodes, ACS Appl. Mater., Interfaces 2022, 5, 331–340.

(42) V. Bachmann, C. Ronda, O. Oeckler, W. Schnick, and A. Meijerink, Color Point Tuning for $(Sr,Ca,Ba)Si_2O_2N_2$: Eu^{2+} for White Light LEDs, Chem. Mater., 2009, 21, 316–325.

(43) M. Zhao, Q. Zhang, and Z. Xia, Structural Engineering of Eu^{2+}-Doped Silicates Phosphors for LED Applications, Accounts Mater. Res., 2020, 1, 137–145.

(44) Z. Yang, G. Liu, Y. Zhao, Y. Zhou, J. Qiao, M. S. Molokeev, H. C. Swart and Z. Xia, Competitive Site Occupation toward Improved Quantum Efficiency of $SrLaScO_4$:Eu Red Phosphors for Warm White, Adv. Opt. Mater., 2022, 10, 1–9.

(45) H. C. Huang,T. Y. Lai, S. T. Chan, T. Y. Yeh, and R. W. Liu, A Novel Green-Emitting $SrCaSiAl_2O_7:Eu^{2+}$ Phosphor for White LEDs, RSC Adv., 2014,4, 7811-7817.

(46) J. Wang, S. Huang, M. Shang, P. Dang, H. Lian, and J. Lin, The Effect of Local Structure on the Luminescence of Eu^{2+} in Ternary Phosphate Solid Solutions by Cationic Heterovalent Substitution and Their Application in White LEDs, Inorg. Chem. 2021, 60, 19440–19447.

(47) S. Liao, X. Ji, Y. Liu, and J. Zhang, Highly Efficient and Thermally Stable Blue-Green $(Ba_{0.8}Eu_{0.2}O)(Al_2O_3)_{4.575x(1+x)}$ Phosphor through Structural Modification, ACS Appl. Mater. Interfaces, 2018, 10, 39064–39073.

(48) Y. Wei, L. Cao, L. Lv, G. Li, J. Hao, J. Gao, C. Su, C. C. Lin, S. H. Jang, P. Dang, and J. Lin, Highly Efficient Blue Emission and Superior Thermal Stability of $BaAl_{12}O_{19}:Eu^{2+}$ Phosphors Based on Highly Symmetric Crystal Structure, Chem. Mater., 2018, 30, 2389–2399.

(49) J. Zhang, Q. Guo, L. Liao, Y. Wang, M. He, H. Ye, L. Mei, H. Liu, T. Zhou, and B. Ma, Structure and Luminescence Properties of $La_6Ba_4(SiO_4)_6F_2:Dy^{3+}$ Phosphor with Apatite Structure, RSC Adv., 2018, 8, 38883–38890.

(50) S. Dutta, S. Som, M. L. Meena, R. Chaurasiya, T. M. Chen and W. Zhou, Multisite-Occupancy-Driven Intense Narrow-Band Blue Emission from $Sr_5SiO_4Cl_6:Eu^{2+}$ Phosphor with Excellent Stability and Color, Inorg. Chem., 2020, 59, 1928–1939.

(51) Z. H. Z. Hang and Y. O. W. Ang, Tunable Photoluminescence in $Ba_{1-x}Sr_xSi_3O_4N_2:Eu^{2+}/Ce^{3+}, Li^{+}$ Solid Solution Phosphors Induced by Linear Structural Evolution, Optical Material Express, 2019, 9, 1922–1932.

4.7 Supplementary Information

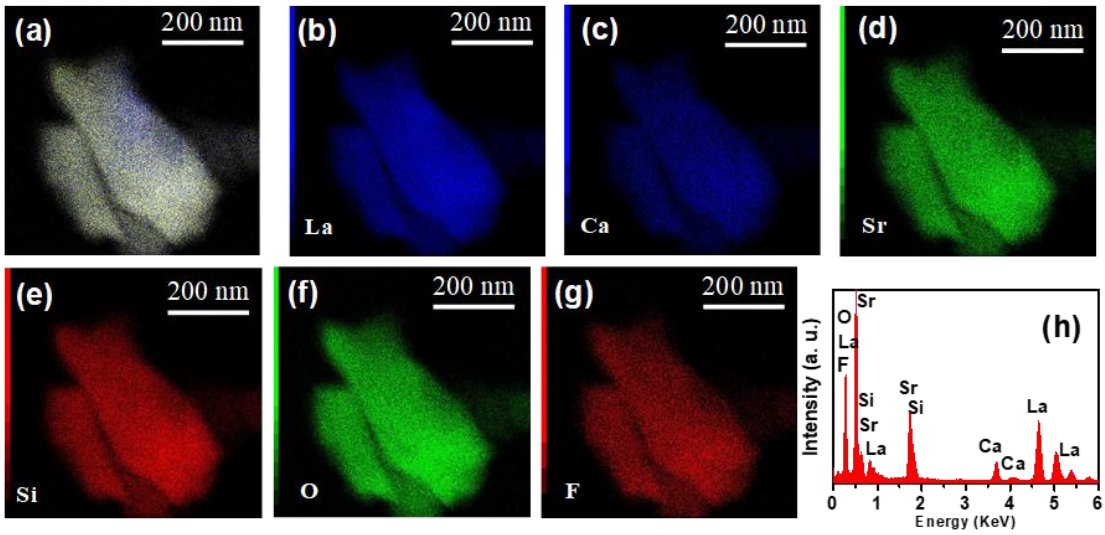

Figure 4.S1 *(a) TEM spectrum, (b-g) elemental mapping images, and (h) EDX spectra of CSLOF.*

Table 4.S1 *Rietveld refined lattice parameters of CLOF, CLOF: 0.04Eu^{2+}, CSLOF, CSLOF: 0.04Eu^{2+} and CSLOF: 0.04Eu^{2+};1.2Ba^{2+}.*

Formula	**CLOF**	**CLOF:0.04Eu^{3+}**	**CSLOF**	**CSLOF:0.04Eu^{2+}**	**CSLOF:0.04 Eu^{2+};1.2Ba^{2+}**
Structure	Hexagonal	Hexagonal	Hexagonal	Hexagonal	Hexagonal
Space group	P 63/m (#176)	P 63/m (# 176)	P 63/m (#176)	P 63/m (# 176)	P 63/m (# 176)
a = b [Å]	9.6553 (3)	9.6494 (5)	9.6855 (5)	9.6902 (4)	9.7247 (2)
c [Å]	7.1224 (1)	7.1202 (2)	7.1622 (8)	7.1649 (5)	7.2090 (3)
v [$Å^3$]	575.03 (1)	574.15 (6)	582.19 (7)	582.65 (1)	590.42 (3)
Z	2	2	2	2	2
$\chi 2$	1.527	2.171	5.323	3.856	3.234
R_p(%)	3.76	4.94	5.57	6.02	5.44
R_{wp} (%)	4.98	6.59	9.13	8.58	8.67
GOF (S)	1.24	1.47	2.31	1.96	1.80
Temperature	298 K	298 K	298 K	298 K	298 K

Table 4.S2 *The atomic coordinates and fractional occupancies of CLOF and CSLOF hosts*

Atom	Wyck. pos.	x	y	z	U_{iso}	Occ.
			CLOF			
La1	6h	0.23691 (3)	-0.01380	1/4	0.0176 (2)	0.75
Ca1	6h	0.23691 (3)	-0.01380	1/4	0.0176 (2)	0.25
La2	4f	2/3	1/3	0.00238 (9)	0.0046 (1)	0.375
Ca2	4f	2/3	1/3	0.00238 (9)	0.0046 (1)	0.625
Si	6h	0.39769 (4)	0.36628 (1)	1/4	0.0215 (4)	1.0
O1	6h	0.58661 (8)	0.47220 (4)	1/4	0.0249 (8)	1.0
O2	6h	0.33204 (5)	0.48359 (2)	1/4	0.0087 (4)	1.0
O3	12i	0.34109 (1)	0.26277 (4)	0.06359 (6)	0.0170 (8)	1.0
F	2a	0	0	1/4	0.1475 (2)	1.0
			CSLOF			
La1	6h	0.24120 (6)	-0.01259 (3)	1/4	0.0199 (9)	0.75
Ca1	6h	0.24120 (6)	-0.01259 (3)	1/4	0.0199 (9)	0.125
Sr1	6h	0.24120 (6)	-0.01259 (3)	1/4	0.0199 (9)	0.125
La2	4f	2/3	1/3	0.00198 (3)	0.0057 (6)	0.375
Ca2	4f	2/3	1/3	0.00198 (3)	0.0057 (6)	0.3125
Sr2	4f	2/3	1/3	0.00198 (3)	0.0057 (6)	0.3125
Si	6h	0.39272 (5)	0.35948 (9)	1/4	0.0220 (5)	1.0
O1	6h	0.57470 (2)	0.45330 (2)	1/4	0.0463 (5)	1.0
O2	6h	0.33411 (1)	0.48183 (8)	1/4	0.0385 (4)	1.0
O3	12	0.34445 (9)	0.25447 (1)	0.05584 (6)	0.0196 (3)	1.0
F	2	0	0	1/4	0.0598 (8)	1.0

Chapter 5

Violet light excitable, highly efficient single broadband emitting oxyfluoride phosphor and polymer composite for conventional and laser-triggered lighting applications

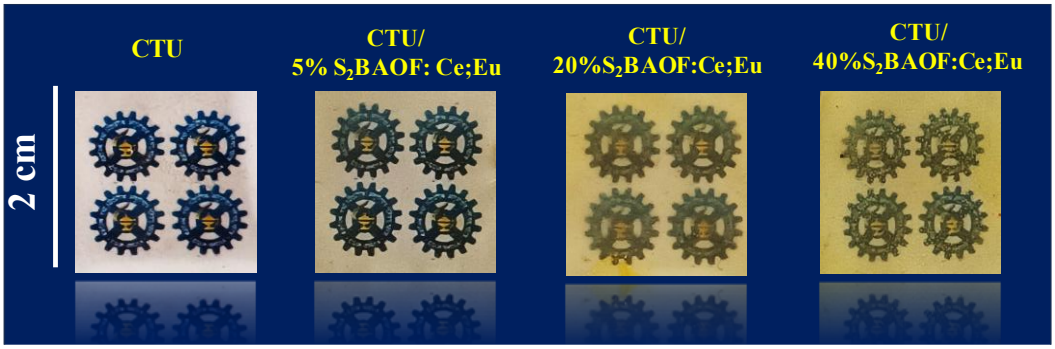

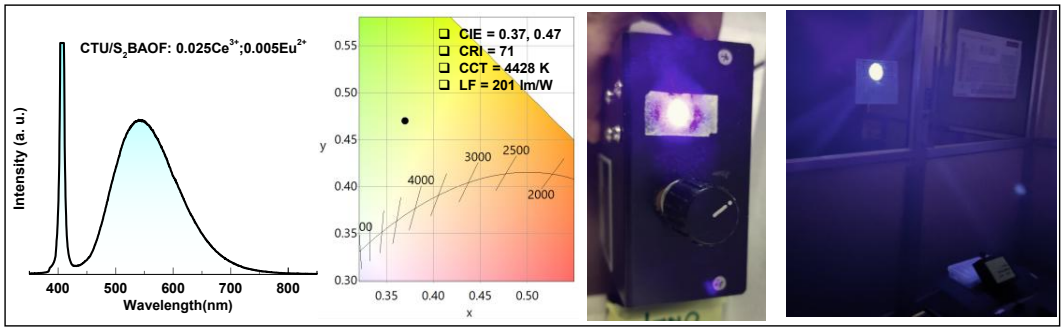

5.1 Abstract

Full-spectral emitting violet light excitable flexible luminescent converters favor user-friendly and human-centric lighting technologies due to simplified white-LED (WLED) integration, lower strain lighting, and long-term color constancy. This research proposed a new broadband-emitting phosphor composition (Sr, Ba)$_3$(Al, Si)O$_4$F: Ce^{3+},Eu^{2+}, which is structurally optimized based on Eu^{2+} and Ce^{3+} site occupancy. Aided from the sensitization effect of Ce^{3+} ions, a wider band emission composed of $4f^6 5d^1$ - $4f^7$ transitions of Ce^{3+} and Eu^{2+} ions is effectively recognized under 410 nm violet radiation with a high quantum efficiency of 86% and thermal stability of 78%. High-quality phosphor polymer composite films are fabricated using the emission red-shifted $Sr_{1.995}Ba_{1-x}Al_{0.5}Si_{0.5}O_4F$: $0.025Ce^{3+};0.005Eu^{2+}$ powders and thiourethane (CTU), which do not require any organic binders for WLED assembly, and exhibit high photobleaching and enhanced photoluminescent stability due to polymer encapsulation. The WLEDs assembled by the CTU/40%S_2BAOF: $0.025Ce^{3+};0.005Eu^{2+}$ flexible composite as a single converter layer of a 410 nm violet-LED chip and a violet laser of 405 nm generates eco-friendlier white light with CRI ~75 and low CCT < 4000 K without a noticeable chromatic shift under various powers and after prolonged illuminations. This research highlights the potential of structurally distorted phosphor-polymer composites with outstanding lighting stability.

5.2 Introduction

Phosphor-based white light emitting diodes (pc-WLEDs) are promising in fourth-generation artificial lighting because of their long lifespans, tunable color, good stability, environmental friendliness, high energy-saving performance, and compactness [1-3]. The most frequently produced commercial pc-WLEDs are made by uniting a blue LED chip with yellow emitting $Y_3Al_5O_{12}:Ce^{3+}$ (YAG: Ce) phosphor, considering its high photoluminescence efficiency and excellent chemical stability [4]. However, the lack of red components in the PL spectrum of YAG: Ce phosphor results in cool white light emission with a low color rendering index (CRI ~ 75) and high correlated color temperature (CCT > 6000 K) [5-7]. To elevate the color quality of this combination, several blue light excitable Eu^{2+}-activated nitride and sulfide red phosphors can be added in a powder blend [7]. However, the poor chemical stability of sulfide phosphors allows

enormous usage of chemically stable nitride phosphors for commercial WLED packaging. Yet, the representative wide-band emission and excitation spectra of Eu^{2+}-activated nitrides create photon reabsorption concerns when mixed with YAG: Ce powders [7]. Meanwhile, the presence of a major content of costly rare-earth oxide containing Y^{3+} ions in the $Y_3Al_5O_{12}$ host, and high synthesis temperature negatively affect the market potential of YAG: Ce phosphor-based solid-state lighting [8-9].

The conventional blue LEDs with peaks ranging from 450 nm to 470 nm are used for generating white light through the potential blue-to-broadband green and yellow phosphor converters including YAG: Ce. In this line, extensive research has been conducted on different phosphors for generating healthier white light emission with low CCT, and high CRI. Huang *et al.* fabricated warm white light-emitting pc-LEDs with CRI of 91 and CCT of 4080 K by uniting green emitting $CaY_2HfGa(AlO_4)$: Ce^{3+} and red-emitting $CaAlSiN_3$: Eu^{2+} phosphors with a 450 nm LED chip [10]. Xia *et al.* demonstrated a pc-WLED with high CRI (93) and low CCT (4013 K) by uniting the blend of $Rb_3YSi_2O_7$: Eu^{2+} red phosphor and Ba_2SiO_4: Eu^{2+} commercial green phosphor with a 460 nm InGaN LED chip [11]. In the above reports, even though the additional red emitting component lowered the CCT value, however, the pervasiveness of the blue light from the LED chip remained in the final white light output. Nevertheless, continuous exposure to blue light (450 nm to 470 nm) may unbalance the human circadian rhythm leading to insomnia, mood disorders, fatigue, cataract formation, and macular degeneration [12-16]. For producing human-centric lighting, nowadays researchers have focused on violet LEDs (λ_{em} = 400 nm) as a suitable alternative for conventional InGaN blue LEDs (λ_{em}= 450 – 470 nm), which can reduce the cyan gap and may enhance uniform white light distribution when combined with full-spectral emitting phosphors. Importantly, violet LEDs can provide high luminous efficiency, wider color gamut, and higher CRI than conventional blue LEDs by choosing selective phosphors with high quantum yield to avoid inherent Stokes loss [17]. To avoid blue light hazards, adopting eye-friendly violet light as the excitation source would be preferable for future health-conscious illumination [17-18]. Several research of violet excitable broadband emitting Ce^{3+}/Eu^{2+}-activated phosphors for full-spectra pc-WLEDs have recently published [19-25]. Nevertheless, efficient violet LED excitable yellow-emitting phosphors and subsequent full-spectral pc-WLED encapsulations that can create glare-free white-light emission with high quantum efficiency are rarely reported [17].

Oxyfluoride phosphors gained wide attention towards WLED application because of their noticeable structural stability and rigidity, adequate thermal and chemical stability, tunable luminescence property, high quantum efficiency, environmentally friendly, and low content of rare earth ions [26-27]. The incorporation of highly electronegative fluoride ions into the oxide host lattice produces distortion in the centrosymmetric cationic sites of polyhedrons in the oxyfluoride host lattice leading to broad emission band and tunable emissive properties [28]. Sr_3AlO_4F is one of the prominent oxyfluoride hosts for lighting applications owing to its high luminous efficiency [29]. W. B. Im *et al.* observed greenish-white light emission from (Sr, Ba)$_3AlO_4F$: Ce^{3+} phosphor with CRI of 62, CCT of 6500 K, and very high quantum efficiency under ultraviolet (UV) LED chip [30]. According to this report, the Sr_3AlO_4F host might be converted to a violet excitable full spectral band emitting phosphor with high efficiency, which could be appropriate for generating desired lighting devices.

Integrating phosphor powders and LED devices using organic binders is a cost-effective and easy process to assemble pc-LED devices. Nonetheless, when phosphor powder is glued in organic binders, pc-LEDs face carbonization reactions due to the continuous exposure to the excitation source, resulting from the low thermal stability and poor heat resistance of the used binder. To overcome the mentioned problem of epoxy coatings, instead of traditional powder color converters, modern color converters such as phosphor in glasses (PiGs), phosphor ceramics and single crystals have been used for advanced lighting applications [31-34]. Recently P. Zhang *et al.* reported blue laser-triggered YAG: Ce films deposited on a sapphire plate with high luminescence for future lighting technologies [32]. They generated uniform white light with a CCT of 6538 K and a luminous efficiency of 127 lmW^{-1}. However, they face poor thermal conductivity and high production cost. Q. Yao *et al.* reported blue laser-driven transparent ceramic YAG: Ce phosphor with good conversion efficiency [33]. It may possess a high luminous efficiency of 223 lm W^{-1}, however, CCT is observed to be 7293 K. Both cases fail to achieve warm white light emission and face difficult synthesis conditions of glass and ceramics. Furthermore, the usability of continuous exposure to 460 nm blue laser may cause health issues for humans, and the rigid nature of the composite restricts its application towards advanced flexible lighting technologies. To overcome these problems, developing polymer composite-based color converters could be an appropriate

solution because of their potential applications for flexible optoelectronic devices [35-37]. Here we have chosen a thiol urethane-based polymer to encapsulate phosphor particles and this may protect the particles from environmental variations and induce flexibility for devices. In addition, thiourethane has characteristic advantages like a high refractive index, solubility in aqueous solutions, transparency, flexibility, high thermal and moisture stability, non-absorption in visible regions, and reliable optical performance applicable for potential flexible lighting devices [38].

Surprisingly, no research has been carried out on violet LED excitable Eu^{2+} and Ce^{3+} codoped $Sr_{1.975}Ba_{1-x}Al_{0.5}Si_{0.5}O_4F$ (S_2BAOF) yellow phosphors for warm white light emitting pc-LEDs. Herein, we have strategically designed a single-phased Sr_2BaAlO_4F host matrix-based system to generate warm white light emission under violet excitation with good optical performance. Recently, our group reported cool white light emission from two prominent oxyfluoride phosphors $Sr_{2.9}Al_{1-x}Si_xO_{4+x}F_{1-x}$: $Eu^{2+/3+}$ and $Ca_4La_6Si_6O_{24}F_2$: Eu^{2+} through cationic substitution strategy [39, 40]. Eventually, we explored new systems to achieve warm white light with lower CCT via modulating the structural properties and dopant varieties in the Sr_2BaAlO_4F host matrix. Selectively, Ce^{3+} and Eu^{2+} activators are used to produce full spectral broadband emission because of their parity-allowed $5d \rightarrow 4f$ transition, which is more applicable for white light-emitting applications [41]. The above discussions and studies motivated us to synthesize a series of highly efficient trigonal structured yellow emitting S_2BAOF: $0.025Ce^{3+}$; xEu^{2+} phosphors under violet excitation. The Eu^{2+}/Ce^{3+} site occupation mechanism and photoluminescent properties of single-phase warm white light emitting SBAOF phosphors were studied in detail. The warm white light-emitting optimized phosphors were further used to fabricate phosphor-polymer composite membranes for application in flexible lighting devices. To encounter the issues of organic binders, herein, a thiourethane-based polymer matrix with a high refractive index, and high thermal and moisture stability, for encapsulating optimized yellow emitting phosphor particles.

5.3 Experimental Section

5.3.1 Materials and synthesis

A series of $Sr_{1.975}Ba_{1-x}Al_{0.5}Si_{0.5}O4F$: $0.025Ce^{3+}$; xEu^{2+} (S_2BAOF: $0.025Ce^{3+}$; xEu^{2+}; x = 0.001 to 0.01) phosphors were synthesized by conventional solid-state method by using stochiometric amount of $SrCO_3$ (99.999%), SrF_2 (99.999%), $BaCO_3$ (99.999%), Al_2O_3

(99.999%), SiO_2 (99.99%) CeO_2 (99.999%)and Eu_2O_3 (99.999%) obtained from Sigma-Aldrich were ground together in an agate mortar by using ethanol as mixing agent. The mixture was loaded into an alumina crucible and sintered for 5h at 1250 °C in the N_2 – H_2 (95% - 5%) reduction atmosphere. Finally, the obtained powder samples are grounded further for measurements.

Cardanol was procured from Cardolite Corporation. 3-chloro-1,2-propane diol, NaOH, para-toluenesulfonic acid (TSA), 3-mercaptopropionic acid, and sodium sulfate were brought from TCI chemicals. Aliphatic polyisocyanate (IC-25NY) was purchased from Antares Chemical Private Limited in Mumbai. All the chemicals were used as such without further purification.

5.3.1.1. Synthesis of Cardanol-2,3-dihydroxypropylether (CPE)

The synthesis of Cardanol-2,3-dihydroxypropylether is carried out as reported earlier by our group (1). The cardanol (0.15 mol) and 3-chloro-1,2-propane diol (0.174 mol) are reacted in the mole ratio 1:1.16 in a two-neck R.B. flask equipped with a condenser. After 15 minutes, NaOH solution was added to the mixture. The mixture was heated at 75°C for 3 hours. The salt (NaCl) was filtered, and the product was washed with distilled water and dichloromethane. The oil layer was purified using rotary evaporation under vacuum, the brown liquid was obtained.

5.3.1.2. Synthesis of thiolated CPE (TCPE)

The grafting of thiol groups onto CPE was performed by adding 8 g of CPE, 0.16 g of pTSA, and 50 mL of toluene into a round-bottom flask. The mixture was stirred continuously at 110°C. Subsequently, 3.9 mL of 3-mercaptopropionic acid was added dropwise and the reaction was stirred for an additional 3 hours. The resulting product was then washed with distilled water and dichloromethane (DCM). After washing, the product was dried using sodium sulfate, and excess DCM was removed via rotary evaporation.

5.3.1.3. Preparation of thiourethane films (CTU)

About 0.5 g of TCPE was mixed with 0.62 g of industrial aliphatic isocyanate (IC-25NY) at 45°C with stirring for 15 min. Then the viscous solution was poured into a silicon mold and allowed to cure at room temperature overnight.

5.3.1.4. Preparation of CTU/S_2BAOF: Ce; Eu composite films

Phosphor particles (S_2BAOF: Ce; Eu) were dispersed in acetone using a sonicator. Then 0.50 g TCPE and 0.62 g IC-25NY were added to the dispersed solution and stirred for 10 min. Subsequently, S_2BAOF: Ce; Eu dispersed CTU prepolymer solution was poured into the silicon mold and cured at room temperature overnight. The compositions for the composite were tabulated in **Table 5.1**.

Table 5.1: *The compositions for the composite preparations*

Sample	TCPE (g)	IC-25NY (g)	S_2BAOF: Ce; Eu (g)
CTU	0.5	0.62	0.000
CTU/5% S_2BAOF:Ce;Eu	0.5	0.62	0.056
CTU/20% S_2BAOF:Ce;Eu	0.5	0.62	0.224
CTU/40% S_2BAOF:Ce;Eu	0.5	0.62	0.488

5.3.2 Characterizations

The crystalline phase purity of synthesized (S_2BAOF: $0.025Ce^{3+}$; xEu^{2+}; x = 0.001 to 0.01 phosphors was studied by using powder X-ray diffraction pattern collected using PC-controlled X-ray Diffractometer powder collected using X-ray diffractometer EMPYREAN 3 Malvern Panalytical B.V with Cu-Kα radiation (wavelength: 1.54056 Å). The general structural analysis system GSAS II software was used for the Rietveld refinement of samples and crystal structure was generated using VESTA software. The X-ray photoelectron spectroscopy (XPS) measurements were carried out by using a PHI 5000 Versa probe Scanning ESCA Microprobe. The high-resolution spectra of, Sr 3d, O 1s, Ba 3d, Si 2p, Eu 3d, F 1s, Ce 3d, and Al 2p were obtained using Al Kα radiation (1.487 keV) at a resolution of 0.1 eV. The EPR measurements are recorded on a Bruker EMX Series spectrometer using X band frequency (9.5 GHz) and 100 kHz field modulation. The morphological studies and elemental compositions of the synthesized phosphors were analyzed by using a high-resolution transmission electron microscope (HR-TEM), JEOL JEM-F200. The UV-Vis diffuse reflectance spectra (UV-Vis DRS) of the phosphors were collected using a UV-Vis Spectrophotometer (Shimadzu UV 3600). The FT-IR (Perkin Elmer) and ^{1}H NMR (60MHz, Bruker Ascend) analysis were carried

out to verify the structure and functional groups of TCPE. To understand the temperature stability of films, TGA measurement was employed using the TA Q50 Analyzer. The surface morphology of the bare and composite films was analyzed using ZEISS EVO 18, scanning electron microscope. The photoluminescence excitation and emission spectra of samples were analyzed using a Yvon Fluorolog 3 spectrofluorometer with a 450 W Xenon flash lamp as the exciting source. The low-temperature photoluminescence studies were carried out using a cryostat assembly equipped with the FLS-1000 fluorescence spectrometer (Edinburgh Instruments, UK) and liquid nitrogen was used as the coolant. The decay studies were carried out using a nanosecond H_2 flashlamp. The electroluminescence properties of the obtained devices were measured using a high-sensitivity CCD spectrophotometer (Maya 2000 Pro) by using a 3W violet LED and 12 mW laser source (405 nm).

5.4 Results and Discussions

5.4.1 Structural analysis of SBAOF, SBAOF: 0.025Ce^{3+};0.005$Eu^{2+/3+}$, and S_2BAOF: 0.025Ce^{3+}; xEu^{2+} (x = 0.0 to 0.01) phosphors

The 2D view of SBAOF phosphor's crystal structure, as shown in **Fig. 5.1(a),** consists of a rigid cationic polyhedral unit framework. The SBAOF phosphor belongs to a tetragonal Sr_3AlO_4F (JCPDS No. 89 – 4485) phase, where Ba, Sr, and Al atoms are occupied in the *4a*, *8h,* and *4b* sites in the formation of BaO_8F_2, SrO_6F_2, and AlO_4 polyhedrons, respectively. The BaO_8F_2 polyhedrons are arranged parallel to each other, whereas the SrO_6F_2 polyhedrons are organized in a zig-zag manner throughout the chain, and every single unit is edge and corner shared with isolated AlO_4 tetrahedra to form a whole framework structure. The powder X-ray diffraction (XRD) pattern of the synthesized S_2BAOF: 0.025Ce^{3+}; xEu^{2+} phosphors (x = 0.00 to 0.01) are illustrated in Fig. 5.1(b). The diffraction peaks are well-matched with the reported pattern of the tetragonal Sr_3AlO_4F (JCPDS No. 89 – 4485) phase. Meanwhile, a small fraction of SrF_2 impurity phase could also be traced in all the XRD patterns decomposition of the host phosphor due to moisture [30]. The corresponding diffraction angle shifted towards a lower 2θ after the larger Ba^{2+} and Eu^{2+} ions' substitutions in the Sr^{2+} sites, as seen in **Fig. 5.1**(b).

The crystallographic insights of undoped SBAOF, SBAOF: 0.025Ce^{3+}; 0.005$Eu^{2+/3+}$ and S_2BAOF: 0.025Ce^{3+}; xEu^{2+} (x = 0.001 and 0.01) phosphors are evaluated by the

Rietveld refinement of their obtained XRD patterns. The estimated lattice parameters and fraction of occupation are tabulated in **Table 5.S1** to **Table 5.S3**. As compared the refinement result of SBAOF with the literature reports of Sr_3AlO_4F, it is found that without Ba incorporation Sr_3AlO_4F host is a highly strained system and is difficult to accommodate larger rare earth ions like Eu^{2+} or Ce^{3+} ions, etc. into the lattice **[42]**. After incorporating Ba^{2+} ions in the lattice the cationic site strain is reduced means the substitution of larger ions results in the expansion of the crystal lattice, which subsequently increases the polyhedral volume and cationic bond lengths. The cationic site and metal-oxygen bond length enlargement after Ba^{2+} substitution in Sr_3AlO_4F phosphor is schematically shown in **Fig. 5.S1**. Henceforth, it is easy to accommodate larger rare earth ions like Eu^{2+} or Ce^{3+} ions in the SBAOF host after the Ba^{2+} substitution-induced cationic site enhancement. As compared the refinement results of SBAOF: $0.025Ce^{3+}$; $0.005Eu^{2+/3++}$ phosphor with undoped SBAOF slight contraction in lattice parameter is observed (as illustrated in **Table S1**) because of the smaller ionic substitution of Ce^{3+}(r^{8h} = 1.143Å; r^{4a} = 1.25Å) / Eu^{3+} (r^{8h} = 1.066) ions with bigger Ba^{2+} (r^{8h} = 1.42Å; r^{4a} = 1.52Å) / Sr^{2+} (r^{8h} = 1.26Å; r^{4a} = 1.36Å) ions in the lattice. Owing to the unsuitability of cationic sites for hosting bigger Eu^{2+} ions, based on our previous findings we demonstrated that the heterovalent substitution of Al^{3+} ion with Si^{4+} ions in the host may promote the reduction of Eu^{3+} ions and enhance the occupancy of more Eu^{2+} ions in the lattice [39].

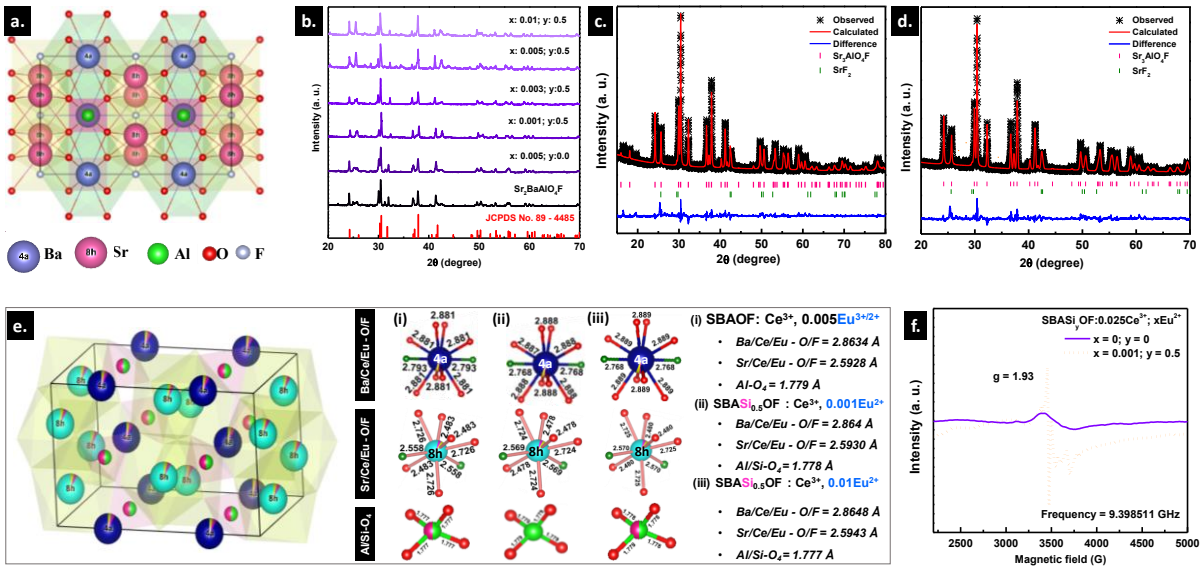

Fig. 5.1: (a) *2D crystal structure view of SBAOF phosphor.* ***(b)*** *The powder XRD patterns of SBAOF (xEu^{2+} = 0.0; ySi^{4+} = 0.0) and S_2BAOF: 0.025Ce^{3+}; xEu^{2+} (xEu^{2+} = 0.001, 0.003, 0.005, and 0.01; ySi^{4+} = 0.5) phosphors.* ***(c)*** *and* ***(d)*** *Rietveld refinement pattern of S_2BAOF: 0.025Ce^{3+}; xEu^{2+} (x = 0.001 and 0.01) phosphors. The asterisk symbols (⋆) in the Rietveld refinement patterns indicate SrF_2 impurity phase.* ***(e)*** *The 3D crystal structure of S_2BAOF: 0.025Ce^{3+};0.001Eu^{2+} phosphor generated using VESTA software and schematic representation of average metal - oxygen bond length variation in SBAOF: 0.025Ce^{3+};0.005$Eu^{2+/3+}$ and S_2BAOF: 0.025Ce^{3+}; xEu^{2+} (x = 0.001 and 0.01) phosphors.* ***(f)*** *Electron spin resonance spectra of SBAOF: 0.025Ce^{3+}; 0.005$Eu^{2+/3+}$ and S_2BAOF: 0.025Ce^{3+};0.001Eu^{2+} phosphors.*

The Rietveld refinement pattern of S_2BAOF: 0.025Ce^{3+}; xEu^{2+} (x = 0.001 and 0.01) phosphors as illustrated in **Fig. 5.1** (c) and (d), respectively. Their crystal structure belongs to a non-centrosymmetric tetragonal phase with a space group of *I4/mcm*. In the case of S_2BAOF: 0.025Ce^{3+}; 0.001Eu^{2+} phosphor, a very weak diffraction peak of the impure phase of SrF_2 appears at 2θ ~ 42.6 and the main phase mass fraction is obtained to be 96.4%. Whereas for S_2BAOF: 0.025Ce^{3+};0.01Eu^{2+} phosphor, the main phase mass fraction is calculated to be 97%.

In S_2BAOF: 0.025Ce^{3+};0.001Eu^{2+} phosphor, Ce^{3+}, and $Eu^{2+/3+}$ cations are statistically substituted Ba^{2+} ions and Sr^{2+} ions occupied *4a* and *8h* sites, respectively. With the Si^{4+} ion incorporation in the Al-O_4 sites, *4a* (BaO_8F_2) or *8h* (SrO_6F_2) sites are expected to be

enlarged due to the probable contraction of Al-O_4 sites because of lower-sized Si^{4+} ion substitutions. Such enlarged *4a* sites may allow the reduction of europium from 3+ to 2+ oxidation sates. To understand such an interpretation clearly, the corresponding 3D crystal structure for the doped S_2BAOF: $0.025Ce^{3+}$;$0.001Eu^{2+}$ phosphor was obtained from the Rietveld refinement, as shown in **Fig. 5.1(e).** After incorporating Si^{4+} ions, the lattice parameters a and b are slightly enlarged and c is contracted for S_2BAOF: $0.025Ce^{3+}$; xEu^{2+} (x = 0.001 and 0.01) phosphors due to the smaller and larger ionic substitution of Si^{4+}(r^{4a} = 0.26) and Eu^{2+}(r^{8h} = 1.25Å; r^{4a} = 1.35Å) ions with Al^{3+}(r^{4a} = 0.39Å) and Sr^{2+}(r^{8h} = 1.26Å; r^{4a} = 1.36Å) ions in the lattice. As an increasing Eu concentration, the lattice parameters are observed to be enhanced because of the incorporation of larger Eu^{2+} ions in the lattice. This cationic substitution distorts the crystal environment and leads to variations in metal-ligand bond length among doped phosphors. The comparative bond length variation of SBAOF: $0.025Ce^{3+}$; $0.005Eu^{2+}$ and S_2BAOF: $0.025Ce^{3+}$; xEu^{2+}(x = 0.001 and 0.01) phosphors are shown in **Fig. 1(e)**. By the introduction of Si^{4+} ions to the lattice Al-O bond length of S_2BAOF: $0.025Ce^{3+}$; xEu^{2+} (x = 0.001 and 0.01) phosphors are found to be decreases (from 1.779 Å to 1.777 Å and metal-ligand bond length enhanced (4a sites: from 2.8634 Å to 2.8648 Å; 8h sites: from 2.5928 Å to 2.5943 Å) as compared with SBAOF: $0.025Ce^{3+}$; $0.005Eu^{2+}$ phosphor because of the neighbouring inductive effect in the lattice. This causes the easiest reduction of Eu^{3+} ions and suitable occupation of bigger Eu^{2+} ions in the two cationic sites.

The reduction and occupation mechanism of Eu ions in the host lattice by the incorporation of Si^{4+} ion is again proven from the X-ray photoelectron spectroscopy (XPS), photoluminescence spectroscopy study as well as Electro paramagnetic resonance (EPR) spectral analysis of SBAOF: $0.025Ce^{3+}$; $0.005Eu^{2+}$ and S_2BAOF: $0.025Ce^{3+}$; $0.001Eu^{2+}$ phosphors respectively. **Fig. 5.S2(a)** represents the XPS survey spectra of SBAOF: $0.025Ce^{3+}$; $0.005Eu^{2+/3+}$ and S_2BAOF: $0.025Ce^{3+}$; $0.005Eu^{2+}$ phosphors, confirming the presence of Sr, Ba, Al, Si, O, F, Ce and Eu. The oxidation states and bonding nature of all elements in S_2BAOF: $0.025Ce^{3+}$; $0.001Eu^{2+}$ phosphor is further confirmed from the high-resolution XPS spectra fitting with carbon correction as illustrated in **Fig. 5.S2(b).** The core level spectra of Sr consist of two peaks centered at 134.78 eV and 136.76 eV corresponding to the $3d_{5/2}$ and $3d_{3/2}$ orbitals, respectively. Similarly, the two deconvoluted peaks of Ba correspond to the $3d_{5/2}$ and $3d_{3/2}$ orbitals with

peak maxima at 780.94 eV and 796.26 eV, respectively. The elemental Si and oxidized silicon contents are also confirmed by the high-resolution XPS spectra of Si. The O 1S core level spectra consist of two peaks corresponding to the presence of lattice oxygen in the form of metal oxides/ SiO_2. The existence of the 2p orbital of Al and 1S orbital of F atoms are confirmed from their core level spectra as shown in **Fig. 5.S2(b)**. The refinement results have been correlated with the XPS of $S_2BASi_{0.5}OF$: $0.025Ce^{3+};0.001Eu^{2+}$ phosphor. The core level spectrum of the Ce atom is deconvoluted into two peaks maxima around 890.88 eV and 903.05 eV corresponding to $3d_{5/2}$ and $3d_{3/2}$ orbitals of Ce^{3+} ions, respectively.

In the case of Eu atoms' core level spectra, the binding energy value at 1130.43 eV corresponds to the presence of $3d_{5/2}$ orbital of Eu^{2+} ions in S_2BAOF: $0.025Ce^{3+};0.001Eu^{2+}$ phosphor (**Fig. 5.S2(b)**). These results again prove the refinement findings that the incorporation of Si^{4+} ion to the host may contract the AlO_4 tetrahedra and consequently enlarge the *4a* and *8h* site which may enhance the reduction and occupation of more Eu^{3+} to Eu^{2+} ions in the lattice. The paramagnetic nature of Eu^{2+} ions in the SBAOF: $0.025Ce^{3+};0.005Eu^{2+/3+}$ and S_2BAOF: $0.025Ce^{3+};0.001Eu^{2+}$ phosphor is studied by using EPR spectroscopy as shown in **Fig. 5.1(f).** It is known that the electronic configuration of Eu^{2+} ($4f^7$) ion in ground term $8S_{7/2}$ is EPR active whereas Eu^{3+} ($4f^6, 7f_0$) is EPR inert. So, the dominant signal observed in the range of 3000(G) to 4000(G) in the S_2BAOF: $0.025Ce^{3+};0.001Eu^{2+}$ phosphor corresponds to the Eu^{2+} ions, and the g value is found to be 1.9374, which confirms the presence of Eu^{2+} ions in the S_2BAOF: $0.025Ce^{3+}$; $0.001Eu^{2+}$ phosphor. The hyperfine structure observed in the EPR spectrum of S_2BAOF: $0.025Ce^{3+}$; $0.001Eu^{2+}$ indicated the presence of a single Eu^{2+} species [44, 45]. In the case of SBAOF: $0.025Ce^{3+};0.005Eu^{2+/3+}$ phosphor, signals at g = 1.9368, 4.3894, and 5.7125 can be attributed to Eu^{2+}ions and. signal broadening may be observed due to increase in Eu^{2+} ion concentration compared to S_2BAOF: $0.025Ce^{3+};0.001Eu^{2+}$ phosphor [43]. The higher g values can be observed for Eu^{2+} ions in anisotropic coordination [33]. These results are reliable with the XRD Rietveld refinement findings [43, 44].

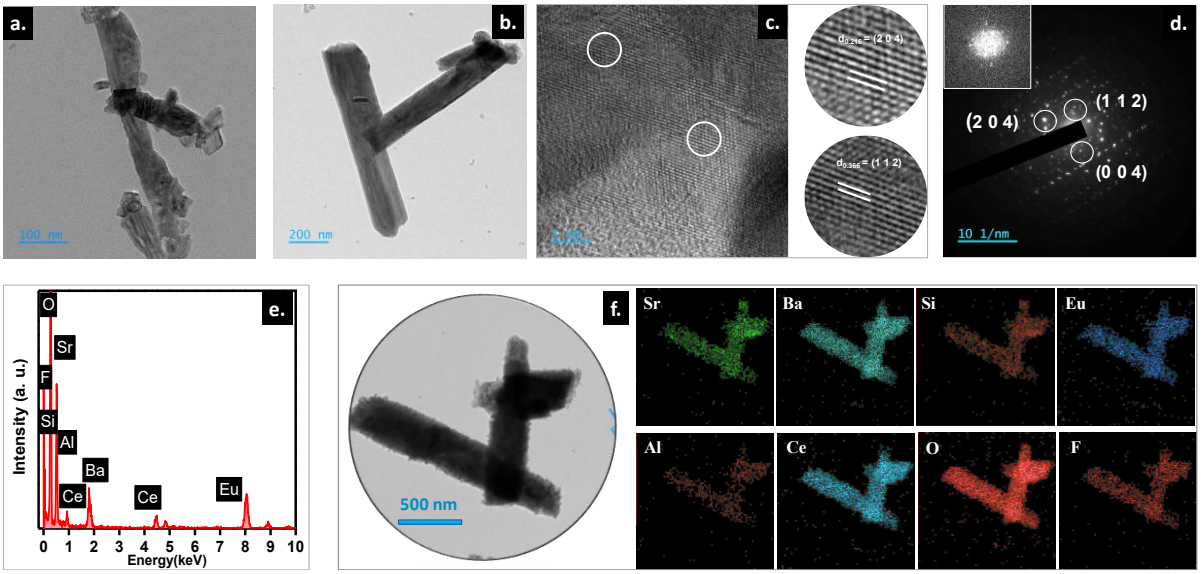

Fig.5.2: (a) and (b) *TEM images of $S_2BAOF: 0.025Ce^{3+}; xEu^{2+}$ (x = 0.001 and 0.01) phosphors.* ***(c)*** *The HR-TEM of $S_2BAOF: 0.025Ce^{3+};0.001Eu^{2+}$ phosphor.* ***(d)*** *Selected area diffraction (SAED) pattern of $S_2BAOF: 0.025Ce^{3+};0.001Eu^{2+}$ phosphor.* ***(e)*** *and* ***(f)*** *The TEM – EDX mapping of $S_2BAOF: 0.025Ce^{3+};0.001Eu^{2+}$ phosphor.*

Fig. 5.2(a) and **(b)** represent the TEM images of $S_2BAOF: 0.025Ce^{3+}; xEu^{2+}$ (x = 0.001 and 0.01) phosphors indicate well-defined rod-like morphology of the synthesized samples. The high-resolution transmission electron microscopy (HR-TEM) of $S_2BAOF: 0.025Ce^{3+};0.001Eu^{2+}$ phosphor as shown in **Fig. 5.2(c)**. The interplanar spacing around 0.216 nm and 0.366 nm corresponds to the lattice planes (2 0 4) and (1 1 2) of the tetragonal phase of $S_2BAOF: 0.025Ce^{3+};0.001Eu^{2+}$ phosphor, respectively, as determined from their XRD refinement. **Fig. 5.2(d)** illustrates the selected area electron diffraction (SAED) pattern of $S_2BAOF: 0.025Ce^{3+};0.001Eu^{2+}$ phosphor. The well-defined diffraction spots indicate the good crystallinity of the sample and the miller indices (2 0 4), (1 1 2), and (0 0 4) observed in the lattice corresponds to the tetragonal phase as indicated in the XRD refinement results. The elemental composition of $S_2BAOF: 0.025Ce^{3+};0.001Eu^{2+}$ phosphor is confirmed from the TEM-EDX mapping and scanning of each element, as shown in **Fig. 5.2(e)** and **5.2(f)**, respectively. The HR-TEM lattice plane identification is correlated with the refinement results and again proves the XRD refinement outcome of $S_2BAOF: 0.025Ce^{3+};0.001Eu^{2+}$ phosphor.

5.4.2 Photoluminescence analysis of SBAOF, SBAOF: 0.025Ce^{3+}; 0.005$Eu^{2+/3+}$, and S_2BAOF: 0.025Ce^{3+}; xEu^{2+} (x = 0.0 to 0.01) phosphors

Fig. 5.3(a) represents the excitation and emission spectra of SBAOF: 0.025Ce^{3+} and S_2BAOF: 0.025Ce^{3+} phosphors. In the case of SBAOF: 0.025Ce^{3+} phosphor, an asymmetric broad excitation band covering from 4.5 eV to 2.5 eV nm with maxima at 3.12 eV is deconvoluted into five peaks, and its broad emission band covering from 2.9 eV to 1.8 eV peaked at 2.47 eV that is deconvoluted into four peaks corresponding to the $5d^1 - 4f^1$ allowed transitions of Ce^{3+} ions. According to Van Uitert, the Ce^{3+} ions' occupancy in both the *4a* and *8h* cationic sites can be explained via the equation [45],

$$E(cm^{-1}) = Q\left[1 - \left(\frac{V}{4}\right)^{\frac{1}{v}} \times 10^{-\left(\frac{nE_a r}{80}\right)}\right] \qquad (5.1)$$

where E is the Ce^{3+} ions' emission band maxima, Q is the lower d-band position for free Ce^{3+} ions (Q = 50000 cm^{-1}), V represents the Ce^{3+} valence (V = 3), r is the cationic radius substituted by Ce^{3+} ion, E_a is the electron affinity and n represents the coordination number of Ce^{3+} ion occupied site [45]. Consequently, E directly depends on the coordination number of the cationic sites in the particular host lattice. Deliberating this formula and XRD refinement results, the occupation of activator ions is defined as longer wavelength emission corresponding to a smaller coordination site and vice versa. Based on these facts, in SBAOF: 0.025Ce^{3+} phosphor, Ce^{3+} ions that occupied ten coordinated *4a* sites that were designated by two deconvoluted peaks at 2.72 eV and 2.52 eV, and eight coordinated *8h* sites, that again designated by two deconvoluted peaks at 2.46 eV and 2.38 eV, respectively. An asymmetric excitation spectrum of S_2BAOF: 0.025Ce^{3+} phosphor maximum at 3.12 nm and is deconvoluted into five peaks similar to that of SBAOF: 0.025Ce^{3+} phosphor. The Gaussian deconvoluted emission spectrum of S_2BAOF: 0.025Ce^{3+} phosphor also illustrates the selective occupation of Ce^{3+} ions in both the cationic sites. The PL results of both the phosphors indicate similar spectral behaviour, however, the occupation of Ce^{3+}ion is enhanced after incorporating Si^{4+} ions because of the cationic site enlargement (as represented in **Fig. 5.1(e)),** which further results in the broadening of excitation and emission spectra and enhanced the emission peak intensity.

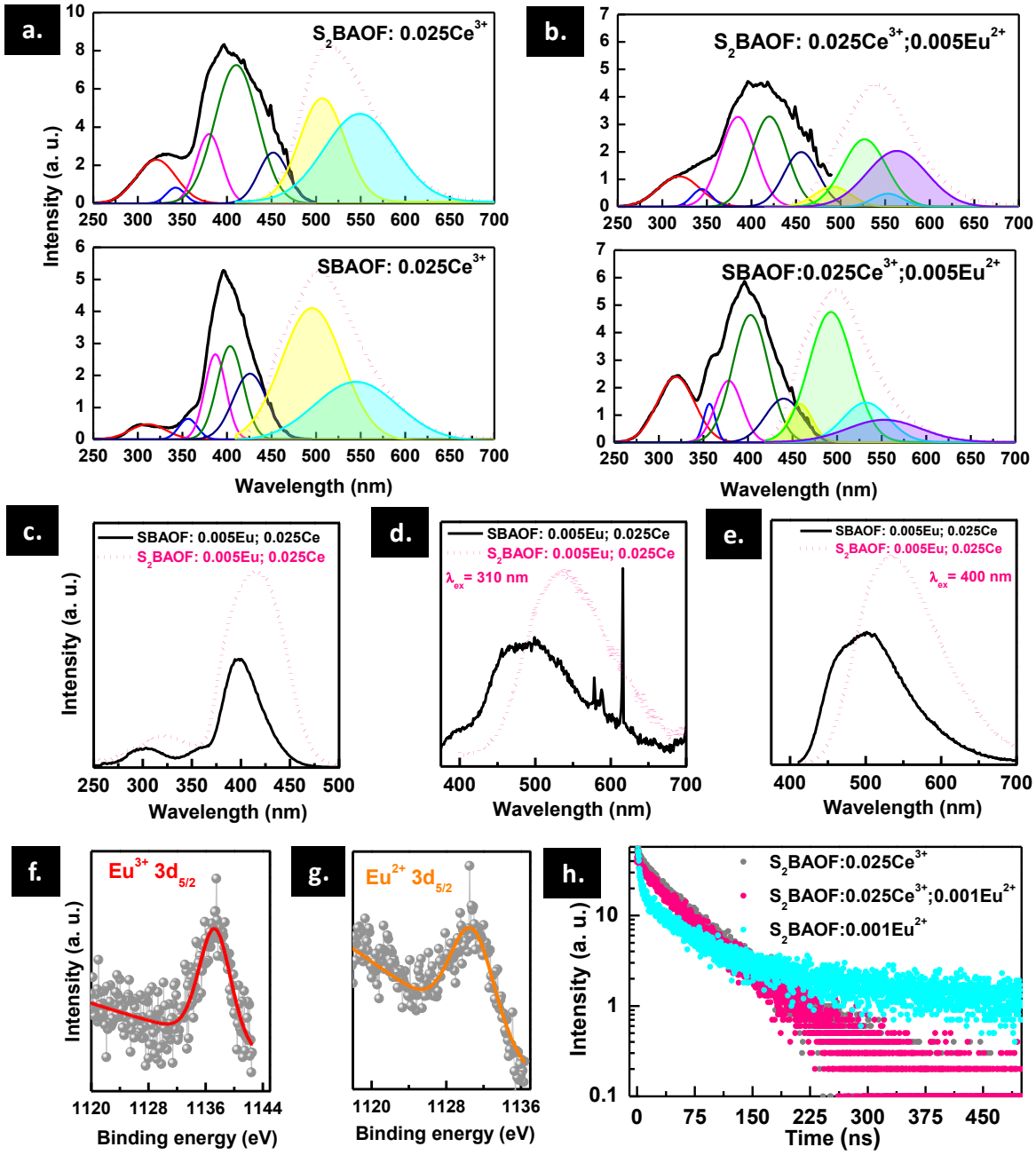

Fig. 5.3: (a) *PL emission and excitation spectra of SBAOF: 0.025Ce^{3+} and S_2BAOF: 0.025Ce^{3+} phosphors.* ***(b)*** *PL emission and excitation spectra of SBAOF: 0.025Ce^{3+}; 0.005$Eu^{2+/3+}$ and S_2BAOF: 0.025Ce^{3+};0.005Eu^{2+} phosphors.* ***(c)*** *PL excitation spectra of SBAOF: 0.025Ce^{3+}; 0.005$Eu^{2+/3+}$ (λ_{em} = 501 nm) and S_2BAOF: 0.025Ce^{3+};0.005Eu^{2+} (λ_{em} = 545 nm) phosphors.* ***(d and e)*** *PL emission spectra of SBAOF: 0.025Ce^{3+};0.005$Eu^{2+/3+}$ and S_2BAOF: 0.025Ce^{3+};0.005Eu^{2+} phosphors recorded at λ_{em} = 310 nm, and λ_{em} = 400 nm, respectively.* ***(f and g)*** *High-resolution XPS of europium atoms in SBAOF: 0.025Ce^{3+};0.005$Eu^{2+/3+}$ and S_2BAOF: 0.025Ce^{3+};0.005Eu^{2+} phosphors, respectively.* ***(h)*** *PL emission lifetime of S_2BAOF: 0.025Ce^{3+};xEu^{2+} (x = 0.0 and 0.001) and S_2BAOF: 0.001Eu^{2+} phosphors.*

To further study the effect of Si^{4+} ionic substitutions in $Eu^{2+/3+}$ oxidation states, the excitation and emission spectra of SBAOF: $0.025Ce^{3+}$; $0.005Eu^{2+/3+}$ and S_2BAOF: $0.025Ce^{3+}$; $0.005Eu^{2+/3+}$ phosphors are presented in **Fig. 5.3(b)**. The excitation and emission maxima are similar to those of SBAOF: $0.025Ce^{3+}$ phosphor might be due to weak energy transfer among the activator ions. In addition, the characteristic excitation peaks of Eu^{3+} ions around 3.87 eV and 3.44 eV are observed to be enhanced. Its Gaussian deconvoluted emission spectrum shows two additional peaks corresponding to $Eu^{3+/2+}$ ions occupancy in *4a* and *8h* sites (**Fig. 5.3(b)**). In the case of S_2BAOF: $0.025Ce^{3+}$; $0.005Eu^{2+/3+}$ phosphor, an asymmetric broad excitation band maximum at 3.02eV nm is deconvoluted into five peaks belonging to both Eu^{2+} and Ce^{3+} ions' transitions. Compared to SBAOF: $0.025Ce^{3+}$ phosphor excitation, the peaks around 3.2 eV and 2.75 eV are observed to be dominating due to the presence of $Eu^{2+/3+}$ ions in the lattice, and the emission peak is slightly red-shifted. The broad emission spectrum of S_2BAOF: $0.025Ce^{3+}$; $0.005Eu^{2+/3+}$ phosphor maxima at 2.28 eV that recorded at 3.02 eV is further deconvoluted into six peaks: 2.48, 2.44, 2.36, 2.28, 2.18 and 2.10 eV (**Fig. 5.3(b)**). The similar peak positions of Ce^{3+} ions are due to its unchanged cationic substitutions, however, the occupancy ratio is found to be decreased, as indicated by the reduced peak intensities compared to that of S_2BAOF: $0.025Ce^{3+}$; $0.005Eu^{2+/3+}$. Meanwhile, two additional predominant peaks around 2.36 eV and 2.10 eV are corresponding to Eu^{2+} ions' occupancy in *4a* and *8h* sites, respectively. Hence, incorporating Si^{4+} ions in SBAOF: $0.025Ce^{3+}$; $0.005Eu^{2+/3+}$ phosphor, the site occupation of Eu^{2+} ions is drastically enhanced, whereas Ce^{3+} site occupation reduced, and the emission maxima red-shifted by around 45 nm. These findings can be correlated with the XRD refinement results, i.e. after doping the Si^{4+} ion to the Al^{3+} sites, the neighboring two cationic sites 4a (Ba-O_8F_2) and 8h (Sr-O_6F_2) are enlarged along with the increase in the Eu^{3+} to Eu^{2+} conversion rate.

The Eu valence states in SBAOF: $0.025Ce^{3+}$; $0.005Eu^{2+/3+}$ and S_2BAOF: $0.025Ce^{3+}$; $0.005Eu^{2+/3+}$ phosphors are further confirmed by detailed photoluminescence analysis. Fig. 5.3(c) depicts the excitation and emission spectra of SBAOF: $0.025Ce^{3+}$; $0.005Eu^{2+/3+}$ and S_2BAOF: $0.025Ce^{3+}$; $0.005Eu^{2+/3+}$ phosphors recorded at 310 nm and 400 nm, respectively. In the case of emission spectra of SBAOF: $0.025Ce^{3+}$; $0.005Eu^{2+/3+}$ phosphor, a broad peak at 501 nm corresponding to $5d^1 - 4f^1$ transition of Ce^{3+} ions and additional sharp peaks at 577 nm, 588 nm, and 616 nm correspond to intra *f-f* transition

peaks of Eu^{3+} ions. But no Eu^{3+} ions' *f-f* excitation transition peaks are observed for S_2BAOF: 0.025Ce^{3+}; 0.005Eu^{2+} phosphor, and a broader red-shifted emission band maximum at 545 nm with enhanced intensity is detected. The europium 2+/3+ oxidation states in SBAOF: 0.025Ce^{3+}; 0.005$Eu^{2+/3+}$ and S_2BAOF: 0.025Ce^{3+}; 0.005$Eu^{2+/3+}$ phosphors are again confirmed by recording the high-resolution XPS spectra of Eu atoms in the respective phosphors, as illustrated in **Fig. 5.3(f)** and **Fig. 5.3(g)**, respectively. The binding energy values around 1136 eV and 1161 eV are corresponding to the presence of $3d_{5/2}$ and $3d_{3/2}$ orbitals of Eu^{3+} ions, respectively, in SBAOF: 0.025Ce^{3+}; 0.005$Eu^{2+/3+}$ phosphor (**Fig. 3(f)**). The binding energy value observed around 1129 eV and 1157 eV are corresponding to the presence of $3d_{5/2}$ and $3d_{3/2}$ orbitals of Eu^{2+} ions in S_2BAOF: 0.025Ce^{3+};0.005$Eu^{2+/3+}$ phosphor, respectively (**Fig. 5.3(g**)). These results are correlated with the XRD refinement results and again prove the findings that after Si incorporation more Eu^{3+} ions are converted to Eu^{2+} ions and easily occupied in the respective enlarged cationic sites (as represented in **Fig. 5.1(e)**) and involved in the energy transfer mechanism with Ce^{3+} ions in the same cationic sites of S_2BAOF: 0.025Ce^{3+}; 0.005Eu^{2+} phosphor.

When Ce^{3+} and Eu^{2+} are in the same crystal environment, the *5d-4f* transition energy of Ce^{3+} is slightly higher than that of Eu^{2+} ions due to the superior effective nuclear charge practiced by the 5d electrons in Ce^{3+} ions because of its greater positive charge, triggering a stronger attraction and a greater energy gap between the 4f and 5d levels [42]. To investigate the energy transfer mechanism in S_2BAOF: 0.025Ce^{3+}; xEu^{2+} phosphor, the excitation and emission spectra of S_2BAOF: 0.025Ce^{3+} and S_2BAOF: 0.025Ce^{3+}; 0.001Eu^{2+} phosphors are further analyzed and shown in **Fig. S3(a)**. There is a significant spectral overlap observed in the range between 430 nm to 500 nm indicating the effective energy transfer from Ce^{3+} to Eu^{2+} in S_2BAOF: 0.025Ce^{3+};0.001Eu^{2+} phosphor. With the increase in Eu doping concentrations, the emission intensity of Ce^{3+} ions in S_2BAOF: 0.025Ce^{3+}; xEu^{2+} phosphor (x = 0.00 to 0.01) reduced and emission maxima shifts towards the higher wavelength side. The energy transfer efficiency in S_2BAOF: 0.025Ce^{3+}; xEu^{2+} (x = 0.00 to 0.01) phosphor can be calculated by using the equation:

$$\eta T = 1 - Is/I_{S0} \qquad (5.2)$$

Where η_T is the energy transfer efficiency, I_{so} and I_s are the emission intensity of Ce^{3+} ions in the absence and presence of Eu^{2+} ions in $S_2BAOF: 0.025Ce^{3+}; xEu^{2+}$ phosphors [42]. As on increasing Eu^{2+} ion doping concentration the energy transfer efficiency is found to be increased and the Ce^{3+} emission intensity recorded at 400 nm decreases. The corresponding intensity variation and calculated η_T for different Eu concentrations is represented in Fig. S3(b). These results again prove the existence of energy transfer from Ce^{3+} to Eu^{2+} in $S_2BAOF: 0.025Ce^{3+}; xEu^{2+}$ phosphor (x = 0.00 to 0.01). For understanding the energy transfer behavior from Ce^{3+} to Eu^{2+} ions, Dexter's energy transfer expression and Reisfeld's approximation are used for the evaluation as given below.

$$\frac{Iso}{Is} \alpha C^{\alpha}/3 \qquad (5.3)$$

Here, C is the total concentration of Ce^{3+} and Eu^{2+} ions, I_s and I_{so} is the emission intensities of Ce^{3+} ions in the presence and absence of Eu^{2+} ions in $S_2BAOF: 0.025Ce^{3+}; xEu^{2+}$ phosphors. The value of α equal to 3, 6, 8, and 10 corresponds to exchange interaction, d - d, d - q, and q - q multipolar interactions [42]. The conforming fitting results are shown in Fig. S4, among which, the best linear relation is observed to be α equal to 8 and 10 which signifies that the energy transfers from Ce^{3+} to Eu^{2+} are dominated by the multipolar interactions like d - q, or q - q in $S_2BAOF: 0.025Ce^{3+}; xEu^{2+}$ phosphors. This energy transfer mechanism is further proven from the emission lifetime data of $S_2BAOF: 0.025Ce^{3+}; xEu^{2+}$ (x = 0.00 and 0.001) phosphors recorded at λ_{ex} = 400 nm and λ_{em} = 516 nm, as shown in **Fig. 5.3(h)**. The average lifetime value τ_{av} is calculated to be 57.22 ns, and 56.80 ns for $S_2BAOF: 0.025Ce^{3+}; xEu^{2+}$ (x = 0.00 and 0.001) phosphors, respectively. Introducing Eu^{2+} ions in $S_2BAOF: 0.025Ce^{3+}$ phosphor may directly enhance the additional decay channels of Ce^{3+} ions, due to which the emission lifetime may reduce. These results confirm the existence of energy transfer from Ce^{3+} to Eu^{2+} in $S_2BAOF: 0.025Ce^{3+;} xEu^{2+}$ phosphors. The τ_{av} value for $S_2BAOF: 0.001Eu^{2+}$ phosphor is observed to be 48.87 ns, which is lesser than that of the codoped sample, further confirming the energy transfer from Eu^{2+} - Ce^{3+} [43].

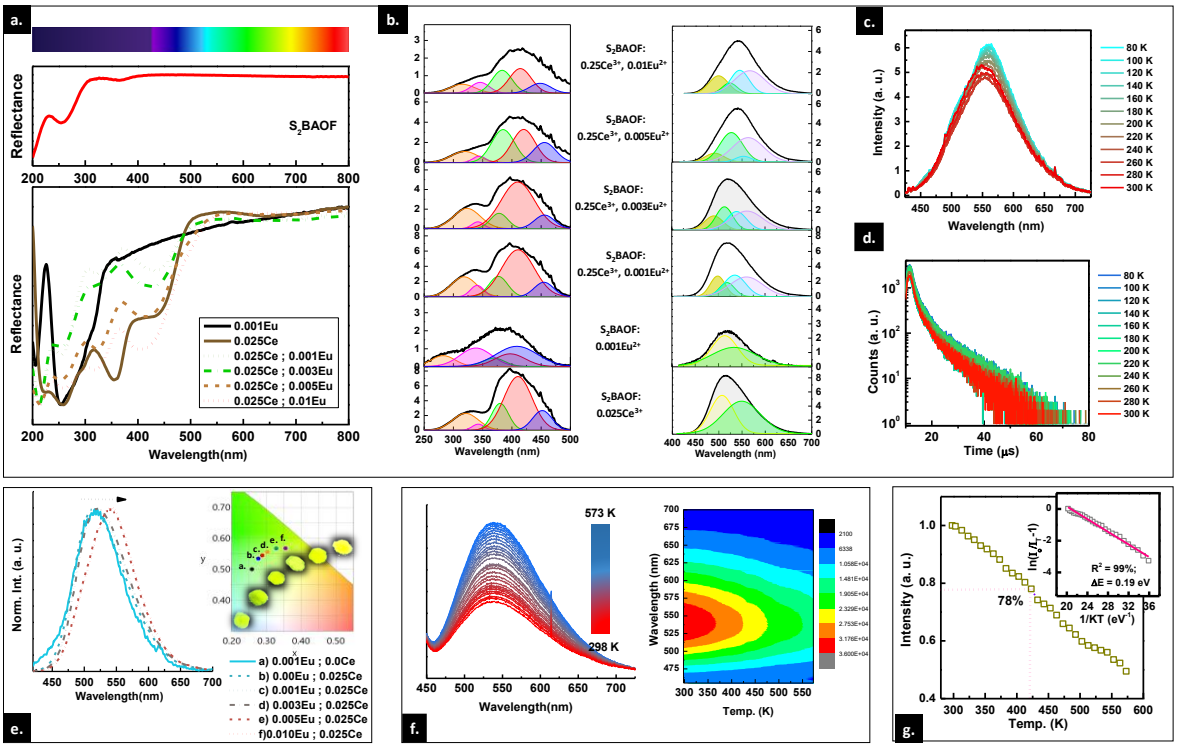

Fig. 5.4: (a) *UV-Vis DRS of S_2BAOF, S_2BAOF: $0.001Eu^{2+}$, S_2BAOF: $0.025Ce^{3+}$ and S_2BAOF: $0.025Ce^{3+}$; xEu^{2+} (x = 0.001 to 0.01) phosphors.* ***(b)*** *Decovoluted PL excitation and emission spectra of S_2BAOF: $0.001Eu^{2+}$, S_2BAOF: $0.025Ce^{3+}$ and S_2BAOF: $0.025Ce^{3+}$; xEu^{2+} (x = 0.001 to 0.01) phosphors recorded at λ_{ex} = 400 nm and λ_{em} = 500 - 550 nm.* ***(c and d)*** *Low-temperature PL emission spectra and decay plots of S_2BAOF: $0.025Ce^{3+}$;$0.005Eu^{2+}$ phosphor, respectively.* ***(e)*** *Normalized PL emission spectra and corresponding CIE diagram of S_2BAOF: $0.001Eu^{2+}$, S_2BAOF: $0.025Ce^{3+}$, and S_2BAOF: $0.025Ce^{3+}$; xEu^{2+} (x = 0.001 to 0.01).* ***(f)*** *Temperature-dependent PL emission spectra and corresponding contour representation of S_2BAOF: $0.025Ce^{3+}$;$0.005Eu^{2+}$ phosphor.* ***(g)*** *Temperature-dependent PL intensity variation along with the Arrhenius plotting (inset) of S_2BAOF: $0.025Ce^{3+}$;$0.005Eu^{2+}$ phosphor.*

Fig. 5.4(a) represents the diffuse reflectance spectra of S_2BAOF and S_2BAOF: $0.025Ce^{3+}$; xEu^{2+} (x = 0.00 to 0.01) phosphors. For the S_2BAOF sample, a small absorption peak at 255 nm corresponding to the host charge transfer band (CTB) was observed. After Eu^{2+} ions' doping to this host, two broad absorption peaks have appeared; the major absorption peak covering 225 nm to 340 nm corresponds to Eu^{2+} - O^{2-} CTB and a small absorption band appears in the region 350 nm to 385 nm corresponds to $4f^6 5d^1$ - $4f^7$ transitions of Eu^{2+} ions. In the case of S_2BAOF: $0.025Ce^{3+}$ phosphor, several

broad peaks appear in the UV-Vis region with peak maxima at 255 nm corresponding to Ce^{3+} - O^{2-} CTB, peaks around 356 nm and 440 nm representing the allowed transitions of Ce^{3+} ions. When Eu^{2+} ion doped into S_2BAOF: $0.025Ce^{3+}$ phosphor, the combined absorption of Ce^{3+} and Eu^{2+} ions are observed for S_2BAOF: $0.025Ce^{3+}$; xEu^{2+} (x = 0.00 to 0.01) phosphor series. As of increasing Eu doping concentration the characteristic absorption peak of Eu^{2+} ions centered at 320 nm and the violet centered at around 410 nm are predominant. These interpretations are again correlated with the optical band gap calculation by using the Kubelka – Munk function [47],

$$F(R) = \frac{(1-R)^2}{2R} \qquad (5.4)$$

From the Tauc plot, the band gap value can be calculated by drawing a tangent line at the inflection point (n = ½ for direct allowed transition). For free Eu^{2+} ions in S_2BAOF: $0.001Eu^{2+}$ the band gap between *4f* and *5d* excited states is calculated at about 4.2 eV. After doping into the S_2BAOF: $0.025Ce^{3+}$ system, the excited state of Eu^{2+} ions interact with the surrounding atoms in the same coordination environment and may lead to a red shift in the band gap energy value as illustrated in **Fig. S5**. The wide optical band gap > 4 eV meets the criteria of a suitable host for doping and pc-LED applications.

The PL excitation and emission spectra of a series of S_2BAOF: $0.025Ce^{3+}$; xEu^{2+} (x = 0.00 to 0.01) phosphors as shown in **Fig. 5.4(b)**. The broad excitation peak covering from 250nm to 500 nm is recorded at an emission range of 515 nm to 550 nm and is further deconvoluted into five peaks. The overall excitation and emission spectra of S_2BAOF: $0.025Ce^{3+}$; xEu^{2+} (x = 0.00 to 0.01) phosphor is a combination of both Ce^{3+} and Eu^{2+} transitions. Comparing the emission spectra of S_2BAOF: $0.025Ce^{3+}$ and S_2BAOF: $0.001Eu^{2+}$ phosphors with that of S_2BAOF: $0.025Ce^{3+;}$ xEu^{2+} (x = 0.00 to 0.01) phosphors recorded at 400 nm, the emission peaks corresponding to Ce^{3+} ions' occupancy in the *4a* and *8h* sites keeps the peak position at 500 nm and 550 nm, respectively, however, these peaks' intensities are found to be decreased after increasing the Eu^{2+} ions' concentrations. Whereas for S_2BAOF: $0.001Eu^{2+}$ phosphor, transition peaks of Eu^{2+} ions' located in the *4a* and *8h* sites are found to be at 513 nm and 538 nm, respectively. Gradually increasing the doping concentrations of Eu^{2+} ions in S_2BAOF: $0.025Ce^{3+}$ phosphor elaborated two increasingly additional peaks of Eu^{2+} ions located in both the cationic sites, as observed

in the photoluminescence profiles of $S_2BAOF: 0.025Ce^{3+}; xEu^{2+}$ (x = 0.00 to 0.01) phosphor series. Increasing the Eu concentration from 0.001 to 0.01 redshifted the Eu^{2+} peak positions from 513 nm to 527 nm in the *4a* sites and 538 nm to 564 nm in the *8h* sites, respectively. Whereas the Ce^{3+} peak positions remained as same as that in $S_2BAOF: 0.025Ce^{3+}$ phosphor. Furthermore, the peak intensity for Eu^{2+} transitions in *4a* and *8h* sites are observed to be enhanced and Ce^{3+} transition peaks in both the cationic sites are diminishing. These results signify the fact that there is an effective energy transfer happens from Ce^{3+} to Eu^{2+} centers.

The site occupation and emission behavior of activator ions in $S_2BAOF: 0.025Ce^{3+}; xEu^{2+}$ phosphor series is again correlated with the low-temperature emission and decay studies of $S_2BAOF: 0.025Ce^{3+}; 0.005Eu^{2+}$ phosphor as shown in **Fig. 5.4(c)** and **(d)**. The emission behavior of $S_2BAOF: 0.025Ce^{3+}; 0.005Eu^{2+}$ phosphor has been studied in the temperature range of 80 K to 300 K as shown in **Fig. 5.4(c)**. The electron-phonon interaction is normally weaker at lower temperatures, which reduces the dissociation of excitons and subsequently enhances the emission intensity at temperatures lower than room temperature [5, 48]. The site occupation of Ce^{3+}/Eu^{2+} ions is again confirmed from the deconvolution Gaussian fitting of $S_2BAOF: 0.025Ce^{3+}; 0.005Eu^{2+}$ phosphor recorded at 280 K and 300 K as shown in **Fig. 5.S6**. The broad emission band is deconvoluted into four peaks at 498 nm, 530 nm, 554 nm and 590 nm corresponding to Ce_{4a}, Eu_{4a}, Ce_{8h}, and Eu_{8h} occupied transition peaks recorded at 300 K, respectively. Among this, the Ce^{3+} ion transition peaks are the same as that of $S_2BAOF: 0.025Ce^{3+}$ phosphor. But the peak intensity of Ce^{3+} occupied sites decreases and Eu^{2+} ion occupied sites peak intensity, as well as broadness of peaks, are enhanced and more shifted towards the right as compared with $S_2BAOF: 0.025Ce^{3+}$ and $S_2BAOF: 0.001Eu^{2+}$ phosphors Gaussian fitting results as shown in **Fig. 5.4(b)**. These low-temperature emission deconvolutions results are similar with the Gaussian fitting results of $S_2BAOF: 0.025Ce^{3+}; xEu^{2+}$ phosphor series recorded at RT as shown in **Fig. 5.4(b).** The decay behavior of Ce^{3+} ions in $S_2BAOF: 0.025Ce^{3+}; 0.005Eu^{2+}$ phosphor emission at 550 nm and excitation at 400 nm recorded in the temperature range of 80 K to 300 K is well fitted by double exponential functions with fast and slow components of the decay time by using the formula:

$$I = A1\exp(-t/\tau 1) + A2\exp(-t/\tau 2) \qquad (5.5)$$

A_1 and A_2 are the fitting parameters, τ_1, and τ_2 are the fast and slow decay time and I is the luminous intensity [49]. Double exponential indicates that there are two dominant types of activator ions in the lattice. Faster luminescence decay time, which is the cause of long-wavelength emission, and shorter luminescence decay time is the cause of short-wavelength emission. The calculated average lifetime value for S_2BAOF: $0.025Ce^{3+;}$ $0.005Eu^{2+}$ phosphor at 80K and 300K obtained to be 1.95 ms and 1.67 ms, respectively. As temperature increases the decay channels of Ce^{3+} are found to be decreases. Because at the higher temperature, there is a greater chance for Ce^{3+} - Eu^{2+} energy transfer to happen than at low temperatures. Consequently, the Ce^{3+} peak intensity at both the cationic sites is found to be decreased and the Eu^{2+} ion occupied sites intensity becomes enhanced as well as broadness of emission peak towards the higher wavelength side is observed. These results again confirm the fact that in S_2BAOF: $0.025Ce^{3+;}$ $0.005Eu^{2+}$ phosphor Ce^{3+} - Eu^{2+} energy transfer happens and as on increasing Eu doping concentration, more Eu^{2+} ions are easily occupied in the enlarged cationic sites and consequently, the emission intensity decreases and emission spectra are shifted more towards higher wavelength side. The corresponding PL emission shift of S_2BAOF: $0.025Ce^{3+;}$ xEu^{2+} (x = 0.00 to 0.01) phosphors and their CIE coordinates representation is shown in **Fig. 5.4(e)**. There is a spectral shift from 515 nm to 550 nm i.e. around 35nm peak shift is observed in S_2BAOF: $0.025Ce^{3+;}$ xEu^{2+} (x = 0.00 to 0.01) phosphor series. The inset of the CIE diagram shows the UV images of corresponding phosphors from greenish to yellow region.

To further examine the thermal quenching behavior of S_2BAOF: $0.025Ce^{3+}$; xEu^{2+} phosphors for the performance in WLED application, we recorded the temperature dependant emission spectra of S_2BAOF: $0.025Ce^{3+}$; $0.005Eu^{2+}$ phosphor in the range of 298 K to 573K as represented in **Fig. 4(f)**. The PL emission intensity variation and the corresponding condor representations are shown in **Fig. 5.4(f)**. As the temperature increases the emission intensity is found to decrease and retain the integrated emission intensity at around 78% as compared with the room temperature initial intensity (Fig. 4(g)). The activation energy of the S_2BAOF: $0.025Ce^{3+;}$ $0.005Eu^{2+}$ phosphor can be calculated by using the Arrhenius equation [50],

$$I_T = \frac{I_0}{1+A\exp\left(-\frac{\Delta E}{kT}\right)} \qquad (5.6)$$

where I_0 and I_T is the initial emission intensity and emission intensity at various temperatures, A is a constant, ΔE is the activation energy, k is the Boltzmann's constant (8.62×10^{-5} eV K^{-1}), and T is the temperature in K [51]. The inset of Fig. 4(g) represents the activation energy (ΔE) calculation plot. The obtained value of activation energy for S_2BAOF: 0.025Ce^{3+}; 0.005Eu^{2+} phosphor is 0.19 eV, which is comparable with the ΔE value for commercial BAM: Eu^{2+} phosphor [51]. The high thermal stability of this phosphor meets the criteria for practical warm WLED applications.

The comparative emission spectra of S_2BAOF: 0.025Ce^{3+};0.005Eu^{2+} phosphor and absorption spectrum of $BaSO_4$ are recorded using a Yvon Fluorolog 3 spectrofluorometer instrument for calculating the internal quantum efficiency (IQE), and the resultant spectra are displayed in **Fig. 5.S6(c)** in the supporting information. The IQE value was calculated using equation 7 given below [50],

$$\eta_{IQE} = \frac{\int L_S}{\int E_R - \int E_S} \qquad (5.7)$$

where $\int L_S$ is the integrated area under the emission curve of the sample, $\int E_S$ and $\int E_R$ indicate the area under the excitation spectra with and without the sample in the integrating sphere, respectively. The IQE of the emission res shifted yellow emitting S_2BAOF: 0.025Ce^{3+};0.005Eu^{2+} phosphor under 400 nm is observed to be 86%.

5.4.3. Structural and photoluminescence analysis of CTU/n%S_2BAOF: 0.025Ce^{3+};0.005Eu^{2+} composites

Fig. 5.S7(a) shows the FTIR spectra of CPE, TCPE, IC-25NY, S_2BAOF: 0.025Ce^{3+};0.005Eu^{2+}, CTU, and CTU/40%S_2BAOF: 0.025Ce^{3+};0.005Eu^{2+}, respectively. The characteristic peak at 3372 cm^{-1} corresponding to -OH has been reduced, and the appearance of an additional peak at 1711 cm^{-1} for -C=O in the TCPE spectrum verifies the esterification reaction between CPE and 3-Mercaptopropionic acid. In addition, the low-intensity peak at 2579 cm^{-1} in TCPE, attributed to the -SH group, confirms the successful modification of CPE with 3-Mercaptopropionic acid (**Fig. S7(b)**) [52-53]. The broad peak at 3291 cm^{-1} in CTU corresponds to the -NH functional group in thiourethane, suggesting the formation of amide bonds. The IC-25NY spectrum shows a unique peak at 2250 cm^{-1}, attributed to the -NCO group, which disappears in the CTU and

CTU/40%S_2BAOF: 0.025Ce^{3+};0.005Eu^{2+} spectra, indicating the complete cross-linking of the film. **Fig. 5.S7(c)** shows a sharp peak at 855 cm^{-1} in CTU/40%S_2BAOF: 0.025Ce^{3+};0.005Eu^{2+} attributed to the metal oxide bonds in the inorganic particles [54]. The ^{1}H NMR spectra of CPE and TCPE are shown in Fig. S7(d). The additional peaks at 2.69 ppm and 2.76 ppm in TCPE correspond to the methyl group adjacent to -C=O and -SH, respectively [55]. From the FTIR and ^{1}H NMR spectra, the thiolation of CPE using 3-Mercaptopropionic acid and the formation of thiourethane after reaction with IC-25NY has been confirmed.

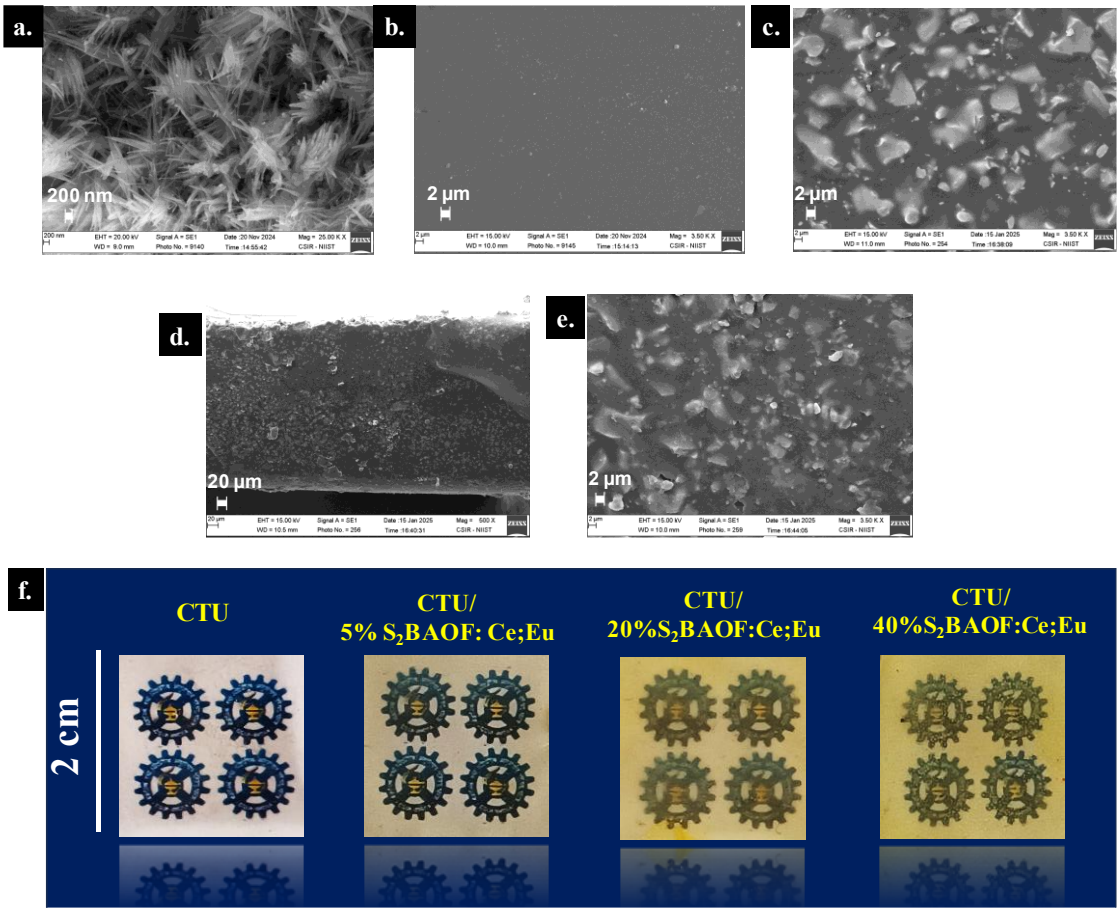

Fig. 5.5: *SEM images of (a) S_2BAOF: 0.025Ce^{3+};0.005Eu^{2+} powders, (b) CTU, (c) CTU/40%S_2BAOF: 0.025Ce^{3+};0.005Eu^{2+}, (d) lower and (e) higher magnification cross-sectional micrograph of CTU/40%S_2BAOF: 0.025Ce^{3+};0.005Eu^{2+}. (f) Daylight images of CTU and CTU/n%S_2BAOF: 0.025Ce^{3+};0.005Eu^{2+} (n = 0, 5, 20, and 40).*

Fig. 5.S7(e) depicts the TGA thermogram of CTU and CTU/40%S_2BAOF: 0.025Ce^{3+};0.005Eu^{2+}. In the CTU thermogram, a two-stage degradation pattern has been

identified and first-stage degradation starts around 200°C and completes at 412°C with a weight loss of 65% attributed to urea bond cleavage and aliphatic chain scission [56]. The second degradation happens at the temperature range from 400°C to 480°C with 25% loss corresponding to rupture of aromatic rings and residual degradation. In contrast, CTU/40%S_2BAOF: 0.025Ce^{3+};0.005Eu^{2+} shows two-stage degradation with initial degradation starting at much lower temperatures corresponding to the dehydration and ending at 370°C with 50% degradation. The second degradation mass loss of CTU/40%S_2BAOF: 0.025Ce^{3+};0.005Eu^{2+} is lower compared to CTU with a 10% reduction in weight loss attributed to the incorporation of S_2BAOF: Ce; Eu and modified the rigidity of polymer backbone and improved thermal stability. Likewise, CTU/40%S_2BAOF: 0.025Ce^{3+};0.005Eu^{2+} composite exhibited a higher char residue value of 31% up to 700°C, wherein CTU displayed no char residue due to complete degradation of thiourethane. From the TGA thermogram of CTU and CTU/40%S_2BAOF: Ce; Eu composite shows good temperature stability and incorporation of S_2BAOF: Ce; Eu helps to inhibit the weight loss of CTU composite in high temperature. **Fig. 5.S7(f)** shows the comparative UV-Vis spectra of CTU and CTU/40%S_2BAOF: 0.025Ce^{3+};0.005Eu^{2+} composite. Herein, CTU does not show any dominant absorption in the UV region, which makes it suitable for phosphor-polymer composite synthesis. CTU/40%S_2BAOF: 0.025Ce^{3+};0.005Eu^{2+} composite shows broad UV-to-violet absorption dip corresponding to the *4f-5d* transitions of activator ions. These results directly indicate that the CTU polymer matrix is not preventing phosphor irradiations under UV to violet spectra.

The SEM micrographs of S_2BAOF: 0.025Ce^{3+};0.005Eu^{2+} powder particles, CTU matrix, and CTU/40%S_2BAOF: 0.025Ce^{3+};0.005Eu^{2+} composite are shown in **Fig. 5(a)** to **5.5(c)**, respectively. **Fig. 5.5(a)** again confirmed nanorod-type morphology for the synthesized phosphor particles. Fig. 5(b) displayed the surface of the CTU film and showed no defects indeed suggesting the uniformity of the surface without phase separation during the formation of thiourethane. Additionally, **Fig. 5.5(c)** exhibits the surface SEM micrograph of S_2BAOF: Ce; Eu embedded CTU film and shows a uniform distribution of phosphor particles in the CTU matrix. Moreover, the uniform distribution of particles can also be seen in cross-sectional images of CTU/40%S_2BAOF: 0.025Ce^{3+};0.005Eu^{2+} in **Fig. 5.5(d)** (lower magnification) and **Fig. 5.5(e)** (higher magnification). Eventually, the homogeneity in the phosphor particles' distribution and

transparency can also be well understood from the daylight images of CTU and CTU/n%S_2BAOF: 0.025Ce^{3+};0.005Eu^{2+} (n = 0, 5, 20, and 40), as shown in **Fig. 5.5(f)**. Further, the cross-sectional EDX elemental analysis of the CTU matrix and CTU/40%S_2BAOF: 0.025Ce^{3+};0.005Eu^{2+} composite are shown in the supporting information **(Fig. S8** and **Fig. S9**, respectively). The traces of all the elements that belong to the CTU matrix and CTU/40%S_2BAOF: 0.025Ce^{3+};0.005Eu^{2+} composite are clearly seen in the conforming EDX spectrum and inset tables (**Fig. S8(a**) and **Fig. 5.S9(a)**). The corresponding cross-sectional scanned SEM images **(Fig. 5.S8(b)** and **Fig. 5.S9(b))** and the mapped elemental distributions **(Fig. S8(c)** and **Fig. S9(c))** of the CTU matrix and CTU/40%S_2BAOF: 0.025Ce^{3+};0.005Eu^{2+}composite are observed to be almost uniform.

To understand the mechanical properties of the obtained composites, tensile tests have been carried out using the ASTM D638 standards, and results are shown in **Fig. 5.S10(a)** and **5.S10(b)**. In contrast to bare, the composite film possesses ~12% increase in tensile strength and ~10% increment in elongation. This outcome is attributed to the effective stress transfer that takes place from the polymer matrix to the filler particles, which helps to absorb more energy. The densely packed elemental distribution of the phosphor powder within the CTU matrix and the uniform distribution of phosphor particles enable applied stress to transfer symmetrically and improve the load-bearing capacity of the composite.

5.4.4 Analysing WLED performances of S_2BAOF: 0.025Ce^{3+}; 0.005Eu^{2+} powder and CTU/40%S_2BAOF: 0.025Ce^{3+}; 0.005Eu^{2+} composite

Eventually, the CTU/40%S_2BAOF: 0.025$Ce^{3+;}$ 0.005Eu^{2+} flexible composite also retained around 78% PL emission intensity compared to the room temperature emission intensity, as shown in **Fig. 5.S11**. For further evaluating the WLED performances, two WLEDs are fabricated; one with S_2BAOF: 0.025Ce^{3+}; 0.005Eu^{2+} phosphor coated on a violet LED chip (3 W) and another with CTU/40%S_2BAOF: 0.025Ce^{3+};0.005Eu^{2+} flexible composite placed on a similar violet LED chip (3 W). The electroluminescence (EL) spectrum of phosphor powder and composite-based WLEDs along with the respective CIE diagrams and illuminated WLED images, are shown in **Fig. 5.6(a)** and **(b)**, respectively. The phosphor powder-based WLED exhibited warm white light with a CCT ~3767 K and CRI ~75 with high lumen efficiency (136 lm/W). The composite-based WLED exhibited warm white light with a CCT of 4087 K, CRI of 78, and lumen

efficiency of 117 lm/W. The results indicated that the high refractive index CTU-based polymer encapsulation improved the optical performance of the used phosphor. To further investigate this point, we performed the photobleaching study and power-dependant EL study for both S_2BAOF: $0.025Ce^{3+};0.005Eu^{2+}$ phosphor powder and CTU/40%S_2BAOF: $0.025Ce^{3+};0.005Eu^{2+}$ flexible composite.

Fig. 5.S12(a) and **5.S12(b)** represent the plots of emission intensity vs irradiation time of S_2BAOF: $0.025Ce^{3+}$; $0.005Eu^{2+}$ phosphor and CTU/40%S_2BAOF: $0.025Ce^{3+};0.005Eu^{2+}$ composite, respectively, under a violet LED (410 nm) exposure over a period of time. As compared with the initial intensity, a 6% emission intensity reduction is observed in the case of S_2BAOF: $0.025Ce^{3+};0.005Eu^{2+}$ phosphor powder upon 1 h continuous exposure of violet LED light with 3 W power. Whereas, only 2% emission intensity decay is observed for the phosphor-polymer composite under identical conditions. Such improved photo-stability of CTU/40%S_2BAOF: $0.025Ce^{3+};0.005Eu^{2+}$ composite may be due to the reduced moisture absorption content because of phosphor powder's encapsulation into a highly stable CTU polymer matrix. Further, the comparative photoluminescence properties (λ_{EXC}, λ_{EM}, IQE, CRI, and CCT) of S_2BAOF: $0.025Ce^{3+}$; $0.005Eu^{2+}$ with those of recently reported violet excitable and broadband emitting Ce^{3+}/Eu^{2+}-activated phosphors used as a single component for making WLED prototypes are listed in Table S4 of the supporting information.

The power-dependent EL spectra of phosphor powder and composite, recorded under 12 V forward bias with current in the range of 600 mW to 1200 mW are illustrated in **Fig. 5.6(c)** and **5.6(d)**. As the forward bias current increases, the EL intensity under violet LED for both the phosphor and composites is also increased drastically. The trend of intensity enhancement for the composite is better than that of phosphor powder, which might be due to the influence of the high refractive index of CTU polymer in the optical performance of the composite. Meanwhile, the color coordinates, CRI, and CCT have not shifted significantly with the change of LED powers from 600 mW to 1200 mW, as represented in **Fig. 5.6(c)** and **5.6(d).** As shown in these insets, white light with CRI of ~76, CCT ~3804 K has been obtained for CTU/40%S_2BAOF: $0.025Ce^{3+};0.005Eu^{2+}$ composite-based WLED at 1200 mW (**Fig. 5.6(c)**). Under the same power, S_2BAOF: $0.025Ce^{3+};0.005Eu^{2+}$ phosphor powder-based WLED slightly underperformed by showing the CRI of ~75 and CCT of ~4122 K.

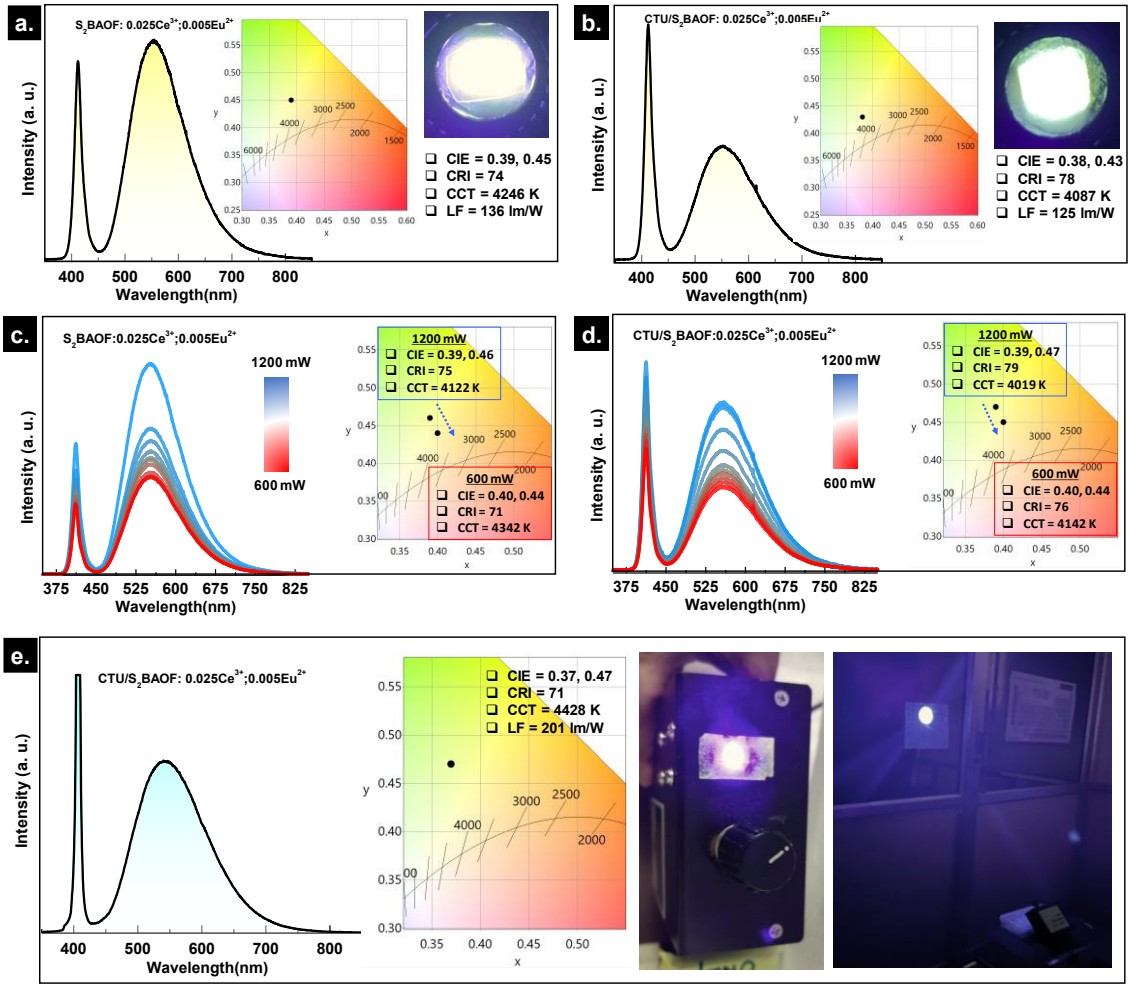

Fig. 5.6: *Electroluminescence spectra, the corresponding chromatic diagrams (insets) and device illumination images (insets) of violet source-based pc-WLEDs assembled with* ***(a)*** *$S_2BAOF: 0.025Ce^{3+};0.005Eu^{2+}$ powder and* ***(b)*** *$CTU/40\%S_2BAOF: 0.025Ce^{3+};0.005Eu^{2+}$ composite. Power-dependent electroluminescence spectra and corresponding chromatic drift (insets) of violet source-based pc-WLEDs assembled with* ***(c)*** *$S_2BAOF: 0.025Ce^{3+};0.005Eu^{2+}$ powder and* ***(d)*** *$CTU/40\%S_2BAOF: 0.025Ce^{3+};0.005Eu^{2+}$ composite.* ***(e)*** *EL spectrum, the corresponding chromatic diagram, and performance (inset) of the laser-triggered $CTU/40\%S_2BAOF: 0.025Ce^{3+};0.005Eu^{2+}$ composite.*

Thermally stable and highly efficient phosphor polymer composites are rarely reported as a color converter for high-power laser lighting applications. To assess the same, finally, the laser-irradiated emission properties of both yellow emitting $S_2BAOF: 0.025Ce^{3+};0.005Eu^{2+}$ phosphor powder and $CTU/40\%S_2BAOF: 0.025Ce^{3+}; 0.005Eu^{2+}$

composite are studied under a 405 nm violet laser of power 1.4 W/mm^2. Its electroluminescence (EL) spectrum is plotted in Fig. 6(e), and the corresponding CIE (x, y), CCT, and CRI are calculated to be (0.37, 0.47), ~4428 K, and ~71, respectively. The luminous flux was estimated to be ~201 lm/W. Meanwhile, the emission intensity variation of CTU/40%S_2BAOF: 0.025Ce^{3+};0.005Eu^{2+} composite under prolonged 405 nm laser irradiation indicates the sustainability of around 86% of emission intensity after 24 h of laser exposure (**Fig. 5.S13**).

The laser-triggered optical features of the optimized CTU/40%S_2BAOF: 0.025Ce^{3+}; 0.005Eu^{2+} composite are comparable with those of recently reported YAG: Ce^{3+} ceramic phosphor or composite (**Table 5.S5**). It is observed that the optimized yellow emitting S_2BAOF: 0.025Ce^{3+};0.005Eu^{2+} phosphor and CTU/S_2BAOF: 0.025Ce^{3+};0.005Eu^{2+} composite could able to replace the disadvantages of commercial YAG: Ce^{3+} ceramic phosphor i.e. with comparable lm/W as well as CRI, however, lower CCT, and most importantly with negligible blue light hazards. Further, the 405 nm laser-triggered lighting performance of the CTU/S_2BAOF: 0.025Ce^{3+};0.005Eu^{2+} composite is also shown in **Fig. 5.6(e).** This type of laser-triggered lightning could be very useful to make vehicle headlights for the extended visibilities which could enable better road sign legibility farther away and allow for responding to threats faster.

5.5. Conclusions

In summary, a series of efficient violet excitable single-component broadband-emitting S_2BAOF: 0.025Ce^{3+}; xEu^{2+} phosphors are developed, which are crystallized in non-centrosymmetric tetragonal phase with space group of *I4/mcm*. The obtained S_2BAOF: 0.025Ce^{3+}; xEu^{2+} phosphors displayed a broadband yellow emission at ~400 nm with the red-shifted peak positions from 501 nm to 545 nm with the increase in Eu^{2+} concentrations from 0.0 to 0.01. The connection between the photoluminescent behaviors and XRD-evaluated lattice information is analyzed in detail. The Ce^{3+}, and Eu^{2+} codoped S_2BAOF phosphors exhibited elevated luminescent properties because of the nonradiative energy transitions between Ce^{3+} to Eu^{2+} ions in the present host. Besides, the encapsulation of S_2BAOF: 0.025Ce^{3+};0.005Eu^{2+} phosphor in a thiourethane (CTU) matrix with high refractive index results in flexible phosphor-polymer composite films with higher photoluminescent stability. The as-obtained pc-WLED assembled with CTU/40%S_2BAOF: 0.025Ce^{3+};0.005Eu^{2+} composite film and a 410 nm violet LED chip

generated white light with a CRI ~75 and CCT ~3767 K and a luminous flux of 117 lm/W. The laser-triggered warm white light has been realized from the same composite with a CRI of 71 and CCT of 4428 K and a luminous flux of 201 lm/W. The outcomes indicate that S_2BAOF: $0.025Ce^{3+};0.005Eu^{2+}$ phosphor and CTU/S_2BAOF: $0.025Ce^{3+};0.005Eu^{2+}$ composite film are promising candidates for violet excitable next-generation lighting appliances.

5.6 References

[1] S. Dutta, S. Som, M. L. Meena, R. Chaurasiya, T. M. Chen, Multisite-Occupancy-Driven Intense Narrow-Band Blue Emission from $Sr_5SiO_4Cl_6:Eu^{2+}$ Phosphor with Excellent Stability and Color Performance, *Inorg. Chem.* **2020**, *59*, 1928.

[2] J. Li, Y. Sheng, G. Tang, H. Zhu, X. Tao, Y. Jiag, Anti-Solvent Synthesis of Three-Color Indium-Based Halide Perovskite Microplate/Microcrystal Phosphors for High Color Rendering WLEDs, *Adv. Opt.* Mater. **2023**, *11*, 2300100.

[3] M. Cao, J. Tian, W. Zhuang, R. Li, Y. Liu, G. Chen, G. Zhou, L. Wang, J. Wang, Multisite Cation Regulation of Broadband Cyan-Emitting $(Ba_{1-x}Sr_x)_9Lu_2Si_6O_{24}/Eu^{2+}$ Phosphors for Full-Spectrum WLEDs, *Inorg. Chem.* **2022**, *61*, 1805.

[4] Y. Gao, S. Murai, K. Shinozaki, J. Qiu, K. Tanaka, Phase-Selective Distribution of Eu^{2+} and Eu^{3+} in Oxide and Fluoride Crystals in Glass-Ceramics for Warm White-Light-Emitting Diodes, *ACS Appl. Electron. Mater.* **2019**, *1*, 961.

[5] M. Zhao, Z. Yang, L. Ning, Z. Xia, Tailoring of White Luminescence in a $NaLi_3SiO_4:Eu^{2+}$ Phosphor Containing Broad-Band Defect-Induced Charge-Transfer Emission, *Adv. Mater.* **2021**, *33*, 2101428.

[6] R. Verstraete, G. Rampelberg, H. Rijchaert, I. V. Driessche, E. Coetsee, M. M. Duvenhage, P. F. Smet, C. Detavernier, H. Swart, D. Poelman, Stabilizing fluoride phosphors: surface modification by atomic layer deposition, *Chem. Mater.* **2019**, *31*, 7192-7202.

[7] C. Y. Wang, O. M. Kate, S. Funahashi, M. Tansho, K. Deguchi, N. Hirosaki, T. Taketa, Single White-Emitting Phosphor $(Ba,Sr,Ce)_{4-m}Li(Si,Al)_{19+2m}(O,N)_{29+m}$ for White LEDs, *Chem. Mater.* **2023**, *35*, 2947-2955.

[8] C. Wang, Z. Yao, Y. Lei, K. Wu, W. Dai, M. Xu, Photoluminescence Tuning of Stable $CaYGaO_4$: Bi/Eu via Compositional Modulation and Crystallographic Site Engineering for nUV WLEDs, *Inorg. Chem.* **2024**, 63, *16056*.

[9] H. Chen, Y. Wang, $Sr_2LiScB_4O10:Ce^{3+}/Tb^{3+}$: A Green-Emitting Phosphor with High Energy Transfer Efficiency and Stability for LEDs and FEDs, *Inorg. Chem.* **2019**, *58*, 7440.

[10] J. Chan, L. Cao, W. Li, N. Ma, Z. Xu, X. Huang, Highly Efficient Broad-Band Green-Emitting Cerium(III)-Activated Garnet Phosphor Allows the Fabrication of Blue-Chip-Based Warm-White LED Device with a Superior Color Rendering Index, *Inorg. Chem.* **2022**, *61*, 6953.

[11] J. Qiao, L. Ning, M. S. Molokeev, Y. C. Chuang, Q. Zhang, K. R. Poeppelmeier, Z. Xia, Site-Selective Occupancy of Eu^{2+} Toward Blue-Light-Excited Red Emission in a $Rb_3YSi_2O_7$:Eu Phosphor, *Angew. Chemie - Int. Ed.* **2019**, *58*, 11521.

[12] S. Hariyani, J. Brgoch, Advancing Human-Centric LED Lighting Using $Na_2MgPO_4F:Eu^{2+}$, *ACS Appl. Mater. Interfaces* **2021**, *13*, 16669.

[13] J. D. Bullough, S. Peana, Investigating Blue-Light Exposure from: Lighting and Displays, *Frontier. Technology* **2020**, *36*, 17-20.

[14] G. Tosini, I. Ferguson, K. Tsubota, *Mol. Vis.* **2016**, 26900325.

[15] R. Shi, X. Zhang, Z. Qiu, J. Zhang, S. Liao, W. Zhou, X. Xu, L. Yu, S. Lian, Composition and Antithermal Quenching of Noninteger Stoichiometric Eu^{2+}-Doped Na-β-Alumina with Cyan Emission for Near-UV WLEDs, *Inorg. Chem.* **2021**, *60*, 19393.

[16] X. Chen, X. Huang, Full-Visible-Spectrum White LEDs Enabled by a Blue-Light-Excitable Cyan Phosphor, *ACS Appl. Mater. Interfaces* **2024**, *16*, 57376.

[17] Z. Leng, H. Bai, Q. Qing, H. He, J. Hou, B. Li, Z. Tang, F. Song, H. Wu, A Zero-Thermal-Quenching Blue Phosphor for Sustainable and Human-Centric WLED Lighting, *ACS Sustain. Chem. Eng.* **2022**, *10*, 10966.

[18] S. D. Baek, D. K. Kwan, Y. C. Kim, J. M. Myoung, Violet light-emitting diodes based on p-CuI thin film/n-MgZnO quantum dot heterojunction, *ACS Appl. Mater.* Interfaces **2020**, *12*, 6047.

[19] C. Y. Yang, S. Som, S. Das, C. H. Lu, Synthesis of $Sr_2Si_5N_8:Ce^{3+}$ phosphors for white LEDs via efficient chemical vapor deposition, *Scientific Reports* **2017**, *7*, 45832.

[20] D. Wen, H. Kato, M. Kakihana, Highly Robust Oxynitride Phosphor against Thermal Oxidization and Hydrolysis, *ACS Sustainable Chem. Eng.* **2020**, *8,* 12286−12294.

[21] B. Zhan, Y. Wang, T. Seto, Broadband Yellow-Emitting Oxynitride Phosphor $Sr_2Si_7Al_3ON_{13}:Ce^{3+},Eu^{2+}$ for White Light-Emitting Diodes with a High Color Rendering Index, *Inorg. Chem.* ***2024****, 63,* 7334−7342.

[22] H. Zheng, X. Wang, F. Dou, T. Liu, S. Yang, J. Song, Z. Yang, H. Jiao, Highly Humidity-Resistant Oxynitride Phosphor $BaSi_6N_8O:Ce^{3+}$ for pc-LEDs, *Inorg. Chem.* ***2025****, 64,* 213−223.

[23] Y. Lv, Y. Li, S. Fan, C. Chen, Y. Cai, H. Xu, R. J. Xie, A broadband yellow Yb^{2+}-doped oxynitride phosphor for high-performance white light-emitting diodes, *Inorg. Chem.Front.* ***2022****, 9,* 4930−4938.

[24] J. Hou, J. Wu, Y. Fang, Y. Wei, L. Dong, G. Zhang, Y. Liu, H. Chen, G. Li, $Cs_2MnCl_4:Eu^{2+}$: A Near-Violet Light-Triggered Single-Component White Light Emitter, *ACS Appl. Mater. Interfaces* **2024***, 16,* 30176−30184.

[25] G. Xie, J. Si, G. Li, G. Cai, Environment-Dependent Eu^{2+}-Activated $Ba_3CaK(PO_4)_3$ toward White-Light Emission by Chemical Cosubstitution of the $(BO_3)_3$−Anion Group, *Inorg. Chem.* **2022***, 61,* 14845−14856.

[26] Y. Zhan, S. Zhang, X. Wang, H. Jiao, Structure and Luminescence Properties of Mn^{4+}-Activated K3TaO2F4 Red Phosphor for White LEDs, *Inorg. Chem.* **2019**, *58*, 4412.

[27] K. W. Huan, W. T. Chen, C. I. Chu, S. F. Hu, H. S. Sheu, B. M. Chang, J. M. Chen, R. Shi. Liu, Controlling the activator site to tune europium valence in oxyfluoride phosphors, *Chem. Mater.* **2012**, *24*,11, 2220-2227.

[28] Z. Lu, G. Peng, D. Sun, Z. Lyu, X. Zhang, P. Luo, L. Zhou, C. Chen, Q. Xu, F. Cheng, H. Ypu, Customized Cyan Phosphors for Efficient Full-Spectrum Illumination and Fingerprint Detection, *Small,* **2025**, 2406504.

[29] R. L. Green, Structural and Photoluminescence Characterization of Oxyfluorides for Phosphor Applications, *Acc. Chem.Res.* **2023**, *56*, 11, 1304-1312.

[30] W. B. Im, N. George, J. Kurzman, S. Brinkley, A. Mikhailovsky, J. Hu, B. F. Chmelka, S. P. Denbaars, R. Seshadri, Efficient and Color-Tunable Oxyfl uoride Solid Solution Phosphors for Solid-State White Lighting*Adv. Mater.* **2011**, *23*, 2300.

[31] Z. Yang, T. de Boer, P. M. Braun, B. Su, Q. Zhang, A. Moewes, Z. Xia, Thermally stable red-emitting oxide ceramics for laser lighting, *Adv. Mater.* **2023**, *35*, 1.

[32] P. Zhang, Y. Zhang, B. Xue, S. Liu, YAG:Ce films for laser-driven white lighting: Annealing temperature and atmosphere-controlled luminescence performances, *J. Alloys Compd.* 2024, 972, 172826.

[33] Q. Yao, P. Hu, P. Sun, M. Liu, R. Dong, K. Chao, Y. Liu, J. Jiang, H. Jiang, YAG:Ce^{3+} Transparent Ceramic Phosphors Brighten the Next-Generation Laser-Driven Lighting, *Adv. Mater.* **2020**, *32*, 1907888.

[34] S. B. Kwon, J. H. Yoo, S. H. Choi, M. Y. Na, B. Y. Kim, S. Y. Lee, H. J. Jeong, W. H. Kim, S. H. Park, H. S. Yoon, B. K. Kang, Y. H. Song, D. H. Yoon, Preparation of high-quality YAG:Ce^{3+} ceramic phosphor by high-frequency induction heated press sintering methods, *Scientific Reports* **2022**, 23094.

[35] A. Potdevin, G. Chadeyron, S. Thérias, R. Mahiou, Luminescent Nanocomposites Made of Finely Dispersed $Y_3Ga_5O_{12}$:Tb Powder in a Polymer Matrix: Promising Candidates for Optical Devices, *Langmuir* **2012**, *28*, 13526.

[36] J. Dang, Z. Yang, W. Guo, Y. Ji, H. Wang, J. Deng, M. Wang, In Situ Fabrication of Mn-Doped 2D Perovskite-Polymer Phosphor Films with Green-Red Dual Emissions for Yellow Lighting, *Adv. Mater.* Interfaces **2021**, *8*, 2100560.

[37] P. Kim, C. Li, R. E. Riman, J. Watkins, *ACS Appl. Mater. Interfaces* **2018**, *10*, 9047.

[38] S. Lee, J. Lyu, A. Jeong, M. Jung, J. H. Kang, H. Jung, Y. I. Park, J.-E. Jeong, J. C. Kim, *ACS Sustainable Chem. Eng.* **2024**, *12*, 12386.

[39] S. Sreevalsa, P. A. Parvathy, S. K. Sahoo, S. Das, Full-color emitting crystal engineered $Sr_3Al_{1-x}Si_xO_{4+x}F_{1-x}$: $Eu^{2+/3+}$ oxyfluorides for developing bendable lighting composites, *J. Alloys Compd.* **2021**, *880*, DOI 10.1016/j.jallcom.2021.160483.

[40] S. Subhagan, S. Ahmad, P. Kundu, M. K. Pandey, S. Som, S. Das, Governing the crystallographic sites for tuning Eu^{2+} emission in an apatite oxyfluoride host to be applied for superior white light emitting diodes, *Dalt. Trans.* **2022**, *51*, 14601.

[41] X. Zhang, D. Zhang, B. Zheng, Z. Zheng, Y. Song, K. Zheng, Y. Sheng, Z. Shi, H. Zou, Luminescence and Energy Transfer of Color-Tunable $Y_2Mg_2Al_2Si_2O_{12}$:Eu^{2+},Ce^{3+} Phosphors, *Inorg. Chem.* **2021**, *60*, 5908.

[42] M. Shang, G. Li, X. Kang, D. Yang, G. Geng, J. Lin, Tunable Luminescence and Energy Transfer properties of Sr_3AlO_4F:RE^{3+} (RE = Tm/Tb, Eu, Ce) Phosphors, *Appl. Mater. Interfaces.* **2011**, *3*, 7, 2738.

[43] Z. Li, G. Zhu, H. Li, Q. Zhu, Y. Cong, X. Bai, J. G. Li, B. Dong, Visible Light Excited Yb3+-Doped Phosphor Via Eu^{2+} Bridged Energy Transfer Toward NIR-II Spectroscopy Application, *Laser Photonics Revi.* **2025***, 2402162.*

[44] J. N. Spencer, D. Merrikin, S. J. A. Pope, D. J. Morgan, N. Carthey, D. M. Murphy, CW EPR Investigation of Red-Emitting CaS:Eu Phosphors: Rationalization of Local Electronic Structure, *Adv. Opt. Mater.* **2020**, *8*, 2001241.

[45] H. Xie, J. Lu, Y. Guan, Y. Huang, D. Wei, H. J. Seo, Abnormal Reduction, $Eu^{3+} \rightarrow Eu^{2+}$, and Defect Centers in Eu^{3+}-Doped Pollucite, $CsAlSi_2O_6$, Prepared in an Oxidizing Atmosphere, *Inorg. Chem.* **2014**, *53*, 827.

[46] W. Geng, X. Zhou, J. Ding, G Li, Y. Wang, $K_7Ca_9[Si_2O_7]_4F:Ce^{3+}$: A Novel Blue-Emitting Phosphor with Good Thermal Stability for Ultraviolet-Excited Light Emitting Diode, *J.Mater. Chem. C* **2017**, *5*, 11605 - 11613.

[47] C. Maak, P. Strobel, V. Weiler, P. J. Schmidt, W. Schnick, Unprecedented Deep-Red Ce^{3+} Luminescence of the Nitridolithosilicates $Li_{38.7}RE_{3.3}Ca_{5.7}[Li_2Si_{30}N_{59}]O_2F$ (RE = La, Ce, Y), *Chem. Mater.* **2018**, *30*, 5500.

[48] X. Ji, J. Ma, X. Wei, R. Duan, J. Wang, X. Yi, Y. Zeng, G. Wang, F. Yang, J. Li, Investigation into low-temperature photoluminescence internal quantum efficiency and defect-recombination in InGaN light-emitting diodes, *Phys. Status Solidi C,* **2014**, *11*, 718 - 721

[49] F. Su, B. Lou, Y. Ou, Y. Yang, W. Zhan, C. K. Puan, H. Liang, VUV–UV–vis Luminescence, Energy Transfer Dynamics, and Potential Applications of Ce^{3+}- and Eu^{2+}-Doped $CaMgSi_2O_6$, Jour. Phys. Chem. C, **2021**, *125, 10, 5957 - 5967*.

[50] M. Abraham, K. K. Thejas, A. K. Kunti, N. Amador-Mendez, R. Hernandez, J. Duras, K. G. Nishanth, S. K. Sahoo, M. Tchernycheva, S. Das, Strategically Developed Strong Red-Emitting Oxyfluoride Nanophosphors for Next-Generation Lighting Applications, *Adv. Opt. Mater.* **2024**, *2401356*, 2401356.

[51] K. B. Kim, Y. Kim, H. G. Chan, T.Y. Cho, J. S. Jung, J. G. Kang, Structural and Optical Properties of $BaMgAl_{10}O_{17}:Eu^{2+}$ Phosphor, *Chem. Mater.* **2002**, 14, 12, 5045 - 5052.

[52] S. P. Vijayan, B. John, S. K. Sahoo, Two-dimensional lamellar polyimide/cardanol-based benzoxazine copper polymer composite coatings with excellent anti-corrosion performance, *Progress in Organic Coatings* **2022**, *162*, 106586.

[53] T. Wang, L. Li, Q. Wang, G. Xie, C. Guo, *Industrial Crops and Products* **2019**, *141*, 111798.

[54] I. P. Sahu, D. P. Bisen, R. K. Tamrakar, K. V. R. Murthy, M. Mohapatra, Studies on the Luminescence Properties of $CaZrO_3:Eu^{3+}$ Phosphors Prepared by the Solid State Reaction Method, *Journal of Science: Advanced Materials and Devices* **2017**, *2*, 59

[55] Q. Shang, C. Liu, J. Chen, X. Yang, Y. Hu, L. Hu, Y. Zhou, X. Ren, Sustainable and robust superhydrophobic cotton fabrics coated with castor oil-based nanocomposites for effective oil–water separation, *ACS Sustainable Chem. Eng.* **2020**, *8*, 7423.

[56] W. Zhang, N. Jiang, T. Zhang, T. Zhang, Preparation and properties of silane-modified cardanol–benzoxazine for hydrophobic coating, *Journal of Elastomers & Plastics* **2021**, *53*, 296.

5.7 Supplementary information

Table 5.S1 *The refined lattice parameters of SBAOF, SBAOF: 0.025Ce^{3+}; 0.005$Eu^{2+/3+}$ and S_2BAOF: 0.025Ce^{3+}; xEu^{2+} (x = 0.001 and 0.01) phosphors.*

Formula	**SBAOF**	**SBAOF: 0.025Ce^{3+}; 0.005$Eu^{2+/3+}$**	**S_2BAOF: 0.025Ce^{3+}; 0.001Eu^{2+}**	**S_2BAOF: 0.025Ce^{3+}; 0.01Eu^{2+}**
Crystal System	Tetragonal	Tetragonal	Tetragonal	Tetragonal
Space Group	I4/mcm	I4/mcm	I4/mcm	I4/mcm
a = b [Å]	6.8963 (5)	6.8881(5)	6.9173(4)	6.92109(13)
c [Å]	11.1891 (10)	11.1726(8)	11.0724(8)	11.0719(5)
Volume [Å]	532.14 (7)	530.10(10)	529.80(9)	530.36(3)
R_p (%)	13	11	12	11
R_{wp} (%)	16	15.246	15.370	14.815
GOF	1.934	3.965	2.014	2.731

Table 5.S2 *Fraction of occupation of SBAOF and SBAOF:0.025Ce^{3+};0.005$Eu^{2+/3+}$ phosphors.*

Atom	**Wyck. pos.**	**x**	**y**	**z**	**U_{iso}**	**Occ.**
			SBOF			
Al	4b	0.0000	0.5000	0.25000	0.0000	1.0000
F	4c	0.0000	0.0000	0.0000	0.0000	1.0000
Ba	4a	0.0000	0.0000	0.25000	0.0000	1.0000
O	4f	0.14180	0.64180	0.64960	0.0000	1.0000
Sr	8h	0.16960	0.66960	0.00000	0.0000	1.0000
			SBOF:0.025Ce^{3+}; 0.005$Eu^{2+/3+}$			
Al1	4b	0.00000	0.50000	0.25000	0.0000	1.0000
F1	4c	0.00000	0.00000	0.00000	0.0000	1.0000
Ce1	4a	0.00000	0.00000	0.25000	0.0100	0.0125
Eu1	4a	0.00000	0.00000	0.02500	0.0100	0.0025
Ba1	4a	0.00000	0.00000	0.25000	0.0000	0.9850
O1	16l	0.14180	0.64180	0.64960	0.0000	1.0000
Ce2	8h	0.16960	0.66960	0.00000	0.0100	0.0125
Eu2	8h	0.16960	0.66960	0.00000	0.0100	0.0025
Sr2	8h	0.16960	0.66960	0.00000	0.0000	0.9850

Table 5.S3 *The refined lattice parameters and fraction of occupation of $S_2BAOF: 0.025Ce^{3+}; xEu^{2+}$ (x = 0.001 and 0.01) phosphors.*

Atom	Wyck. pos.	x	y	z	U_{iso}	Occ.
			$S_2BOF:0.025Ce^{3+};0.001Eu^{2+}$			
Al1	4b	0.00000	0.50000	0.25000	0.0000	0.5000
F1	4c	0.00000	0.00000	0.00000	0.0000	1.0000
Ce1	4a	0.00000	0.00000	0.25000	0.0100	0.0125
Eu1	4a	0.00000	0.00000	0.02500	0.0100	0.0050
Ba1	4a	0.00000	0.00000	0.25000	0.0000	0.9825
O1	16l	0.14180	0.64180	0.64960	0.0000	1.0000
Ce2	8h	0.16960	0.66960	0.00000	0.0100	0.0125
Eu2	8h	0.16960	0.66960	0.00000	0.0100	0.0050
Sr2	8h	0.16960	0.66960	0.00000	0.0000	0.9825
Si1	4b	0.00000	0.50000	0.25000	0.0100	0.5000
			$S_2BOF:0.025Ce^{3+};0.01Eu^{2+}$			
Al1	4b	0.00000	0.50000	0.25000	0.0000	0.5000
F1	4c	0.00000	0.00000	0.00000	0.0000	1.0000
Ce1	4a	0.00000	0.00000	0.25000	0.0100	0.0125
Eu1	4a	0.00000	0.00000	0.02500	0.0100	0.0050
Ba1	4a	0.00000	0.00000	0.25000	0.0000	0.9825
O1	16l	0.14180	0.64180	0.64960	0.0000	1.0000
Ce2	8h	0.16960	0.66960	0.00000	0.0100	0.0125
Eu2	8h	0.16960	0.66960	0.00000	0.0100	0.0050
Sr2	8h	0.16960	0.66960	0.00000	0.0000	0.9825
Si1	4b	0.00000	0.50000	0.25000	0.0100	0.5000

Table 5.S4 *The photoluminescence properties (λ_{EXC}, λ_{EM}, IQE, CRI, and CCT) of $S_2BAOF: 0.025Ce^{3+}; 0.005Eu^{2+}$ are compared with those of recently reported violet excitable and broadband emitting Ce^{3+} and Eu^{2+} activated phosphors.*

Phosphors	λ_{EXC} / λ_{EM} (nm)	IQE (%)	CRI (Ra) /CCT (K) (@ LED used)	Ref.
$Sr_2Si_5N_8:Ce^{3+}$	432 / 550	71	64 / 8167 (@ 460 nm LED)	[19]
$Sr_2Al_3Si_7ON_{13}:Ce^{3+}$	420 / 535	52	--	[20]
$Sr_2Si_7Al_3ON_{13}:Ce^{3+},Eu^{2+}$	420 / 568	58.63	86.2 / 4810 (@ 450 nm LED)	[21]
$BaSi_6N_8O:Ce^{3+}$	410 / 523	38.02	63 / 5142 (@ 410 nm LED)	[22]
$(Ba,Sr)Si_3Al_3O_4N_5:Yb^{2+}$	414 / 538 & 450 / 554	86.9 (@ 414 nm) & 70.2 (@ 450 nm)	80 / 5650 (@ 450 nm LED)	[23]
$Cs_2MnCl_4:Eu^{2+}$	404 / 444 (Eu^{2+}) & 566 (Mn^{2+})	66.4	82.3 / 5710 (@ 400 nm LED)	[24]
$Ba_3CaK(PO_4)_{3-x}(BO_3)_x:0.02Eu^{2+}$	365 & 405 / 452, 481 & 539	62.08	70.2 / 6295	[25]
$S_2BAOF: 0.025Ce^{3+}; 0.005Eu^{2+}$	**400 / 545**	**86%**	**74 / 4246 (@ 410 nm LED)**	**Present work**

Table 5.S5 *The laser-driven photoluminescence properties (CCT, CRI and luminous flux) of CTU/40%S_2BAOF: $0.025Ce^{3+}$;$0.005Eu^{2+}$ composite compared with those of recently reported converters for laser-driven lighting.*

Phosphor	Laser wavelength	CCT	CRI	Luminous efficiency	Ref.
YAG: Ce films	450 nm	6530 K	71.7	127 lm/W	[32]
YAG: Ce transparent ceramic phosphor	460 nm	7293 K	73	223 lm/W	[33]
CTU/40%S_2BAOF: $0.025Ce^{3+}$;$0.005Eu^{2+}$ composite	405 nm	4656 K	72	201 lm/W	Present work

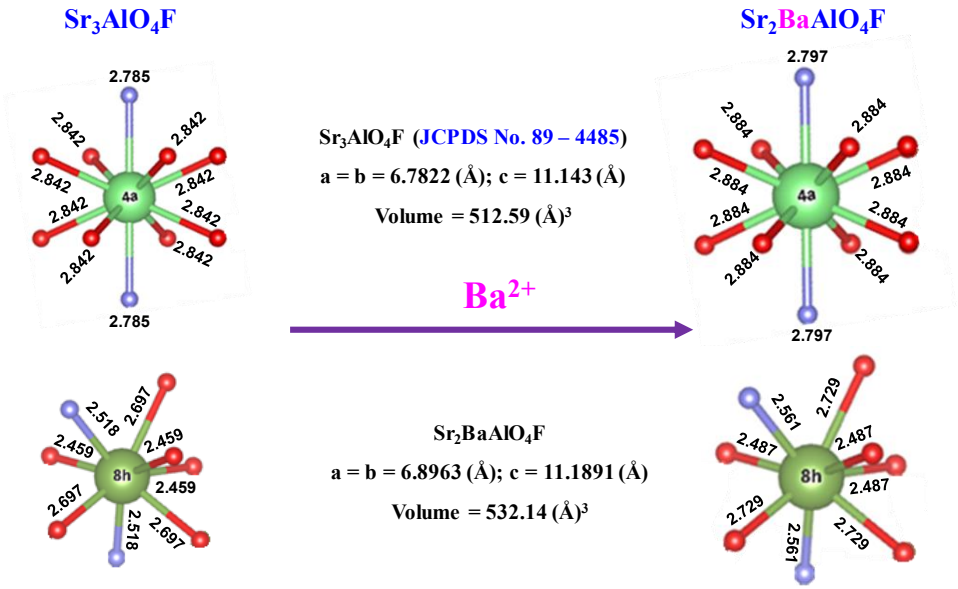

Fig. 5.S1 *The schematic representation of cationic site enlargement in SBAOF phosphor as compared with the standard phase of Sr_3AlO_4F (JCPDS No. 89 – 4485).*

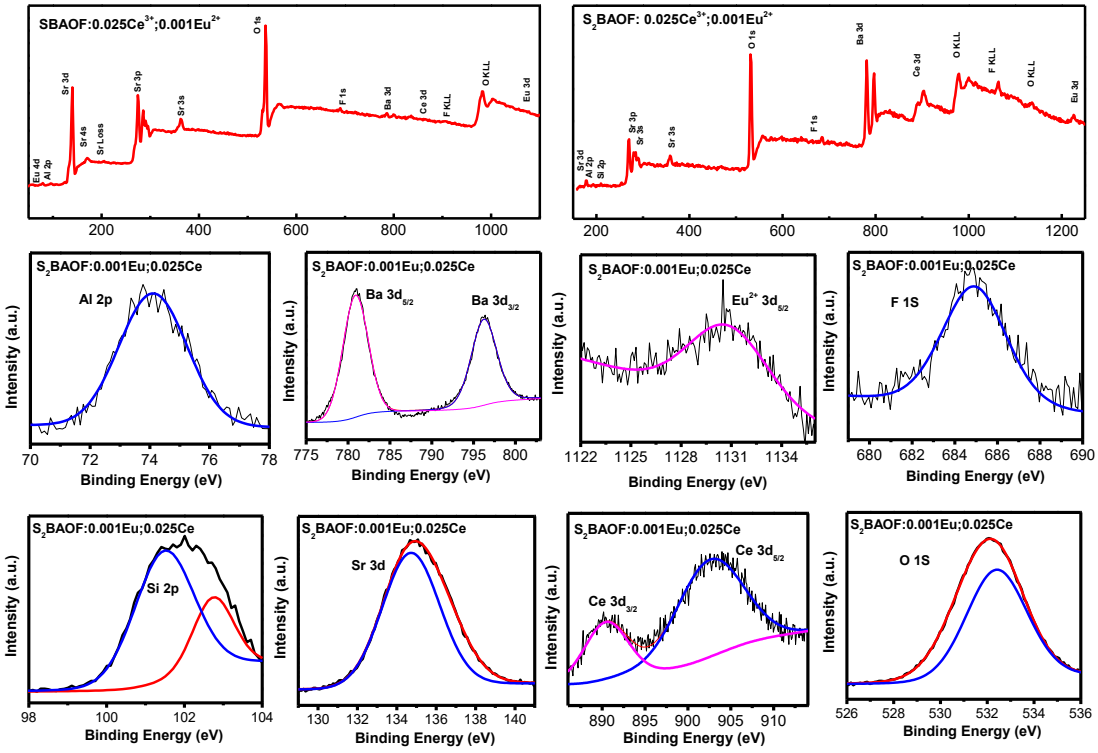

Fig. 5.S2 (a) *The XPS survey spectra of SBAOF: $0.025Ce^{3+}$; $0.005Eu^{2+/3+}$ and S_2BAOF: $0.025Ce^{3+}$;$0.005Eu^{2+}$ phosphors (without and with Si^{4+} doping). (b) High resolution XPS spectra of in S_2BAOF: $0.025Ce^{3+}$;$0.001Eu^{2+}$ phosphor.*

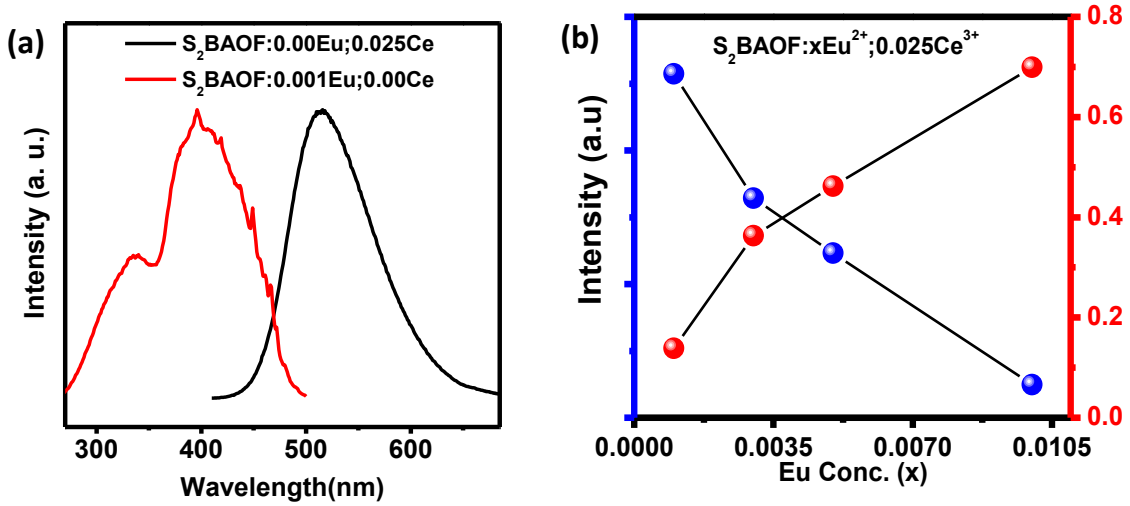

Fig. 5.S3 (a) *The emission and Excitation Spectra of $S_2BAOF: 0.025Ce^{3+}$ and $S_2BAOF: 0.025Ce^{3+};0.001Eu^{2+}$ phosphors.* ***(b)*** *The intensity variation and calculated energy transfer efficiency for $S_2BAOF: 0.025Ce^{3+}; xEu^{2+}$ (x = 0.00 to 0.01) phosphors.*

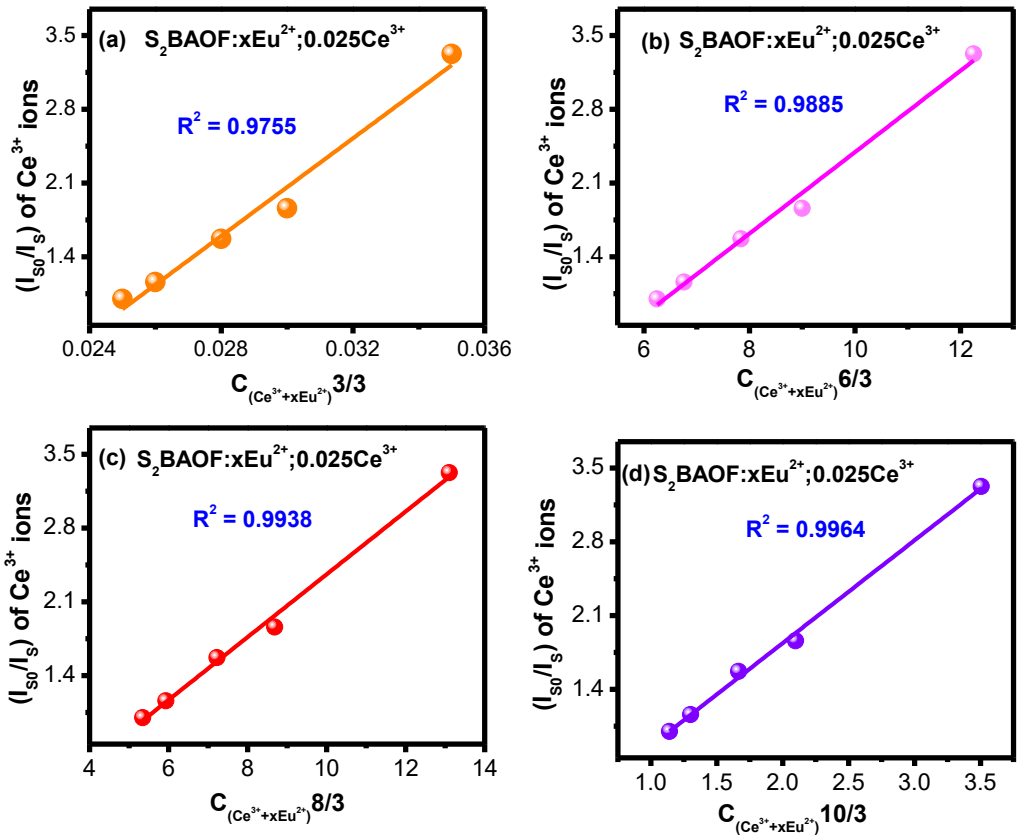

Fig. 5.S4 The dependence of $\frac{Iso}{Is}$ on $C^{\alpha}/3$ (α equal to 3, 6, 8 and 10) for $S_2BAOF: 0.025Ce^{3+}; xEu^{2+}$ (x = 0.00 to 0.01) phosphors.

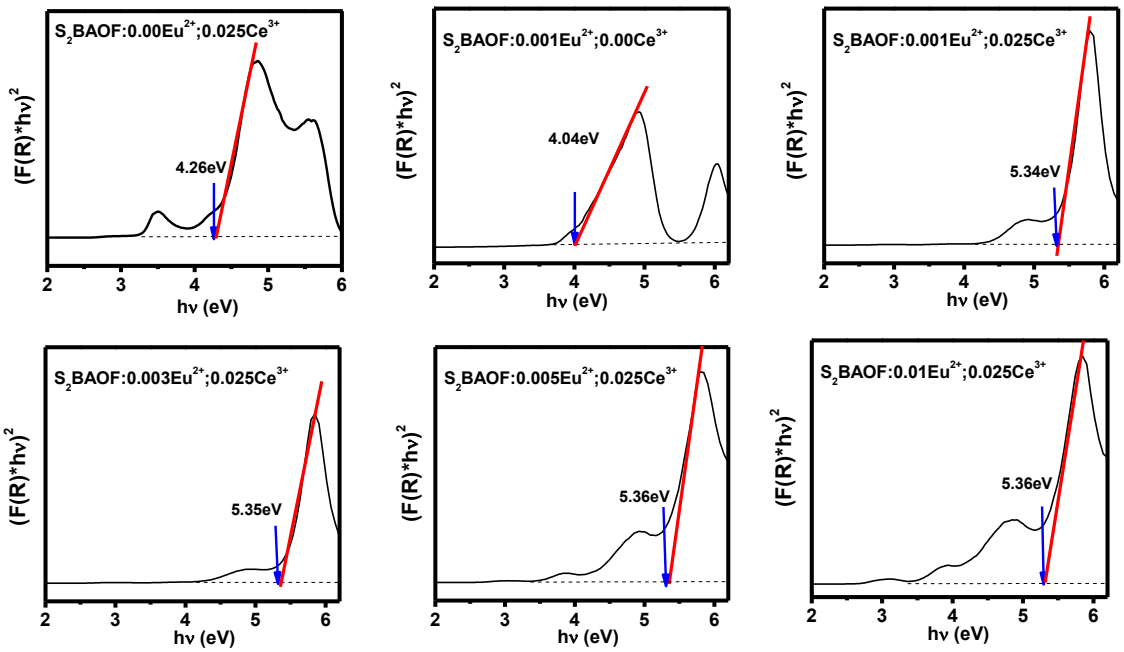

Fig. 5.S5 *The Tauc plots and band gap values of S2BAOF and S2BAOF: 0.025Ce3+; xEu2+ (x = 0.001 to 0.01) phosphors.*

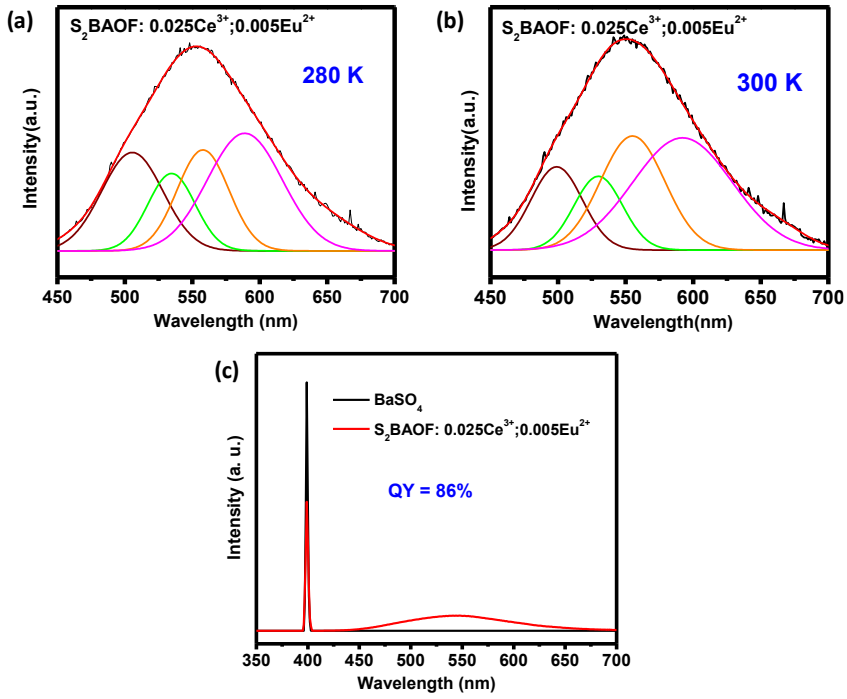

Fig. 5.S6 *The deconvolution Gaussian fitting of S2BAOF: 0.025Ce3+; 0.005Eu2+ phosphor recorded at* ***(a)*** *280 K and* ***(b)*** *300 K, respectively.* ***(c)*** *Comparative emission spectra of S2BAOF: 0.025Ce3+; 0.005Eu2+ phosphor and absorption spectrum of BaSO4 for calculating the PL emission quantum efficiencies.*

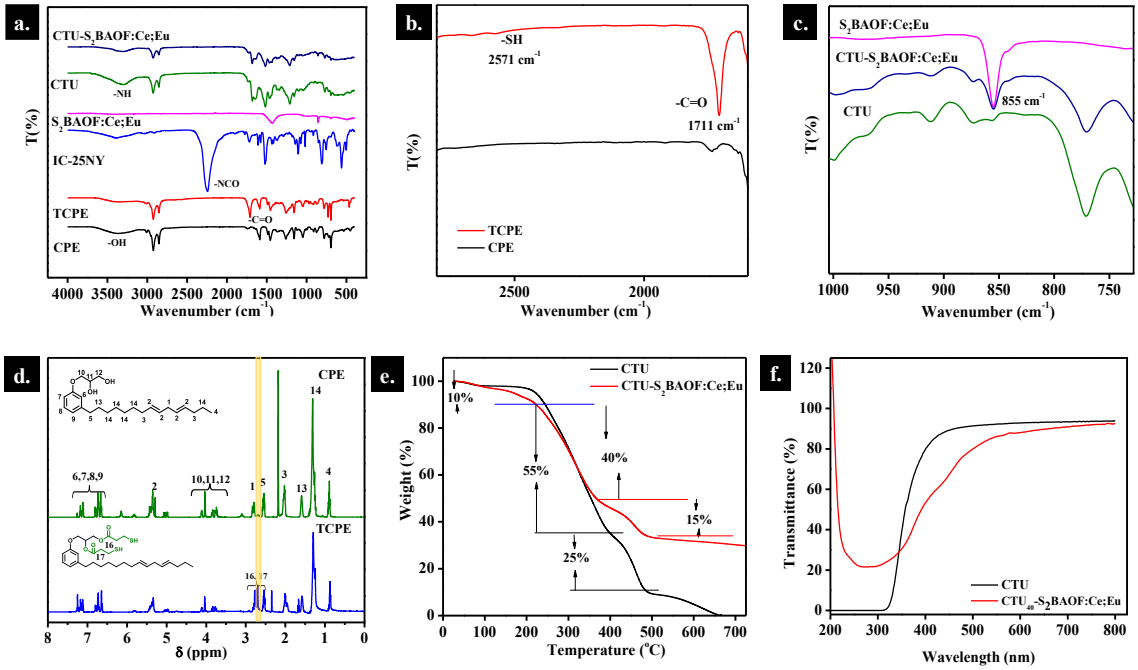

Fig. S7 ***(a)*** *FTIR spectrum of CPE, TCPE, IC-25NY, S2BAOF: 0.025Ce^{3+}; 0.005Eu^{2+}, CTU, and CTU/40% S2BAOF: 0.025Ce^{3+}; 0.005Eu^{2+}.* ***(b)*** *-SH and -C=O,* ***(c)*** *metal-oxygen bonds* ***(d)*** *^{1}H NMR spectra of CPE and TCPE,* ***(e)*** *TGA curves of CTU and CTU/40%S2BAOF: 0.025Ce^{3+}; 0.005Eu^{2+}, and* ***(f)*** *U-V transmittance of CTU and CTU/40%S2BAOF: 0.025Ce^{3+}; 0.005Eu^{2+}.*

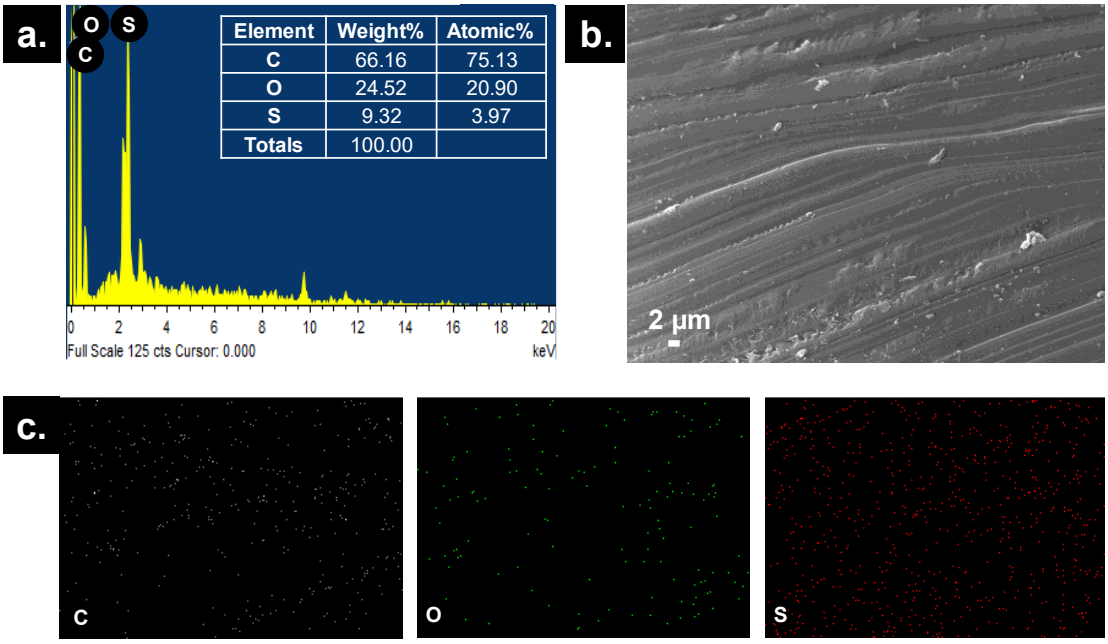

Fig. 5.S8 (a) EDX spectrum, (b) cross-sectional SEM image, and (c) elemental mapping of the CTU matrix.

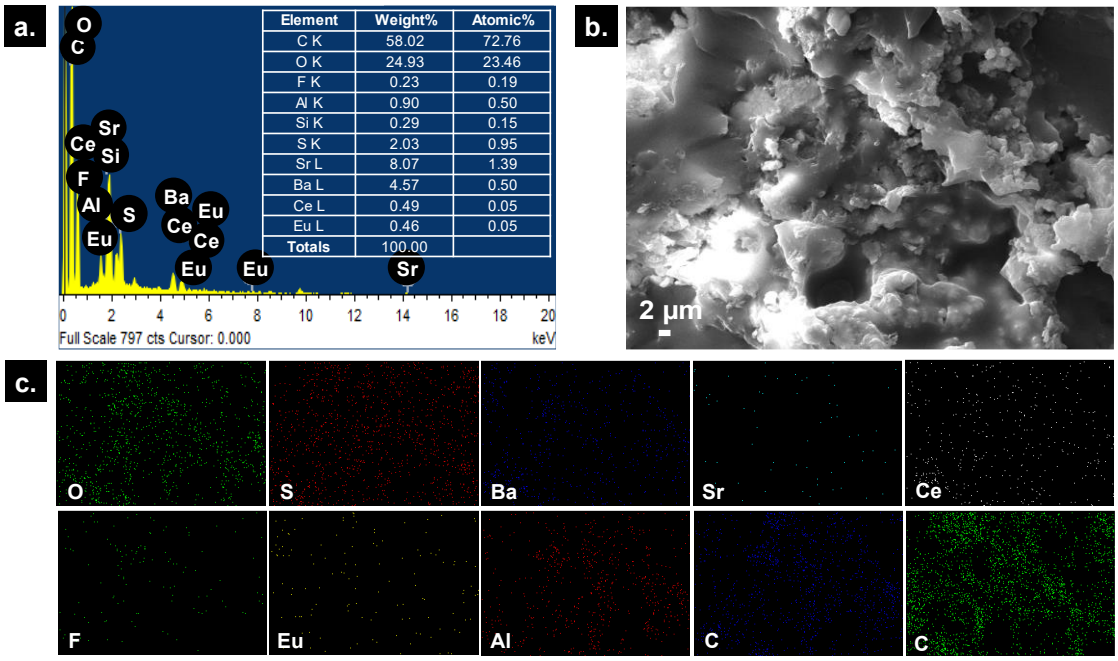

Fig. 5.S9 *(a) EDX spectrum, (b) cross-sectional SEM image, and (c) elemental mapping of CTU/40%S_2BAOF: Ce^{3+}; Eu^{2+} composite.*

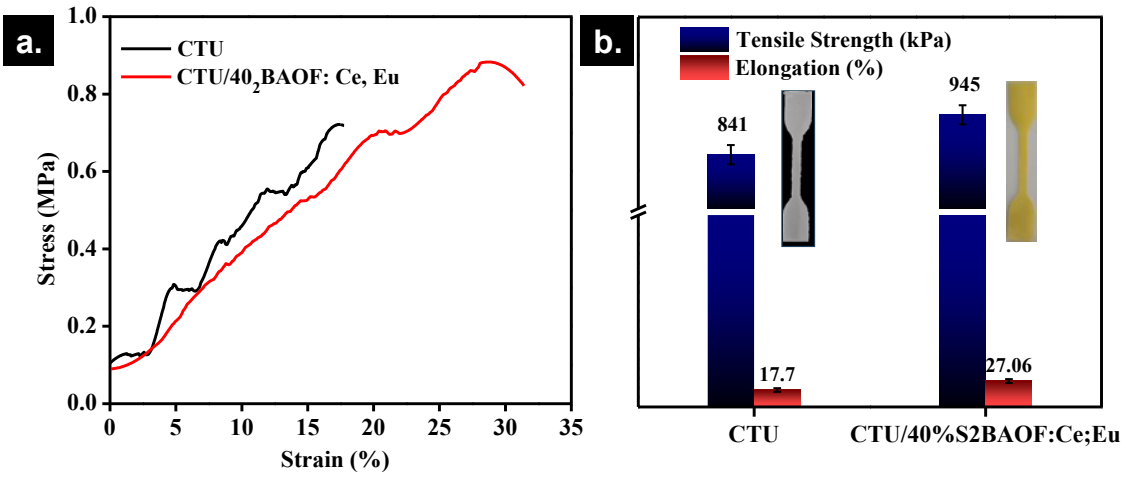

Fig. 5.S10 *(a) Stress vs strain curves and (b) bar chart of strength and elongation for CTU matrix and CTU/40%S_2BAOF: Ce; Eu composite film, respectively.*

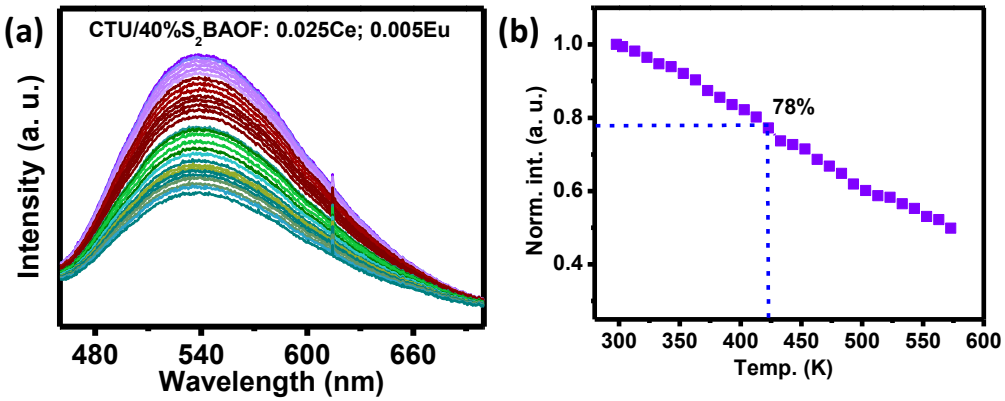

Fig. 5.S11 ***(a)*** *Temperature-dependent PL emission spectra of CTU/40%S_2BAOF: Ce^{3+}; Eu^{2+} phosphor.* ***(b)*** *Temperature-dependent PL intensity variation of CTU/40%S_2BAOF: Ce^{3+}; Eu^{2+} phosphor.*

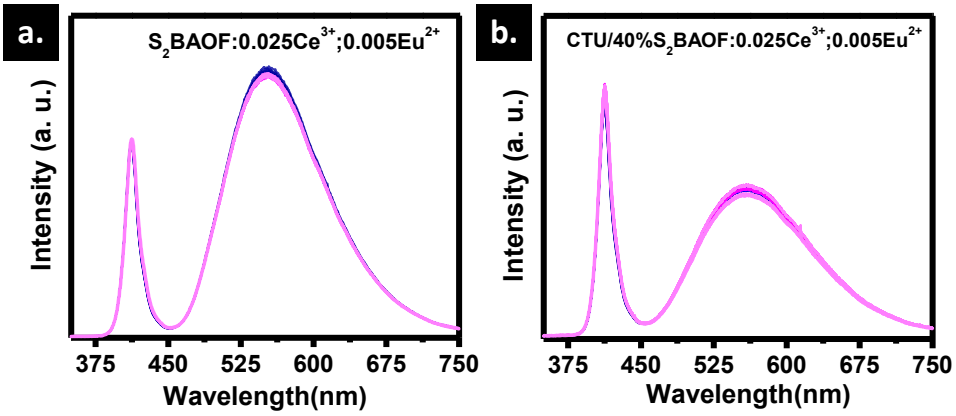

Fig. S12 *Violet LED irradiation time-dependent PL performance evaluation of* ***(a)*** *S_2BAOF: 0.025Ce^{3+}; 0.005Eu^{2+} phosphor and* ***(b)*** *CTU/40%S_2BAOF: 0.025Ce^{3+}; 0.005Eu^{2+} composite under a violet LED (3W) exposure for 1 hour.*

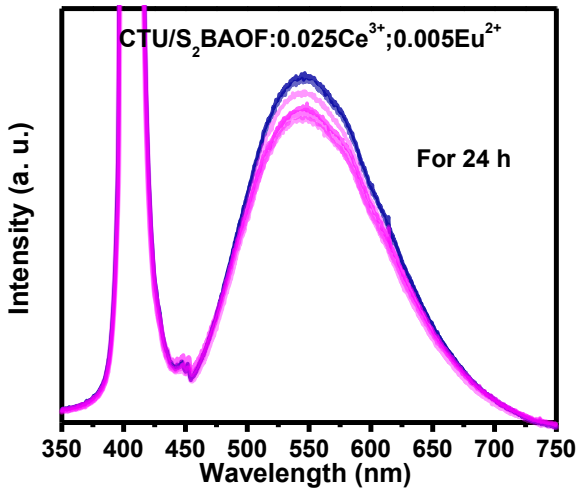

Fig. 5.S13 *The 405 nm laser irradiation time dependent luminescence performance evaluation of CTU/40%S_2BAOF: 0.025Ce^{3+}; 0.005Eu^{2+} composite under a violet laser (1.4 W/mm^2) exposure for 24 hours.*

Chapter 6

Summary and Future Scope of Research

In the recent era of lighting technology, phosphor converted white light emitting diodes (WLEDs) have been used as a suitable substitute for traditional incandescent lamps because of their significant advantages like good luminescent property, long life time, high temperature with standing power, better color rendering, high efficiency and very low energy consumption with good stability. Nowadays, the modification and construction of WLEDs have been concerned much attention due to their vast application in solid state lighting technology. In the construction of phosphor converted WLEDs mainly focused on two things, phosphor material and LED chips. For LED chips, researchers are mainly investigating its thermal diffusivity and stability, chosen short wavelength chips and focused on the manipulation of high power. Another factor which directly influence the LED device is the phosphor material chosen, It must have high thermal and chemical stability, good luminescent property, mild synthesis condition etc. The widely used method for fabricating WLED is combining InGaN LED chip with yellow emitting YAG: Ce^{3+} phosphor. Which facing problems like low CRI (Color Rendering Index) and high CCT (Correlated Color Temperature) owing to the lack of red component in the phosphor.

Fluoride-containing oxide hosts doped with rare-earth ions have shown great potential as light emitting diode (LED) phosphors with their tunable luminescence properties. The introduction of fluoride ions into an oxide crystal lattice leads to a distortion of the coordination polyhedrons i.e. generation of non-centrosymmetric sites, which causes unusual spectroscopic properties. Moreover, the fluoride host matrices are known to provide a wide bandgap, low phonon energy and inter-configurational transitions whereas the oxides host matrices are known to provide high chemical stability and high absorption in UV-vis region. Based on aforementioned facts, the oxyfluorides which combine the advantages of both fluorides and oxides are favorable to serve as the host materials for luminescence properties. This thesis is mainly studied the structural and optical properties of $Eu^{2+/3+}/Ce^{3+}$ doped single white light emitting oxyfluoride phosphors for flexible lighting and display applications.

Herein, the first chapter deals with a detailed description of phosphor and their photoluminescence mechanisms, application of phosphors in different sectors mainly in solid state lighting and their market potential, development of phosphors in WLEDs, rare earth based broad band emitting phosphors and the mechanism, particularly $Eu^{2+/3+}/Ce^{3+}$ doped oxyfluoride phosphors, phosphor polymer composite as a color converter and their significant applications.

In the second chapter, we developed a series of 0.1 mol% of Eu^{3+} doped $Sr_{2.9-3x/2}(Gd/Y)_xAlO_4F$ (x = 0.01 to 0.10) phosphors showing an intense red-orange emission (Eu^{3+}: $^5D_0 \rightarrow {}^7F_{1,2}$) under the UV and near-UV excitations. As per the report of global instability index (GII) estimation the structure of the tetragonal Sr_3AlO_4F phase is under highly strained. Moreover, our results of X-ray photoelectron spectroscopy (XPS) also ascertained that the Sr_3AlO_4F is under highly strained with some oxygen vacancies. In order to study the structure defect and suitability of the host towards luminescence first we done the aliovalent substitution of Sr ions with trivalent Gd and Y ions are carried out which improve the stability of Sr_3AlO_4F lattice. The structural and optical properties are analyzed from powder X-ray diffraction (XRD), X-ray photoelectron spectroscopy (XPS), Photo luminescent study and Judd-Ofelt theory etc. The optimized $Sr_{2.76}Gd_{0.09}AlO_4F:0.1Eu^{3+}$ and $Sr_{2.79}Y_{0.07}AlO_4F:0.1Eu^{3+}$ samples showed high red color purity (~99 %), correlated color temperature (~1300 K), and CIE coordinates of (0.62, 0.38) indicating that these samples are a suitable red-emitting component for fabricating white-LEDs and flexible optical film under UV and blue excitations. Furthermore, flexible polydimethylsiloxane (PDMS) based films were also fabricated using optimized $Sr_{2.76}Gd_{0.09}AlO_4F:0.1Eu^{3+}$ phosphors. The electroluminescence (EL) of a flexible PDMS-phosphor composite film device shows a cool-red color suggesting its suitability in flexible display devices.

In the third chapter, a series of intense Eu^{2+}/Eu^{3+}-coexisted $Sr_{2.9}Al_{1-x}Si_xO_{4+x}F_{1-x}$: $0.1Eu^{2+/3+}$ ($SASi_xOF$: $Eu^{2+/3+}$) oxyfluorides were prepared through conventional solid-state method in an oxygen-deficient atmosphere. By cationic substitution strategy we successfully generate single white light emission from Sr_3AlO_4F host under UV excitation. The structural changes in Sr_3AlO_4F (SAOF) owing to the Si^{4+} ions' doping were visualized from the Rietveld refinement analysis and the valence conversion of

europium ions confirmed from X-ray photoelectron spectroscopy studies. By the substitution of Al^{3+} with Si^{4+} ions enlarged the activator sites that enabled Eu^{3+} ions to be reduced to Eu^{2+} ions and on varying the Si^{4+} ions doping concentration we tuned the emission color from orange-red to nearly white and eventually to the bluish zone. The most suitable compositions were further used to fabricate proposed phosphor - polymer composite membranes to avoid silicon-based phosphor binders for device applications. Here we choose castor oil as the polymer host matrix because of its good binding, transparency, eco-friendly nature, and flexibility. Combining polymer matrix with phosphor could be a suitable alternate for generating high-performance and thermally stable composite materials for LED packaging. These composite membranes could able to maintain a certain distance between the phosphor and LED chip for improving the life-time of the fabricated LED by the ease of heat dissipation. Therefore, the composite made with near white emitting $SASi_{0.03}OF$: $Eu^{2+/3+}$ phosphor was integrated with a near UV-LED which showed intense cool white emission with the CIE of (0.29, 0.32), CCT of 7629, and CRI of 96.

In the fourth chapter, we further choosen a promising silicate apatite oxyfluroride host $Ca_4La_6Si_6O_{24}F_2$ to understand the mechanism of generation of white light from a single-phase composition activated with europium. The study started with the structural evaluations of a series of Eu^{3+} activated $Ca_4La_6Si_6O_{24}F_2$ phosphors using X-ray diffractions and Eu^{3+} photoluminescence to elucidate the local environment of rare-earth ions and symmetry of the lattice sites. By the introduction of divalent Sr^{2+} ion a series of intense green-emitting $Ca_2Sr_2La_6Si_6O_{24}F_2$: Eu^{2+} phosphors were synthesized. Herein, X-ray diffraction Rietveld refinement tool and Eu^{3+} spectroscopy was used to identify the site occupancy, symmetry, and lattice distortion in the $Ca_2Sr_2La_6Si_6O_{24}F_2$ host. The emission of Eu^{2+} was further tuned from cyan to greenish-yellow via the doping of Mg^{2+} and Ba^{2+} ions into the appropriate lattice sites. Detailed local environment investigations reveal that the change of symmetry owing to the Mg^{2+}/Ba^{2+} substitution led to the centroid shift, which was responsible for the blue- or red-shift of the emission spectra. The optimized phosphors were having comparable emission intensity with commercial YAG and has high quantum yield with good thermal stability exhibited decent photoluminescence above 70% at 150 ºC as compared with that at room temperature. Finally, several prototype WLEDs were fabricated using the single phosphor $Ca_{1.365}Sr_{1.365}La_6Si_6O_{24}F_2$:$0.07Eu^{2+}$, $1.2Ba^{2+}$ with near-UV and violet-LED

chips. The outcomes indicated the promising nature of this single composition phosphor for indoor lighting.

In the fifth chapter, we developed full spectral emitting violet-excitable $(Sr,Ba)_3(Al,Si)O_4F$: Ce^{3+}, Eu^{2+} phosphors with a high quantum efficiency of 86% and thermal stability of 78%. The wider band emission composed of $4f^6 5d^1$ - $4f^7$ transitions of Ce^{3+} and Eu^{2+} ions is effectively recognized under 410 nm violet radiation and which is structurally optimized based on Eu^{2+} and Ce^{3+} site occupancy. The highly red-shifted $Sr_{1.995}Ba_{1-x}Al_{0.5}Si_{0.5}O_4F$: $0.025Ce^{3+}$; $0.005Eu^{2+}$ phosphor powders were further chosen for fabricating thiourethane (CTU) based phosphor polymer composite films which is showing high photobleaching and enhanced photoluminescent stability due to polymer encapsulation. The performance of the developed CTU/40%S_2BAOF: $0.025Ce^{3+}$; $0.005Eu^{2+}$ flexible composite converter under 410 nm violet-LED chip and a violet lesser of 405 nm is generate warm white light with high CRI~80 and low CCT~4000 K without a noticeable chromatic shift under various powers and after prolonged illuminations.

Specific recommendations for each chapter work: Chapter 2: The optimized $Sr_{2.765}Gd_{0.09}AlO_4F$: $0.1Eu^{3+}$/PDMS composite film exhibited a cool-red emission, indicating its high potential for application in flexible display technologies. Chapters 3 and 4: The developed phosphor systems achieved optimized cool white light emission recommended for commercial environments, where visually comfortable white light is essential. Chapter 5: The optimized CTU/S_2BAOF: $0.025Ce^{3+}$; $0.005Eu^{2+}$ composite film shows promise for advanced flexible optoelectronic devices, including wearable health-monitoring systems, smart lighting panels, and adaptive illumination solutions.

Future scope:

- The DFT simulation can be studied to get clear insights about the host. Based on DFT results, the emission quantum yield can be further enhanced by lattice modifications.
- The absorption width can be enhanced to further blue to make it suitable for multiple LED applications.
- The particle size can be reduced to make the membrane more transparent.
- The compatibility of the synthesized size reduced phosphors in the development of luminescent ink has to be analyzed.
- The potential oxyfluoride host can be used for generating IR-emitting phosphors.

APPENDIX

Experimental Techniques

1. X-Ray Diffraction (XRD):

i. X-Ray diffractograms were collected using Phillip's X'pert pro diffractometer with Ni filtered Cu-Kα radiation using an X-ray source of Cu- Kα1 (λ = 1.54060 Å) with generator settings of 30 mA, 40kV

ii. X-Ray diffractograms were also collected using PANalytical EMPYREAN X-ray diffractometer using an X-ray source of Cu- Kα1 (λ = 1.54060 Å) with generator settings of 40 mA, 45kV.

2. X-ray Photoelectron Spectroscopy (XPS):

The X-ray photoelectron spectroscopy (XPS) analysis was performed using a PHI 5000 VersaProbe II equipped with a micro-focused (200 μm, 15 kV) monochromatic Al-Kα X-ray source (1486.6 eV).

3. Scanning Electron Microscopy (SEM):

The morphology and elemental analysis of the prepared samples were examined using scanning electron microscopy (Zeiss EVO 18 cryo-SEM operating at an accelerating voltage of 15 kV).

4. Transmission Electron Microscopy (TEM):

i. The high-resolution microscopic studies and selected area electron diffraction (SAED) pattern of the samples were carried out using a high-resolution transmission electron microscope (HR-TEM), FEI Tecnai F20, operated at 300 kV. Gatan Digital Micrograph Software was employed to find out the values of d-spacing of the recorded lattice fringes.

ii. The high-resolution microscopic studies of the samples were also carried out using a high-resolution transmission electron microscope (HR-TEM), JEOL JEM-F200.

5. Energy Dispersive X-ray Spectroscopy (EDAX or EDS):

i. The EDS analysis of the prepared samples was examined using scanning electron microscopy (Zeiss EVO 18 cryo-SEM operating at an accelerating voltage of 15 kV).

ii. The EDS analysis of the samples was also carried out using a high-resolution transmission electron microscope (HR-TEM), FEI Tecnai F20, operated at 300 kV. Gatan Digital Micrograph Software was employed to find out the values of d-spacing of the recorded lattice fringes.

iii. The EDS analysis of the samples was also carried out using a high-resolution transmission electron microscope (HR-TEM), JEOL JEM-F200.

6. Fourier Transform Infrared (FT-IR) Spectroscopy:

The metal oxide bond of the samples was analyzed with the Bruker Fourier Transform Infrared (FT-IR) spectrometer.

7. Photoluminescence Studies:

The photoluminescence excitation and emission spectra, photoluminescence decay curves, and quantum yield were investigated using a Yvon Fluorolog 3 spectrofluorimeter with a 450 W Xenon flash lamp as the exciting source.

8. UV- Diffuse Reflectance Spectroscopy (UV-DRS):

UV-DRS measurements were carried out using a Shimadzu UV-3600 UV-Vis spectrophotometer in the 200-500 nm wavelength range using barium sulfate as a reference.

9. EPR Measurements:

EMX Series spectrometer using X band frequency (9.5 GHz) and 100 kHz field modulation.

10. Low-Temperature Photoluminescence Studies:

(i) Low-temperature PL measurements were performed using a continuous-flow liquid He cryostat mounted on a three-axis motorized translation stage to control the sample position. The excitation of the sample was provided by a continuous-wave Oxxius laser with a wavelength of 266 nm operating at a constant power of 4 mW, focused into a spot of about 5 μm. The PL spectra were recorded for temperatures from 7 K to 300 K using a Horiba HR460 spectrometer with 600 grooves/mm grating equipped with a Si charge-coupled device (CCD) detectors.

(ii) The low temperature-dependent photoluminescence studies were performed using FLS-1000 fluorescence spectrometer equipped with cryostat assembly, and liquid nitrogen was used as the coolant. The temperature was increased by 10 K within the ± 0.5 K limit using a temperature controller unit. Low temperature-dependent decay curves were recorded with a μF2 lamp (Edinburgh Instruments) at a frequency of 10 Hz.

11. ^{1}H NMR:

The ^{1}H NMR measurements were carried out with the help of a 60 MHz Bruker Ascend.

12. TGA Measurement:

The TGA measurement was employed using the TA Q50 Analyzer.

13. Electroluminescence Studies:

The electroluminescence properties of the obtained devices were measured using a high-sensitivity CCD spectrophotometer (Maya 2000 Pro).

ABSTRACT

Name of the student: Sreevalsa. S	**Registration No.:** 10CC20A39007
Faculty of Study: Chemical Sciences	**Year of Submission:** 2025
CSIR Lab: National Institute for Interdisciplinary Science & Technology (CSIR-NIIST), Trivandrum, Kerala	**Name of the Supervisor:** Dr. Subrata Das

Title of the thesis: Compositionally Tuned Single-Phase Oxyfluoride Phosphor Converters for Advanced Full Spectral White Light Emitting Devices

The thesis widely analyses the structural and optical properties of rare-earth-based (particularly $Eu^{2+/3+}$/Ce^{3+}) broadband emitting oxyfluoride phosphors and their applicability in solid-state lighting applications. Chapter 1 describes Eu^{3+} doped $Sr_{2.9-3x/2}(Gd/Y)_xAlO_4F$ (x = 0.01 to 0.10) phosphors, their structural and photoluminescence properties, the phosphor composite film making and their suitability in flexible display devices. In Chapter 2, intense Eu^{2+}/Eu^{3+}-coexisted $Sr_{2.9}Al_{1-x}Si_xO_{4+x}F_{1-x}$: $0.1Eu^{2+/3+}$ ($SASi_xOF$: $Eu^{2+/3+}$) oxyfluorides were prepared through a conventional solid-state method. By the substitution of Al^{3+} with Si^{4+} ions enlarged the activator sites that enabled Eu^{3+} ions to be reduced to Eu^{2+} ions, and on varying the Si^{4+} ions doping concentration, we tuned the emission color from orange-red to nearly white and eventually to the bluish zone. The most suitable compositions were further used to fabricate proposed phosphor-polymer composite membranes to avoid silicon-based phosphor binders for device applications. The composite made with near white emitting $SASi_{0.03}OF$: $Eu^{2+/3+}$ phosphor was integrated with a near UV-LED, which showed intense cool white emission with the CIE of (0.29, 0.32), CCT of 7629 K, and CRI of 96. In Chapter 4, generate single white light emission from a promising silicate apatite oxyfluroride host, $Ca_4La_6Si_6O_{24}F_2$, via the following cationic substitution strategy. By the introduction of divalent Sr^{2+} ion, a series of intense green-emitting $Ca_2Sr_2La_6Si_6O_{24}F_2$: Eu^{2+} phosphors were synthesized. The emission of Eu^{2+} was further tuned from cyan to greenish-yellow via the doping of Mg^{2+} and Ba^{2+} ions into the appropriate lattice sites. Detailed local environment investigations reveal that the change of symmetry owing to the Mg^{2+}/Ba^{2+} substitution led to the centroid shift, which was responsible for the blue- or red-shift of the emission spectra. The optimized phosphors had comparable emission intensity with commercial YAG and has high quantum yield with good thermal stability, exhibiting decent photoluminescence above 70% at 150 ^oC as compared with that at room temperature. In Chapter 5, we developed full spectral emitting violet-excitable $(Sr,Ba)_3(Al,Si)O_4F$: Ce^{3+}, Eu^{2+} phosphors with a high quantum efficiency of 86% and thermal stability of 78% via solid-state route. The highly red-shifted $Sr_{1.995}Ba_{1-x}Al_{0.5}Si_{0.5}O_4F$: $0.025Ce^{3+}$; $0.005Eu^{2+}$ phosphor powders were further chosen for fabricating thiourethane (CTU) based phosphor polymer composite films. The developed phosphor polymer composite showing promising optical performance under 410 nm violet-LED chip and a violet lesser of 405 nm. The generated warm white light showing very high CRI~80 and very low CCT~ 4000 K.

Thesis Outcomes

List of Publications Emanating from Thesis Work

1. **S. Sreevalsa**, P.A. Parvathy, S.K. Sahoo, Subrata Das, Full-color emitting crystal engineered $Sr_3Al_{1-x}Si_xO_4F$: $Eu^{2+/3+}$ oxyfluorides for developing bendable lighting composites, J. Alloys Compd., 880 (2021) 160483. https://doi.org/10.1016/j.jallcom.2021.160483

2. **S. Sreevalsa,** S. Ahmad, P. Kundu, M. K. Pandey, S. Som, Subrata Das, Governing the Crystallographic Sites for Tuning Eu^{2+} Emission in an Apatite Oxyfluoride Host to be Applied for Superior White Light Emitting Diodes, Dalton Trans., 51 (2022) 14601. https://doi.org/10.1039/d2dt02236b

3. **S. Sreevalsa**, B. John, A. Balhara, S.K. Sahoo, S.K. Gupta, S. Das, Violet excitable, highly efficient single broadband emitting oxyfluoride phosphor and polymer composite for conventional and laser-triggered lighting applications, Chem. Eng. Journal, (2025). (Manuscript communicated after revision)

List of Publications Not Related to Thesis Work

1. **S. Sreevalsa**, P. Ranjith, S. Ahmad, S. K. Sahoo, S. Som, S. Das, Host sensitized photoluminescence in $Sr_{2.9-3x/2}Ln_xAlO_4F$: $0.1Eu^{3+}$ (Ln = Gd, Y) for innovative flexible lighting applications, Ceramics International, 46 (2020) 21448. https://doi.org/10.1016/j.ceramint.2020.05.243

2. P. Ranjith, **S. Sreevalsa**, J. Tyagi, K. Jayanthi, G. Jagannath, P. Patra, S. Ahmad, K. Annapurna, A.R. Allu, S. Das, Elucidating the structure and optimising the photoluminescence properties of $Sr_2Al_3O_6F$: Eu^{3+} oxyfluorides for cool white-LEDs, J. Alloys Compd., 826 (2020) 154015. https://doi.org/10.1016/j.jallcom.2020.154015

3. P. Ranjith, **S. Sreevalsa**, P. Patra, S. Som, A. Menon, K.Annapurna, A.R. Allu, S. Das, Realizing cool and warm white – LEDs based on color controllable $(Sr,Ba)_2Al_3O_6F$:Eu^{2+} phosphors obtained via a microwave-assisted diffusion method, Phys. Chem. Chem. Phys, 23 (2021) 15245-15256. https://doi.org/10.1039/D1CP01593A

List of posters and oral presented

1. **S. Sreevalsa**, Governing the crystallographic sites for tuning Eu^{2+} emission in an apatite oxyfluoride host to generate white light, International Conference on Optoelectronic and Nanomaterials for Advanced Technology (icoNMAT 2025), 12 to 14 February 2025, Cohin University of Science and Technology, Kochi - Kerala, India, Feb. (Poster Presentation)
2. **S. Sreevalsa**, Subrata Das, Governing the crystallographic sites for tuning Eu^{2+} emission in an apatite oxyfluoride to generate white light, New Vistas in Critical Minerals and Materials conclave held at CSIR-NIIST on 1st August 2025. (Poster Presentation) (Best Poster Award)

Abstract for conference presentations

(icoNMAT 2025)

Governing the Crystallographic Sites for Tuning Eu^{2+} Emission in an Apatite Oxyfluoride Host to Generate White Light

Sreevalsa Subhagan,[1,2] Shahzad Ahmad,[3] Partha Kundu,[2.4], Mukesh Kumar Pandey,[5] Sudipta Som,[6] Subrata Das,[1,2,*]

[1]*Materials Science and Technology Division, CSIR – National Institute for Interdisciplinary Science and Technology, Thiruvananthapuram, Kerala, 695019, India.*
[2]*Academy of Scientific and Innovative Research (AcSIR), Ghaziabad, 201002, India*
[3]*Department of Chemistry, Zakir Husain Delhi College, University of Delhi, Delhi, 110002, India.*
[4]*Environmental Technology Division, CSIR-National Institute for Interdisciplinary Science and Technology (CSIR-NIIST), Thiruvananthapuram, Kerala, 695019, India*
[5]*Department of Physics, National Taiwan University, Taipei,10617, Taiwan*
[6]*Department of Chemical Engineering, National Taiwan University, Taipei,10617, Taiwan*

* *Corresponding author's E-mail address: subratadas@niist.res.in*

This study aimed at the generation of white light from a single-phase composition activated only with europium. Eu^{3+}-activated $Ca_4La_6Si_6O_{24}F_2$ phosphors showed predominant $^5D_0$-$^7F_2$ electric dipole transition at 614 nm, and the non-splitting as well as the zero-shifting behaviour of $^5D_0$-$^7F_0$ at 578 nm, suggested rare-earth ionic substitutions at the larger asymmetric sites. Introducing Sr^{2+} ions in $Ca_4La_6Si_6O_{24}F_2$:Eu^{3+}/Eu^{2+} that is synthesized in a reducing atmosphere suppressed Eu^{3+} emission. From the optimized $Ca_{1.98}Sr_{1.98}La_6Si_6O_{24}F_2$:$0.04Eu^{2+}$, and M^{2+}-codoped (M=Mg/Ba) $Ca_{1.98}Sr_{1.98}La_6Si_6O_{24}F_2$: $0.04Eu^{2+}$ phosphors were further developed. The substitutions of Mg^{2+} and Ba^{2+} altered the crystal field by changing the lattice parameters. The Mg^{2+} doped samples showed a blue-shift from 520 nm (Mg^{2+}=0) to 471 nm (Mg^{2+}=1.0). Whereas the Ba^{2+} doped compositions showed a red-shift from 520 nm (Ba^{2+}=0) to 536 nm (Ba^{2+}=1.2). Finally, several prototype WLEDs were fabricated using the single phosphor $Ca_{1.365}Sr_{1.365}La_6Si_6O_{24}F_2$:$0.07Eu^{2+}$, $1.2Ba^{2+}$ with near-UV and violet-LED chips. The outcomes indicated the promising nature of this single composition phosphor for indoor lighting.

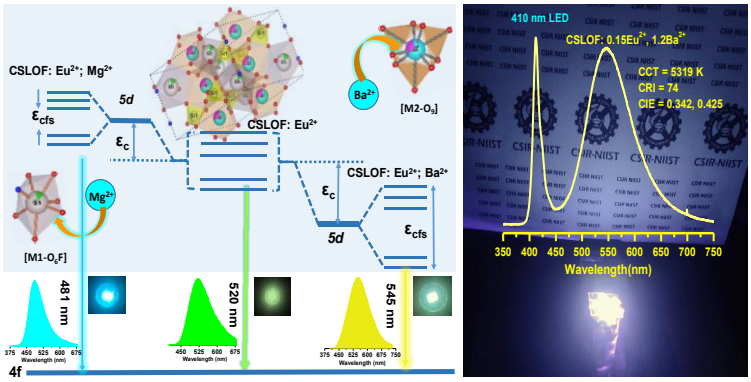

Abstract for conference presentations

(New Vistas in Critical Minerals and Materials-2025)

Governing the Crystallographic Sites for Tuning Eu^{2+} Emission in an Apatite Oxyfluoride to Generate White Light

Sreevalsa Subhagan,[1,2] and Subrata Das,[1,2,*]

[1]*Materials Science and Technology Division, CSIR – National Institute for Interdisciplinary Science and Technology, Thiruvananthapuram, Kerala, 695019, India.*
[2]*Academy of Scientific and Innovative Research (AcSIR), Ghaziabad, 201002, India*

** Corresponding author's E-mail address: subratadas@niist.res.in*

This study aimed at the generation of white light from a single-phase composition activated only with europium. Eu^{3+}-activated $Ca_4La_6Si_6O_{24}F_2$ phosphors showed predominant $^5D_0$-$^7F_2$ electric dipole transition at 614 nm, and the non-splitting as well as the zero-shifting behaviour of $^5D_0$-$^7F_0$ at 578 nm, suggested rare-earth ionic substitutions at the larger asymmetric sites. Introducing Sr^{2+} ions in $Ca_4La_6Si_6O_{24}F_2$:Eu^{3+}/Eu^{2+} that is synthesized in a reducing atmosphere suppressed Eu^{3+} emission. From the optimized $Ca_{1.98}Sr_{1.98}La_6Si_6O_{24}F_2$:$0.04Eu^{2+}$, and M^{2+}-codoped (M=Mg/Ba) $Ca_{1.98}Sr_{1.98}La_6Si_6O_{24}F_2$: $0.04Eu^{2+}$ phosphors were further developed. The substitutions of Mg^{2+} and Ba^{2+} altered the crystal field by changing the lattice parameters. The Mg^{2+} doped samples showed a blue-shift from 520 nm (Mg^{2+}=0) to 471 nm (Mg^{2+}=1.0). Whereas the Ba^{2+} doped compositions showed a red-shift from 520 nm (Ba^{2+}=0) to 536 nm (Ba^{2+}=1.2). Finally, several prototype WLEDs were fabricated using the single phosphor $Ca_{1.365}Sr_{1.365}La_6Si_6O_{24}F_2$:$0.07Eu^{2+}$, $1.2Ba^{2+}$ with near-UV and violet-LED chips. The outcomes indicated the promising nature of this single composition phosphor for indoor lighting.[1]

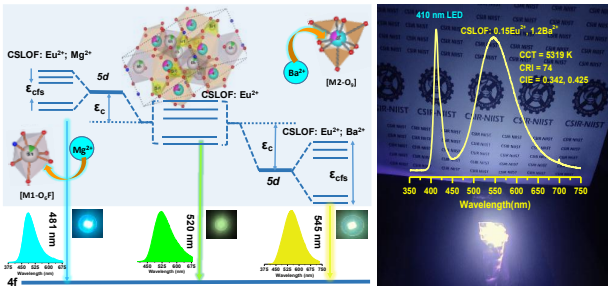

Fig. 1 – Multi-sized cationic substitution strategies to tune and improvise the Eu^{2+} broadband emission to yellowish region which is compatible for the near-UV and violet LEDs for generating superior quality white light for indoor lighting.

Reference

[1] S. Subhagan, S. Das et al., Dalton Trans 2022, 51, 14601. https://doi/10.1039/d2dt02236b

Dalton Transactions

ROYAL SOCIETY OF CHEMISTRY

PAPER

View Article Online
View Journal | View Issue

Cite this: *Dalton Trans.*, 2022, **51**, 14601

Governing the crystallographic sites for tuning Eu^{2+} emission in an apatite oxyfluoride host to be applied for superior white light emitting diodes†

Sreevalsa Subhagan,[a,b] Shahzad Ahmad,[c] Partha Kundu,[b,d] Mukesh Kumar Pandey,[e] Sudipta Som [f] and Subrata Das *[a,b]

Single white light-emitting phosphors for near-UV-converted white light-emitting diodes (WLEDs) are the best alternatives to tricolour phosphor blends and blue light converted yellow-emitting garnets. Nevertheless, achieving white light with elevated colour rendering (CRI) from a single-phase phosphor activated with a lone activator ion is a major challenge. This study aimed at the generation of white light from a single-phase composition activated only with europium. The study started with structural evaluations of Eu^{3+}-activated $Ca_4La_6Si_6O_{24}F_2$ phosphors using X-ray diffraction (XRD) and Eu^{3+} photoluminescence to elucidate the local environment of rare-earth ions and the symmetric nature of the lattice sites. $Ca_4La_6Si_6O_{24}F_2$ crystallized in the hexagonal $P6_3/m$ space group. The predominant $^5D_0-^7F_2$ electric dipole transition at 614 nm, and the non-splitting as well as the zero-shifting behaviour of $^5D_0-^7F_0$ at 578 nm, suggested that the rare-earth ionic substitutions preferably took place at the larger asymmetric sites. Introducing Sr^{2+} ions in $Ca_4La_6Si_6O_{24}F_2$:Eu^{3+}/Eu^{2+} that is synthesized under a reducing atmosphere suppressed Eu^{3+} emission. From the optimized $Ca_{1.98}Sr_{1.98}La_6Si_6O_{24}F_2$:0.04$Eu^{2+}$, a sequence of M^{2+}-codoped (M = Mg/Ba) $Ca_{1.98}Sr_{1.98}La_6Si_6O_{24}F_2$:0.04$Eu^{2+}$ phosphors were further developed. The substitutions of Mg^{2+} and Ba^{2+} altered the crystal field by changing the lattice parameters. The Mg^{2+}-doped samples showed a blue-shift from 520 nm (Mg^{2+} = 0) to 471 nm (Mg^{2+} = 1.0), whereas the Ba^{2+}-doped compositions showed a red-shift from 520 nm (Ba^{2+} = 0) to 536 nm (Ba^{2+} = 1.2). The change of symmetry owing to the Mg^{2+}/Ba^{2+} substitution could have led to the centroid shift, which was responsible for the blue- or red-shift of the emission spectra. The XRD of $Ca_{1.38}Sr_{1.38}La_6Si_6O_{24}F_2$:0.04$Eu^{2+}$,1.2$Ba^{2+}$ indicated a Ba^{2+}-induced lattice site expansion. Keeping this in view, the Eu^{2+} ions concentrations were further enhanced from 0.04 to 0.3, and the resultant photoluminescence was further enhanced and red-shifted. The optimized sample showed better intensity compared with the commercial $Y_3Al_5O_{12}$:Ce^{3+} and exhibited decent photoluminescence above 70% at 150 °C as compared with that at room temperature. Finally, several prototype WLEDs were fabricated using the single phosphor $Ca_{1.365}Sr_{1.365}La_6Si_6O_{24}F_2$:0.07$Eu^{2+}$,1.2$Ba^{2+}$ with near-UV and violet-LED chips. The outcomes indicated the promising nature of this single-composition phosphor for indoor lighting.

Received 11th July 2022,
Accepted 27th July 2022

DOI: 10.1039/d2dt02236b

rsc.li/dalton

1. Introduction

The technology related to the phosphor-converted white light-emitting diodes is a revolution because of some significant features including high-quality lighting output for illumination, long lifetime, excellent efficiency, the high thermal stability of luminescence at higher temperatures, and very low energy consumption.[1–3] Generating white light from the combination of tricolour LED chips is becoming limited owing to the high price and complex drive circuit,[4] while the production of white light using phosphor-converted LEDs (pc-LEDs) has become mainstream. Nowadays, the modification and construction of WLEDs are mainly focused on phosphors and LED

[a]*Materials Science and Technology Division, CSIR – National Institute for Interdisciplinary Science and Technology, Thiruvananthapuram, Kerala, 695019, India. E-mail: subratadas@niist.res.in*
[b]*Academy of Scientific and Innovative Research (AcSIR), Ghaziabad, 201002, India*
[c]*Department of Chemistry, Zakir Husain Delhi College, University of Delhi, Delhi, 110002, India*
[d]*Environmental Technology Division, CSIR-National Institute for Interdisciplinary Science and Technology (CSIR-NIIST), Thiruvananthapuram, Kerala695019, India*
[e]*Department of Physics, National Taiwan University, Taipei, 10617, Taiwan*
[f]*Department of Chemical Engineering, National Taiwan University, Taipei, 10617, Taiwan*

† Electronic supplementary information (ESI) available. See DOI: https://doi.org/10.1039/d2dt02236b

chips. The crucial factor that directly influences the performance of LED devices is the phosphor material chosen; it must have an efficient emission nature, high thermal and chemical stability, mild synthetic conditions, *etc*.[5]

The widely used method for fabricating WLEDs is combining an InGaN blue-LED chip with a yellow-emitting $Y_3Al_5O_{12}$:Ce^{3+} phosphor,[6,7] but the prolonged blue-LED emission causes severe health issues for humans, such as mood disorders, macular degeneration, circadian disruption, *etc*.[8] To reduce the usage of blue-LED chips, nowadays near-UV LEDs (n-UV LEDs) are used as the excitation sources for obtaining the primary colour emissions from the corresponding phosphor materials.[9] n-UV LEDs offer a long lifetime, and greater reliability, and enable lighting designers to achieve a better CRI at a given colour point.[10] However, suitable single white-emitting phosphor systems for commercial n-UV LEDs are rarely obtained, due to the undefined distribution and uncontrolled emission behaviour of rare-earth ions.

These days, important research is focused on developing broad-band-emitting n-UV-excited oxyfluoride phosphors for lighting applications as an outcome of their high quantum efficiency and noticeable structural stability and rigidity.[11] Most importantly, the presence of fluorine ions introduces robust electronegativity, which can generate flexible emissive properties.[12] For the recently reported oxyfluorides, the presence of multiple crystallographic sites was able to provide versatile cationic environments for Ce^{3+} or Eu^{2+} ions, which are effective in generating broad emissions from these ions.[13] Eventually, an appropriate cationic replacement can drive the luminescent centers to produce emission wavelength shifts very effectively. Arunkumar *et al.* recently reported a broad-band-emitting $Ca_4F_2Si_2O_7$:Ce^{3+} phosphor based on the occupation of Ce^{3+} ions at multiple crystallographic sites in the host under n-UV excitation. In this host, Ce^{3+} ions can emit broad band emissions because of their accommodation at four available polyhedra of Ca atoms, namely CaF_4O_3 and $CaFO_6$, CaF_5O_3, and CaF_5O.[10] W. B. Im *et al.* reported intense green-emitting $Sr_{2.975-x}Ba_xCe_{0.025}AlO_4F$ oxyfluoride phosphors in response to 400 nm excitation.[14] In this system, Sr and Ba atoms are associated with SrO_6F_2 and BaO_8F_2 polyhedral units, which are substituted by Ce^{3+} ions and result in a broad band emission.

Similar to Ce^{3+} systems, Eu^{2+}-activated phosphors are also able to generate broadband emission bands, and hence, they are considered to have potential for WLED applications.[15]

Silicate apatite-based phosphors are emerging as promising hosts for rare-earth ions thanks to their high chemical and thermal stability.[16] Apatite host compounds crystallize in a hexagonal system with a $P6_3/m$ space group with the general structural formula $M_{10}(XO_4)_6Y_2$, in which M corresponds to divalent cations like Mg^{2+}, Ca^{2+}, Sr^{2+}, Ba^{2+}, *etc*., X represents Si^{4+}, Ge^{4+}, P^{5+}, As^{5+}, *etc*. which forms tetrahedra with oxygen, and Y represents anions like O^{2-}, F^-, and Cl^-. In this structure, M ions are situated in two sites; one is a seven-coordinated 6h site with C_s point symmetry, and the other is a nine-coordinated 4f site with C_3 point symmetry.[17–19] These hosts show decent luminescence properties because of the strong covalent X–O frameworks connected to two cationic polyhedra through edge- and corner-sharing, which distort the coordination environment around the cations.[17]

Following the general structural formula of apatite, Njema *et al.* reported the structural features of $Ca_{10-x}Ln_x(PO_4)_{6-x}(SiO_4)_xF_2$ phosphosilicate.[20,21] In this structure, the incorporation of La^{3+} and $(SiO_4)^{4-}$ pairs for Ca^{2+} and $(PO_4)^{3-}$ expanded the [Ca/La–O9] and [Ca/La–O6F] polyhedra, and contracted the [Si/P–O4] tetrahedra. The expansion of nine- and seven-coordinated polyhedra makes them suitable for the larger ionic substitutions.[20,21] To produce multiple coloured emissions including white light, apatite could be the ideal host because of the allowed tuning of various crystal sites either by multiple activator doping mechanisms or *via* the cationic substitution strategies within these hosts.[22–26] The fluorapatite structure ($M_{10}(XO_4)_6F_2$) is known for its abundant nature and high stability. The presence of fluoride ions in this system can generate potential luminescence properties in solid-state lighting due to the presence of a mixed ligand system.[19] Among the fluorapatite family, $Ca_{10}(PO_4)_6F_2$ is the most widely investigated composition for various applications because of its robust tolerance to numerous replacements.[19] In the present work, the $Ca_4La_6Si_6O_{24}F_2$ composition has been designed initially *via* the partial substitution of Ca^{2+} by La^{3+} and then $(PO_4)^{3-}$ was completely substituted by $(SiO_4)^{4-}$. The study of the structural and luminescence properties of this phosphor containing different valences of europium ions to achieve tuneable broadband emission is not reported yet.

In the europium-doped host lattice, the valences of Eu (2+ and 3+) coexist in the host. The parity-forbidden sharp 4f–4f transitions in the Eu^{3+}-activated phosphor lead to a low colour rendering index (CRI), and the 4f–5d transitions in Eu^{2+} cause an intensely broad band emission, which is more applicable for white-light-emitting applications.[27] The spectroscopic properties of Eu^{3+} ions highly depend on the local environment. For instance, if the dopant enters the specific site under examination, then its emission behaviour depends on the symmetry of the site, which can be changed because of the slight alteration in the ligand field. Thus, the characteristics of any crystallographic site could be revealed by studying the splitting of the emission bands of the Eu^{3+} ions located at that specific site.[28] Therefore, the Eu^{3+} ions' luminescence is a good probe and is favourable for the investigation of the symmetry of various sites of any host material. Because of the similar ionic radius, the site occupancy for Eu^{3+} in the $Ca_4La_6Si_6O_{24}F_2$ host can be, to some extent, considered as a reference for broadband-emitting Eu^{2+} ions in the same host matrix. Meanwhile, adjusting the concentrations and emission ratio of Eu^{3+} and Eu^{2+} ions could effectively tune the emission colour. For example, Y. Zhang *et al.* generated a series of $Ca_{0.99+x}Y_{1-x}Al_{1-x}Si_xO_4$:$Eu_{0.01}$ phosphors where the substitution of Al^{3+}–Y^{3+} by Si^{4+}–Ca^{2+} was initiated. Such a strategy shrinks the [AlO_6] octahedra, followed by expanding the [CaO_9] polyhedra, which enhanced the Eu^{3+}-to-Eu^{2+} reduction effectively.[29] Recently, our group has also reported cool white-light-emitting $Sr_{2.9}Al_{1-x}Si_xO_4F$:$0.1Eu^{2+/3+}$ phosphors through a similar cation substitution strategy.[30] Nonetheless, a high Eu^{2+}-to-Eu^{3+} ratio is required for generat-

ing a wide gamut for WLEDs, and the search to find a suitable oxyfluoride host that can accommodate large sized Eu^{2+} ions is still in progress.

As per the above discussions, we initiated our research for developing broad band-emitting and apatite-structured Eu^{2+}-doped oxyfluoride systems for the wide gamut of WLED applications. Initially, a series of intense green-emitting $Ca_2Sr_2La_6Si_6O_{24}F_2$:$Eu^{2+}$ phosphors were synthesized. Herein, an X-ray diffraction Rietveld refinement tool and Eu^{3+} spectroscopy were used to identify the site occupancy, symmetry, and lattice distortion in the $Ca_2Sr_2La_6Si_6O_{24}F_2$ host. The emission of Eu^{2+} was further tuned from green to cyan and to greenish-yellow *via* the doping of Mg^{2+} and Ba^{2+} ions into the appropriate lattice sites, respectively. The optimized phosphors had comparable emission intensity to commercial $Y_3Al_5O_{12}$:Ce^{3+} phosphors. Eventually, the optimized systems showed adequate photoluminescence intensity at 150 °C. These research outcomes make the presently optimized systems interesting for WLED applications.

2. Experimental

2.1. Preparation of a phosphor

A series of $Ca_4La_6Si_6O_{24}F_2$:xEu^{3+} (CLOF:xEu^{3+}; x = 0.0, 0.01 to 0.1) and $Ca_2Sr_2La_6Si_6O_{24}F_2$:$xEu^{2+}$ (CSLOF:xEu^{2+}; x = 0.0 to 0.055) phosphors were synthesized through a conventional solid-state method. Stoichiometric amounts of $CaCO_3$ (99.999%), $SrCO_3$ (99.999%), La_2O_3 (99.999%), SiO_2 (99.99%), NH_4F (99.99%), and Eu_2O_3 (99.999%) purchased from Sigma-Aldrich were ground together in an agate mortar for 30 min. After the homogeneous mixing, the ground mixture was transferred into an alumina crucible and annealed at 1300 °C for 4 h under a reduction atmosphere (10%H_2–90%N_2). For convenience, the $Ca_4La_6Si_6O_{24}F_2$ sample will be named CLOF and all other synthesised phosphors are represented accordingly, as illustrated in Table 1.

2.2. Material characterization

The structural insights into the experimental phosphors were studied by using a X-ray diffractometer EMPYREAN 3 Malvern Panalytical B.V with Cu-Kα radiation (wavelength: 1.54056 Å). The Rietveld refinements were carried out using GSAS software. The elemental composition of the synthesised phosphor was analysed by using a transmission electron microscope (TEM), JEOL JEM-F200. A Yvon Fluorolog 3 spectrofluorimeter was used to measure the photoluminescence. The electroluminescence spectra were recorded by using a CCD spectrophotometer (OCEAN-FX-XRI-EX).

Table 1 Short representations of the obtained samples

Synthesised phosphor	Short representation
$Ca_4La_6Si_6O_{24}F_2$	CLOF
$Ca_{4-3x/2}La_6Si_6O_{24}F_2$:$xEu^{3+}$	CLOF:xEu^{3+}
$Ca_2Sr_2La_6Si_6O_{24}F_2$	CSLOF
$Ca_{2-x}Sr_{2-x}La_6Si_6O_{24}F_2$:$xEu^{2+}$	CSLOF:xEu^{2+}
$Ca_{1.98-y}Sr_{1.98-y}La_6Si_6O_{24}F_2$:0.04$Eu^{2+}$,$yMg^{2+}$	CSLOF:0.04Eu^{2+},yMg^{2+}
$Ca_{1.98-z}Sr_{1.98-z}La_6Si_6O_{24}F_2$:0.04$Eu^{2+}$,$zBa^{2+}$	CSLOF:0.04Eu^{2+},zBa^{2+}

3. Results and discussion

3.1. Structural characterizations of $Ca_{4-3x/2}La_6Si_6O_{24}F_2$:$xEu^{3+}$ (CLOF:xEu^{3+}) and $Ca_{2-x}Sr_{2-x}La_6Si_6O_{24}F_2$:$xEu^{2+}$ (CSLOF:xEu^{2+})

Fig. 1(a) and (b) represent the Rietveld refinement patterns of the $Ca_4La_6Si_6O_{24}F_2$ (CLOF) host and $Ca_{3.94}La_6Si_6O_{24}F_2$:0.04$Eu^{3+}$ (CLOF:0.04Eu^{3+}) phosphor, respectively. The estimated structural parameters are tabulated in Table S1.† As per the refinement data analysis, both undoped and doped apatite phosphors belonged to the hexagonal structure with a $P6_3/m$ space group without any predominant impure phase (ICSD # 170852). The probable crystal structure and coordination environment for different cationic sites of the CLOF host are shown in Fig. 1(c). The structure consists of two independent crystallographic cationic sites: seven-coordinated 6h sites and nine-coordinated 4f sites. Both the sites are asymmetric. The 6h sites are occupied by M1 (La^{3+}/Ca^{2+}) cations, which form a distorted pentagonal bipyramid [M1–O_6F] with C_s point symmetry, whereas M2 (La^{3+}/Ca^{2+}) cations occupy 4f sites and form a three-fold capped trigonal prism [M2–O_9] with C_3 point symmetry. Simultaneously, Si^{4+} ions are tetrahedrally coordinated with oxygen atoms to form [Si–O_4] polyhedra. Each [M1–O_6F] polyhedron is connected to the [SiO_4] tetrahedron by edge- or corner-sharing. The [M2–O_9] polyhedra are on a three-fold axis and each of these polyhedra is connected to three [SiO_4] tetrahedra through edge-sharing.

In the CLOF host, 75% of the 6h sites are occupied by La^{3+} ions and 25% of them by Ca^{2+} ions., while the occupancy of La^{3+} and Ca^{2+} ions in the 4f sites are predicted to be 37.5% and 62.5%, respectively, as indicated in Table S2.† Among the two cationic sites, the nine-coordinated 4f sites have a larger size than the seven-coordinated 6h sites. The ionic radii of the La^{3+} and Ca^{2+} ions in the nine- and seven-coordinated sites are (La^{3+}: R_{4f} = 1.216 Å; R_{6h} = 1.10 Å) and (Ca^{2+}: R_{4f} = 1.18 Å; R_{6h} = 1.06 Å), respectively. After incorporating Eu^{3+} ions into the CLOF host, the cell volume and lattice parameters are found to be decreased slightly due to the substitution of smaller Eu^{3+} ions (Eu^{3+}: R_{4f} = 1.12 Å; R_{6h} = 1.01 Å) at both the ionic sites (Table S1†). Eventually, the average (La2/Ca2–O) bond length at the 4f sites is slightly contracted (CLOF = 2.657 Å, CLOF:Eu^{3+} = 2.629 Å) while the average (La1/Ca1–O) bond length at the 6h sites remains almost unchanged (CLOF = 2.549 Å, CLOF:Eu^{3+} = 2.547 Å) due to the Eu^{3+} ion doping in the CLOF host. Such observations confirm that the 4f sites could be preferable for Eu^{3+} ion substitution. The powder diffraction pattern of a series of synthesized $Ca_{4-3x/2}La_6Si_6O_{24}F_2$:$xEu^{3+}$ (CLOF:xEu^{3+}) phosphors, shown in Fig. 1(d), does not elaborate on any characteristic impure phase after increasing the Eu^{3+} ion concentrations. In addition, there is a slight shift of the main diffraction peak of CLOF after increasing the Eu^{3+} ion concentration towards the right, which ensures the

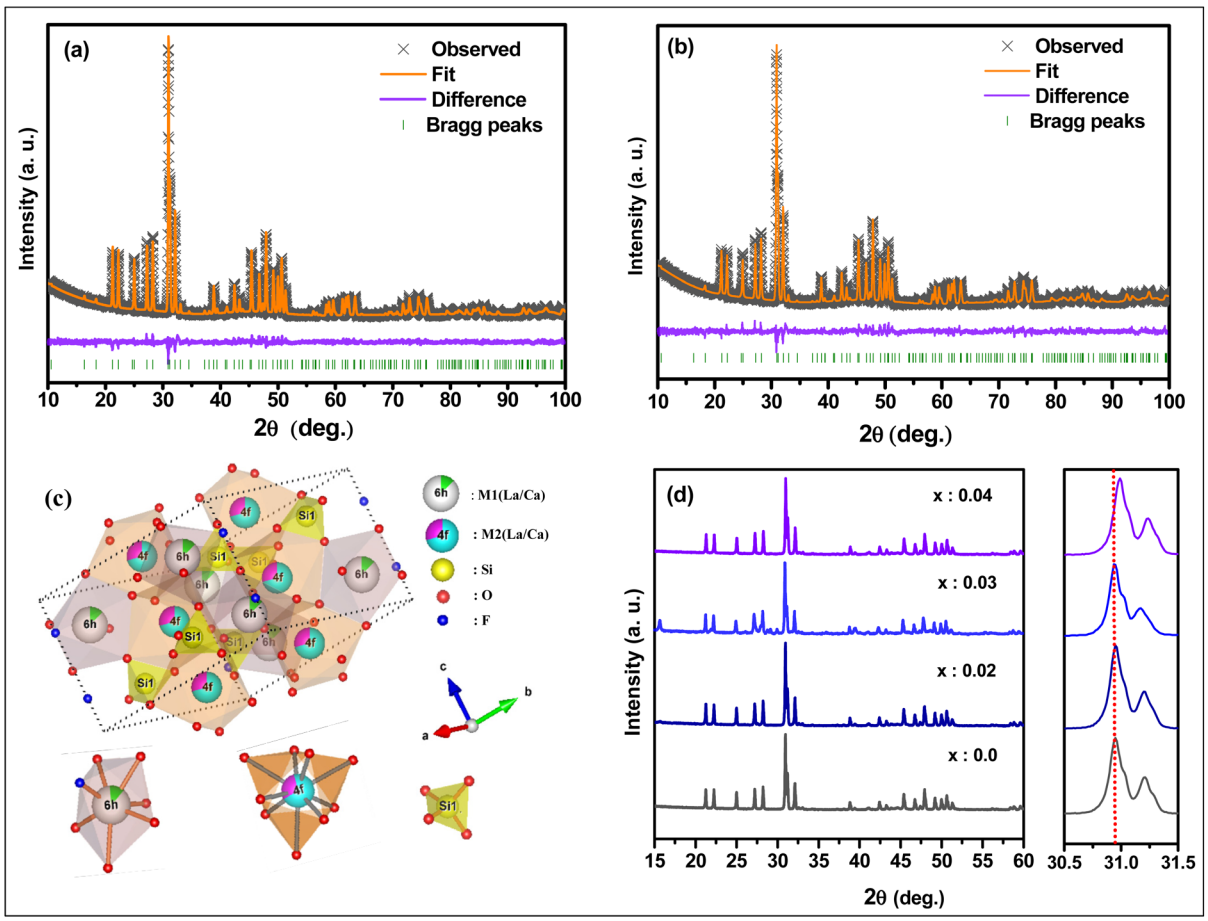

Fig. 1 Rietveld refinement of (a) CLOF and (b) CLOF:0.04Eu^{3+}. (c) Crystal structure and different coordination environment of CLOF:0.04Eu^{3+}. (d) Powder XRD patterns of CLOF:xEu^{3+} (x = 0, 0.02, 0.03, and 0.04).

preferable substitution of Eu^{3+} ions at the larger Ca^{2+}/La^{3+} ionic sites in the host lattice.

Normally, it would be quite difficult to accommodate Eu^{2+} ions in the CLOF host because of the large ionic radius difference of a Eu^{2+} ion in the two cationic sites (Eu^{2+}: R_{4f} = 1.3 Å; R_{6h} = 1.2 Å). The comfortable substitution of Eu^{2+} ions in this host might need cationic site expansion. Thus, larger Sr^{2+} ions are incorporated into the CLOF host. Fig. 2(a) and (b) represent the Rietveld refinement patterns of $Ca_2Sr_2La_6Si_6O_{24}F_2$ (CSLOF) and $Ca_{1.98}Sr_{1.98}La_6Si_6O_{24}F_2$:0.04$Eu^{2+}$ (CSLOF:0.04Eu^{2+}) phosphors. The parameters evaluated from the crystal structure refinement are listed in Table S1.† The lattice parameters of CSLOF are found to be increased as compared with the CLOF host due to the larger Sr^{2+} ion incorporation (R_{4f} = 1.31 Å; R_{6h} = 1.21 Å) into the host lattice compared with the Ca^{2+}/La^{3+} ions, owing to which more Eu^{2+} ions can be easily accommodated in the cationic sites. The average metal–oxygen bond lengths in the 4f and 6h cationic sites are slightly enhanced from 2.657 to 2.668 Å and 2.549 to 2.560 Å, respectively, after the Sr^{2+} ion incorporation (Fig. 2(c)). Fig. 2(d) shows the powder diffraction patterns of a series of $Ca_{2-x}Sr_{2-x}La_6Si_6O_{24}F_2$:$xEu^{2+}$ (CSLOF:xEu^{2+}) phosphors. With the increase in Eu^{2+} concentration, there is no characteristic phase change, indicating the proper incorporation of Eu^{2+} ions in the lattice without causing any phase defects. Eventually, the lattice parameters are also increased slightly owing to the Eu^{2+}-doping of the CSLOF host (Table S1†). Replacing Ca^{2+} ions with relatively bigger Eu^{2+} ions could be the reason for the left-shift and the lattice expansion. Fig. S1† describes the HRTEM spectrum and elemental mapping of undoped CSLOF. All its constituent elements, *i.e.*, Ca, La, Si, O, and F in particular, are distributed homogeneously, with no clustering or segregation of any of the elements. Thus, the results of electron mapping further ascertained the formation of single-phase phosphor and sample homogeneity.

3.2. Photoluminescence of $Ca_{4-3x/2}La_6Si_6O_{24}F_2$:$xEu^{3+}$ (CLOF:xEu^{3+}) synthesized in air

It is shown from the XRD of CLOF:Eu^{3+} that Eu^{3+} ions preferably occupy non-centrosymmetric 4f sites, which have a larger size than the asymmetric 6h sites. This prediction might be supported by the M–O bond length calculation for the 4f and 6h sites. Based on the ionic radii, Eu^{3+} ions can replace both La^{3+} and Ca^{2+} ions in the CLOF host. It is already mentioned

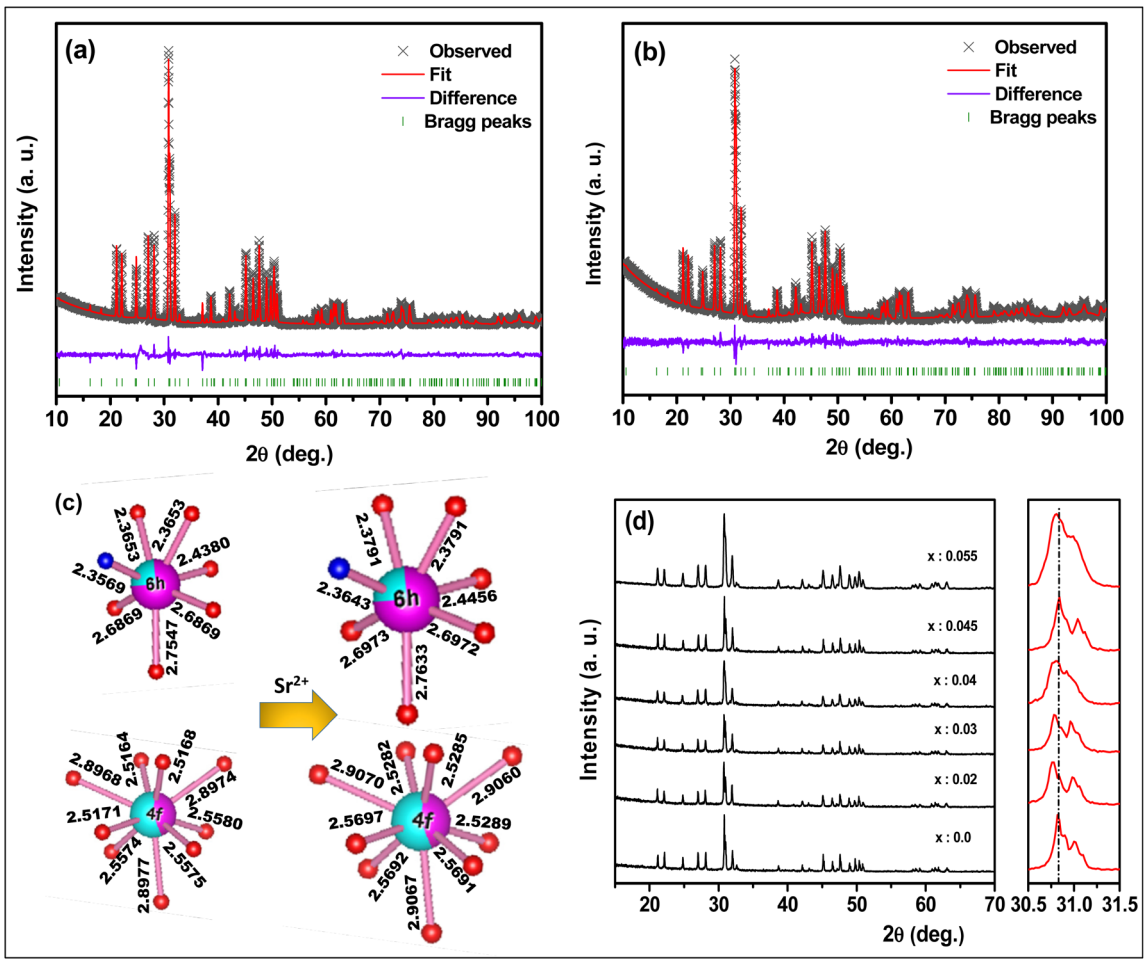

Fig. 2 Rietveld refinement of (a) CSLOF and (b) CSLOF:0.04Eu^{2+}. (c) Schematic representation of the average metal–oxygen bond length variation in undoped CLOF and CSLOF. (d) XRD patterns of CSLOF:xEu^{2+} (x = 0.0, 0.02, 0.03, 0.04, 0.045, and 0.055).

in the XRD section that the occupancy of Ca^{2+} ions is much higher at the 4f sites and the occupancy of La^{3+} ions is higher at the 6h sites (Table S2†). For the suitable occupation of bigger Eu^{2+} ions in the CLOF system, identifying the nature of the site symmetry and the appropriate cation is very important. Eventually, the emission intensity of the activator ion directly depends on the crystallographic site symmetry of that particular host. Herein, Eu^{3+} ion spectroscopy is used as the structural probe to get more insight into the site symmetries in the present host system. Fig. 3(a) represents the comparative photoluminescence of $C_{3.94}$LOF:0.04Eu^{3+} and $CL_{5.96}$OF:0.04Eu^{3+} samples synthesized in the air by replacing the Ca^{2+} ions and La^{3+} ions with Eu^{3+} ions, respectively. Both the combinations show similar photoluminescence since the Eu^{3+} ions substituted Ca^{2+} and La^{3+} ions which share similar lattice sites and have similar ionic radii to those of Eu^{3+}. However, the excitation spectra of $C_{3.94}$LOF:0.04Eu^{3+} exhibit a slightly red-shifted charge transfer band (CTB) of O^{2-} to Eu^{3+} ions in comparison with the CTB of $CL_{5.96}$OF:0.04Eu^{3+}. In the $C_{3.94}$LOF:0.04Eu^{3+} system, the Eu–O bonds might be more covalent than in $CL_{5.96}$OF:0.04Eu^{3+} owing to the charge difference between the Ca^{2+} and Ln^{3+} (Ln = La^{3+}, Eu^{3+}) ions. This could be the reason for the red-shift of the CTB band when Eu^{3+} ions replace Ca^{2+} ions rather than La^{3+} ions. According to Feng *et al.*, the CTB red-shift can be observed in the case of Eu^{3+} ions substituting the less electronegative metal ions and *vice versa*.[31] La^{3+} ions (13.07×10^{-30} m^3) have a higher polarizability value than that of Ca^{2+} ions (5.91×10^{-30} m^3) because of this reason, and a red-shift in CTB of $C_{3.94}$LOF:0.04Eu^{3+} as compared with $CL_{5.96}$OF:0.04Eu^{3+} is observed.[20]

Fig. 3(b) shows the PLE of a series of $Ca_{4-3x/2}La_6Si_6O_{24}F_2$:$xEu^{3+}$ (CLOF:xEu^{3+}) samples recorded at 614 nm. The spectra consist of a broad band covering from 240 to 340 nm corresponding to the O^{2-}–Eu^{3+} CTB, and several sharp lines are observed in the region after 350 nm due to the intra-configurational f–f transitions of the Eu^{3+} ions. A red-shift in the CTB is observed up to x = 0.04, above which the CTB peak shifted to the lower wavelength side. This is attributed to the occupation of Eu^{3+} ions at 4f sites with C_3 symmetry. In CLOF:0.04Eu^{3+}, the average metal–oxygen bond length at 4f sites (2.629 Å) is observed to be higher than that at the 6h sites (2.547 Å). The larger bond length at 4f sites might reduce the energy of the

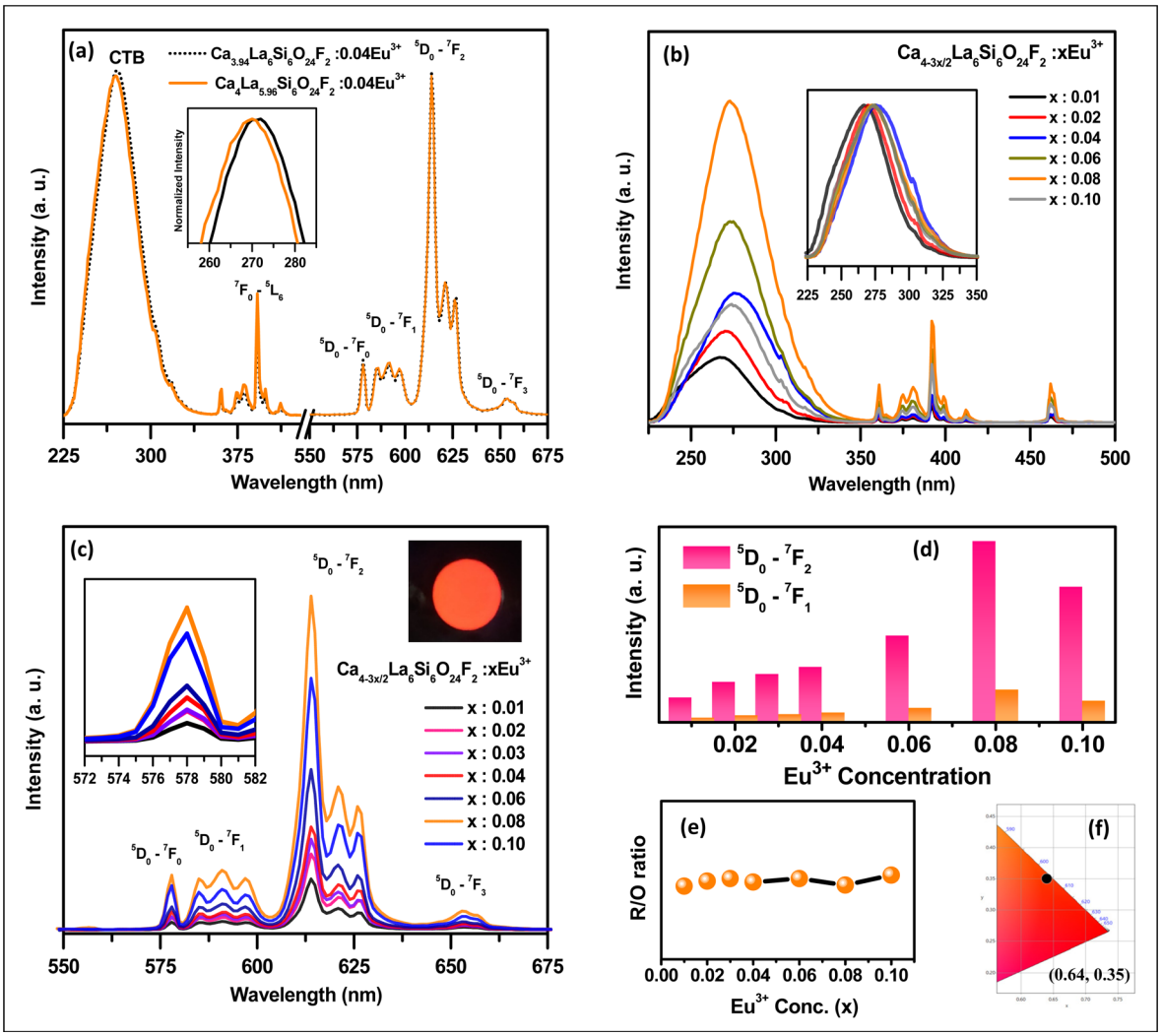

Fig. 3 (a) The comparative excitation and emission spectra of $Ca_{3.94}La_6Si_6O_{24}F_2$:0.04$Eu^{3+}$ and $Ca_4La_{5.96}Si_6O_{24}F_2$:0.04$Eu^{3+}$ samples synthesized in air and recorded at 614 nm and 280 nm, respectively. (b) Excitation and (c) emission spectra of $Ca_{4-3x/2}La_6Si_6O_{24}F_2$:$xEu^{3+}$ (x = 0.01, 0.02, 0.04, 0.06, 0.08, and 0.10) recorded at 614 nm and 280 nm, respectively. (d) The variation in the intensity of red ($^5D_0$–$^7F_2$) and orange ($^5D_0$–$^7F_1$) transitions, and (e) the variations in the red-to-orange ratio for $Ca_{4-3x/2}La_6Si_6O_{24}F_2$:$xEu^{3+}$ phosphors. (f) CIE diagram and colour coordinates of CLOF:0.08Eu^{3+} phosphor under 280 nm UV illumination.

CTB and may cause the initial red-shift. Above a certain level of doping concentration, Eu^{3+} ions started to occupy smaller 6h sites with C_s symmetry and having shorter bond lengths, and thus a blue shift in excitation is observed.[31]

Fig. 3(c) describes the PL emission spectra of a series of CLOF:$x$$Eu^{3+}$ phosphors synthesized in air and excited under a 280 nm CTB peak wavelength. The emission spectra consist of several sharp peaks of Eu^{3+} ion intra f–f transitions. Herein, the sharp emission at 585 nm (ΔJ = ±1) corresponds to the electric dipole transition ($^5D_0$–$^7F_1$). The most intense peak at 614 nm (ΔJ = ±2) corresponds to the magnetic dipole transition ($^5D_0$–$^7F_2$), which means that Eu^{3+} ions are located at non-centrosymmetric sites.[32] Although both the sites in CLOF do not possess a centre of symmetry, however, the 4f site having C_3 point symmetry is comparatively less asymmetric than the 6h site with C_s point symmetry. Moreover, the observed peak at 578 nm is because of the $^5D_0$–$^7F_0$ forbidden transition, and it determines the Eu^{3+} ions' site occupancy in the CLOF host. According to the electric dipole selection rule, the $^5D_0$–$^7F_0$ transition usually appears for Eu^{3+} ions, which are situated at low symmetries like C_s, C_1, C_2, C_3, C_4, C_6, C_{2v}, C_{3v}, C_{4v}, and C_{6v}, respectively.[33] Therefore, the aforementioned observation shows that Eu^{3+} ions might have occupied both of the sites in the CLOF host. However, the zero splitting and non-shifting behaviour of the $^5D_0$–$^7F_0$ transition due to the increase of Eu^{3+} ion concentrations might be due to a more preferable occupancy of Eu^{3+} ions at the 4f sites, which are bigger and more asymmetric than the 6h sites.

The inset of Fig. 3(c) represents the direct PL image of the optimum CLOF:0.08Eu^{3+} sample in response to a 280 nm UV source. Fig. 3(d) represents the intensity variations of the $^5D_0$–$^7F_2$ and $^5D_0$–$^7F_1$ transitions in the emission spectra of the

CLOF:xEu^{3+} phosphors. It is observed that, on increasing the Eu^{3+} ion concentration, the intensity of the corresponding transition increases systematically up to x = 0.08 (critical concentration). However, the asymmetric ratio (red to orange ratio) plotted as a function of the Eu^{3+} ion concentrations does not appreciably change (Fig. 3€). Because of the above reasons, the overall emission colour does not change considerably with the Eu^{3+} ion concentration. The colour chromaticity (CIE) coordinates of the optimum CLOF:0.08Eu^{3+} phosphor are represented in Fig. 3(f). Based on the report of Duke *et al.*, a compound with high symmetry has minimal distortion and can produce narrowband emission from Ce^{3+} or Eu^{2+} ions and *vice versa* by suitable cationic substitutions.[34] In the CSLOF host, both the cationic sites are asymmetric in nature, and therefore more lattice distortion can be expected, due to which broad emission can be predicted if the valence of the europium ions could be changed from 3+ to 2+.

3.3. Photoluminescence of $Ca_{2-x}Sr_{2-x}La_6Si_6O_{24}F_2$:$x$Eu^{2+} (CSLOF:$x$Eu^{2+}) synthesized under a reduction atmosphere

According to the Dorenbos predictions, the variation in covalency or polarizability always leads to a centroid shift in the Eu polyhedra. Theoretically, the centroid shift is inversely proportional to the cationic electronegativity.[35] The energy difference between the lowest and the highest 5d levels is related to the symmetry and size of the Eu^{2+} coordination polyhedra.[36] In the CLOF host, the Ca^{2+} ions are less electronegative than the La^{3+} ions, based on the Pauling electronegativity scale of periodic elements. Hence, the broad emission from Eu^{2+} polyhedra situated at the Ca atomic sites can be preferably tuned to get the desired wavelength emission *via* cationic substitution strategies. Therefore, we have synthesized $Ca_{3.96}La_6Si_6O_{24}F_2$:0.04Eu^{2+} (CLOF:0.04Eu^{2+}) and $Ca_{1.98}Sr_{1.98}La_6Si_6O_{24}F_2$:0.04Eu^{2+} (CSLOF:0.04Eu^{2+}) under a N_2–H_2 reduction atmosphere. Fig. 4(a) and (b) represent the excitation and emission spectra of CLOF:0.04Eu^{2+} and CSLOF:0.04Eu^{2+} recorded at 520 nm and 340 nm, respectively. The asymmetric broadband excitation of CLOF:0.04Eu^{2+} covering from 250 to 450 nm further deconvoluted into six Gaussian components located at 284 nm (P1: 4.37 eV), 297 nm (P2: 4.18 eV), 319 nm (P3: 3.89 eV), 341 nm (P4: 3.64 eV), 375 nm (P5: 3.31 eV) and 407 nm (P6: 3.05 eV), while with the deconvoluted peak positions for CSLOF,0.04Eu^{2+} phosphor are observed at 264 nm (P1: 4.70 eV), 294 nm (P2: 4.22 eV), 316 nm (P3: 3.92 eV), 329 nm (P4: 3.77 eV), 356 nm (P5: 3.48 eV) and 407 nm (P6: 3.05 eV), respectively. The peak P1 represents the CTB of the activator ion to a ligand of the host. The other peaks from P2 to P5 correspond to the 5d–4f electronic transitions of the Eu^{2+} ions, which are generated because of the variation of crystallographic changes around the five degenerated d orbitals of the Eu^{2+} ions. A possible schematic energy level diagram for the degenerated 5d orbitals is also pro-

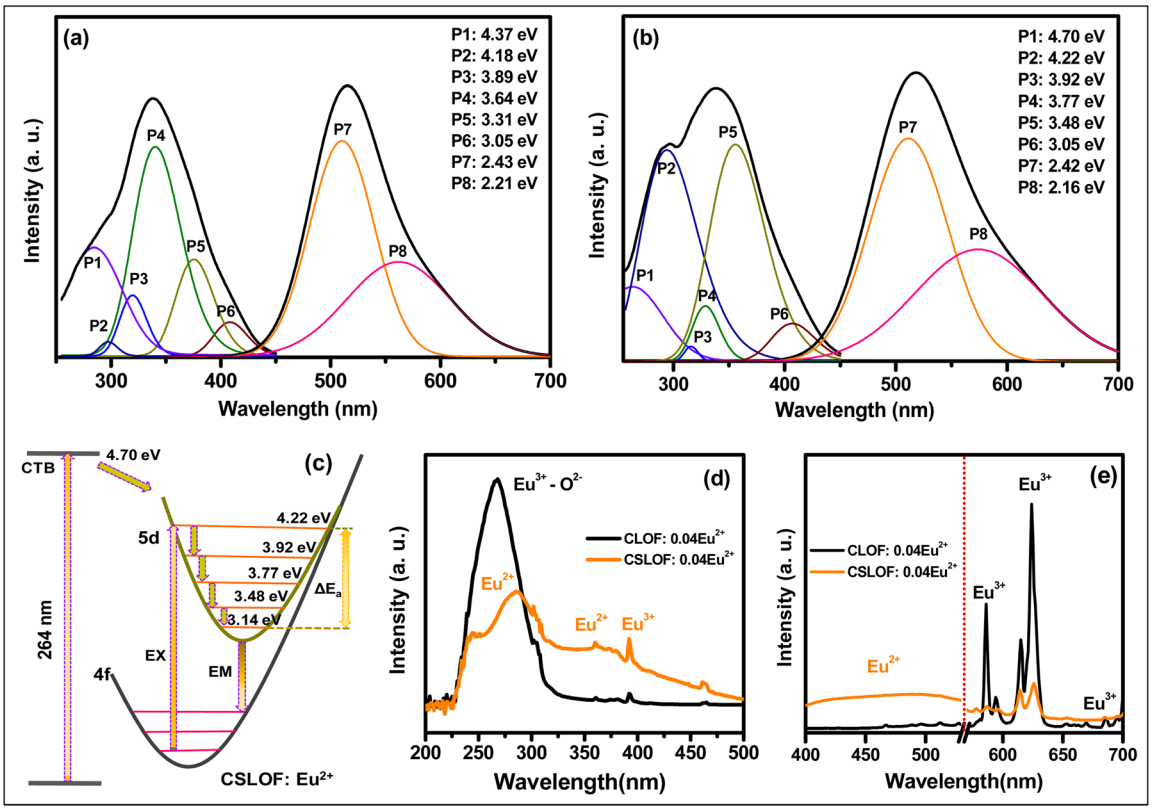

Fig. 4 The deconvoluted excitation and emission spectra of (a) CLOF:0.04Eu^{2+} and (b) CSLOF:0.04Eu^{2+} synthesized under a N_2–H_2 atmosphere and recorded at 520 nm and 340 nm, respectively. (c) Schematic energy level diagram for CSLOF:0.04Eu^{2+}. Comparative (d) excitation and (e) emission spectra of CLOF:0.04Eu^{2+} and CSLOF:0.04Eu^{2+} recorded at 280 nm and 614 nm, respectively.

posed in Fig. 4(c). As seen from the PLE of CLOF:0.04Eu^{2+} and CSLOF:0.04Eu^{2+}, after the introduction of the Sr^{2+} ions, the peak intensity of the CTB band (P1) is decreased and shifted towards the lower wavelength region (from 284 to 264 nm). The incorporation of Sr^{2+} ions might reduce he Eu^{3+} ions in the lattice and hence reduce the excitation charge transfer energy and thus the CTB band (P1) intensity.[37]

The incorporation of Sr^{2+} ions into the CLOF host lattice also results in lattice expansion, due to which the Eu^{3+} ions might be easily reduced to Eu^{2+} ions preferably in the larger cationic sites. Huang *et al.* introduced a crystal chemistry approach to reduce Eu^{3+} to Eu^{2+} ions in the lattice by replacing the appropriate ions with large dopants like Si^{4+} ions, which enlarged the Ca^{2+} sites and thus enabled Eu^{3+} reduction.[38] The Eu^{2+} occupancy is expected to enhance in the nine-coordinated 4f sites which substantially accelerate Eu^{3+} ion occupation of the seven-coordinated 6h sites. Thus, the average Eu–O bond length in the 4f sites of CSLOF:0.04Eu^{2+} will be higher than in CLOF:0.04Eu^{3+}. Because of this reason, the CTB (P1) of Eu^{3+} ions in CSLOF:0.04Eu^{2+} might have appeared at 264 nm.[37] The other five Eu^{2+} ion transition peaks are more dominant, and peak broadening is also observed owing to the incorporation of Sr^{2+} ions. After the incorporation of larger Sr^{2+} ions into the CLOF host, certain lattice expansion around the crystallographic sites of the activator ions might take place, which might reduce the strain on the Eu^{2+} ion occupancy. Such lattice modifications due to the introduction of Sr atoms are also confirmed through the XRD refinement data of CLOF and CSLOF, as indicated in the XRD analysis part.

To confirm the change in Eu valence from 3+ to 2+ due to the Sr^{2+} incorporation in the CLOF, the comparative excitation and emission spectra of CLOF:0.04Eu^{2+} and CSLOF:0.04Eu^{2+} were also recorded at 614 nm emission of Eu^{3+}: $^5D_0$–$^7F_2$ transition and 280 nm of O^{2-}–Eu^{3+} CTB excitation, as shown in Fig. 4(d) and (e), respectively. On recording the excitation at 614 nm, it was found that in CLOF:0.04Eu^{2+} no dominant Eu^{2+} ion 4f–5d transition peak appears rather than an intense O^{2-}–Eu^{3+} CTB. After the incorporation of Sr^{2+} ions (CSLOF:0.04Eu^{2+}) the intensity of the Eu^{3+} ions' CTB band decreases, and the asymmetric broadband of Eu^{2+} ions appears. Similar phenomena are also observed from the emission spectra recorded at 280 nm (Fig. 4(e)). It is observed that the emission spectra of CLOF:0.04Eu^{2+} contain only several sharp peaks of intra f–f Eu^{3+} ions, and broad-emitting Eu^{2+} ion peaks are not observed. However, in the CSLOF:0.04Eu^{2+} system, the Eu^{3+} ions' emission drastically decreased and the broad emission of Eu^{2+} ions increased. This is because the incorporation of Sr^{2+} ions results in increased structural defects and enhances the lattice size; consequently, more Eu^{3+} ions are converted to Eu^{2+} ions. In addition, there is a slight change in the emission behaviour of Eu^{3+} ions in CSLOF:0.04Eu^{2+} observed in the spectra as the red to orange ratio ($^5D_0$–$^7F_2$ to $^5D_0$–$^7F_1$) intensity is decreased effectively compared with that in CLOF:0.04Eu^{2+}. The enhanced occupation of Eu^{2+} ions in the 4f and 6h sites might reduce the number of Eu^{3+} ions in both the asymmetric sites.

The PL emission spectra of CLOF:0.04Eu^{2+} and CSLOF:0.04Eu^{2+} exhibit an intense green-emitting asymmetric band peaked at 520 nm covering the range of 450 nm to 600 nm due to the 5d–4f electronic transitions of the Eu^{2+} ions. The observed emission spectra are deconvoluted into two broad Gaussian bands peaked at 510 nm (P7: 2.43 eV) and 561 nm (P8: 2.21 eV) for CLOF:0.04Eu^2 (Fig. 4(a)), and at 512 nm (P7: 2.42 eV) and 574 nm (P8: 2.16 eV) for CSLOF:0.04Eu^{2+} (Fig. 4(b)). This asymmetric behaviour of the emission band indicates multiple crystallographic site occupancy by Eu^{2+} ions. Based on the empirical formula proposed by Van Uitert, the Eu^{2+} ion occupancy on both the cationic sites can be explained *via* the equation,

$$E(\mathrm{cm}^{-1}) = Q\left[1 - (V/4)^{\frac{1}{V}} \times 10^{-\left(\frac{nE_a r}{80}\right)}\right] \quad (1)$$

where E is the emission band of the Eu^{2+} ion, Q is the lower d-band position for free Eu^{2+} ions (Q = 34 000 cm^{-1}), V represents the Eu^{2+} valence (V = 2), r is the cationic radius substituted by Eu^{2+} ions, E_a is the electron affinity and n represents the coordination number of Eu^{2+} ion-occupied sites.[39] Accordingly, E directly depends on the coordination number of the cationic sites in the particular host lattice. Conforming to this formula, a lower wavelength emission corresponds to the sites with high coordination numbers and *vice versa*. Consequently, in the emission spectra of CLOF:0.04Eu^{2+} and CSLOF:0.04Eu^{2+}, the peak P7 represents the $4f^6 5d^1$–$4f^7$ transition of Eu^{2+} ions located in the nine-coordinated 4f sites, whereas P8 represents emission from Eu^{2+} ions occupying the seven-coordinated 6h sites. Comparing both the Eu^{2+} ions' occupied polyhedra $[M–O_6F]_{6h}$ and $[M–O_9]_{4f}$, the Eu^{2+} ions in the 6h sites are surrounded by more non-equivalent anionic atoms than the Eu^{2+} ions occupying the 4f sites. Because of this reason, Eu^{2+} ions in the 6h sites might experience higher crystal field splitting than Eu^{2+} ions situated in the 4f sites. Because of larger splitting, Eu^{2+} ions occupying the 6h sites exhibited higher wavelength emission (P8) than Eu^{2+} ions located at the 4f sites.[40]

It can be predicted that the transitions from Eu^{2+} ions are observed in both the cationic sites, and among them P7 has a higher intensity than P8 which means that a greater number of Eu^{2+} ions are preferably occupying the bigger 4f sites. Compared with CLOF:0.04Eu^{2+}, the emission spectra of CSLOF:0.04Eu^{2+} slightly red-shifted. Additionally, a broadening of the emission peak is also observed after the introduction of Sr^{2+} ions. The XRD analysis indicated that by the introduction of Sr^{2+} ions in CLOF:Eu^{3+}, the average metal–oxygen length in 4f and 6h coordination is changed (from CLOF:Eu^{3+}; 2.629 Å to CSLOF:Eu^{2+}; 2.668 Å and from CLOF:Eu^{3+}; 2.547 Å to CSLOF:Eu^{2+}; 2.560 Å, respectively). Such a bond length distortion reduces the strain in the lattice and more trivalent Eu ions are changed to their divalent analogues, and the peak broadening is observed. Eventually, the increment in the FWHM value due to the presence of Sr^{2+} ions also illustrates the enhancement of Eu^{2+} ion occupancy of both the cationic sites.

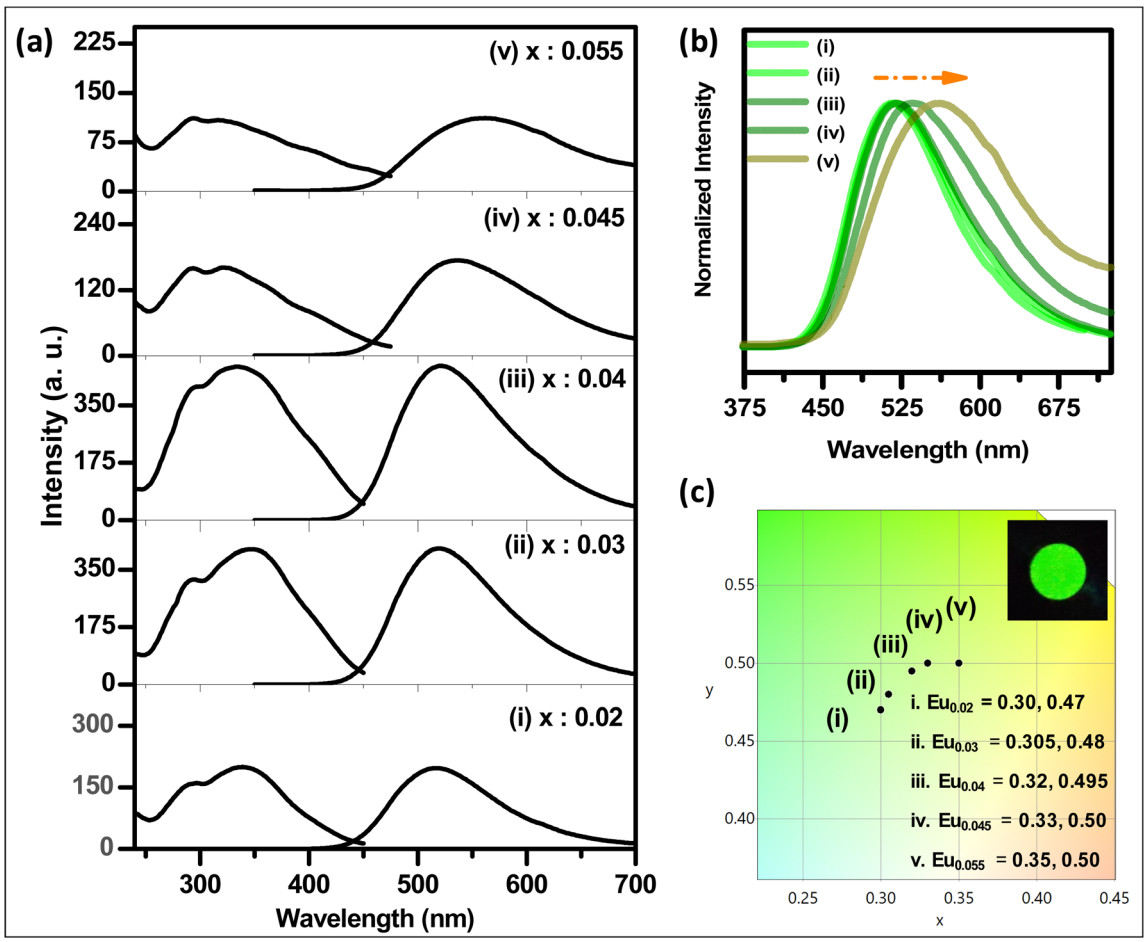

Fig. 5 (a) The excitation and emission spectra of CSLOF:xEu^{2+} (x = 0.02, 0.03, 0.04, 0.045, 0.055) phosphors recorded in the range of 520–562 nm and 322–340 nm, respectively. (b) A red-shift in emission spectra as a function of increasing Eu^{2+} ion concentration. (c) CIE diagram and colour coordinates for the corresponding emission spectra of CSLOF:xEu^{2+} phosphors along with the luminescence photograph of the optimum CSLOF:0.04Eu^{2+} phosphor.

Fig. 5(a) describes the excitation and emission spectra of a series of CSLOF:xEu^{2+} phosphors recorded in the range of 520–562 nm and 322–340 nm, respectively. As the Eu^{2+} ion doping concentration increases, the peak intensity also increases and reaches the maximum at x = 0.04, above which quenching of emission intensity is observed. The concentration quenching behaviour of Eu^{2+} ions is studied by evaluating the critical distance (R_c) based on the Blasse equation reported elsewhere:[41]

$$R_c \approx 2\left[\frac{3V}{4\pi X_c N}\right]^{1/3} \quad (2)$$

where V is the volume of the unit cell (582.65 Å^3), N is the number of molecules per unit cell (2) and X_c is the critical concentration of Eu^{2+} ions (0.04) for the CSLOF:0.04Eu^{2+} phosphor. The critical distance is found to be 24.05 Å. The R_c value is greater than 5 Å, indicating that the exchange interaction is not dominant in Eu^{2+} ions in the CSLOF host.

The emission spectra CSLOF:xEu^{2+} consist of asymmetric broadband emission ranging from 450 nm to 650 nm arising due to the 4f^{6}5d^1–4f^7 electronic transitions of the Eu^{2+} ions. The reason for an asymmetric band is due to the difference in the occupancy of Eu^{2+} ions at the multiple crystallographic sites of the host. In addition to the intensity variation, a red-shift of the emission band is also observed during the increment in Eu^{2+} ion concentration, as shown in Fig. 5(b). The substitution of Eu^{2+} ions at the smaller cationic sites of CSLOF:0.04Eu^{2+} causes a greater relaxation of the equilibrium distance of the excited states of Eu^{2+} ions and results in the emission Stokes shift.[42,43] Fig. 5(c) describes the CIE diagram and calculated colour coordinates for the emission spectra of CSLOF:xEu^{2+} phosphors, along with the luminescence photograph of the optimum CSLOF:0.04Eu^{2+} phosphor. There is a gradual emission shift from greenish (0.30, 0.47) to yellowish-green (0.35, 0.50) with the increase in Eu^{2+} ion concentration.

3.4. Photoluminescence of $Ca_{1.98-y}Sr_{1.98-y}La_6Si_6O_{24}F_2$:0.04Eu^{2+},$y$Mg^{2+} (CSLOF:Eu^{2+},$y$Mg) and $Ca_{1.98-z}Sr_{1.98-z}La_6Si_6O_{24}F_2$:0.04Eu^{2+},$z$Ba^{2+} (CSLOF:Eu^{2+}, zBa) synthesized under a N_2–H_2 atmosphere

According to the structural and optical outcomes of europium ion-doped CSLOF systems, a controlled operation of the Eu^{2+}

ionic distributions at the multiple cationic sites can result in a flexible colour output from the presently adopted compositionally tuned single-phased system. Eventually, a compositionally tuned white-emitting system could also be achieved *via* modifying the CSLOF:Eu^{2+} system. With such an aim, the emission property of the CSLOF:0.04Eu^{2+} phosphor has been further tuned by altering the distortion of metal–anion polyhedra with a suitable cationic substitution strategy. For the optimum CSLOF:0.04Eu^{2+} green-emitting composition, the substitution of smaller Mg^{2+} ions for relatively larger Sr^{2+} and Ca^{2+} ions is being initially focused on.

Fig. 6(a) represents the excitation and emission spectra of a series of CSLOF:0.04Eu^{2+},*y*Mg^{2+} (*y* = 0.0 to 1.0) phosphors recorded in the range of 480–505 nm and 330–340 nm, respectively. The intensity of the emission peak gradually increases (Fig. 6(a)) and the emission band becomes narrower with the increase of Mg^{2+} ion concentration, as visible in Fig. 6(b). Smaller-sized Mg^{2+} ions prefer to occupy the 6h sites. In order to minimize the distortion, more Eu^{2+} ions are then substituted at the 4f sites, which results in a narrower emission. Moreover, a blue-shift in the emission peak from 520 nm to 481 nm is also noted, as is visible in Fig. 6(c). This is again attributed to the preferential occupation of more Eu^{2+} ions in the nine-coordinated 4f sites, since the larger coordination gives lower wavelength emission. The CIE diagram and the colour coordinates of the corresponding emission spectra along with the luminescence photographs of the CSLOF:0.04Eu^{2+},*y*Mg^{2+} phosphors are shown in Fig. 6(d). Clearly, the emission blue-shift from the greenish (0.32, 0.495) to cyan-blue (0.18, 0.25) region with the increase of Mg^{2+} ion concentration from *y* = 0.0 to 1.0 can be realized *via* the digital images.

The PL results of CSLOF:Eu^{2+} are further probed *via* synthesizing a series of CSLOF:0.04Eu^{2+},*z*Ba^{2+}. Fig. 7(a) represents the excitation and emission spectra of CSLOF:0.04Eu^{2+},*z*Ba^{2+} (*z* = 0.0 to 2.0) phosphors recorded in the range of 520–540 nm and 340 nm, respectively. With increasing Ba^{2+} ion concentration, the emission intensity as well as broadening of the

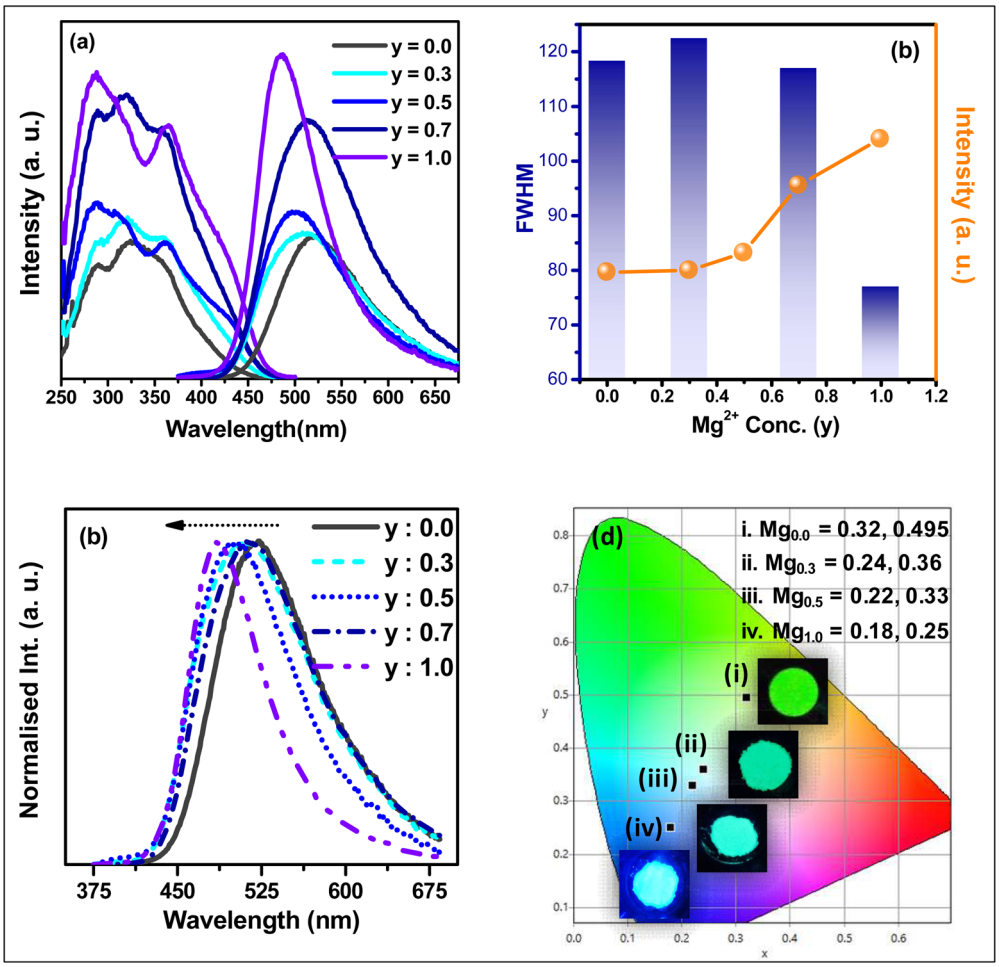

Fig. 6 (a) The excitation and emission spectra of CSLOF:0.04Eu^{2+},*y*Mg^{2+} phosphors recorded in the range of 480–505 nm and 330–340 nm, respectively. (b) The variations in intensity and FWHM of the emission spectra with the increase in Mg^{2+} ion concentration. (c) A blue-shift in the emission spectra as a function of increasing Mg^{2+} ion concentration. (d) CIE diagram for the corresponding emission spectra of CSLOF:0.04Eu^{2+}, *y*Mg^{2+} phosphors along with the corresponding luminescence photographs.

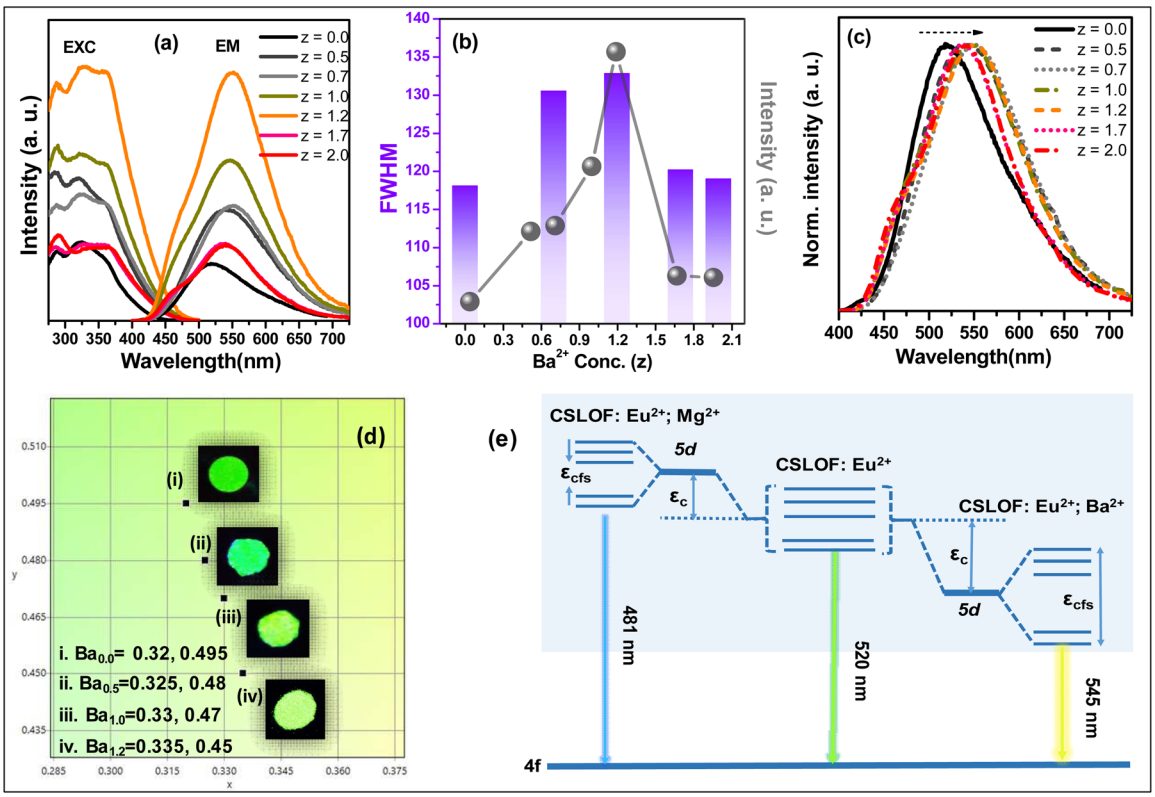

Fig. 7 (a) The excitation and emission spectra of CSLOF:0.04Eu^{2+},zBa^{2+} (z = 0, 0.5, 1.0, and 1.2) phosphors recorded in the range of 520–540 nm and 340 nm, respectively. (b) Variation in the intensity and FWHM of the emission spectra with the increase in Ba^{2+} ion concentration. (c) A red-shift in the emission spectra as a function of increasing Ba^{2+} ion concentration. (d) CIE diagram and colour coordinates for the corresponding emission spectra of CSLOF:0.04Eu^{2+},zBa^{2+} (z = 0, 0.5, 1.0, and 1.2) phosphors along with the luminescence photographs of the phosphors. (e) Overall energy splitting diagram of Mg^{2+} or Ba^{2+}-codoped $Ca_{1.98}Sr_{1.98}La_6Si_6O_{24}F_2$:0.04$Eu^{2+}$ phosphors.

emission peak gradually increases and reaches a maximum at z = 1.2, and after that, luminescence quenching occurs. Initially, larger Ba^{2+} ions occupied both the available cationic sites. This might have enhanced the size of the polyhedra, which then efficiently accommodated the Eu^{2+} ions. The significant enhancement of FWHM indicates the possibility of generating broader emissions covering the entire visible spectrum. The emission intensity variation and FWHM changes are also shown in Fig. 7(b). It is also observed that on increasing the Ba^{2+} ion concentration, a red-shift in emission spectra from the greenish (520 nm) to yellowish-green (540 nm) region is observed (Fig. 7(c)). The chromaticity diagram and the colour coordinates along with the luminescence photographs of the corresponding emission spectra of CSLOF:0.04Eu^{2+}, zBa^{2+} phosphors are shown in Fig. 7(d). A slight red-shift has been noted from greenish (0.32, 0.495) to greenish-yellow (0.335, 0.45) with the increase of Ba^{2+} ion concentration.

The overall energy splitting mechanism in Mg^{2+} or Ba^{2+} codoped $Ca_{1.98}Sr_{1.98}La_6Si_6O_{24}F_2$:0.04$Eu^{2+}$ phosphors is illustrated in Fig. 7(e). As illustrated in Fig. 7(e), the 5d energy band of the activated Eu^{2+} ions is influenced by the cationic substitutions in the host lattice, which results in the crystal field splitting (ε_{cfs}) and a centroid shift (ε_c). Due to the substitution of smaller Mg^{2+} ions for larger Ca^{2+}/Sr^{2+} ions at 6h sites, the [M1–O_6F] polyhedra might be contracted due to the preferable substitution of smaller-sized Mg^{2+} ions at the 6h sites. Subsequently, [M2–O_9] polyhedra could be expanded. Because of this reason, Eu^{2+} ions situated at the 4f sites might experience a lower ε_{cfs} in CSLOF:0.04Eu^{2+},Mg^{2+} than in CSLOF:0.04Eu^{2+}, which led to a blue-shift in the emission peak from 520 nm to 481 nm. As compared with the XRD refinement data of CSLOF:0.04Eu^{2+}, the cell volume enhancement from 582.65 [Å^3] to 590.42 [Å^3] for CSLOF:0.04Eu^{2+},1.2Ba^{2+} might be caused by the replacement of Ba^{2+} ions with Eu^{2+} ions.[44] When less electronegative and larger Ba^{2+} ions are introduced to the cationic sites of CSLOF:0.04Eu^{2+}, it causes an enhancement in the lattice size and also increases the centroid shift (ε_c) of the 5d orbital of the Eu^{2+} ions. This reduces the energy gap in the 5d–4f electronic transition of Eu^{2+} ions and results in a higher wavelength emission.[45,46]

Since the size of Ba^{2+} ion is more than the Ca^{2+}/Sr^{2+} ion, the cationic replacement of Ca^{2+}/Sr^{2+} by Ba^{2+} in $Ca_{1.98}Sr_{1.98}La_6Si_6O_{24}F_2$:0.04$Eu^{2+}$ should enhance the lattice size of $Ca_{1.98}Sr_{1.98}La_6Si_6O_{24}F_2$:0.04$Eu^{2+}$. For validation, the Rietveld refinement has also been carried out for the XRD pattern of CSLOF:0.04Eu^{2+},1.2Ba^{2+} using a similar structure used for the Ca^{2+}/Sr^{2+} analogue, as shown in Fig. 8(a).

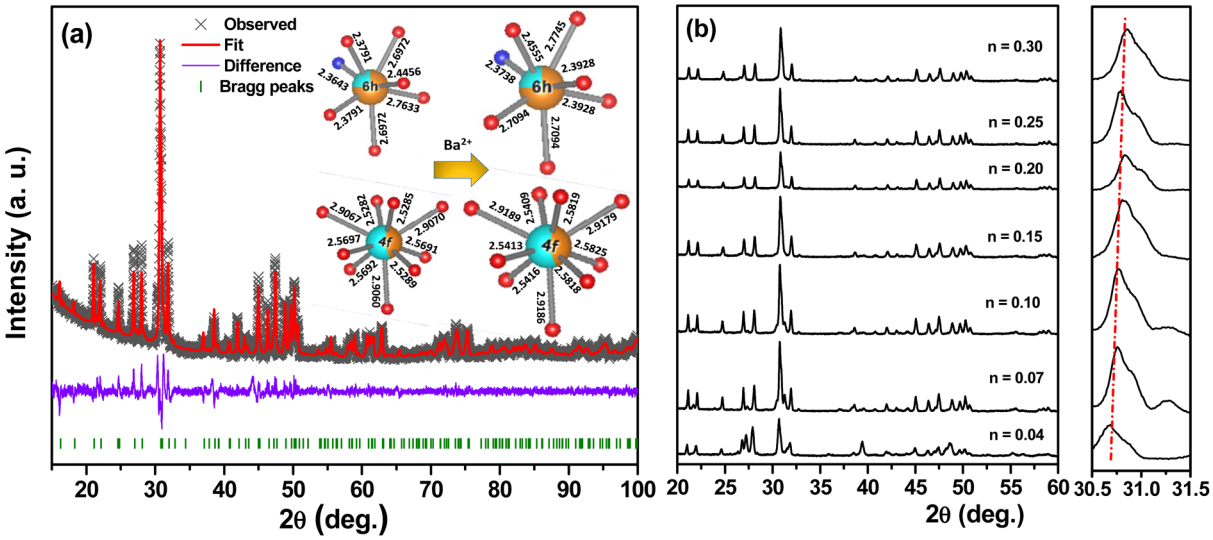

Fig. 8 (a) Rietveld refinement of CSLOF:0.04Eu^{2+},1.2Ba^{2+}. Inset: Schematic representation of average metal–oxygen bond length variation in CSLOF:0.04Eu^{2+},$z$$Ba^{2+}$ (z = 0 and 1.2). (b) XRD patterns of a series of CSLOF:$n$$Eu^{2+}$,1.2$Ba^{2+}$ (n = 0.04 to 0.3).

Compared with CSLOF:0.04Eu^{2+}, the lattice parameters as well as the lattice volume of CSLOF:0.04Eu^{2+},1.2Ba^{2+} are slightly enhanced (Table S1†). The lattice expansion can also be verified from higher [M–O] bond length values at different sites of CSLOF:0.04Eu^{2+},1.2Ba^{2+} compared with the [M–O] bond lengths of CSLOF:0.04Eu^{2+}, as shown in the inset of Fig. 8(a). Such a lattice expansion may allow more Eu^{2+} ions to occupy the lattice sites of CSLOF:0.04Eu^{2+},1.2Ba^{2+}. Keeping the structural results of CSLOF:0.04Eu^{2+},1.2Ba^{2+} in view, the Eu^{2+} ion concentration of the optimum $Ca_{1.38}Sr_{1.38}La_6Si_6O_{24}F_2$:0.04$Eu^{2+}$,1.2$Ba^{2+}$ phosphor has been further enhanced from 0.04 to 0.3. Fig. 8(b) represents the XRD patterns of a series of $Ca_{1.38-n}Sr_{1.38-n}La_6Si_6O_{24}F_2$:$n$$Eu^{2+}$,1.2$Ba^{2+}$ (n = 0.04 to 0.3) phosphors. The basic crystal structure has not been altered due to the increasing Eu^{2+} ion concentrations. However, the successful adaptation of Eu^{2+} ions (higher than n = 0.04) can be confirmed in the magnified XRD patterns where the main diffraction peaks continuously shift toward higher 2θ with increasing n values from 0.04 to 0.3 (Fig. 8(b)).

Fig. 9(a) represents the photoluminescence of a series of $Ca_{1.38-n}Sr_{1.38-n}La_6Si_6O_{24}F_2$:$n$$Eu^{2+}$,1.2$Ba^{2+}$ (n = 0.04 to 0.3) phosphors recorded at 360 nm. On increasing the Eu^{2+} ion concentration, the emission intensity rises initially and reaches a maximum at n = 0.07, above which luminescence quenching is observed. Based on Blasse's equation,[41] the critical distance is calculated to be 20.01 Å for CSLOF:0.07Eu^{2+},1.2Ba^{2+}. Eventually, a slight emission red-shift is also observed from 540 nm to 545 nm at higher Eu^{2+} concentrations, as shown in Fig. 9(a). The smaller size of the Eu^{2+} ion than the Ba^{2+} ion might increase the lattice covalency, and hence longer wavelength emission has been observed.[46,47] The overall colour tuning from greenish-yellow (0.30, 0.49) to the yellowish region (0.34, 0.45) can be realized from the colour chromaticity diagram, and from the corresponding luminescence photographs, as shown in Fig. 9(b). Fig. 9(c) represents the comparative emission spectra of commercial $Y_3Al_5O_{12}$:Ce^{3+} with $Ca_{1.38-n}Sr_{1.38-n}La_6Si_6O_{24}F_2$:$n$$Eu^{2+}$,1.2$Ba^{2+}$ (n = 0.07, 0.15) phosphors recorded at 460 nm and 360 nm, respectively. Not only the emission intensity but also the emission FWHM of the optimized phosphors is found to be comparable with those of the commercial phosphor.

The temperature-dependent PL intensity variation of CSLOF:0.04Eu^{2+},$z$$Ba^{2+}$ (z = 0 and 1.2) phosphors from 300 to 450 K recorded at 360 nm excitation is shown in Fig. 9(d). With enhancing the temperature, the PL intensity drops regularly because of the relaxation of non-radiative transitions leading to the quenching of the Eu^{2+} ions' emissive transitions.[47] At 423 K, the PL emission intensity of CSLOF:0.04Eu^{2+} retained almost 81% of its initial intensity, showing the high thermal stability of the phosphor suitable for WLED applications, while the PL emission intensity of CSLOF:0.04Eu^{2+},1.2Ba^{2+} reduced to 72% of the room temperature emission intensity. The thermal stability of the phosphor can be described by the Arrhenius equation,

$$I_T = \frac{I_0}{1 + c\exp\left(-\frac{\Delta E}{kT}\right)} \quad (3)$$

where I_0 and I_T are the starting emissive intensity and emission intensity at numerous temperatures. c is a constant for the host, ΔE is the activation energy, k is the Boltzmann's constant (8.62 × 10^{-5} eV K^{-1}), and T is the temperature in K.[48] Fig. 9(e) shows the plots between In $[(I_0/I_T) - 1]$ *vs.* $[1000/T]$ and the slopes of the corresponding lines give the activation energy (ΔE). The activation energy of CSLOF:0.04Eu^{2+} is found to be 0.26 eV, which supports the high thermal stability of this composition,[49] while the activation energy of CSLOF:0.04Eu^{2+},1.2Ba^{2+} phosphor is

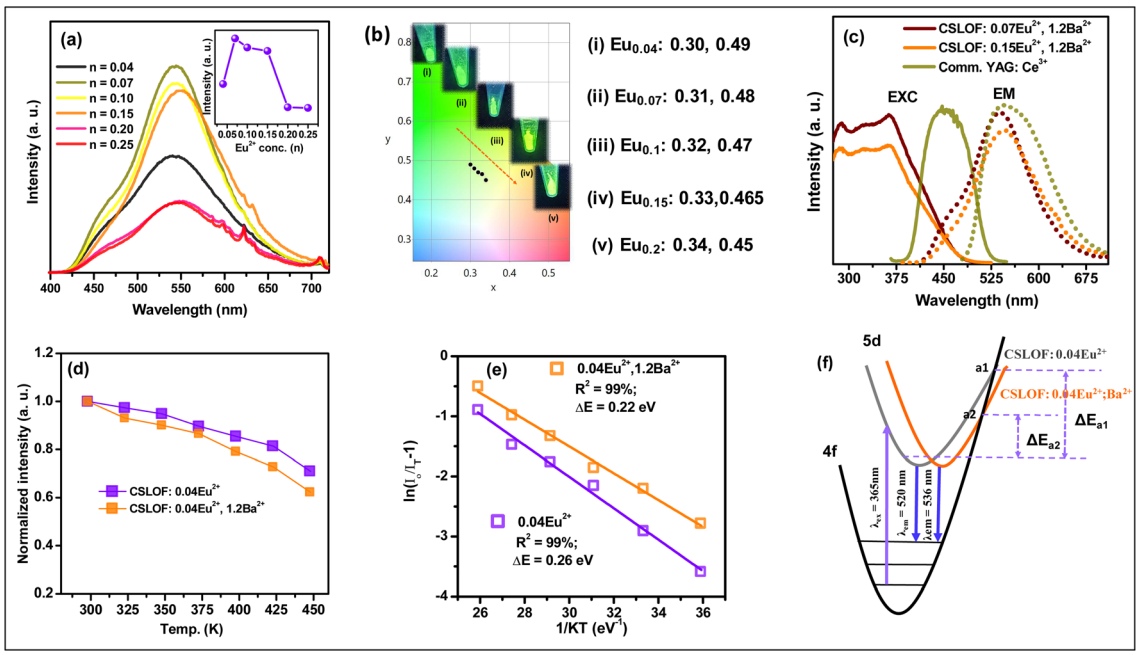

Fig. 9 (a) The emission spectra of CSLOF:nEu^{2+},1.2Ba^{2+} (n = 0.04 to 0.25) phosphors recorded at 360 nm. (b) CIE diagram and colour coordinates for the corresponding emission spectra of CSLOF:nEu^{2+},1.2Ba^{2+} along with the luminescence photographs of the phosphors. (c) The comparative excitation and emission spectra of commercial $Y_3Al_5O_{12}$:Ce^{3+} and with CSLOF:nEu^{2+},1.2Ba^{2+} (n = 0.07, 0.15). (d) Temperature-dependent PL intensity variation of CSLOF:0.04Eu^{2+},zBa^{2+} (z = 0 and 1.2) phosphors recorded at 360 nm. (e) Arrhenius fitting of CSLOF:0.04Eu^{2+},zBa^{2+} (z = 0 and 1.2) phosphors. (f) The energy level diagram illustrates the relationship between non-radiative relaxation process and the wavelength shift.

observed to be reduced to 0.22 eV. Fig. 9(f) shows the energy level diagram of CSLOF:0.04Eu^{2+},zBa^{2+} (z = 0 and 1.2). In this figure, the cross-over points of the ground state and the excited state are denoted by a1 and a2 for CSLOF:0.04Eu^{2+},zBa^{2+} (z = 0 and 1.2) phosphors, respectively. The activation energy is the energy difference between the CRP and the lowest excited state as indicated in Fig. 9(f). As the temperature increases, electrons are stimulated from the lowest excited level to the highest excited level (engaged with the CRP) because of the phonon energy and get back to the ground state through non-radiative

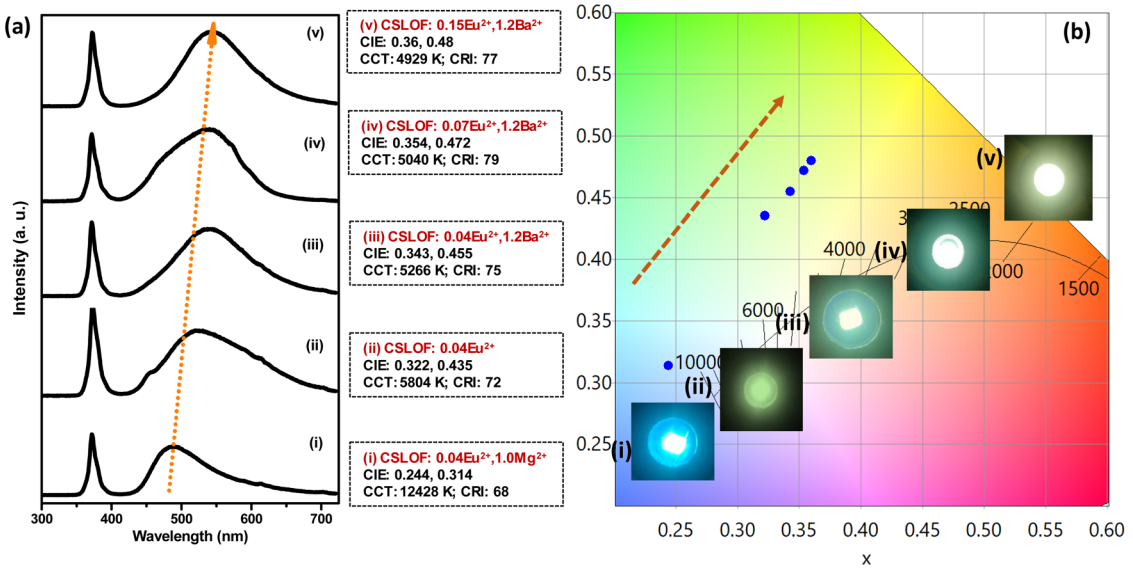

Fig. 10 (a) The electroluminescent spectra of (i) CSLOF:0.04Eu^{2+},1.0Mg^{2+}, (ii) CSLOF:0.04Eu^{2+}, (iii) CSLOF:0.04Eu^{2+},1.2Ba^{2+}, (iv) CSLOF:0.07Eu^{2+},1.2Ba^{2+}, and (v) CSLOF:0.15Eu^{2+},1.2Ba^{2+} recorded with a 370 nm n-UV LED chip. (b) The corresponding chromaticity diagram and colour coordinates, and the digital images of the obtained pc-LEDs are also illustrated.

emission.[50] This phenomenon reduces the emission intensity of Eu^{2+} ions at higher temperatures. Eventually, Ba^{2+} ion introduction to CSLOF:0.04Eu^{2+} caused a centroid shift followed by the emission red-shift. This lowers the ground and excited state CRP from a1 (CSLOF:0.04Eu^{2+}) to a2 (CSLOF:0.04Eu^{2+},1.2Ba^{2+}).[51] Consequently, the energy difference among the highest and the lowest excited states reduces, owing to which non-radiative relaxation takes place more rapidly in the case of CSLOF:0.04Eu^{2+},1.2Ba^{2+} than CSLOF:0.04Eu^{2+}. Due to this reason, the activation energy is observed to be reduced from ΔE_{a1} = 0.26 eV (CSLOF:0.04Eu^{2+}) to ΔE_{a2} = 0.22 eV (CSLOF:0.04Eu^{2+},1.2Ba^{2+}). However, no wavelength shift is observed upon increasing the temperature, which indicates that there is no predominant colour loss happening for phosphors owing to the enhancement in temperatures. The relationship between the Stokes shift and the non-radiative relaxation process is described in the energy level scheme, as shown in Fig. 9(f).

To understand the practical performance of the optimized yellow-, green-, and blue-emitting phosphors, these phosphors are deposited on to a 370 nm n-UV LED chip. Fig. 10(a): (i to v) to Fig. 10(b): (i to v) represent the electroluminescent (EL) spectra and CIE diagram of cyan-blue-emitting CSLOF:0.04Eu^{2+},1.0Mg^{2+}, green-emitting CSLOF:0.04Eu^{2+},zBa^{2+} (z = 0 and 1.2) and yellow-emitting CSLOF:$n$$Eu^{2+}$,1.2$Ba^{2+}$ (n = 0.07 and 0.15) phosphors, respectively. The estimated colour coordinates, CCT, and CRI values are also mentioned in the insets of Fig. 10(a). The 370 nm n-UV converted EL spectrum of the cyan-blue-emitting CSLOF:0.04Eu^{2+},1.0Mg^{2+} is has a CCT of 12 428 K and CRI of 68 (Fig. 10(a): (i)). However, the combination of a 370 nm n-UV LED chip and a CSLOF:0.04Eu^{2+} phosphor exhibits a green band maximum at 520 nm with a CCT of 5804 K and CRI of 72 (Fig. 10(a): (ii)). The cationic substitution strategy *via* the smaller sized Mg^{2+} ions in the CSLOF:0.04Eu^{2+} phosphor considerably tuned the colour chromaticity from greenish (0.322, 0.435) to the cyan-blue region (0.244, 0.314), as shown in Fig. 10(a and b): (ii) to (i), whereas CSLOF:0.04Eu^{2+},1.2Ba^{2+} resulted in a red-shifted EL spectrum from green (0.322, 0.435) to greenish-yellow (0.343, 0.455). The corresponding CCT and CRI of CSLOF:0.04Eu^{2+},1.2Ba^{2+} are observed to be 5266 K and 75, respectively (Fig. 10(a and b): (iii)). Eventually, the EL spectral emission of CSLOF:0.04Eu^{2+},1.2Ba^{2+} has been further tuned *via* enhancing the Eu^{2+} concentrations. The observed CCT and CRI values for CSLOF:$n$$Eu^{2+}$,1.2$Ba^{2+}$ (n = 0.07, 0.15) are observed to be (5040 K, 79) and (4929 K, 77), respectively, while the chromaticity coordinates are also shifted from greenish yellow (0.343, 0.455) to the yellow region (0.36, 0.48) due to the increase in Eu^{2+} concentrations from 0.04 to 0.15 in CSLOF:$n$$Eu^{2+}$,1.2$Ba^{2+}$ (n = 0.04, 0.07, 0.15), as shown in Fig. 10 (a and b): (iii) to (v). The inset of Fig. 10(b): (i) to (v) shows the photographs of the 370 nm LED packages using cyan-blue-emitting CSLOF:0.04Eu^{2+},1.0Mg^{2+}, green-emitting CSLOF:0.04Eu^{2+},zBa^{2+} (z = 0 and 1.2) and yellow-emitting CSLOF:$n$$Eu^{2+}$,1.2$Ba^{2+}$ (n = 0.07 and 0.15) phosphors, respectively, under a forward bias current of 350 mA.

A WLED has also been fabricated *via* depositing CSLOF:0.15Eu^{2+},1.2Ba^{2+} phosphor on a 410 nm violet-LED chip, and the corresponding EL spectrum is illustrated in Fig. 11(a). Herein, the driving current that is having a substantial effect on the EL performance of the phosphor-based WLEDs has been varied. At 50 mA of current, this combination emits white light having a CCT of 5319 K and a CRI of 66. Eventually, the CIE coordinates are observed to be (0.342, 0.425) (Fig. 11(b)). Clearly, the broad emission of CSLOF:0.15Eu^{2+},1.2Ba^{2+} phosphor substantially increased along the sharper LED emission at 410 nm with the increase in driven current. Meanwhile, no emission saturation has been seen in the yellow phosphor, which might be due to the presence of a high concentration of Eu^{2+} luminescent centers. Enhancing the current from 50 mA to 90 mA changed the CCT and the CRI values from 5319 K to 4689 K and 74 to 70, respectively. Most importantly, the CIE coordinates are also slightly tuned from (0.342, 0.425) to (0.324, 0.413), as can be

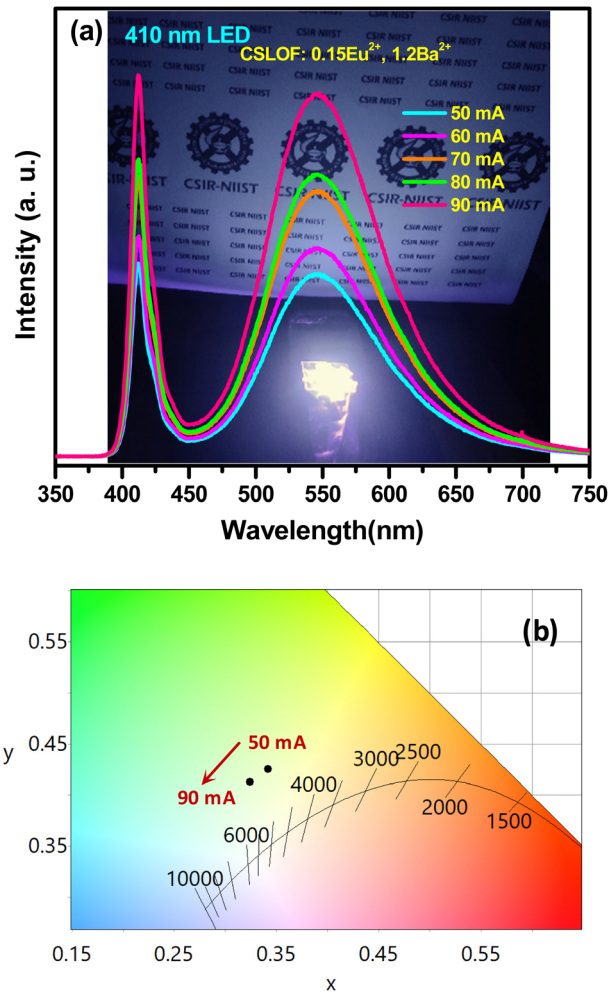

Fig. 11 (a) Electroluminescent spectra and (b) the analogous chromaticity diagram of CSLOF:0.15Eu^{2+},1.2Ba^{2+} recorded with a 410 nm violet-LED chip at different currents. Inset: the digital image of the obtained pc-LED operated at 90 mA.

seen in Fig. 11(b). The captured image of fabricated WLED indicates warm white light emission. The inset in Fig. 11(a) presents the as-appeared direct image of a prototype WLED and its illumination capacity. These results demonstrate that CSLOF:nEu^{2+},1.2Ba^{2+} (n = 0.07, 0.15) compositions are promising for the n-UV and violet-LED based pc-white-LEDs.

4. Conclusions

A sequence of M^{2+} (M = Mg/Ba) codoped $Ca_{1.98-x}Sr_{1.98-x}La_6Si_6O_{24}F_2$:0.04Eu^{2+} phosphors was synthesised based on multiple cationic substitution strategies to achieve multicolour emission from a single composition. The detailed structural studies of (Ca, Sr)$_{3.96}La_6Si_6O_{24}F_2$:0.04Eu^{2+} revealed that broadband green emission could be tuned to either the blue or yellow spectral region *via* the smaller or larger cationic substitutions. As per this thought, smaller Mg^{2+} ions and bigger Ba^{2+} ions were codoped in (Ca, Sr)$_{3.96}La_6Si_6O_{24}F_2$:0.04Eu^{2+} to study the individual sequences. The incorporation of Mg^{2+} and Ba^{2+} ions showed a blue-shift from 520 nm to 481 nm and a red-shift from 520 nm to 545 nm, respectively, owing to the deviation of the crystal field environment around the activator ions. The expanded lattice sites due to the Ba^{2+} codoping allowed more Eu^{2+} ions to be accommodated in the expanded lattice sites. The resultant photoluminescence was further improved and red-shifted in its emission because of the enrichment of more Eu^{2+} ions in the lattice. As compared with the commercial $Y_3Al_5O_{12}$:Ce^{3+}, the presently optimized phosphors showed comparable intensity to the commercial $Y_3Al_5O_{12}$:Ce^{3+}, and had exhibited enough thermal stability (70% at 150 °C) to be used for WLEDs. The WLEDs fabricated using the optimized sample and commercial n-UV and violet LEDs showed a remarkable CCT and CRI. The present research provided a promising hint for developing colour-tuneable apatite phosphors for n-UV and violet LED-based single-component WLEDs.

Conflicts of interest

The authors announce zero competing financial interests.

Acknowledgements

This research is financed by the Science and Engineering Research Board (SERB), DST, Government of India, through the Early Career Research Award (ECR/2017/002210).

References

1 Z. Xia, Z. Xu, M. Chen and Q. Liu, Recent developments in the new inorganic solid-state LED phosphors, *Dalton Trans.*, 2016, **45**, 11214–11232.
2 T. Hasegawa, M. Iwaki, R. Tanaka, S. W. Kim, S. Yin and K. Toda, Phase stabilization of red-emitting olivine-type NaMgPO4:Eu^{2+} phosphors via molten-phase quenching, *Inorg. Chem. Front.*, 2020, **7**, 4040–4051.
3 M. Cao, J. Tian, W. Zhuang, R. Liu, Y. Liu, G. Chen, G. Zhou, L. Wang and J. Wang, Multisite Cation Regulation of Broadband Cyan-Emitting $(Ba_{1-x}Sr_x)_9Lu_2Si_6O_{24}$/Eu^{2+}Phosphors for Full-Spectrum WLEDs, *Inorg. Chem.*, 2022, **61**, 1805–1815.
4 Y. Zhu, Y. Liang, S. Liu, H. Li, J. Chen and W. Lei, A strategy for realizing tunable luminescence and full-color emission in $Sr_3Gd_2(Si_3O_9)_2$:Eu phosphors by introducing dual functional Mn^{2+}, *Inorg. Chem. Front.*, 2018, **5**, 2527–2539.
5 N. W. Wang, Y. Kaihatsu, F. Iskandar and K. Okuyama, Highly Luminous Hollow Chloroapatite Phosphors Formed by a Template-Free Aerosol Route for Solid-State Lighting, *Chem. Mater.*, 2009, **21**, 4685–4691.
6 Y. Liu, G. Liu, J. Wang, X. Dong and W. Yu, Single-Component and Warm-White-Emitting Phosphor Transfer, and Tunable Color, *Inorg. Chem.*, 2014, **53**, 11457–11466.
7 A. De, B. Samanta, K. A. Dey, N. Chakraborty, K. T. Parya, S. Saha and K. U. Ghorai, $ZnAl_2O_4$:Eu^{3+} Nanoparticle Phosphors Co-Doped with Li^+ for Red Light-Emitting Diodes, *ACS Appl. Nano Mater.*, 2022, **5**, 331–340.
8 S. Hariyani and J. Brgoch, Advancing Human-Centric LED Lighting Using Na $_2MgPO_4F$:Eu^{2+}, *ACS Appl. Mater. Interfaces*, 2021, **13**, 16669–16676.
9 C. Yan, X. Du, J. Li, X. Ding, Z. Li and Y. Tang, Effect of Excitation Wavelength on Optical Performances of Quantum-Dot-Converted Light-Emitting Diode, *Nanomaterials*, 2019, **9**(8), 1100.
10 P. Arunkumar, H. Y. Kim and B. W. Im, Versatile $Ca_4F_2Si_2O_7$ Host from Defect-Induced Host Emission to White-Light-Emitting Ce^{3+}-Doped $Ca_4F_2Si_2O_7$ Phosphor for Near-UV Solid-State Lighting, *J. Phys. Chem. C*, 2016, **120**, 4495–4503.
11 P. Dai, J. Cao, X. Zhang and Y. Liu, Bright and High-Color-Rendering White Light-Emitting Diode Using Color-Tunable Oxychloride and Oxyfluoride Phosphors, *J. Phys. Chem. C*, 2016, **120**, 18713–18720.
12 P. Ranjith, S. Sreevalsa, P. Patra, S. Som, A. Menon, K. Jayanthi, K. Annapurna, N. M. Anoop Krishnan, A. R. Allu and S. Das, Realizing cool and warm white-LEDs based on color controllable $(Sr,Ba)_2Al_3O_6F$:Eu^{2+} phosphors obtained via a microwave-assisted diffusion method, *Phys. Chem. Chem. Phys.*, 2021, **23**, 15245–15256.
13 A. Arredondo, H. Desirena, I. Moreno and I. E. Hinostroza, Dual Color Tuning in Ce^{3+}-Doped Oxyfluoride Ceramic Phosphor Plate for White LED Application, *J. Am. Ceram. Soc.*, 2019, **102**, 1425–1434.
14 W. B. Im, S. Brinkley, J. Hu, A. Mikhailovsky, P. S. Denbaars and R. Seshadri, $Sr_{2.975-x}Ba_xCe_{0.025}AlO_4F$: A Highly Efficient Green-Emitting Oxyfluoride Phosphor for Solid State White Lighting, *Chem. Mater.*, 2010, **22**, 2842–2849.
15 Z. Ming, J. Qiao, S. M. Molokeev, J. Zhao, C. H. Swart and Z. Xia, Multiple Substitution Strategies toward Tunable

Luminescence in $Lu_2MgAl_4SiO_{12}$:Eu^{2+} Phosphors, *Inorg. Chem.*, 2020, **59**, 1405–1413.

16 M. Jiao, L. Dong, Q. Xu, L. Zhang, D. Wang and C. u Yang, The structures and luminescence properties of Sr4Gd3Na3(PO4)6F2:Ce^{3+},Tb^{3+} green phosphors with zero-thermal quenching of Tb^{3+} for WLEDs, *Dalton Trans.*, 2020, **49**, 667–674.

17 M. Kirm, E. Feldbach, H. Mägi, V. Nagirnyi, E. Tõldsepp, S. Vielhauer, T. Jüstel, T. Jansen, M. N. Khaidukov and N. V. Makhov, Silicate Apatite Phosphors for Pc-LED Applications, *Proc. Est. Acad. Sci.*, 2017, **66**, 383.

18 Z. Xia, S. M. Molokeev, B. W. Im, S. Unithrattil and Q. Liu, Crystal Structure and Photoluminescence Evolution of $La_5(Si_{2+x}B_{1-x})(O_{13-x}N_x)$:$Ce^{3+}$ Solid Solution Phosphors, *J. Phys. Chem. C*, 2015, **119**, 9488–9495.

19 K. Li, D. Geng, M. Shang, Y. Zhang, H. Lian and J. Lin, Color-Tunable Luminescence and Energy Transfer Properties of $Ca_9Mg(PO_4)_6F_2$:Eu^{2+}, Mn^{2+} Phosphors for UV-LEDs, *J. Phys. Chem. C*, 2014, **118**, 11026–11034.

20 H. Njema, K. Boughzala, H. Boughzala and K. Bouzouita, Structural analysis by Rietveld refinement of calcium and lanthanum phosphosilicate apatites, *J. Rare Earths*, 2013, **31**, 897–904.

21 H. Njema, M. Debbichi, K. Boughzala, M. Said and K. Bouzouita, Structural, electronic and thermodynamic properties of britholites $Ca_{10-x}La_x(PO_4)_{6-x}(SiO_4)_xF_2$ ($0 \le x \le 6$): Experiment and theory, *Mater. Res. Bull.*, 2014, **51**, 210–216.

22 Q. Guo, L. Liao and Z. Xia, Luminescence properties and energy transfer in $La_6Ba_4(SiO_4)_6F_2$:Ce^{3+},Tb^{3+} phosphors, *J. Lumin.*, 2014, **145**, 65–70.

23 J. Ding, Q. Wu, Y. Li, Q. Long, C. Wang and Y. Wang, $Sr_{7.3}Ca_{2.7}(PO_4)_6F_2$:$Eu^{2+}$,$Mn^{2+}$: a novel single-phased white light-emitting phosphor for NUV-LEDs, *Dalton Trans.*, 2015, **44**, 9630–9636.

24 N. An, F. Xu, Q. Guo, L. Liao, L. Mei and H. Liu, Structure and luminescence properties of a novel broadband green-emitting oxyapatite-type phosphorLEDs, *RSC Adv.*, 2020, **10**, 11608–11614.

25 R. Li, J. Zhang, Z. Qui, J. Han, J. Zhang, W. Zhou, L. Yu and S. Lian, Multispectral Tunability in Single Eu^{2+}-doped (Br, Sr)$_5(PO_4)_3$Br Phosphor, *Inorg. Chem. Front.*, 2020, **7**, 2515–2522.

26 H. M. Fang, C. Ni, X. Zhang, T. Y. Tsai, S. Mahlik, A. Lazarowska, M. Grinberg, S. H. Sheu, F. J. Lee, M. B. Cheng and S. R. Liu, Enhance Color Rendering Index via Full Spectrum Employing the Important Key of Cyan Phosphor, *ACS Appl. Mater. Interfaces*, 2016, **8**, 30677–30682.

27 Y. Pan, W. Wang, Y. Zhu, H. Xu, L. Zhou, M. H. Noh, H. J. Jeong, X. Liu and L. Li, $Eu^{3+/2+}$ Co-Doping System Induced by Adjusting Al/Y Ratio in Eu Doped $CaYAlO_4$: Preparation, Bond Energy, Site Preference and $^5D_0$–$^7F_4$ Transition Intensity, *RSC Adv.*, 2018, **8**, 23981–23989.

28 D. V. Deyneko, I. V. Nikiforov, D. A. Spassky, Y. Y. Dikhtyar, S. M. Aksenov, S. Y. Stefanovich and B. I. Lazoryak, Luminescence of Eu^{3+} as a probe for determination of the local site symmetry in the β-$Ca_3(PO_4)_2$ related structures, *CrystEngComm*, 2019, **21**, 5235–5242.

29 Y. Zhang, X. Li, K. Li, H. Lian, M. Shang and J. Lin, Crystal-Site Engineering Control for the Reduction of Eu^{3+} to Eu^{2+} in $CaYAlO_4$: Structure Refinement and Tunable Emission Properties, *ACS Appl. Mater. Interfaces*, 2015, **7**, 2715–2725.

30 S. Sreevalsa, A. P. Parvathy, K. S. Sahoo and S. Das, Full-Color Emitting Crystal Engineered $Sr_3Al_{1-x}Si_xO_{4+x}F_{1-x}$:$Eu^{2+/3+}$ Oxyfluorides for Developing Bendable Lighting Composites, *J. Alloys Compd.*, 2021, **880**, 160483.

31 J. Feng, Z. Wang, H. Xu, M. Jia, Y. Wei and Z. Fu, The Charge Transfer Band as a Key to Study the Site Selection Preference of Eu^{3+} in Inorganic Crystals, *Inorg. Chem.*, 2021, **60**, 19440–19447.

32 V. D. Deyneko, V. I. Nikiforov, A. D. Spassky, Y. Y. Dikhtyar, M. S. Aksenov, Y. S. Stefanovich and I. B. Lazoryak, Luminescence of Eu^{3+} as a Probe for the Determination of the Local Site Symmetry in β-$Ca_3(PO_4)_2$-Related Structures, *CrystEngComm*, 2019, **21**, 5235–5242.

33 K. S. Gupta, C. Reghukumar and M. R. Kadam, Eu^{3+} Local Site Analysis and Emission Characteristics of Novel $Nd_2Zr_2O_7$:Eu Phosphor: Insight into the Effect of Europium Concentration on Its Photoluminescence Properties, *RSC Adv.*, 2016, **6**, 53614–53624.

34 C. A. Duke, S. Hariyani and J. Brgoch, $Ba_3Y_2B_6O_{15}$:Ce^{3+} - A High Symmetry, Narrow-Emitting Blue Phosphor for Wide-Gamut White Lighting, *Chem. Mater.*, 2018, **30**, 2668–2675.

35 S. Wang, Z. Song, Y. Kong, Z. Xia and Q. Liu, 5d-Level Centroid Shift and Coordination Number of Ce^{3+} in Nitride Compounds, *J. Lumin.*, 2018, **200**, 35–42.

36 M. Xie, H. Wei and W. Wu, Site occupancy studies and Luminescence Properties of Emission Tunable Phosphors $Ca_9La(PO_4)_7$: Re(Re = Ce^{3+},Eu2+), *Inorg. Chem.*, 2019, **58**, 1877–1885.

37 J. Feng, Z. Wang, H. Xu, M. Jia, Y. Wei and Z. Fu, The Charge Transfer Band as a Key to Study the Site Selection Preference of Eu^{3+} in Inorganic Crystals, *Inorg. Chem.*, 2021, **60**, 19440–19447.

38 K. W. Huang, W. T. Chen, C. I. Chu, S. F. Hu, H. S. Sheu, B. M. Cheng, J. M. Chen and R. S. Liu, Controlling the Activator Site to Tune Europium Valence in Oxyfluoride Phosphor, *Chem. Mater.*, 2012, **24**, 2220–2227.

39 X. Zhang, Z. An, R. Dong, Y. Song, K. Zhang, Y. Sheng, Z. Shi and H. Zou, Properties and Application of Single Eu^{2+} - Activated Color Tuning Phosphors, *ACS Sustainable Chem. Eng.*, 2019, **7**, 10724–10733.

40 H. Jiang, Y. Jia, T. Qu, Y. Pan, K. Yang and H. Luo, Yellow Persistent Phosphors $Ba_{13.35}Al_{30.7}Si_{5.3}O_{70}$:$Eu^{2+}$, from the Energy Regulation of Rare Earth Ions, *ACS Omega*, 2019, **4**, 6923–6930.

41 A. D. B. Samanta, A. K. Dey, N. Chakraborty, T. K. J. Parya, S. Saha and U. K. Ghorai, $ZnAl_2O_4$:Eu^{2+} Nanoparticle phosphors Co-doped with Li^+ for Red Light-Emitting Diodes, *ACS Appl. Mater. Interfaces*, 2022, **5**, 331–340.

42 V. Bachmann, C. Ronda, O. Oeckler, W. Schnick and A. Meijerink, Color Point Tuning for (Sr,Ca,Ba)$Si_2O_2N_2$: Eu^{2+} for White Light LEDs, *Chem. Mater.*, 2009, **21**, 316–325.

43 M. Zhao, Q. Zhang and Z. Xia, Structural Engineering of Eu^{2+} -Doped Silicates Phosphors for LED Applications, *Acc. Mater. Res.*, 2020, **1**, 137–145.

44 Z. Yang, G. Liu, Y. Zhao, Y. Zhou, J. Qiao, M. S. Molokeev, H. C. Swart and Z. Xia, Competitive Site Occupation toward Improved Quantum Efficiency of $SrLaScO_4$:Eu Red Phosphors for Warm White, *Adv. Opt. Mater.*, 2022, **10**, 1–9.

45 H. C. Huang, T. Y. Lai, S. T. Chan, T. Y. Yeh and R. W. Liu, A Novel Green-Emitting $SrCaSiAl_2O_7$:Eu^{2+} Phosphor for White LEDs, *RSC Adv.*, 2014, **4**, 7811–7817.

46 J. Wang, S. Huang, M. Shang, P. Dang, H. Lian and J. Lin, The Effect of Local Structure on the Luminescence of Eu^{2+} in Ternary Phosphate Solid Solutions by Cationic Heterovalent Substitution and Their Application in White LEDs, *Inorg. Chem.*, 2021, **60**, 19440–19447.

47 S. Liao, X. Ji, Y. Liu and J. Zhang, Highly Efficient and Thermally Stable Blue-Green $(Ba_{0.8}Eu_{0.2}O)(Al_2O_3)_{4.575x(1+x)}$ Phosphor through Structural Modification, *ACS Appl. Mater. Interfaces*, 2018, **10**, 39064–39073.

48 Y. Wei, L. Cao, L. Lv, G. Li, J. Hao, J. Gao, C. Su, C. C. Lin, S. H. Jang, P. Dang and J. Lin, Highly Efficient Blue Emission and Superior Thermal Stability of $BaAl_{12}O_{19}$:Eu^{2+} Phosphors Based on Highly Symmetric Crystal Structure, *Chem. Mater.*, 2018, **30**, 2389–2399.

49 J. Zhang, Q. Guo, L. Liao, Y. Wang, M. He, H. Ye, L. Mei, H. Liu, T. Zhou and B. Ma, Structure and Luminescence Properties of $La_6Ba_4(SiO_4)_6F_2$:Dy^{3+} Phosphor with Apatite Structure, *RSC Adv.*, 2018, **8**, 38883–38890.

50 S. Dutta, S. Som, M. L. Meena, R. Chaurasiya, T. M. Chen and W. Zhou, Multisite-Occupancy-Driven Intense Narrow-Band Blue Emission from $Sr_5SiO_4Cl_6$:Eu^{2+} Phosphor with Excellent Stability and Color, *Inorg. Chem.*, 2020, **59**, 1928–1939.

51 Z. H. Z. Hang and Y. O. W. Ang, Tunable Photoluminescence in $Ba_{1-x}Sr_xSi_3O_4N_2$:Eu^{2+}/Ce^{3+},Li^+ Solid Solution Phosphors Induced by Linear Structural Evolution, *Opt. Mater. Express*, 2019, **9**, 1922–1932.

Journal of Alloys and Compounds 880 (2021) 160483

Contents lists available at ScienceDirect

Journal of Alloys and Compounds

journal homepage: www.elsevier.com/locate/jalcom

Full-color emitting crystal engineered $Sr_3Al_{1-x}Si_xO_{4+x}F_{1-x}$: $Eu^{2+/3+}$ oxyfluorides for developing bendable lighting composites

S. Sreevalsa[a,b], P.A. Parvathy[a,b], Sushanta K. Sahoo[a,b], Subrata Das[a,b,*]

[a] Materials Science and Technology Division, CSIR – National Institute for Interdisciplinary Science and Technology, Thiruvananthapuram, Kerala 695019, India
[b] Academy of Scientific and Innovative Research (AcSIR), Ghaziabad, Uttar Pradesh 201002, India

ARTICLE INFO

Article history:
Received 24 March 2021
Received in revised form 12 May 2021
Accepted 17 May 2021
Available online 21 May 2021

Keywords:
Sr_3AlO_4F
Europium valence
Tunable emission
Flexible composite
White-LED

ABSTRACT

A series of full-color emitting Eu^{2+}/Eu^{3+}-coexisted $Sr_{2.9}Al_{1-x}Si_xO_{4+x}F_{1-x}$: $0.1Eu^{2+/3+}$ ($SASi_xOF$: $Eu^{2+/3+}$) oxyfluorides were synthesized by annealing the solid precursors in oxygen-deficient atmosphere. The structural changes in Sr_3AlO_4F (SAOF) owing to the Si^{4+} ions' doping were visualized from the Rietveld refinement analysis. The substitution of Si^{4+} ions in Al sites contracted the AlO_4 tetrahedra and could enlarge the Sr sites, and enabled the suitable occupation of Eu^{2+} ions in the Sr1 sites. Eventually, the X-ray photoelectron spectroscopy studies confirmed the valence conversion of europium ions from its trivalent to the divalent state owing to the Si^{4+} ions doping in SAOF: $Eu^{2+/3+}$. Photoluminescence studies of $SASi_xOF$: $Eu^{2+/3+}$ showed a bluish emission band at 482 nm for the *4f-5d* transition of Eu^{2+} ions along with several sharp peaks above 550 nm owing to the intra *f-f* transition of Eu^{3+} ions. Increasing the Si^{4+} ions' concentration subsequently, enhanced the Eu^{3+} to Eu^{2+} conversion rate decreased their emission intensity ratio, owing to which the emission color chromaticity was also tuned from orange-red (CIE: 0.48, 0.29) to nearly white (CIE: 0.30, 0.26) and eventually to the bluish region (CIE: 0.18, 0.23). The nearly white light-emitting composition $SASi_{0.03}OF$: $Eu^{2+/3+}$ and the intense bluish light-emitting optimum $SASi_{0.06}OF$: $Eu^{2+/3+}$ phosphors were further chosen for fabricating flexible composites based on phosphor and castor oil (CO). At 150 °C, the composite showed almost double emission than the phosphor powders owing to the thermal encapsulation of the powders provided by the CO matrix. The obtained composite started to degrade at a temperature as high as 300 °C. Therefore, the composite made with near white emitting $SASi_{0.03}OF$: $Eu^{2+/3+}$ phosphor was integrated with a 372 near UV-LED which showed intense cool white emission with the CIE of (0.29, 0.33), CCT of 7562 K, and CRI of 89. The above studies broadly suggested the adaptability of the obtained composites for flexible lighting applications.

1. Introduction

In the present era of lighting technology, white light-emitting diodes (W-LEDs) using phosphor luminescence (pc W-LEDs) have concerned foremost attention because of their exclusive characteristics including higher energy efficiency, robustness, longer durability, eco-friendlier, and more flexible nature compared to existing lighting options [1–4]. Because of these features, pc-LEDS are enormously used in homes, vehicles, backlight displays, and public street lighting [5]. One of the most widespread technologies to produce pc W-LEDs is combining a 460 nm blue InGaN-LED chip and a broad yellow emitting garnet ($Y_3Al_5O_{12}$: Ce^{3+}) phosphor is associated with multiple issues including poor thermal and chemical stability, luminescence efficiency loss, and low color rendering (CRI) [6–9]. Meanwhile, the silicone matrix used for dispersing phosphors and to integrate with blue-LED chips turns to a yellowish tinge owing to the degradation of methyl groups which produce several sub-band defects and subsequently detach from the assembly at high operating temperatures. Such detachment issues result in lowering the optical performance of W-LEDs and possible leakage of excitation light supplied from the LEDs [5,10].

Recently, ultraviolet-excited single-phased phosphors are widely researched by altering doping ions type and concentration for attaining white light because of their substantial advantages like high CRI and an appropriate color temperature (CCT) [11,12]. In the above series, rare-earth ions doped oxyfluorides are promising phosphors for pc-LEDs owing to their efficient and tunable luminescence properties [13,14]. Introducing F^- ions into an oxide matrix results in

* Corresponding author at: Materials Science and Technology Division, CSIR – National Institute for Interdisciplinary Science and Technology, Thiruvananthapuram, Kerala, 695019, India.
E-mail address: subratadas@niist.res.in (S. Das).

https://doi.org/10.1016/j.jallcom.2021.160483
0925-8388/

distorted centrosymmetric sites of the cationic polyhedrons, which origins exciting optical behaviors including high absorption in the UV region and intense emission in the visible region.

Among the oxyfluoride host matrices, the Sr_3AlO_4F host is the most studied phosphor for solid-state lighting applications owing to its facile and simple synthesis, cheap raw materials, and efficient as well as tuneable luminescent characteristics [15,16]. It is crucial to mention that for producing white light, pc-LEDs strongly relied on Eu^{2+} and Ce^{3+} ions which can able to produce broad-band emission covering the entire visible region because of their allowed *d-f* transitions [17,18]. In the Sr_3AlO_4F host lattice, selective cationic or anionic substitutions usually change the covalency of Ce^{3+}-ligand, which afterward modify the wavelength of the excitation ($4f^1 \rightarrow 5d^1$) and emission ($5d^1 \rightarrow 4f^1$) bands of Ce^{3+} ions [19,20]. Earlier, W. B. Im et al. reported $Sr_{2.975}Ce_{0.025}Al_{1-x}Si_xO_{4+x}F_{1-x}$ compositions, which are highly color-tunable (from 474 to 537 nm) that can be efficiently used in solid-state lighting [21]. Here, smaller Si^{4+} ions are replacing larger Al^{3+} cations along with the substitution of smaller F^- ions via larger O^{2-} ions. Such types of substitutions altered the lattice parameters and subsequently produced distortions in the Al/Si tetrahedral, which produced emission redshift [21]. Zheng et al. reported compositions of $Sr_{2.97-1.5x}Ca_xAl_{1-2y}Mg_ySi_yO_4F$: $0.02Ce^{3+}$ in which they successfully redshifted the wideband emission via controlled cationic substitutions at the Sr^{2+} and Al^{3+} sites [22]. The substitution of Mg^{2+} and Si^{4+} ions into the Al^{3+} sites and replacement of Sr^{2+} ions via Ca^{2+} ions in Sr_3AlO_4F: Ce^{3+} not only enhanced the emission intensity but also redshifted the emission curve from 460 nm to 545 nm [22]. Lee et al. reported Ce^{3+}-incorporated $(Sr_3SiO_5)_{1-x}$ - $(Sr_3AlO_4F)_x$ solid solutions which exhibited a wide yellow–orange emission band that has been widened and redshifted owing to Tb^{3+}-codoping [23]. Nevertheless, Eu^{2+}-doped Sr_3AlO_4F compositions are not reported as the single white emitting composition so far because the coordination environment and the size of the crystal site of this host may not be able to change the valence state of europium ions. During the high-temperature annealing process at vacuum condition, certain interstitial defects can be created in the host which can act as the electron donor to Eu^{3+} ions and subsequently converts them to Eu^{2+} [24,25]. However, such reduction probability is very low for the present host owing to the highly compressed Sr^{2+} sites in the Sr_3AlO_4F crystal structure. In the Sr_3AlO_4F framework, the 8-fold and 10-fold coordinated Sr^{2+} sites are surrounded densely by AlO_4 tetrahedral units [21]. It can be inferred that Ce^{3+}, Tb^{3+}, and Eu^{3+} ions can able to substitute the above mentioned Sr^{2+} sites in Sr_3AlO_4F owing to their lower ionic radii compare to Sr^{2+} ions [16]. However, the Sr^{2+} sites in this host need to be enlarged for the occupation of Eu^{2+} ions owing to their similar ionic radius with Sr^{2+} ions or because of the strong oxidative lattice around the Sr^{2+} sites in Sr_3AlO_4F [26].

Recently, the alteration of the covalency, as well as the polarizability of activator - ligand bonds in phosphors are carried out to convert the Eu valance state from 3 + to 2 + [27–29]. With this strategy, it is possible to make Eu^{2+} and Eu^{3+} ions' coexisted phosphors having the ability to emit tunable emission colors including white light emission owing to the combination of different emissions from different valences. Gao et al. reported new phosphor compositions of $MgSrLa_{8-x}(SiO_4)_6O_2$: xEu where the activated europium ions could able to exist in both Eu^{2+} as well as Eu^{3+} ionic forms by occupying non-equivalent crystallographic positions in a lattice [30]. This strategy generated multiple luminescent centers which can produce even white light by combining the broad bluish-green emission of Eu^{2+} ions and sharp the green-yellow-red emission of Eu^{3+} ions. Z. An and co-workers recently reported color-tunable $Ca_{20}Al_{26}Mg_3Si_3O_{68}$: Eu^{2+}, Eu^{3+} phosphors where they achieved multicolor emissions owing to the occupation of europium ions (divalent and trivalent) at distinct crystallographic sites [31].

Inspired by the above studies and concepts, in this work we synthesized a novel oxyfluoride phosphor $Sr_{2.9}Al_{1-x}Si_xO_{4+x}F_{1-x}$: $0.1Eu^{2+/3+}$, which can generate single white light emission under UV excitation. Replacing Al^{3+} with Si^{4+} ions enlarged the activator sites that enabled Eu^{3+} ions to be reduced to Eu^{2+} ions. Varying the Si^{4+} ions doping concentration tuned the emission color from orange-red to nearly white and eventually to the bluish zone. The most suitable compositions were further used to fabricate proposed phosphor - polymer composite membranes to avoid silicon-based phosphor binders for device applications. Here we choose castor oil as the polymer host matrix because of its good binding, transparency, eco-friendly nature, and flexibility. Combining polymer matrix with phosphor could be a suitable alternate for generating high-performance and thermally stable composite materials for LED packaging. These composite membranes could able to maintain a certain distance between the phosphor and LED chip for improving the lifetime of the fabricated LED by the ease of heat dissipation.

2. Experimental

2.1. Preparation of a phosphor

A series of $Sr_{2.9}Al_{1-x}Si_xO_{4+x}F_{1-x}$: $0.1Eu^{2+/3+}$ ($SASi_xOF$: $Eu^{2+/3+}$; x = 0.0, 0.01, 0.03, 0.05, 0.06, 0.1, 0.12, and 0.15) phosphors were synthesized through conventional solid-state method. The stoichiometric amounts of $SrCO_3$ (99.999%), SrF_2 (99.999%), Al_2O_3 (99.999%), SiO_2 (99.99%), and Eu_2O_3 (99.999%) obtained from Sigma-Aldrich were ground together in an agate mortar for 30 min. For maintain the homogeneity of mixing 2.5 wt% NH_4F as a flux was added. The grounded mixture was transferred into an alumina crucible and preheated at 650 °C for 3 h and then annealed in a tube furnace under the near vacuum atmosphere of 10^{-3} torr at 1150 °C for 4 h.

2.2. Preparation of Composite

Appropriate amounts of castor oil (CO) and aliphatic isocyanate is taken in a beaker with an NCO/OH ratio of 1:1. The mixture was stirred at 600 rpm for 15–20 min maintaining the temperature at 70 °C with the help of an oil bath. After the reaction, polyurethane pre-polymer was cast on a glass slide and kept for 2 h in an air-oven at 90 °C for complete curing. The Same procedure was adopted for preparing CO composites with appropriate phosphor content. The reaction scheme for CO synthesis is shown in Scheme 1.

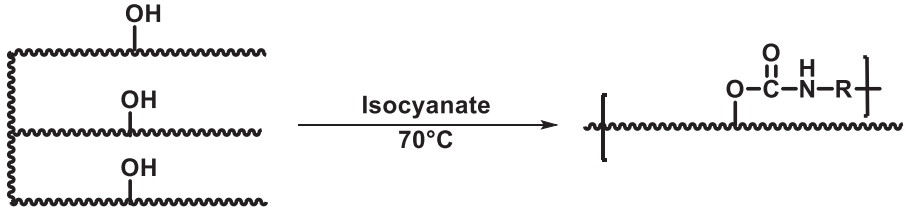

Scheme 1. Synthesis of polyurethane from castor oil.

2.3. Material characterization

The structural part of synthesized phosphors was studied by using a powder X-ray diffraction pattern collected using PANalytical X′Pert Pro diffractometer with Cu-Kα radiation (wavelength: 1.54056 Å) over the 2θ range of 10–80°. The structural parameters of the samples are refined by the Rietveld method using the GSAS II software. The X-ray photoelectron spectroscopy (XPS) measurements were studied with a PHI 5000 Versa probe Scanning ESCA Microprobe. The core-level spectra of O 1s, Si 2p, Eu 3d, F 1s, and Al 2p were obtained using Al Kα radiation (1.487 keV) at a resolution of 0.1 eV. The photoluminescence excitation (PLE) and emission (PL) were measured using a YvonFluorolog 3 spectrofluorometer with a 450 W Xenon flash lamp source. The electroluminescence spectra of synthesized composite phosphors were recorded by using a CCE spectrophotometer (OCEAN-FX-XRI-EX). The UV-Vis diffuse reflectance spectra (UV-Vis DRS) of the phosphors were collected using a UV-Vis Spectrophotometer (Shimadzu UV 3600) in the range of 200–700 nm. The Fourier-transform infrared (FT-IR) spectra of composite membranes were measured using a Bruker Alfa-E FT-IR. The thermal stability of the fabricated composite membranes was tested by a Pyris Diamond TG / DTA (PerkinElmer).

3. Results and discussion

3.1. Structural analysis using XRD and XPS

The Rietveld refinement on the powder XRD patterns of $Sr_3Al_{0.99}Si_{0.01}O_{4.01}F_{0.99}$ ($SASi_{0.01}OF$) and $Sr_{2.9}Al_{0.99}Si_{0.01}O_{4.01}F_{0.99}$: $0.1Eu^{2+/3+}$ ($SASi_{0.01}OF$: $Eu^{2+/3+}$) samples annealed in the oxygen-deficient atmosphere at 1150 °C for 4 h are shown in Fig. 1. The diffraction patterns of both the samples agree well with the tetragonal phase (space group: *I4/mcm*) of Sr_3AlO_4F (SAOF). Meanwhile, the incorporation of Si^{4+} ions results in the generation of several impurity peaks of Sr_3SiO_5 (JCPDS: 26-0984 and 06-0341) and Sr_2SiO_4 (JCPDS 18-1281), which are marked with asterisks, as can be seen in Fig. 1. The estimated lattice parameters, atomic coordinates, and bond lengths are given in Table 1, Table 2, and Table 3, respectively. The cell parameters of SAOF are refined to be a = b = 6.7537 Å, and c = 11.2126 Å. These estimated cell parameters are very close to the previously reported results on the same host material [22]. Meanwhile, the successful incorporation of Si^{4+} ions into the Al^{3+} sites can be realized from the slightly altered lattice parameters, as shown in Table 1. It can be noted from Table 1 that the values of a and b are slightly enlarged while c is contracted owing to the Si^{4+} doping into the Sr_3AlO_4F (SAOF) host, which is in line with the observations and interpretations reported by Bin et al. [21]. Furthermore, the replacing of an Al^{3+} ion by a Si^{4+} ion into the Al^{3+} site creates an excess cationic charge, which can be compensated due to the stoichiometric substitution of F^- ion by O^{2-} ion. A similar interpretation on charge compensation has also been reported earlier in the case of few rare-earth-doped oxyfluoride phosphors [21,32]. However, the refined values of a, b, and c of $SASi_{0.01}OF$: $0.1Eu^{2+/3+}$ slightly reduced in comparison with $SASi_{0.01}OF$ (Table 1) might be due to the anomalous reductions and substitutions of europium ions.

Fig. 2 shows the crystal structure representation of $SASi_{0.01}OF$. In this structure there exist two different Sr sites: 10 coordinated *4a* sites and 8 coordinated *8h* sites. A *4b* site is engaged by Al, *4c* is captured by F atoms, and O atoms are believed to occupy the *16l* site, respectively. It consists of arranging alternatively $Sr(1)O_8F_2/AlO_4$ and $Sr(2)O_6F_2$ polyhedron along the c axis. SAOF belongs to the tetragonal Cs_3-$CoCl_5$-family (space group *I4/mcm*) and is narrowly linked to the tetragonal Sr_3SiO_5 (space group *P4/ncc*). From the bond length calculation obtained from the refinement of SAOF (listed in Table 3), it is clear that the *4a* site is much larger than that of the *8h* site. The incorporation of Si^{4+} ions into the Al^{3+} sites contract the AlO_4

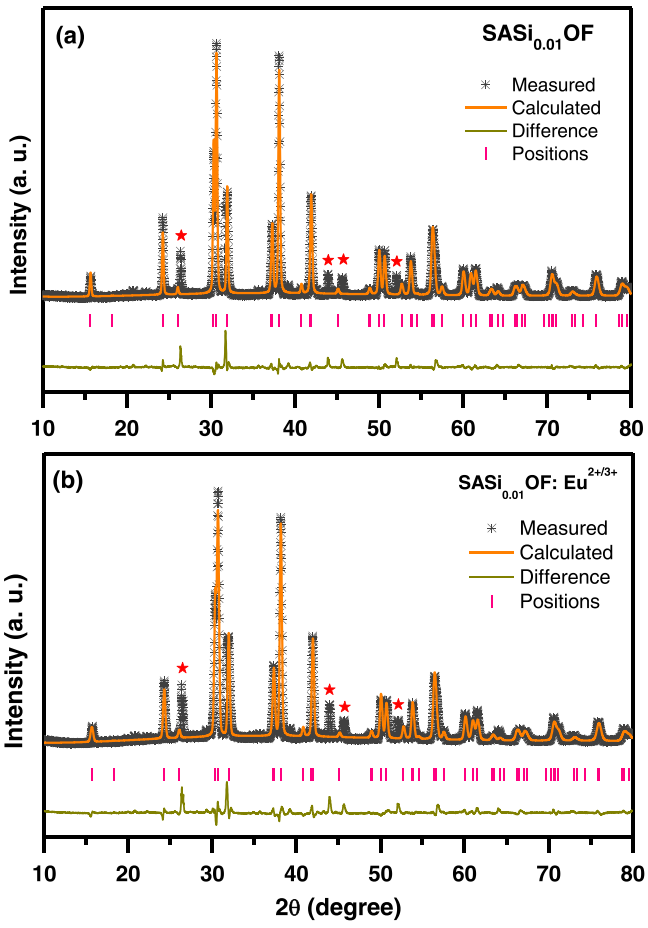

Fig. 1. Rietveld refined XRD patterns of (a) $SASi_{0.01}OF$, and (b) $SASi_{0.01}OF$: $Eu^{2+/3+}$ samples.

Table 1
The lattice parameters of the Rietveld refined samples.

Lattice parameters	SAOF	$SASi_{0.01}OF$	$SASi_{0.01}OF$: $Eu^{2+/3+}$
a [Å]	6.7537	6.7727	6.7634
b [Å]	6.7537	6.7727	6.7634
c [Å]	11.2127	11.1219	11.1072
V [$Å^3$]	506.4	510.157	508.08

Table 2
The atomic coordinates and fractional occupancies of the Rietveld refined samples.

Sample	Atom	Site	x	y	z	Occ.
SAOF	Sr(1)	4a	0.0	0.0	0.25	1
	Sr(2)	8h	0.1696	0.6696	0.0	1
	Al	4b	0.0	0.5	0.25	1
	F	4c	0.0	0.0	0.0	1
	O	16l	0.1418	0.6418	0.6496	1
$SASi_{0.01}OF$	Sr(1)	4a	0.0	0.0	0.25	1
	Sr(2)	8h	0.1678	0.6678	0.0	1
	Al	4b	0.0	0.5	0.25	0.99
	Si	4b	0.0	0.5	0.25	0.01
	F	4c	0.0	0.0	0.0	1
	O	16l	0.13856	0.63856	0.6547	1
$SASi_{0.01}OF$: $Eu^{2+/3+}$	Sr(1)	4a	0.0	0.0	0.25	0.9
	Eu(1)	4a	0.0	0.0	0.25	0.1
	Sr(2)	8h	0.16536	0.66536	0.0	0.9
	Eu(2)	8h	0.16536	0.66536	0.0	0.1
	Al	4b	0.0	0.5	0.25	0.99
	Si	4b	0.0	0.5	0.25	0.01
	F	4c	0.0	0.0	0.0	1
	O	16l	0.13131	0.63131	0.6605	1

Table 3
Selected bonds and corresponding bond lengths that exist between the elements in the following samples.

SAOF		$SASi_{0.01}OF$		$SASi_{0.01}OF$: $Eu^{2+/3+}$	
Bond type	Bond length [Å]	Bond type	Bond length [Å]	Bond type	Bond length [Å]
Sr(1)-O x 8	2.7909(8)	Sr(1)-O x 8	2.8278(8)	Sr(1)/Eu(1)-O x 8	2.8275(8)
Sr(1)-F x 2	2.7781(4)	Sr(1)-F x 2	2.7805(4)	Sr(1)/Eu(1)-F x 2	2.7768(4)
Sr(1)-Sr(2)	3.7428(8)	Sr(1)-Sr(2)	3.7529(8)	Sr(1)/Eu(1)-Sr(2)/Eu(2)	3.7529(8)
Sr(2)-O x 4	2.6873(6)	Sr(2)-O x 4	2.7028(6)	Sr(2)/Eu(2)-O x 4	2.6939(6)
Sr(2)-O x 2	2.4512(3)	Sr(2)-O x 2	2.5298(3)	Sr(2)/Eu(2)-O x 2	2.6382(3)
Sr(2)-F x 2	2.5082(6)	Sr(2)-F x 2	2.5206(6)	Sr(2)/Eu(2)-F x 2	2.5245(2)
Al-O x 4	1.7547(4)	Al/Si-O x 4	1.6984(4)	Al/Si-O x 4	1.6018(4)

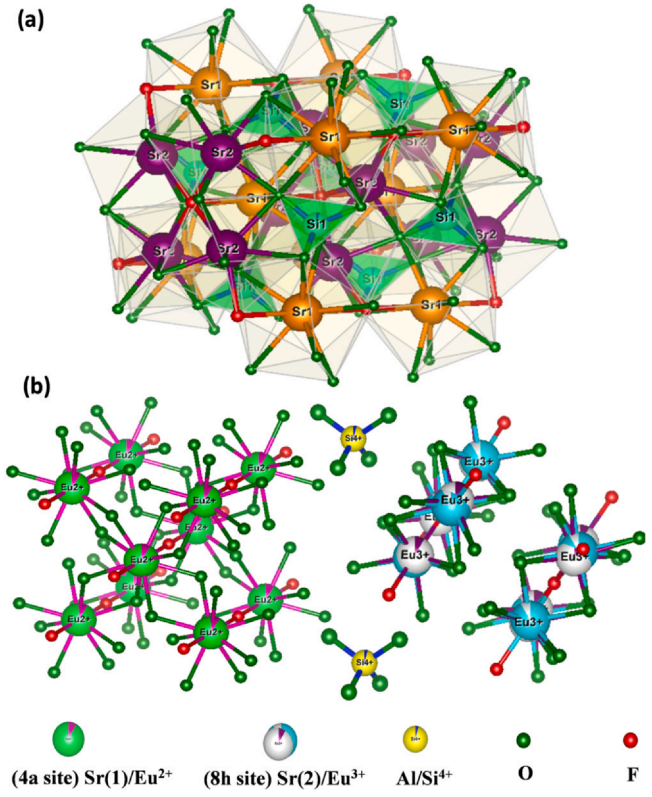

Fig. 2. (a) The basic crystal structure, and (b) the different coordination environment of Sr(1), Sr(2) and Al sites in $SASi_{0.01}OF$: $Eu^{2+/3+}$.

tetrahedral sites because of the smaller ionic substitution. It may affect the neighbouring two Sr polyhedrons since AlO_4 tetrahedra are linked to $Sr(1)O_8F_2$ and $Sr(2)O_6F_2$ through oxygen bridging by the edge and corner-sharing. Due to the inductive effect by the substitution of Si^{4+} ions in Al^{3+} sites, the AlO_4 tetrahedra contracted, and the neighbouring Sr^{2+} sites get enlarged, which is also supported by the calculated bond lengths, as shown in Table 3. After the doping of Si^{4+} ions, the average bond length of Al-O decreases, and Sr(1)-O/F and Sr(2)-O/F bond lengths are considerably enhanced as compared to the SAOF sample. Among the two polyhedrons, $Sr(1)O_8F_2$ is closely related with the AlO_4 tetrahedra owing to two edges and two corner-sharing. Hence, the *4a* site (Sr(1)) is more suitable for Eu^{2+} ions' occupation than the *8 h* site (Sr(2)), which is also clear from the bond length values indicated in Table 3. The average bond length of Sr(1)-O/F is more than that of Sr(2)–O/F. From the refinement data of $SASi_{0.01}OF$: $Eu^{2+/3+}$ it is also clear that because of Si^{4+}-doping, the Al-O bond length decreases and Sr(1)-O/F bond length increases. Hence, the substitution of Si^{4+} ions can enlarge the Sr^{2+} sites and subsequently enhance the occupation of Eu^{2+} ions at the Sr(1) sites. The basic crystal diagram of SASiOF and the corresponding coordination environments of all sites are represented in Fig. 2(a) and (b), respectively. Therefore, it can be concluded that increasing the Si^{4+} ions' content during the synthesis in the oxygen-deficient atmosphere accelerates the conversion of more and more Eu^{3+} ions to Eu^{2+} ions, and these valence states of europium can able to coexist in corresponding *8h* and *4a* sites, respectively.

According to the previous report, Eu^{3+} ions ($r^{8\,h}$ = 1.066 Å) tend to substitute in the 8h sites if Sr^{2+} sites ($r^{8\,h}$ = 1.26 Å) in the Sr_3AlO_4F host via forming surplus positive charges [33]. Such an extra amount of positive charges can easily be compensated via the minor off-stoichiometric adjustment between O^{2-} and F^-, and creates some cation vacancies [32]. Additionally, the high-temperature annealing process at vacuum conditions is also responsible to create certain interstitial defects in the host which can act as the electron donor to Eu^{3+} ions and subsequently reduce them to Eu^{2+} [24,32]. However, the complete reduction of Eu^{3+} is not seen in SAOF: $Eu^{2+/3+}$. The local surroundings and size of the substituted crystal-site also contribute substantially to the Eu^{3+} reduction. In most of the strontium hosts, Eu^{3+} can easily reduce to its divalent form during the synthesis in a reduction atmosphere [34,35]. But the reduction of Eu^{3+} has not observed in Sr_3AlO_4F: Eu compositions synthesized in reduction atmosphere [26,36]. Recently, Fang et al. reported the photoluminescence behaviour of Eu-doped Sr_3AlO_4F synthesized in a reduction atmosphere. But they have only observed Eu^{3+} emission without any wideband emission related to Eu^{2+} ions because of the strong oxidative lattice around the Sr^{2+} sites [26].

The efficient reduction of Eu^{3+} ions are not observed in Sr^{2+} sites of Sr_3AlO_4F host might be also due to the large ionic radii of Eu^{2+} ions ($r^{8\,h}$ = 1.25 Å, r^{4a} = 1.35 Å) in the 8-fold and 10-fold coordination, which are comparable with the Sr^{2+} ions ($r^{8\,h}$ = 1.26 Å, r^{4a} = 1.36 Å). Moreover, both the Sr^{2+} sites are enclosed densely by AlO_4 tetrahedral units, which is also preventing the substitution of Eu^{2+} ions in the Sr^{2+} sites. In order to enlarge the Sr^{2+} sites, we have incorporated $Si^{4+} - O^{2-}$ into the SAOF structure to replace Al^{3+} - F^- resulting in $Sr_{2.9}Al_{1-x}Si_xO_{4+x}F_{1-x}$: $0.1Eu^{2+/3+}$ ($SASi_xOF$: $Eu^{2+/3+}$). This substitution might shrink the AlO_4 tetrahedral units owing to the smaller ionic radii of Si^{4+} ions (r^{4b} = 0.26 Å) than that of Al^{3+} ions (r^{4b} = 0.39 Å). The shrinkage of AlO_4 sites might reduce the strength of the oxidative lattice in the surrounding of the Sr^{2+} sites and enlarged them subsequently. The lower bond length of Al/Si-O in $SASi_{0.01}OF$ than the bond length of Al-O in SAOF is also supporting the above prediction (Table 3). Meanwhile, bigger O^{2-} anions ($r^{16\,l}$ = 1.40 Å) are also assumed to replace smaller F^- anions (r^{4c} = 1.33 Å) to achieve charge balance for the present framework and create some oxygen interstitial defects. These defects probably act as suitable electron donors to Eu^{3+} ions for their reduction. Meanwhile, the enlarged Sr^{2+} sites accelerate their reduction.

A survey XPS spectrum of $SASi_{0.03}OF$: $Eu^{2+/3+}$ heat-treated in the oxygen-deficient environment, shown in Fig. 3(a), confirming the existence of Sr, Al, O, F, Si, and Eu. More precisely, Fig. 3(b)–(g) represent the core spectra of Al, Si, O, F, and Eu, respectively. The spectrum of Al 2p (Fig. 3(b)) is obtained at 71.68 eV, which is slightly shifted towards the lower energy side than the standard value [37,38], indicating the proper binding of Si^{4+} ions in the Al sites. The lower shifting of binding energy value is might be due to shorter ionic radii of Si^{4+} ions than Al^{3+} ions. The core-level spectrum of Si 2p

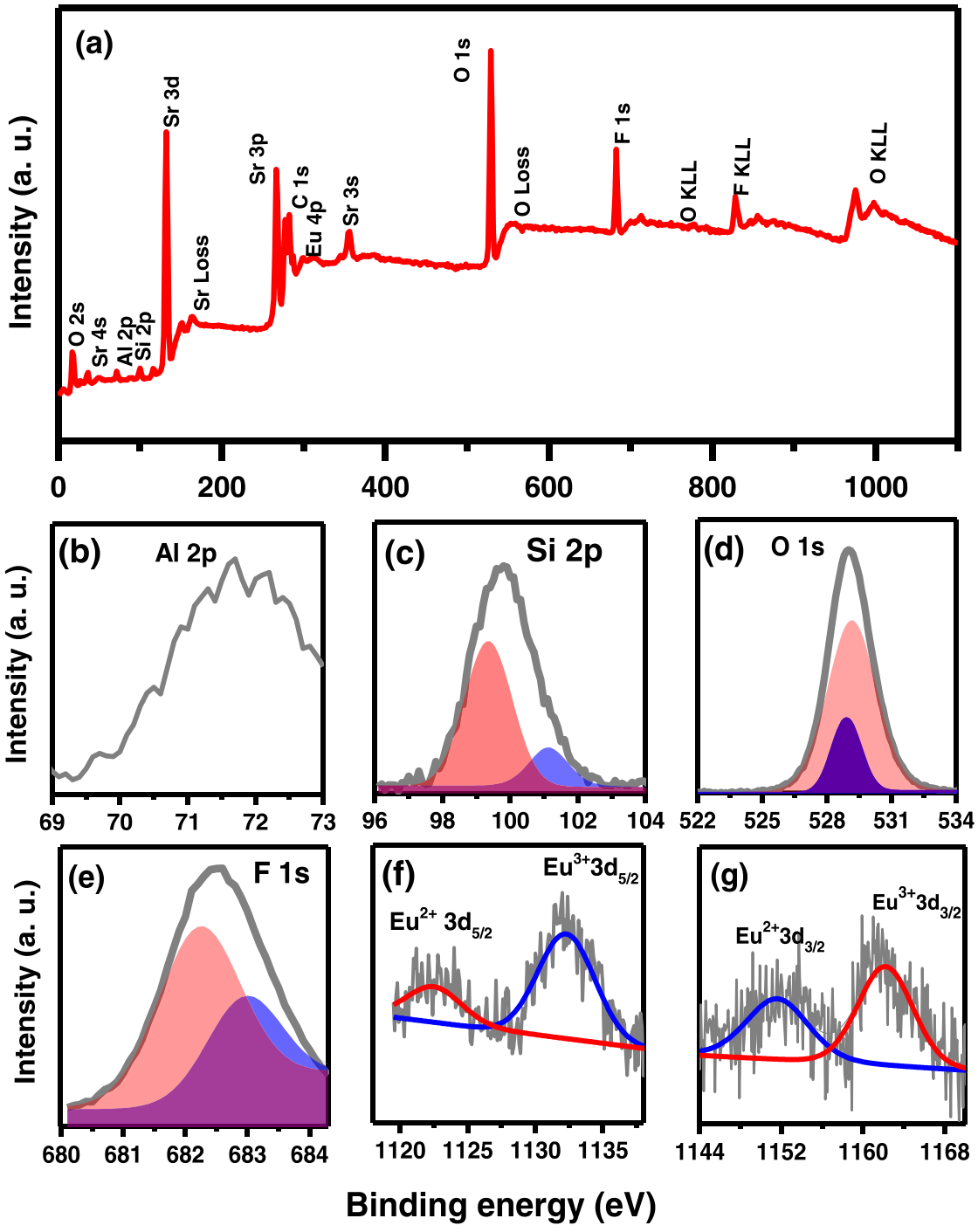

Fig. 3. (a) Survey spectrum of $SAlSi_{0.03}OF: Eu^{2+/3+}$. (b) – (g) represents the core level spectra of each element.

(Fig. 3(c)) consists of two peaks centered at 99.37 eV corresponds to the elemental Si, and 101.21 eV is attributed to the oxidized Si kinds (mainly SiO_2) [39,40]. The later one might enhanced the probability of the formation of some silicate impurity phases [39,40]. Meanwhile, the core level XPS spectrum of O 1s (Fig. 3(d)) elaborates two peaks at 528.92 eV and 529.11 eV corresponds to the lattice oxygen without any surface oxygen peaks. From the XPS results, we can conclude that the excess Si^{4+} ions may be adsorbed (such as SiO_2) on the oxygen-deficient region thereby diminishing the surface oxygen and subsequent formation of silicon dioxide.

The core-level spectrum of F 1s (Fig. 3(e)) is deconvoluted into two peaks centered at 682.26 eV and 683.01 eV [39]. The peak FI is corresponding to the two longer bond lengths of Sr(1) – F. While peak FII corresponds to the shorter Sr2-F bond length. Under the vacuum condition, the surface oxygen can diffuse into the lattice site as oxide ions and electrons. In the deficiency of oxygen more Eu^{3+} ions can receive those electrons and can be reduced to Eu^{2+}. This kind of coexistence of Eu^{3+} and Eu^{2+} ions also confirmed by XRD results. The XPS spectra of Eu 3d consist of four peaks corresponding to Eu^{2+} $3d_{5/2}$ (1122.52 eV), Eu^{3+} $3d_{5/2}$ (1132.23 eV), Eu^{2+} $3d_{3/2}$ (1151.57 eV) and Eu^{3+} $3d_{3/2}$ (1162.23 eV), respectively (Fig. 3(f) and (g)). The difference in binding energy values of Eu $3d_{3/2}$ and Eu $3d_{5/2}$ of Eu^{3+} (29.86 eV) and Eu^{2+} (29.15 eV) is closer to their standard separation gap (29.8 eV) [39]. The XPS results broadly indicate that

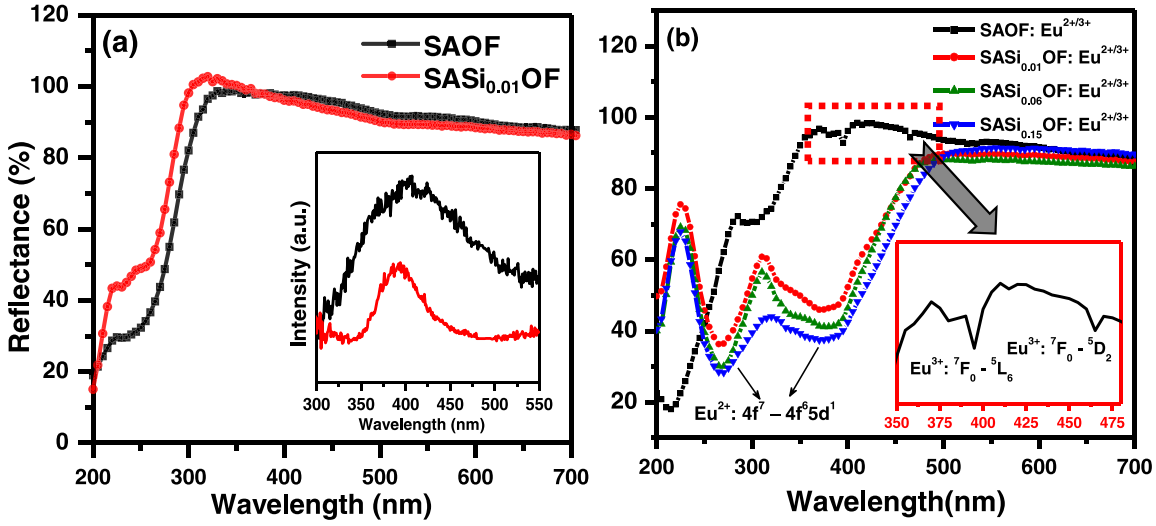

Fig. 4. (a) UV-Vis diffuse reflectance spectra and of SAOF and $SASi_{0.01}OF$ samples. Inset shows the PL emission spectra of corresponding samples recorded at 241 nm UV excitation. 4 (b) UV-Vis diffuse reflectance spectra of $SASi_xOF$: $Eu^{2+/3+}$ (x = 0.0, 0.01, 0.06, and 0.15) phosphors.

under the low oxygen atmosphere and by the doping of Si^{4+} ions enhance the possibility of formation of Eu^{2+} ions.

3.2. Optical characterizations using UV-Vis DRS and photoluminescence emission and excitation

The UV-Vis DRS of SAOF and $SASi_{0.01}OF$ samples, shown in Fig. 4(a), exhibit almost 100% reflectance in the wavelength range of 350 – 700 nm and steep slopes in 250–325 nm. Both the samples show a host absorption band maximized at 241 nm. Compare to SAOF, the intensity of this band is reduced in $SASi_{0.01}OF$, which might be due to the reduction of surface oxygen charge carrier's content due to the Si^{4+} ions' incorporation into SAOF. The inset of Fig. 4(a) shows the PL emission spectra of SAOF and $SASi_{0.01}OF$ at 241 nm UV excitation, which is showing that after Si^{4+} ions' doping, SAOF host emission intensity attributed to the oxygen vacancies is reduced. The XPS core spectra of O 1s and Si 2p already indicated that excess Si^{4+} cations can adsorb free surface O^{2-} ions to form SiO_2. As a result of the low content of free O^{2-} ions, the host emission due to charge transfer decreases after the doping of Si^{4+} ions in SAlOF. Fig. 4(b) elaborate DRS of various content of Si^{4+}-doped $SASi_xOF$: $Eu^{2+/3+}$ (x = 0.0, 0.01, 0.06, and 0.15) phosphors. Without Si^{4+} ions, SAOF: $Eu^{2+/3+}$ phosphor exhibits an additional absorption band peaked at around 295 nm corresponds to the O^{2-} - Eu^{3+} charge transfer band. Besides, several sharp peaks are observed between 350 and 480 nm corresponding to the intra *f-f* Eu^{3+} transitions (inset graph in Fig. 4(b)). Introducing a small amount of Si^{4+} ions in the Al sites of SAOF: $Eu^{2+/3+}$ phosphor results in broadband absorption in the region of 225–450 nm owing to the $4f^65d^1$ - $4f^7$ transitions of Eu^{2+} ions. Meanwhile, the DRS results of $SASi_xOF$: $Eu^{2+/3+}$ phosphors show almost 90% reflectance in the visible region (450–700 nm). The intensity of Eu^{2+} absorption is increased with the increase in Si^{4+} ions in $SASi_xOF$: $Eu^{2+/3+}$ because of the subsequent enhancement in the conversion rate of Eu^{3+} to Eu^{2+}.

Fig. 5 shows the spectral overlap between the excitation spectrum of $SASi_{0.01}OF$: $Eu^{2+/3+}$ and the emission spectrum of $SASi_{0.01}OF$, which indicates the phenomenon of energy transfer between the self-activated host and the activator ions. The emission spectrum of $SASi_{0.01}OF$, recorded upon 240 nm excitation, shows a self-activated emission at 416 nm owing to the trapped exciton emission of a defect center in $SASi_{0.01}OF$. Reportedly, these defects might be related to the anion-deficient nonstoichiometric species which is normally produced during the heating in an oxygen-deficient atmosphere

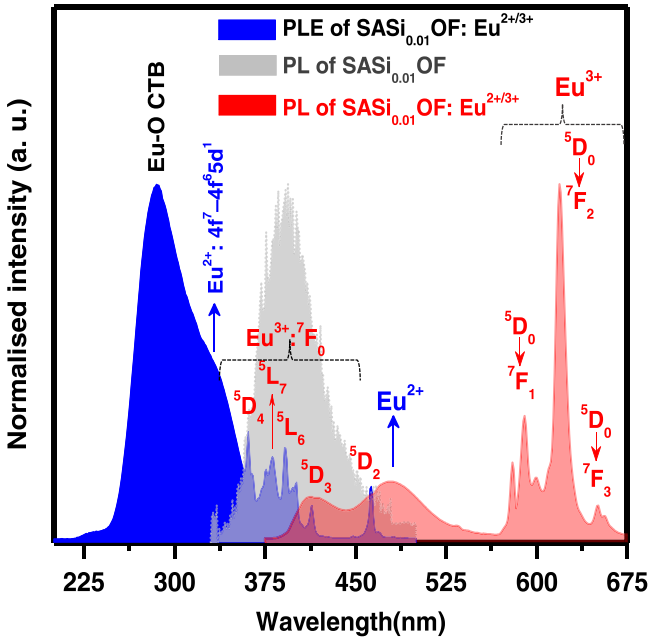

Fig. 5. Spectral overlap between the excitation spectrum (PLE) of $SASi_{0.01}OF$: $Eu^{2+/3+}$ and the emission spectrum (PL) of $SASi_{0.01}OF$. The emission spectrum of $SASi_{0.01}OF$: $Eu^{2+/3+}$ is also added to realize the self-activated emission of $SASi_{0.01}OF$ and its energy transfer process to $Eu^{2+/3+}$ activators.

[41]. It is clear from the emission spectra of $SASi_{0.01}OF$: $Eu^{2+/3+}$ that the corresponding emission intensity of the $SASi_{0.01}OF$ host is significantly diminishes owing to the activator ions doping. Also, the emission spectrum of $SASi_{0.01}OF$: $Eu^{2+/3+}$ comprises a broad emission band in the range of 375–525 nm which is attributed to the *4f - 5d* transitions of Eu^{2+} ion and several sharp peaks located in the 550–675 nm region owing to the *f-f* transitions of Eu^{3+} ions. This result indicates the existence of both europium valency in $SASi_{0.01}OF$: $Eu^{2+/3+}$, and suggesting the tunable emission color can be obtained via tuning the Eu^{2+} to Eu^{3+} ions ratio.

For the precise tuning of emission color, additional insights on the energy levels of both europium ions in the Si^{4+}- doped SAOF and the corresponding energy exchange procedures among the host and activators. Therefore, the recorded excitation spectrum of $SASi_{0.01}OF$ peaking at 5.14 eV (displayed in Fig. 6(a)) is deconvoluted into two

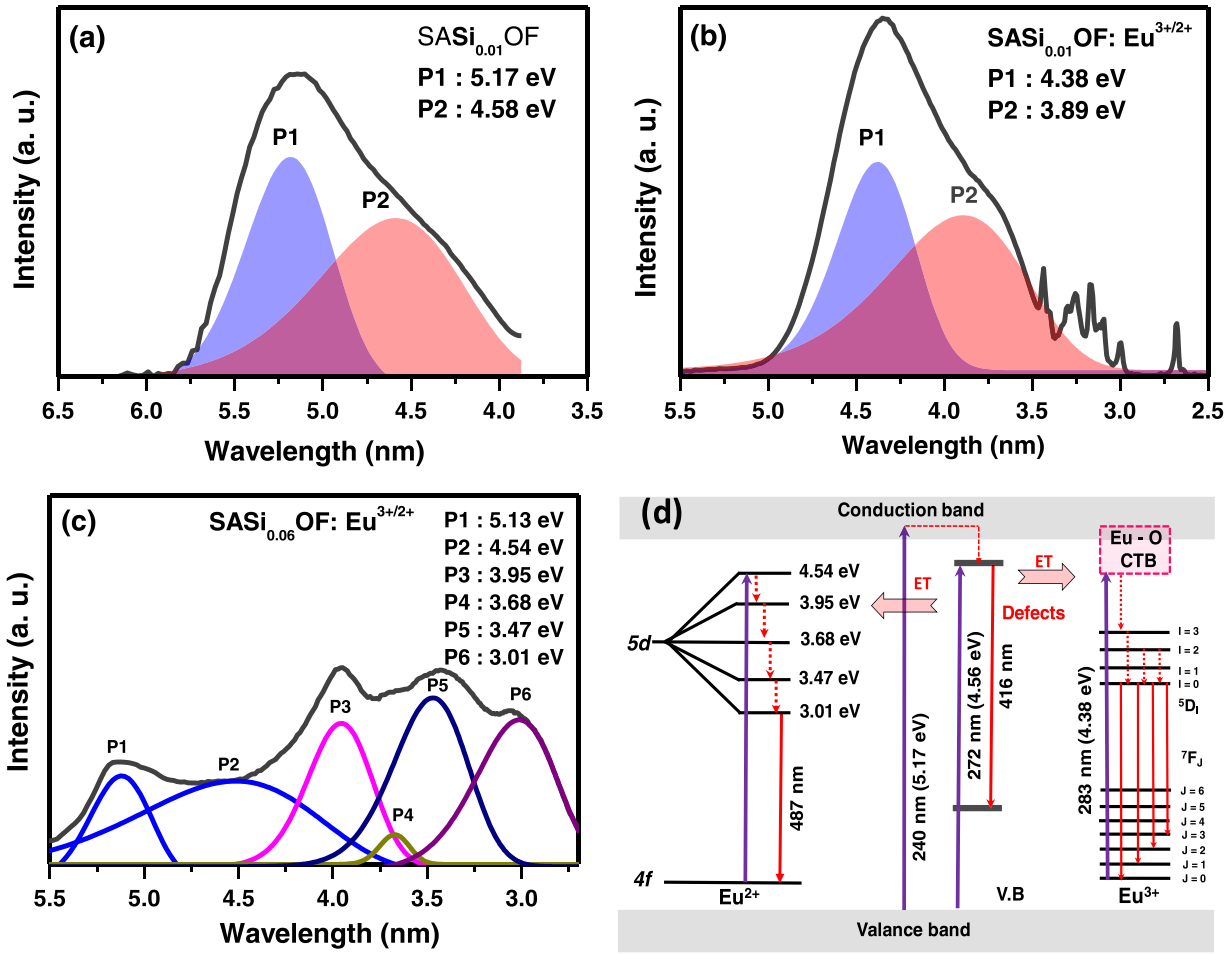

Fig. 6. Deconvoluted excitation spectra of (a) $SASi_{0.01}OF$, (b) $SASi_{0.01}OF: Eu^{2+/3+}$, and (c) $SASi_{0.06}OF: Eu^{2+/3+}$. (d) Illustration of the most probable energy transfer mechanisms in $SASiOF: Eu^{2+/3+}$.

Gaussian curves, which could be attributed to the band to band transitions (P1) and absorption via the defect states (P2) situated near to the conduction band. In the deconvoluted excitation spectra of $SASi_{0.01}OF: Eu^{2+/3+}$ (Fig. 6(b)), P1 belongs to Eu^{3+} - O charge transfer band and P2 is attributed to the *4f - 5d* transitions of Eu^{2+} ions. In addition, the sharp excitation peaks due to the intra-configurational *4f–4f* transitions of Eu^{3+} can also be observed below 3.5 eV. The deconvoluted excitation spectra of $SASi_{0.06}OF: Eu^{2+/3+}$ phosphor (shown in Fig. 6(c)) consists of a host excitation peaked at around 5.13 eV and five *4f - 5d* transition peaks of Eu^{2+} ions. Because of the incorporation of Si^{4+} ions in SAOF: Eu phosphor, the O^{2-} - Eu^{3+} charge transfer band disappears and various Eu^{2+} *4f – 5d* transition peaks arise. The probable energy level diagram of Eu^{2+} and Eu^{3+} ions in the SASiOF host is elaborated in Fig. 6(d). After absorbing the UV energy, the electrons present in the valance band raised to the conduction band. The excited electrons then trapped by the energy level of the defects and subsequently recombine with the holes. The energy produced due to the above recombination process has been transferred to $Eu^{3+/2+}$ ions [42–44].

The emission spectra of a series of $SASi_xOF: Eu^{2+/3+}$ (x = 0.0, 0.01, 0.03, 0.05, 0.06, 0.1, 0.12, and 0.15) phosphors, recorded at 360 nm, is shown in Fig. 7(a). The broadband peaked at 482 nm is attributed to the $4f^6 5d^1$ - $4f^7$ allowed transitions of Eu^{2+} ions. Whereas several sharp peaks of $^5D_0 \rightarrow {}^7F_J$ transitions of Eu^{3+} ions are observed in the 550–675 nm region having the intense red peak at 620 nm owing to the $^5D_0 \rightarrow {}^7F_2$ transitions. As the doping concentration of Si^{4+} ion increases emission intensity of characteristic *5d - 4f* transition of Eu^{2+} ions increases and the emission intensity results from the *f–f* transitions of Eu^{3+} ions decreases. At a particular concentration (x = 0.06) of Si^{4+} ions, the red-orange emission band of Eu^{3+} completely diminished, while the board bluish band intensity of Eu^{2+} ions reach maximum. These results indicate that as the concentration of Si^{4+} ions enhances, more Eu^{3+} ions are reduced to Eu^{2+} ions.

The XRD refinement results indicated that both valence states of Eu may coexist in the obtained $SASi_xOF: Eu^{2+/3+}$ samples, which is proved again by the photoluminescent studies. With increasing the content of Si^{4+} ions, the rate of valence changes from Eu^{3+} to Eu^{2+} has also increased owing to which the emission color of $SASi_xOF: Eu^{2+/3+}$ phosphors also tuned from red-orange (x = 0.0; CIE: 0.48, 0.29) to nearly white (x = 0.03; CIE: 0.30, 0.26) and eventually to bluish color (x = 0.06; CIE: 0.18, 0.23) simply by altering the doping concentration of Si^{4+} ions. The corresponding CIE chromaticity diagram and the coordinates of $SASi_xOF: Eu^{2+/3+}$ phosphors monitored on 360 nm, are shown in Fig. 7(b). The inset digital images in Fig. 7(b) recorded under near-UV light well illustrated the color tuning, and directly supporting the emission results of $SASi_xOF: Eu^{2+/3+}$ phosphors. It is worth mentioning that at an intermediate concentration (x = 0.03) of Si^{4+} ions, both emission peak intensity of Eu^{2+} ions and Eu^{3+} ions are able to tune the emission color to near white indicating the potential of the present host as a single white emitting composition.

3.3. Structural and photoluminescence properties of $SASi_{0.06}OF: Eu^{2+/3+}$ @ CO composite membranes for their usage in lighting devices

From IR spectra as shown in Fig. 8(a), the esterification reaction of the polyol is confirmed by the appearance of characteristic C = O

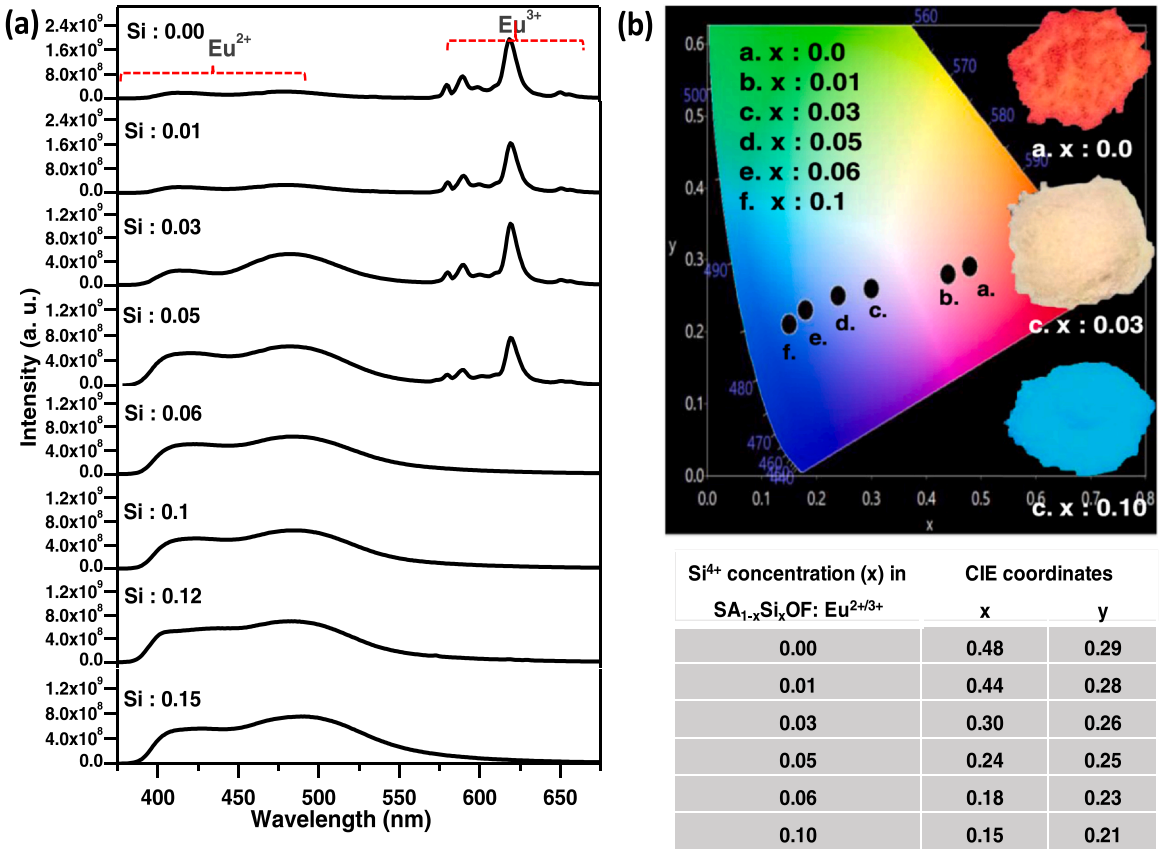

Si^{4+} concentration (x) in $SA_{1-x}Si_xOF: Eu^{2+/3+}$	CIE coordinates	
	x	y
0.00	0.48	0.29
0.01	0.44	0.28
0.03	0.30	0.26
0.05	0.24	0.25
0.06	0.18	0.23
0.10	0.15	0.21

Fig. 7. (a) The emission spectra of $SASi_xOF: Eu^{2+/3+}$ ($0 \le x \le 0.15$) excited by 360 nm. (b) CIE chromaticity diagram and (c) corresponding CIE coordinates of $SASi_xOF: Eu^{2+/3+}$ ($0 \le x \le 0.1$) recorded at 360 nm excitation.

band at 1745 cm^{-1} ($SASi_{0.03}OF: Eu^{2+/3+}$ @ CO). The strong band at 1242 cm^{-1} attributed to the C-O stretching further revealed the esterification of polyol. The presence of a medium absorption band at 3350 cm^{-1} corresponds to N-H (secondary) stretching in the urethane and the peak at 1517 cm^{-1} indicates the urethane linkage (C—N—H). The strong intense band at 2261 cm^{-1} which corresponds to —N=C=O stretching in isocyanate got completely disappeared in polyurethane. The bands analogous to N-H bending at 710–780 cm^{-1} confirms the formation of CO. The peaks at 2922 and 2857 cm^{-1} are attributed to the methylene (CH_2) asymmetric and symmetric stretching vibration of the hydrocarbon chain of castor oil and methyl group (CH_3) stretching that appeared at 3016 cm^{-1} in both polyurethane and castor oil [45].

The thermal stability of polyurethane and its composite is analyzed by TGA analysis and the thermogram profile is depicted in Fig. 8(b). It is important to note that CO is thermally stable up to 230 °C. The initial degradation occurs at 235–240 °C due to the decomposition of urethane linkage, which is unstable compared to other bonding. The next stage of degradation in the range of 380–410 °C corresponds to the decomposition of high energy double

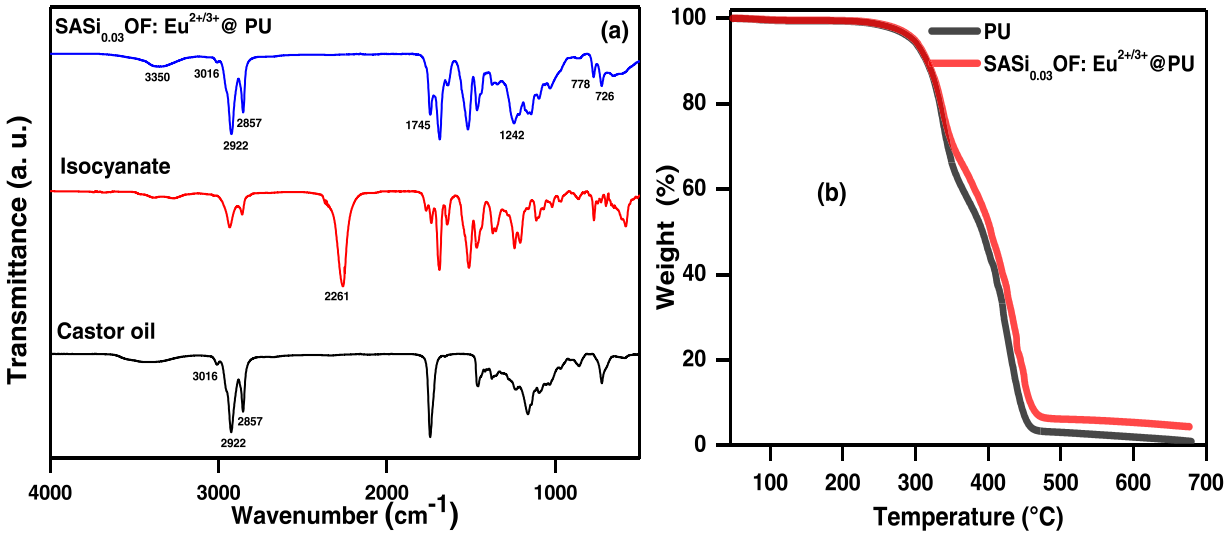

Fig. 8. (a) IR analysis of castor oil, isocyanate and $SASi_{0.03}OF: Eu^{2+/3+}$ @ CO. (b) Thermogravimetric profile of CO and $SASi_{0.03}OF: Eu^{2+/3+}$ @ CO.

Table 4
Thermal parameters of CO and $SASi_{0.03}OF: Eu^{2+/3+}$ @ CO.

Sample	T_{onset}	T_5	T_{10}	T_{50}	T_{endset}
CO	237	295	314	392	465
$SASi_{0.03}OF:Eu^{2+/3+}$ @ CO	241	299	316	403	480

bonds and single bonds including alkyl chain, dissociation of the ester bond through chain scission, dehydrogenation, and depoly-condensation of alkyl groups. The thermal parameters, listed in Table 4, show minor improvement in CO matrix after adding phosphor. The higher residue content in the case of CO composite is due to the presence of non-degraded phosphor [46,47].

Fig. 9(a) and (b) display the optical microscopic images of only CO and $SASi_{0.06}OF: Eu^{2+/3+}$ @ CO composites, respectively, along with their real digital images (insets). The transparency of the CO can be well understood in Fig. 9(a), whereas Fig. 9(b) indicates the even distribution of phosphor particles in the CO matrix. It can be realized from the insets that the transparency of the composite (inset of Fig. 9(b)) is reduced owing to the phosphor incorporation. However, due to the transparent nature of CO (inset of Fig. 9(a)), excitation photons can be easily absorbed by the phosphor particles. Finally, we have checked the device preformation of the fabricated composites. These composite membranes could be used to develop resin-free pc-LED systems for various lighting applications. Fig. 9(c) describes the schematic representation of a pc-LED device having a phosphor – polymer composite layer illuminated by a near-UV LED chip.

The thermal quenching properties of $SASi_{0.06}OF: Eu^{2+/3+}$ phosphor and $SASi_{0.06}OF: Eu^{2+/3+}$ @ CO composite from ambient to 150 °C temperature and the results are presented in Fig. 10 (a). Because of

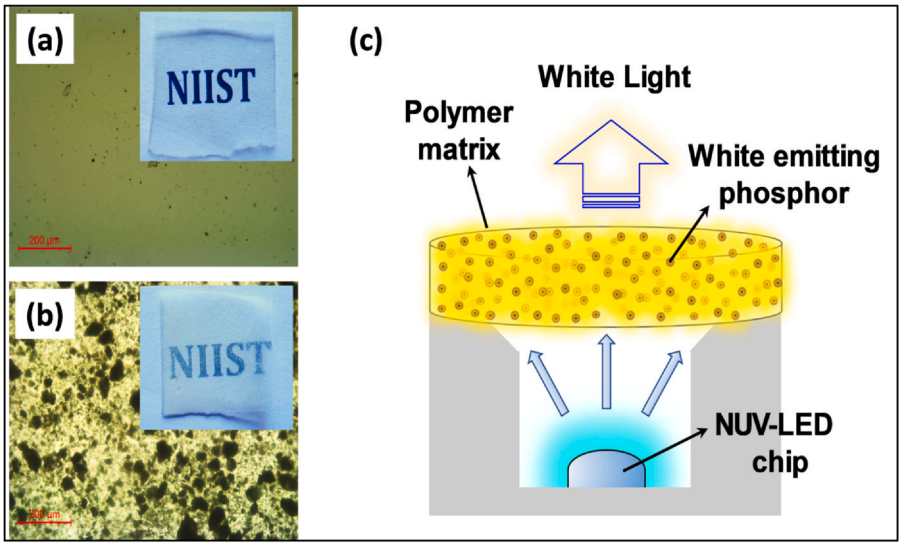

Fig. 9. Optical microscopic image and direct digital image (insets) of (a) a CO matrix, and (b) a $SASi_{0.06}OF: Eu^{2+/3+}$ @ CO composite. (c) Schematic representation of a pc-LED device considering the phosphor @ polymer composite layer and a near-UV LED.

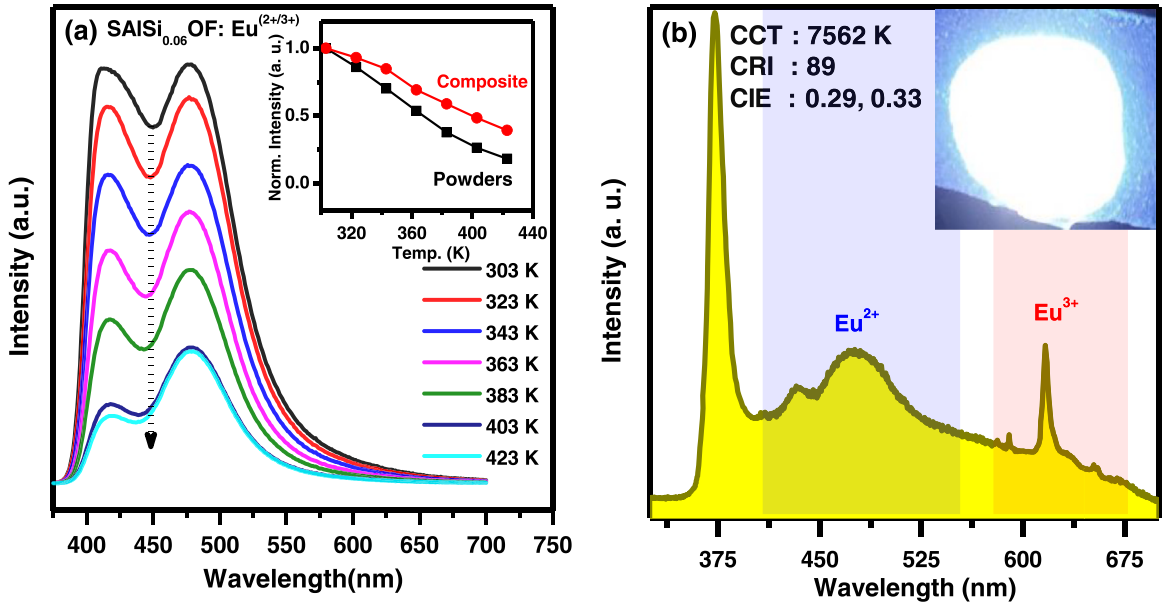

Fig. 10. (a) Temperature dependent PL emission spectra of $SASi_{0.06}OF: Eu^{2+/3+}$ phosphor under 360 nm excitation. The inset shows the PL intensity variation of $SASi_{0.06}OF: Eu^{2+/3+}$ phosphor powders and $SASi_{0.06}OF: Eu^{2+/3+}$ @ CO composite. (b) A 372 nm near-UV LED irradiated EL spectrum of a $SASi_{0.03}OF: Eu^{2+/3+}$ @ CO membrane and the corresponding digital image (inset).

the increase in operating temperature of the LED, the phosphor emissive performance usually degrades owing to the elevated non-radiative transitions. Here also it is observed that at the elevated temperatures, the emission efficiency of $SASi_{0.06}OF: Eu^{2+/3+}$ phosphor decreases gradually with the partial blue shift of the emission band. $SASi_{0.06}OF: Eu^{2+/3+}$ phosphor shows only 20% emission intensity compare to the ambient temperature intensity at 150 °C. While the composite shows almost double intensity $SASi_{0.06}OF: Eu^{2+/3+}$ phosphor at 150 °C since the encapsulated polymer is acting like a protective layer to the phosphor particles. Eventually, a W-LED is also fabricated using the 372 nm near-UV LED and a composite membrane made from CO loaded with 10 wt% $SASi_{0.03}OF: Eu^{2+/3+}$ phosphor. The recorded EL spectrum at 500 mA, shown in Fig. 10 (b), shown cool white emission having the CIE of (0.29, 0.33), CCT of 7562 K, and CRI of 89. The inset of Fig. 10 (b) is illustrating the image of a $SASi_{0.03}OF: Eu^{2+/3+}$ @ CO composite under the illumination of a near-UV 372 nm LED. The intensity and color uniformity of the emitted light indicate the appropriate distribution of phosphor particles in the polymer matrix. The white light-emitting phosphor – polymer membranes, developed in the current research, maybe potential in making lighting and display devices.

4. Conclusions

This work reported various Si^{4+}-codoped $Sr_{2.9}Al_{1-x}Si_xO_{4+x}F_{1-x}: 0.1Eu^{2+/3+}$ oxyfluoride phosphors with the simultaneous existence of Eu^{2+} and Eu^{3+} ions. The substitution of Si^{4+} ions in Al sites contracted the AlO_4 tetrahedral sites and enlarges the Sr sites. Such lattice modifications because of the cationic substitutions enabled the occupancy of Eu^{2+} ions, and thus change the valence of Eu^{3+} to Eu^{2+}. Due to the above valence change of europium ions, the broad bluish emission band of Eu^{2+} ions increased gradually along with the subsequent decrement in the sharp red-orange emission peaks due to the intra *f-f* transitions of Eu^{3+} ions. Because of this, the overall emission color was also tuned from orange-red to near-white and eventually to bluish. The optimum blue-emitting $SASi_{0.06}OF: Eu^{2+/3+}$ and nearly white emitting $SASi_{0.03}OF: Eu^{2+/3+}$ phosphors were utilized further to make phosphor-polymer flexible composites along with castor oil (CO). Integration of $SASi_{0.03}OF: Eu^{2+/3+}$ @ CO composite along with a 372 nm near-UV LED produced cool white emission having the chromaticity coordinates of (0.29, 0.33), CCT of 7562 K, and CRI of 89. Therefore, the substitution of Si^{4+} ions in $Sr_{2.9}AlO_4F: 0.1Eu^{2+/3+}$ successfully tuned the important activator sites as well as changed the Eu valence and an altered amount of Si^{4+} ions concentration generated nearly white light emission. The outcomes are unreported so far for Sr_3AlO_4F based oxyfluorides for flexible lighting applications.

CRediT authorship contribution statement

S. Sreevalsa: Conceptualization, Validation, Methodology, Formal analysis, Writing - original draft. **P. A. Parvathy:** Methodology, Formal analysis. **Sushanta K. Sahoo:** Methodology, Validation, Writing - review & editing. **Subrata Das:** Supervision, Validation, Resources, Writing - review & editing, Visualization, Project administration, Funding acquisition.

Declaration of Competing Interest

The authors declare that they have no known competing financial interests or personal relationships that could have appeared to influence the work reported in this paper.

Acknowledgements

This research is funded by the Science and Engineering Research Board (SERB), DST, Government of India, through the Early Career Research Award (ECR/2017/002210).

References

[1] X. Zhang, Z. An, R. Dong, Y. Song, K. Zheng, Y. Sheng, Z. Shi, H. Zou, Properties and application of single Eu^{2+}-activated color tuning phosphors, ACS Sustain. Chem. Eng. 7 (2019) 10724–10733, https://doi.org/10.1021/acssuschemeng.9b01401

[2] Y. Chen, Z. Wang, W. Ding, X. Li, Q. Bao, J. Liu, K. Qiu, X. Meng, Z. Yang, P. Li, A single-phase white light emitting phosphor $Ba_3Y(PO_4)_3:Ce^{3+}$ /Eu^{2+}/Mn^{2+}: luminescence, energy transfer and thermal stability, J. Lumin. 210 (2019) 322–334, https://doi.org/10.1016/j.jlumin.2019.02.041

[3] N. Zhang, Y.T. Tsai, M.H. Fang, C.G. Ma, A. Lazarowska, S. Mahlik, M. Grinberg, C.Y. Chiang, W. Zhou, J.G. Lin, J.F. Lee, J. Zheng, C. Guo, R.S. Liu, Aluminate red phosphor in light-emitting diodes: theoretical calculations, charge varieties, and high-pressure luminescence analysis, ACS Appl. Mater. Interfaces 9 (2017) 23995–24004, https://doi.org/10.1021/acsami.7b06840

[4] W. Ye, C. Zhao, X. Shen, C. Ma, Z. Deng, Y. Li, Y. Wang, C. Zuo, Z. Wen, Y. Li, X. Yuan, C. Wang, Y. Cao, High Quantum yield $Gd_{4.67}Si_3O_{13}$: Eu^{3+} red - emitting phosphor for tunable white light - emitting devices driven by UV or Blue LED, ACS Appl. Electron. Mater. (2021) 2–11, https://doi.org/10.1021/acsaelm.1c00012

[5] M. Yazdan Mehr, A. Bahrami, W.D. van Driel, X.J. Fan, J.L. Davis, G.Q. Zhang, Degradation of optical materials in solid-state lighting systems, Int. Mater. Rev. 65 (2020) 102–128, https://doi.org/10.1080/09506608.2019.1565716

[6] Y. Chen, W. Ding, P. Li, X. Li, Q. Bao, J. Liu, K. Qiu, X. Meng, Z. Yang, Z. Wang, A single-phase white light emitting phosphor $Ba_3Y(PO_4)_3:Ce^{3+}$/Tb^{3+}/Mn^{2+}: luminescence, energy transfer and thermal stability, RSC Adv. 9 (2019) 30406–30418, https://doi.org/10.1039/c9ra05995d

[7] H. Guo, X. Huang, Y. Zeng, Synthesis and photoluminescence properties of novel highly thermal-stable red-emitting $Na_3Sc_2(PO_4)_3:Eu^{3+}$ phosphors for UV-excited white-light-emitting diodes, J. Alloy. Compd. 741 (2018) 300–306, https://doi.org/10.1016/j.jallcom.2017.12.316

[8] S.A. Khan, H. Zhong, W. Ji, L.Y. Hao, H. Abadikhah, X. Xu, N.Z. Khan, S. Agathopoulos, Single-phase white light-emitting $Ca_xBa_{(9-x)}Lu_2Si_6O_{24}:Eu^{2+}$/$Mn^{2+}$ phosphors, ACS Omega 2 (2017) 6270–6277, https://doi.org/10.1021/acsomega.7b00985

[9] H. Zhang, D. Yuan, X. Mi, X. Liu, J. Lin, Color tuning in $Ca_{3-x}M_x(PO_4)_2:Eu^{2+}$(M = Sr, Ba) phosphors via cation substitution, Dalton Trans. 49 (2020) 8949–8958, https://doi.org/10.1039/d0dt01130d

[10] H. Yoo, Y. Kouhara, H.C. Yoon, S.J. Park, J.H. Oh, Y.R. Do, Sn-P-F containing glass matrix for the fabrication of phosphor-in-glass for use in high power LEDs, RSC Adv. 6 (2016) 111640–111647, https://doi.org/10.1039/C6RA23294A

[11] X. Yang, J. Chen, C. Chai, S. Zheng, C. Chen, Near ultraviolet excited white light emitting diode (WLED) based on the blue $LiCaPO_4:Eu^{2+}$ phosphor, Optik 198 (2019) 163238, https://doi.org/10.1016/j.ijleo.2019.163238

[12] S.A. Khan, A. Jalil, Q. Ullah Khan, R.M. Irfan, I. Mehmood, K. Khan, M. Kiani, B. Dong, N.Z. Khan, J.L. Yu, L. Zhu, S. Agathopoulos, New physical insight into crystal structure, luminescence and optical properties of $YPO_4:Dy^{3+}$،Eu^{3+}،Tb^{3+} single-phase white-light-emitting phosphors, J. Alloy. Compd. 817 (2020) 152687, https://doi.org/10.1016/j.jallcom.2019.152687

[13] C. Suresh, H. Nagabhushana, G.P. Darshan, R.B. Basavaraj, B. Daruka Prasad, S.C. Sharma, M.K. Sateesh, J.P. Shabaaz Begum, Lanthanum oxyfluoride nanostructures prepared by modified sonochemical method and their use in the fields of optoelectronics and biotechnology, Arab. J. Chem. 11 (2018) 196–213, https://doi.org/10.1016/j.arabjc.2017.03.006

[14] Z. Zhao, K. Li, C. Liu, Q. Yin, J. Han, J. Heo, Intense up-conversion emission from Er^{3+}/Yb^{3+} ion co-doped transparent oxyfluoride glass-ceramics containing $Y_5O_4F_7$ nanorods for optical thermometry, J. Mater. Chem. C 7 (2019) 6134–6143, https://doi.org/10.1039/c9tc00280d

[15] J.S. Lee, S. Unithrattil, W.B. Im, Color-tunable binary solid-solution phosphor, $(Sr_3SiO_5)_{1-x}(Sr_3AlO_4F)_x$, for white LEDs: energy transfer mechanism between Ce^{3+} and Tb^{3+}, J. Alloy. Compd. 555 (2013) 297–303, https://doi.org/10.1016/j.jallcom.2012.12.050

[16] M. Shang, G. Li, X. Kang, D. Yang, D. Geng, J. Lin, Tunable luminescence and energy transfer properties of $Sr_3AlO_4F:RE^{3+}$ (RE = Tm/Tb, Eu, Ce) phosphors, ACS Appl. Mater. Interfaces 3 (2011) 2738–2746, https://doi.org/10.1021/am200534u

[17] S.P. Lee, S. De Liu, T.S. Chan, T.M. Chen, Synthesis and luminescence properties of novel Ce^{3+} and Eu^{2+}-doped lanthanum bromothiosilicate $La_3Br(SiS_4)_2$ phosphors for white LEDs, ACS Appl. Mater. Interfaces 8 (2016) 9218–9223, https://doi.org/10.1021/acsami.5b12125

[18] G. Li, Y. Tian, Y. Zhao, J. Lin, Recent progress in luminescence tuning of Ce^{3+} and Eu^{2+}-activated phosphors for pc-WLEDs, Chem. Soc. Rev. 44 (2015) 8688–8713, https://doi.org/10.1039/c4cs00446a

[19] X. Zheng, H. Luo, J. Liu, P. Liu, X. Yu, $Sr_3AlO_4F:Ce^{3+}$-based yellow phosphors: Structural tuning of optical properties and use in solid-state white lighting, J. Mater. Chem. C 1 (2013) 7598–7607, https://doi.org/10.1039/c3tc31460j

[20] W. Bin Im, S. Brinkley, J. Hu, A. Mikhailovsky, S.P. Denbaars, R. Seshadri, $Sr_{2.975-x}Ba_xCe_{0.025}AlO_4F$: a highly efficient green-emitting oxyfluoride phosphor for solid state white lighting, Chem. Mater. 22 (2010) 2842–2849, https://doi.org/10.1021/cm100010z

[21] W. Bin Im, N. George, J. Kurzman, S. Brinkley, A. Mikhailovsky, J. Hu, B.F. Chmelka, S.P. Denbaars, R. Seshadri, Efficient and color-tunable oxyfluoride solid solution phosphors for solid-state white lighting, Adv. Mater. 23 (2011) 2300–2305, https://doi.org/10.1002/adma.201003640

[22] X. Zheng, H. Luo, J. Liu, P. Liu, X. Yu, $Sr_3AlO_4F:Ce^{3+}$-based yellow phosphors: Structural tuning of optical properties and use in solid-state white lighting, J. Mater. Chem. C 1 (2013) 7598–7607, https://doi.org/10.1039/c3tc31460j

[23] J.S. Lee, S. Unithrattil, W. Bin Im, Color-tunable binary solid-solution phosphor, $(Sr_3SiO_5)_{1-x}(Sr_3AlO_4F)_x$, for white LEDs: energy transfer mechanism between Ce^{3+} and Tb^{3+}, J. Alloy. Compd. 555 (2013) 297–303, https://doi.org/10.1016/j.jallcom.2012.12.050

[24] M. Peng, G. Hong, Reduction from Eu^{3+} to Eu^{2+} in $BaAl_2O_4$:Eu phosphor prepared in an oxidizing atmosphere and luminescent properties of $BaAl_2O_4$:Eu, J. Lumin. 127 (2007) 735–740, https://doi.org/10.1016/j.jlumin.2007.04.012

[25] Y.H. Cho, D.H. Park, B.T. Ahn, Synthesis and characterization of Eu^{2+} doped $BaAl_2S_4$ phosphor by vacuum heat treatment, Proc. Int. Meet. Inf. Disp. 2006 (2006) 39–42.

[26] Y. Fang, Y.Q. Li, T. Qiu, A.C.A. Delsing, G. de With, H.T. Hintzen, Photoluminescence properties and local electronic structures of rare earth-activated Sr_3AlO_4F, J. Alloy. Compd. 496 (2010) 614–619, https://doi.org/10.1016/j.jallcom.2010.02.130

[27] X. Liu, W. Xie, Y. Lü, J. Feng, X. Tang, J. Lin, Y. Dai, Y. Xie, L. Yan, Multichannel luminescence properties of mixed-valent Eu^{2+}/Eu^{3+} coactivated $SrAl_3BO_7$ nanocrystalline phosphors for near-UV LEDs, Inorg. Chem. 56 (2017) 13829–13841, https://doi.org/10.1021/acs.inorgchem.7b01938

[28] F. Ruan, D. Deng, M. Wu, C. Wu, S. Xu, Tunable single-host full-color-emitting $Ca_9Zn_{1.5}(PO_4)_7$: Eu, Tb phosphor via Eu^{2+}/Eu^{3+} dual-emitting, J. Lumin. 198 (2018) 1–9, https://doi.org/10.1016/j.jlumin.2018.02.022

[29] B. Marí, K.C. Singh, N. Verma, M. Mollar, J. Jindal, Luminescence properties of Eu^{2+}/Eu^{3+} activated barium aluminate phosphors with Gd^{3+} concentration variation, Trans. Indian Ceram. Soc. 74 (2015) 157–161, https://doi.org/10.1080/0371750X.2015.1082932

[30] X. Gao, H. Liu, X. Yang, Y. Tian, X. Lu, L. Han, A novel Eu^{3+}/Eu^{2+} co-doped $MgSrLa_8(SiO_4)6O_2$ single-phase white light phosphor for white LEDs, RSC Adv. 7 (2017) 1711–1717, https://doi.org/10.1039/c6ra25792e

[31] Z. An, W. Liu, Y. Song, X. Zhang, R. Dong, X. Zhou, K. Zheng, Y. Sheng, Z. Shi, H. Zou, Color-tunable Eu^{2+},Eu^{3+} co-doped $Ca_{20}Al_{26}Mg_3Si_3O_{68}$ phosphor for w-LEDs, J. Mater. Chem. C 7 (2019) 6978–6985, https://doi.org/10.1039/c9tc01974j

[32] K.W. Huang, W.T. Chen, C.I. Chu, S.F. Hu, H.S. Sheu, B.M. Cheng, J.M. Chen, R.S. Liu, Controlling the activator site to tune europium valence in oxyfluoride phosphors, Chem. Mater. 24 (2012) 2220–2227, https://doi.org/10.1021/cm3011327

[33] A.A. Setlur, D.G. Porob, U. Happek, M.G. Brik, Inhomogenous broadening, charge compensation, and luminescence quenching in Ce^{3+} -Doped Sr_3AlO_4 F phosphors, ECS J. Solid State Sci. Technol. 5 (2016) R3089–R3095, https://doi.org/10.1149/2.0111601jss

[34] D. Kim, E. Lee, D. Ha, J. Lee, J.S. Bae, S. Il Ahn, I. Chung, S.J. Kim, J.C. Park, Highly luminous and green-emitting Eu^{2+} activated $Eu_{1-x}Sr_xAl_2O_4$ ($0 \le x \le 1$) materials for NUV-LEDs, Mater. Chem. Phys. 233 (2019) 185–193, https://doi.org/10.1016/j.matchemphys.2019.05.052

[35] Z. Wang, X. Hou, Y. Liu, Z. Hui, Z. Huang, M. Fang, X. Wu, Luminescence properties and energy transfer behavior of colour-tunable white-emitting $Sr_4Al_{14}O_{25}$ phosphors with co-doping of Eu^{2+}, Eu^{3+} $Mn^{4+}$and, RSC Adv. 7 (2017) 52995–53001, https://doi.org/10.1039/c7ra07970b

[36] S. Sreevalsa, P. Ranjith, S. Ahmad, S.K. Sahoo, S. Som, M.K. Pandey, S. Das, Host sensitized photoluminescence in $Sr_{2.9-3x/2}Ln_xAlO_4F$: $0.1Eu^{3+}$ (Ln = Gd, Y) for innovative flexible lighting applications, Ceram. Int. 46 (2020) 21448–21460, https://doi.org/10.1016/j.ceramint.2020.05.243

[37] S. Oswald, H. Wirth, Core-level shifts at B- and Al-doped 6H-SiC studied by XPS, Surf. Interface Anal. 27 (1999) 136–141, https://doi.org/10.1002/(SICI)1096-9918(199903)27:3<136::AID-SIA492>3.0.CO;2-Z

[38] S. Kim, M.C. Kim, S.H. Choi, K.J. Kim, H.N. Hwang, C.C. Hwang, Size dependence of Si 2p core-level shift at Si nanocrystal/ SiO_2 interfaces, Appl. Phys. Lett. 91 (2007) 1–4, https://doi.org/10.1063/1.2776014

[39] J.F. Moulder, W.F. Stickle, P.E. Sobol, K.D. Bomben, Handbook of X-ray Photoelectron Spectroscopy, Physical Electronics, Inc., 1992.

[40] G. Cheng, Q. Liu, L. Cheng, L. Lu, H. Sun, Y. Wu, Z. Bai, X. Zhang, G. Qiu, Synthesis and luminescence property of Sr_3SiO_5:Eu^{2+} phosphors for white LED, J. Rare Earths 28 (2010) 526–528, https://doi.org/10.1016/S1002-0721(09)60146-0

[41] J. Wang, H. Lin, Q. Huang, G. Xiao, J. Xu, B. Wang, T. Hu, Y. Wang, Structure and luminescence behavior of a single-ion activated single-phased $Ba_2Y_{3(}SiO_4)_3F$:Eu white-light phosphor, J. Mater. Chem. C 5 (2017) 1789–1797, https://doi.org/10.1039/c6tc04350j

[42] A.K. Kunti, L. Ghosh, S.K. Sharma, H.C. Swart, Synthesis and luminescence mechanism of white light emitting Eu^{3+} doped $CaZnV_2O_7$ phosphors, J. Lumin. 214 (2019) 116530, https://doi.org/10.1016/j.jlumin.2019.116530

[43] A.K. Kunti, N. Patra, R.A. Harris, S.K. Sharma, D. Bhattacharyya, S.N. Jha, H.C. Swart, Structural properties and luminescence dynamics of $CaZrO_3$:Eu^{3+}phosphors, Inorg. Chem. Front. (2021) 821–836, https://doi.org/10.1039/d0qi01178a

[44] A.K. Kunti, S.K. Sharma, R.J. Choudhary, H.C. Swart, Structural and luminescence properties of laser assisted Eu^{3+} doped $BaZrO_3$ thin films, J. Alloy. Compd. 801 (2019) 99–111, https://doi.org/10.1016/j.jallcom.2019.06.063

[45] Y. Chen, Castor oil-based polyurethane resin for low-density composites with bamboo charcoal, Polymers (2012) 1100, https://doi.org/10.3390/polym10101100

[46] M. Malik, R. Kaur, Mechanical and thermal properties of castor oil–based polyurethane adhesive: effect of TiO_2 filler, Adv. Polym. Technol. 37 (1) (2018) 1–7, https://doi.org/10.1002/adv.21637

[47] K.P. Somani, S.S. Kansara, N.K. Patel, A.K. Rakshit, Castor oil based polyurethane adhesives for wood-to-wood bonding, Int. J. Adhes. Adhes. 23 (4) (2003) 269–275, https://doi.org/10.1016/S0143-7496(03)00044-7